Aβ-driven cellular pathology in human neuronal models of Alzheimer's disease



A thesis submitted for the degree of Doctor of Philosophy

Bryan Zheng Hao Ng

St. John's College
Department of Physiology, Anatomy and Genetics
University of Oxford
Michaelmas Term 2021

Abstract

Alzheimer's disease (AD) is an insidious age-related neurodegenerative disease and the most common type of dementia. AD neuropathology typically involves the accumulation of extracellular plaques as well as intracellular neurofibrillary tangles that mainly consist of amyloid-β (Aβ) and hyperphosphorylated tau aggregates, respectively. Previous studies in animal models lacking the expression of *Mapt*, which encodes for microtubule-associated protein tau that is implicated in AD neuropathology, demonstrated that Aβ-driven toxicity is tau-dependent. However, inconsistent reports of Aβ-driven toxicity in *Mapt* homozygous knockout (*Mapt-/-*) animal models have emerged while a human *MAPT-/-* model remains unavailable to corroborate whether tau is essential to mediate the toxic phenotypes caused by Aβ in human genetic backgrounds. In this thesis, I describe the generation of the first human *MAPT-/-* induced pluripotent stem cell (iPSC) lines in collaboration with the Cowley research group in Oxford. Two isogenic panels of *MAPT-/-*, *MAPT+/-* and *MAPT+/+* iPSC lines, which were derived from two parental iPSC lines of healthy individuals, were identified. These iPSC lines were differentiated into cortical neurons in parallel and these neurons exhibited similar levels of cortical marker and synapse expression regardless of their *MAPT* genotypes. However, tau ablation in the iPSC-derived cortical neurons was sufficient to cause neurite outgrowth impairments, alterations in mitochondrial transport along axons, and reduced electrophysiological activities. Upon the exposure to extrinsic Aβ insults in the forms of synthetic oligomers or AD brain-derived Aβ, the *MAPT+/+* neurons experienced cytotoxicity, reduced number of anterograde motile mitochondria along axons, synapse loss, and hyperactivation *in vitro*. These adverse phenotypes could be reversed in the *MAPT-/-* neurons whereas Aβ-induced neurite outgrowth impairments were not rescued in the *MAPT-/-* neurons. Notably, having a reduced dosage of tau expression in the *MAPT+/-*

neurons was enough to be protective against cell death caused by Aβ. The study on Aβ-driven toxicity was extended to iPSC lines derived from the sporadic AD patients who participated in the Deep and Frequent Phenotyping pilot cohort. Synapse losses caused by extrinsic Aβ insults were quantified in thirteen lines of patient iPSC-derived cortical neurons and these neurons displayed varying levels of synaptic vulnerability to Aβ across patient lines. Their individual vulnerability to Aβ *in vitro* was demonstrated to reflect clinical vulnerability to Aβ burden measured by cognitive readouts from the same patients *in vivo*, suggesting that AD modelling with iPSCs is a tractable method to study individual levels of disease vulnerability. Here I present the experimental evidence on the effects of tau deletion in human iPSC-derived cortical neurons and show that tau is required in certain aspects of Aβ-driven toxicity. The clinical relevance of studying Aβ-driven toxicity using sporadic AD patient iPSC-derived cortical neurons was also investigated by demonstrating that individual clinical vulnerability to Aβ can be modelled *in vitro* using these neurons.

Acknowledgements

First and foremost, I would like to thank Richard, Tara and Natalie for the supervision and support. I have learnt a lot from all of you on how to conduct research as well as how to grow as a researcher. I can certainly say that I have enjoyed my four years here as a DPhil student and thank you for giving me the trust and flexibility as I worked on the research projects especially after the pandemic hit. To the rest of the Wade-Martins group, thank you for your kind support throughout my studies especially Dayne, Nora, Matt, Siv, Pip and Peter for your teaching, assistance, and advice.

I am grateful to Zam and Colin for taking their time to assess my projects during my Transfer of Status and Confirmation of Status milestones. I gained invaluable feedbacks from them, and many of the advice have been incorporated into my projects leading to significant improvements. The cortical neuron differentiation protocol involving co-culture with rat astrocytes was adapted from Colin's group, and I thank Dr Emma Whiteley for taking her time to share the technique with me.

To Jane and Sally, thank you for guiding me early in my DPhil studies as I worked on the *MAPT* knockout lines. I was initially unfamiliar with genetic manipulation on stem cells, but I managed to grasp the concept quickly thanks to their support.

In addition, I thank Prof. Dominic Walsh from Biogen for providing a vial of anti-amyloid antibody-containing rabbit serum which was the source of S97 antibody used in brain homogenate immunodepletion. I am grateful to Amarjit from the Wood group for sharing an ultracentrifuge rotor with me. Many thanks to John and Zam for sharing the multi-electrode array equipment throughout my DPhil studies.

I would like to thank the A*STAR Graduate Academy for funding my studentship here in Oxford. This has been an incredible opportunity and would have been impossible without the support from A*STAR, Singapore.

I am certainly indebted to the participants of the Deep and Frequent Phenotyping pilot cohort. I thank you for actively contributing to the research community especially in this pilot cohort where you needed to undergo many time-consuming and at times painful clinical tests, and I sincerely hope you agree with me that your contributions made a difference in dementia research. Furthermore, I would like to thank the Medical Research Council and National Institute for Health Research for jointly funding the pilot cohort run by the Dementias Platform UK as well as the stem cell study detailed in this thesis.

Finally, I would like to dedicate this thesis to my wife Stefanie and my son Ayden. I cannot imagine how my DPhil journey would be without your support, and I am so glad that I shared it with both of you despite the challenges we faced during the Covid-19 pandemic.

Collaborations

The generation of the *MAPT* knockout induced pluripotent stem cell (iPSC) lines was completed in collaboration with Jane Vowles and Dr Sally Cowley at the Dunn School of Pathology. Jane and Sally designed the gRNA sequences, delivered the Cas9-gRNA ribonucleoprotein into the iPSC lines, and collected the DNA from individual iPSC clones. After I confirmed the genotypes of the iPSC lines, Jane expanded the selected iPSC clones and cryopreserved them.

The project involving the patient-derived iPSC lines of the Deep and Frequent Phenotyping (DFP) pilot cohort is a local collaborative effort among three laboratories. I work with Dr Helen Rowland, Prof Noel Buckley, and Prof Simon Lovestone from the Department of Psychiatry; Dr Tina Wei and Prof Zameel Cader from the Weatherall Institute of Molecular Medicine. We communicate regularly with Dr Ivan Koychev, also from the Department of Psychiatry, regarding the clinical aspect of the DFP pilot cohort. Dr Emma Mee Hayes, previously from the Cader group, reprogrammed the patient erythroblasts into iPSCs before Dr Anne Hedegaard, previously from the Lovestone group, transduced the lines with lentivirus carrying plasmids expressing *Ngn2* and expanded the transduced iPSCs. I then used the transduced iPSC lines for the experiments described in Chapter 6.

Table of Contents

ABSTRACT **2**

ACKNOWLEDGEMENTS **4**

COLLABORATIONS **6**

TABLE OF CONTENTS **7**

LIST OF FIGURES **12**

LIST OF TABLES **15**

ABBREVIATIONS **16**

CHAPTER 1: INTRODUCTION **19**

1.1 ALZHEIMER'S DISEASE 19

1.1.1 Clinical features 20

1.1.2 Neuropathology 22

1.1.3 Genetic and non-genetic aetiology 32

1.2 AMYLOID-β AND TAU PROTEINS 38

1.2.1 Amyloid-β protein formation, functions, and disease associations 38

1.2.2 Tau protein functions and disease associations 42

1.3 ANIMAL MODELS OF ALZHEIMER'S DISEASE 47

1.3.1 Animal models mimicking Alzheimer's disease pathologies – focus on Amyloid-β-tau cooperation 47

1.3.2 Knockout animal models – focus on tau-dependent Amyloid-β-driven toxicity 50

1.4 HUMAN CELLULAR MODELS OF ALZHEIMER'S DISEASE 56

1.4.1 Induced pluripotent stem cell and CRISPR/Cas9 technologies 57

1.4.2 Induced pluripotent stem cell models of Alzheimer's disease 63
1.5 AIMS OF THE THESIS.....67
CHAPTER 2: METHODS AND MATERIALS.....68
2.1 GENERATION OF *MAPT* KNOCKOUT INDUCED PLURIPOTENT STEM CELL LINES.....68
2.2 DNA SEQUENCING, POLYMERASE CHAIN REACTION AND MOLECULAR CLONING.....69
2.3 DEEP AND FREQUENT PHENOTYPING PILOT COHORT AND PATIENT.....74
DERIVED INDUCED PLURIPOTENT STEM CELLS 74
2.4 INDUCED PLURIPOTENT STEM CELL CULTURE AND DIFFERENTIATION INTO.....77
CORTICAL NEURONS.....77
2.4.1 *MAPT* knockout lines 78
2.4.2 Deep and Frequent Phenotyping pilot cohort lines 81
2.5 PACKAGING OF LENTIVIRAL PLASMIDS 81
2.6 HARVESTING CELL LYSATE AND QUANTIFYING PROTEIN CONCENTRATION.....83
2.7 SDS-PAGE AND IMMUNOBLOT 83
2.8 RNA EXTRACTION AND QUANTITATIVE POLYMERASE CHAIN REACTION 85
2.9 EXTRACTION OF BRAIN HOMOGENATE FROM HUMAN ALZHEIMER'S DISEASE.....88
POST-MORTEM CORTICAL TISSUES 88
2.9.1 Isolating human brain-derived amyloid-β 89
2.9.2 Soluble amyloid-β immunoassay 90
2.10 SYNTHETIC AMYLOID-B OLIGOMERISATION 93
2.10.1 Amyloid-β_{1-42}.....93
2.10.2 Amyloid-β_{25-35} 93
2.11 TRANSMISSION ELECTRON MICROSCOPY.....93
2.12 THIOFLAVIN T ASSAY 94
2.13 HIGH-CONTENT IMAGING AND ANALYSIS.....94

2.13.1 Immunocytochemistry 96
2.13.2 Live neurite tracing 98
2.14 CYTOTOXICITY ASSAY MEASURED BY ADENYLATE KINASE 99
2.15 MITOCHONDRIAL AXONAL TRANSPORT LIVE IMAGING IN MICROFLUIDIC DEVICES 99
2.16 MITOCHONDRIAL MEMBRANE POTENTIAL MEASUREMENT WITH JC-10 101
2.17 MULTI-ELECTRODE ARRAY ASSAYS 102
2.18 PATCH-CLAMP ELECTROPHYSIOLOGY 102
2.19 STATISTICAL ANALYSIS 103
CHAPTER 3: IDENTIFICATION AND CHARACTERISATION OF *MAPT-/-* IPSC LINES 105
3.1 INTRODUCTION 105
3.1.1 Aims of this chapter 105
3.2 RATIONALE OF KNOCKOUT STRATEGIES 106
3.3 RESULTS 107
3.3.1 DNA sequencing to identify successful *MAPT-/-* iPSC clones 107
3.3.2 *MAPT* transcript and tau protein expression validation 111
3.3.3 Characterisation of iPSC-derived cortical neurons 114
3.4 DISCUSSION 118
CHAPTER 4: CELLULAR PHENOTYPES OF *MAPT-/-* IPSC-DERIVED CORTICAL NEURONS 122
4.1 INTRODUCTION 122
4.1.1 Aims of this chapter 123
4.2 RESULTS 124

4.2.1 Experimental design- neurite tracing by live imaging.....124
4.2.2 Neurite outgrowth of *MAPT*-/- iPSC-derived neurons.....126
4.2.3 Neurite outgrowth impairment caused by extrinsic Aβ insults.....132
4.2.4 Experimental design - cytotoxicity assays.....135
4.2.5 Aβ-driven cytotoxicity in iPSC-derived neurons.....137
4.2.6 Experimental design - mitochondrial transport by live imaging.....142
4.2.7 Mitochondrial transport along axons in *MAPT*-/- iPSC-derived neurons.....144
4.2.8 Mitochondrial transport deficits caused by extrinsic Aβ insults.....147
4.2.9 Mitochondrial membrane potential in the *MAPT*-/- iPSC-derived neurons and effects caused by extrinsic Aβ insults.....151
4.4 DISCUSSION.....153
CHAPTER 5: SYNAPTIC AND ELECTROPHYSIOLOGICAL PHENOTYPES OF *MAPT*-/- IPSC-DERIVED CORTICAL NEURONS.....158
5.1 INTRODUCTION.....158
5.1.1 Aims of this chapter.....159
5.2 RESULTS.....159
5.2.1 Experimental design - synapse imaging by ICC.....159
5.2.2 Synaptic density and loss in *MAPT*-/- neurons caused by extrinsic Aβ insults162
5.2.3 Experimental design - electrophysiology by MEA.....166
5.2.4 Action potential firing in *MAPT*-/- neurons measured by MEA.....167
5.2.5 Action potential firing changes caused by extrinsic Aβ insults.....170
5.2.6 Electrophysiological properties in *MAPT*-/- neurons by patch-clamp.....173
5.3 DISCUSSION.....175

CHAPTER 6: AD PATIENT IPSC-DERIVED CORTICAL NEURONS FROM THE DFP PILOT COHORT 180

6.1 INTRODUCTION 180

6.1.1 Aims of this chapter 181

6.2 RESULTS 182

6.2.1 Experimental design 182

6.2.2 Characterisation and synapse loss caused by extrinsic Aβ insults of the DFP cohort patient-derived neurons 183

6.2.3 Correlation of synaptic vulnerability in patient-derived neurons with clinical outcomes of the same patients 188

6.3 DISCUSSION 195

CHAPTER 7: GENERAL DISCUSSION AND CONCLUSION 199

REFERENCES 211

List of figures

Figure 1.1.2.1: Gross anatomy of Alzheimer's brain 24

Figure 1.1.2.2: Amyloid plaques visualisation 25

Figure 1.1.2.3: Neurofibrillary tangles (NFT) visualisation.....26

Figure 1.1.2.4: Brain imaging of AD with dementia.....32

Figure 1.1.3.2: Effect sizes of AD associated variants for the respective minor alleles 36

Figure 1.2.1: The process of APP processing and Aβ aggregation 39

Figure 1.2.2.1: Chromosomal location of the gene and protein structure for microtubule-associated protein tau.....43

Figure 1.2.2.2: Putative phosphorylation sites on tau protein and epitopes specific for major tau antibodies.....46

Figure 1.4.1.1: Approaching human iPSC disease modelling.....59

Figure 1.4.1.2: Schematic representation of the CRISPR/Cas9 gene editing system 62

Figure 2.4.1: Schematic of the cortical neuron differentiation protocol used for the *MAPT* knockout lines.....80

Figure 2.4.2: Schematic of the cortical neuron differentiation for the iPSC lines derived from the DFP pilot cohort 81

Figure 2.9.2: Quantification of Aβ in AD brain homogenate and isolated brain-derived Aβ 92

Figure 3.3.3: Characterisation of iPSC-derived cortical neurons.....116

Figure 4.2.1: Representative image of the neurite tracing experiment design 125

Figure 4.2.2: Neurite outgrowth quantification in Day 35-36 iPSC-derived cortical neurons of the isogenic *MAPT-/-* lines.....128

Figure 4.2.3: Quantifications of neurite outgrowth impairment caused by 10 μM of $A\beta_{1-42}$ oligomer in the Day 35-36 iPSC-derived cortical neurons of the *MAPT-/-* isogenic lines133

Figure 4.2.4: Quantification of cytotoxicity measured by CC3 ICC.....136
Figure 4.2.5: Quantifications of cytotoxicity caused by 5-day exposure to 10 μM of $A\beta_{1-42}$ oligomers in Day 79-83 (Exon 1) or Day 79-86 (Exon 4) iPSC-derived cortical neurons from the *MAPT-/-* isogenic lines. 138
Figure 4.2.6: Mitochondrial transport along axons organised in microfluidic chambers..143
Figure 4.2.7: TrackMate analysis of baseline mitochondrial transport along axons in Day 70-95 iPSC-derived cortical neurons from the Exon 4 lines seeded in microfluidic chambers 146
Figure 4.2.8: TrackMate analysis of mitochondrial transport along axons 1 h post-treatment with 2 μM of $A\beta_{1-42}$ oligomers in Day 70-95 iPSC-derived cortical neurons from the Exon 4 lines seeded in microfluidic chambers.....149
Figure 4.2.9: Quantification of mitochondrial membrane potential by measuring JC-10 fluorescence in Day 52-56 iPSC-derived cortical neurons from both *MAPT* isogenic panels 152
Figure 5.2.1: Synapse imaging by ICC.....161
Figure 5.2.2: Quantifications of synaptic density and synapse loss in both isogenic panels of *MAPT-/-* iPSC-derived cortical neurons.....164
Figure 5.2.3: Representative images of the MEA system 166
Figure 5.2.4: Quantification of baseline AP parameters measured by MEA assay in Day 90-100 iPSC-derived cortical neurons from both MAPT-/- isogenic panels.....169
Figure 5.2.5: Quantification of AP parameters under the exposure to extrinsic Aβ insults in Day 90-100 iPSC-derived cortical neurons 171
Figure 5.2.6: Electrophysiological properties by patch-clamp in aged iPSC-derived cortical neurons from the MAPT-/- isogenic panels 174

Figure 6.2.2: Characterisation of iPSC-derived neurons from the DFP pilot cohort and synapse loss caused by various sources of extrinsic Aβ insults 185

Figure 6.2.3.1: Correlating cellular vulnerability measured by synapse loss with clinical vulnerability to Aβ 192

Figure 6.2.3.2: Correlating cellular vulnerability measured by synapse loss with clinical tau biomarkers 194

List of tables

Table 1.1.2: AT(N) biomarker profiles and corresponding interpretations for AD 27

Table 1.3.2: Summary of phenotypes of germline and conditional knockout of proteins associated with the amyloidogenic pathway of APP processing in mouse 51

Table 2.1 List of gRNAs used in CRISPR/Cas9 system targeting *MAPT* gene.....68

Table 2.2.1: Reagents and conditions of sequencing PCR with BigDye™ v3.1 70

Table 2.2.2: List of primers targeting *MAPT* in PCR for DNA amplification prior to sequencing 71

Table 2.2.3: Reagents and conditions of PCR with AmpliTaq Gold™ 73

Table 2.2.4: Reagents of restriction enzyme digest reaction.....74

Table 2.2.5: Reagents of DNA ligation reaction 74

Table 2.3.1: Characteristics of the DFP pilot cohort participants 76

Table 2.3.2: DFP pilot cohort patient-derived iPSC identification numbers.....77

Table 2.7: List of primary and secondary antibodies used for immunoblotting.....85

Table 2.8.1: Conditions of SuperScript™ III Reverse Transcriptase System.....86

Table 2.8.2: Conditions of qPCR with TaqMan Expression Assays.....87

Table 2.8.3: List of TaqMan qPCR primers used to quantify *MAPT* transcripts 87

Table 2.9.1: Calculations of elution efficiency for brain-derived Aβ enrichment over 7 attempts.....90

Table 2.13.1: List of primary and secondary antibodies used for immunocytochemistry ..97

Table 3.3.1: List of genotype-confirmed iPSC lines of the *MAPT* knockout isogenic panels 108

Abbreviations

-/- = Homozygous knockout

+/- = Heterozygous knockout

+/+ = Wild type

ΔE9 = Skipped exon 9, a mutation on the *PSEN1* gene

Aβ = Amyloid-β protein

aCSF = Artificial cerebrospinal fluid

AD = Alzheimer's disease

AICD = APP intracellular domain

AK = Adenylate kinase

ALS = Amyotrophic lateral sclerosis

AP = Action potentials

APP = Amyloid precursor protein

BBB = Blood-brain barrier

BCA = Bicinchoninic acid

bp = Base pair

BSA = Bovine serum albumin

Cas9 = CRISPR-associated protein 9

CBD = Corticobasal degeneration

CC3 = Cleaved caspase 3

CCCP = Carbonyl cyanide m-chlorophenyl hydrazone

cDNA = Complementary DNA

CI = Confidence interval

CNS = Central nervous system

CRISPR = Clustered regularly interspaced short palindromic repeats

crRNA = CRISPR RNA

CSF = Cerebrospinal fluid

DFP = Deep and Frequent Phenotyping

DMSO = Dimethyl sulfoxide

DSB = Double-stranded break

DTT = Dithiothreitol

dNTP = Deoxyribonucleoside triphosphate

EDTA = Ethylenediaminetetraacetic acid

EGTA = Ethyleneglycoltetraacetic acid

EOAD = Early-onset Alzheimer's disease

fAD = Familial Alzheimer's disease

FDG = ^{18}F-fluorodeoxyglucose

FTD = Frontotemporal dementia

FBS = Foetal bovine serum

GFP = Green fluorescent protein

gRNA = Guide RNA

GWAS = Genome-wide association study

HBSS = Hank's balanced salt solution

HC = Healthy control

HRP = Horseradish peroxidase

ICC = Immunocytochemistry

ID = Immunodepletion

IHC = Immunohistochemistry

int4del = Intro 4 deletion, a mutation on the *PSEN1* gene

IP = Immunoprecipitation

iPSC = Induced pluripotent stem cell

LB = Luria-Bertani broth

LBD = Lewy body dementia

LOAD = Late-onset Alzheimer's disease

LTD = Long-term depression

LTP = Long-term potentiation

MAP = Microtubule-associated protein

MAPT = Gene encoding for microtubule-associated protein tau

MCI = Mild cognitive impairment

MEG = Magnetoencephalography

mEPSC = Miniature excitatory postsynaptic current

MMSE = Mini mental state examination

MODEL-AD = Model Organism Development and Evaluation for Late-onset Alzheimer's Disease consortium

MOI = Multiplicity of infection

mRNA = Messenger RNA

NHEJ = Non-homologous end joining

NIA-AA = National Institute on Aging and Alzheimer's Association

NIM = Neural induction medium

NMD = Nonsense-mediated decay

NMM = Neural maintenance medium

NPC = Neural progenitor cell

PAF = Population attributable fraction

PBS = Phosphate-buffered saline

PCR = Polymerase chain reaction

PD = Parkinson's disease

PES = Polyethersulfone

PET = Positron emission tomography

PHF = Paired helical filament

PO/L = Poly-L-ornithine and laminin

PRS = Polygenic risk score

PSEN1 = Presenilin-1

PSEN2 = Presenilin-2

pTau181 = Phospho-tau at the residue Thr181 position

RIPA = Radioimmunoprecipitation assay

sAD = Sporadic Alzheimer's disease

SD = Standard deviation

SDS-PAGE = Sodium dodecyl sulphate–polyacrylamide gel electrophoresis

SEM = Standard error of the mean

sMRI = Structural magnetic resonance imaging

StemBANCC = Stem cells for biological assays of novel drugs and predictive toxicology

TALEN = Transcription activator-like effector nucleases

TBI = Traumatic brain injury

TBST = Tris-buffered saline with 0.1% Tween-20

TEM = Transmission electron microscopy

tracrRNA = Trans-activating CRISPR RNA

tTau = Total tau

qPCR = Quantitative polymerase chain reaction

VaD = Vascular dementia

ZFN = Zinc finger nucleases

Chapter 1: Introduction

1.1 Alzheimer's disease

Alzheimer's disease (AD) is the most common age-related neurodegenerative disease and cause for dementia, estimated to affect close to 50 million people in 2015 worldwide with cases predicted to almost double every 20 years due to ageing populations. As such, the economic cost of AD has been growing rapidly and is estimated to incur USD$ 2 trillion per year by 2030 [1]. According to the World Health Organisation, AD and other dementias were the seventh leading cause of death in 2019 killing almost 2 million people [2], and this was not inclusive of undiagnosed dementia cases which were reported to account for approximately 75% of the true number of people suffering from dementia [3]. These figures signify the pressing need to address the issues associated with AD from diagnosis to treatment.

First described by Dr Alois Alzheimer in 1907 [4] based on a single case of a 50-year-old woman named Auguste D. displaying psychiatric symptoms and memory disturbances. Upon her death, her brain tissues were used for morphological and histological analyses that led to the observation of amyloid plaques and neurofibrillary tangles (NFT) [5] which were later established to be the pathological hallmarks of AD [6]. More than a century later, the precise cause(s) of AD remains elusive and we now know that AD is a heterogeneous and multi-factorial disease.

There had been no disease-modifying treatments available for AD until recently when GV-971 (a sodium oligosaccharide mixture [7] developed by Shanghai Green Valley Pharmaceuticals) and aducanumab (a monoclonal antibody [8] developed jointly by Biogen Inc. and Eisai Co.) were approved to treat AD by the National Medical Products

Administration in China and the Food and Drug Administration in the United States, respectively in November 2018 and June 2021. However, GV-971 has not been approved for use in treating AD by any other country and the approval of aducanumab was met with controversy [9]. As a result, aducanumab was subsequently rejected by both the European Medicines Agency and Japan's Ministry of Health for use in treating AD around the point of writing in December 2021 leaving much of the world still without access to any option of disease-modifying treatment for AD.

1.1.1 Clinical features

AD is an insidious disease characterised by clinical syndromes of dementia with patients displaying progressive loss of cognitive functions and memory. The patients can be categorised into early-onset AD (EOAD; < 65 years old is a common and arbitrary threshold) or late-onset AD (LOAD) based on their age of diagnosis [10]. In a study involving 3,747 AD patients, EOAD accounted for 16.4% of all cases and manifested more aggressive cognitive decline [11]. Another way to collectively differentiate AD patients is to determine if they are of familial AD (fAD) carrying an inherited autosomal dominant gene mutation (more to be discussed in Chapter 1.1.3) that causes AD or sporadic AD (sAD) without a genetic cause. fAD patients generally belong in the EOAD group [12] and it was previously demonstrated that only 1.6% of an EOAD cohort possessed a known gene mutation for AD [13]. Put together, fAD constitutes a small percentage of all AD cases (< 1%) while sAD mainly overlaps with LOAD, but a significant number of sAD patients are early-onset.

In practice, AD clinical manifestations indicate a disease continuum with overlapping symptoms, neuropathological status, and genetic risk factors. The overlapping symptoms

with other major progressive dementias such as frontotemporal dementia (FTD), vascular dementia (VaD) and Lewy body dementia (LBD) made it more difficult to accurately diagnose AD by clinical symptoms on cognition alone [14]. To address this issue, the National Institute on Aging and Alzheimer's Association (NIA-AA) in the United States updated the diagnostic guidelines for AD in 2011 [15–17]. The update recognised progressive stages of AD based on a spectrum of clinical severity and classified the disease mainly into preclinical (pathological change in the brain without significant clinical symptoms), mild cognitive impairment (MCI; some memory and cognitive problems but not sufficient to interfere with independence), and Alzheimer's dementia (memory loss and significant cognitive impairments affecting independence) stages. This is coupled with the recognition for potentially utilising brain imaging and fluid biomarkers (more in Chapter 1.1.2), which were not available before, for clinical diagnosis. The only way to confirm AD diagnosis prior to the advent of biomarkers was through post-mortem histological analyses.

Another important aspect of AD clinical observation to aid diagnosis is the presentation of psychological and behavioural changes such as depression, psychosis, and aggression [18–20]. These neuropsychiatric symptoms often occur early in the progression to AD and have significant impact on patients' quality of life. Moreover, it has been previously reported that such neuropsychiatric symptoms are predictive of worsening cognitive function and subsequently dementia [21–23]. However, noncognitive symptoms like the neuropsychiatric symptoms many AD patients display (notably the first AD case Auguste D. experienced severe delusions) have not been included in the clinical diagnostic criteria [15–17] published by the NIA-AA likely due to the variability along disease progression and lack of specificity to AD [24,25].

Life expectancy post-diagnosis for AD patients ranges from 3 to 10 years depending on the age of diagnosis with younger patients (i.e., in their 60s) generally having longer lifespan [26]. As mentioned before, no disease-modifying treatment is available for AD. In general, clinicians recommend lifestyle changes to manage cardiovascular risks to contribute to overall brain health especially when the extent of cognitive decline is not affecting an individual's everyday life [27]. Pharmacological interventions are also available such as cholinesterase inhibitors (e.g., donepezil) or N-methyl-D-aspartate receptor (NMDAR) antagonists (e.g., memantine) to ameliorate cognitive symptoms in more advanced stages of AD [28].

1.1.2 Neuropathology

Post-mortem AD brain often exhibits macroscopic features that can be used in supporting diagnosis but none of those features alone are specific to AD [29]. Conspicuous cortical atrophy and narrowing of gyri can often be observed in AD brain as compared to a normal brain (Figure 1.1.2.1). These macroscopic changes can also provide useful information for research by estimating the extent of region-specific atrophy of a particular patient. To definitively diagnose AD, however, post-mortem histological identification of dense core amyloid plaques and NFTs in brain tissue is required (Figures 1.1.2.2 and 1.1.2.3, respectively). These microscopic structures used to be visualised via chemical histology using methods such as silver staining, Congo Red staining, or Thioflavin S staining. It was later found that amyloid plaques constitute of primarily aggregates of amyloid-β protein (Aβ; more to be discussed in Chapter 1.2.1) [30] whereas NFTs constitute of primarily hyperphosphorylated tau protein (more to be discussed in Chapter 1.2.2) in an aggregated arrangement of paired helical filaments (PHFs) named after its ultrastructure under an

electron microscope [31,32]. Since then, immunohistochemical (IHC) procedures have been more commonly used instead with anti-Aβ and anti-tau antibodies to detect AD neuropathology. Amyloid plaques can exist in the form of diffuse (Figure 1.1.2.2A) or dense-core (Figure 1.1.2.2B) plaques. While diffuse plaques are commonly present in cognitively normal aged brains, dense-core plaques are found more specifically in AD brain [6]. NFT pathology can also be visualised via IHC showing hyperphosphorylated tau PHFs in soma (Figure 1.1.2.3C) as well as neurites (Figure 1.1.2.3D).

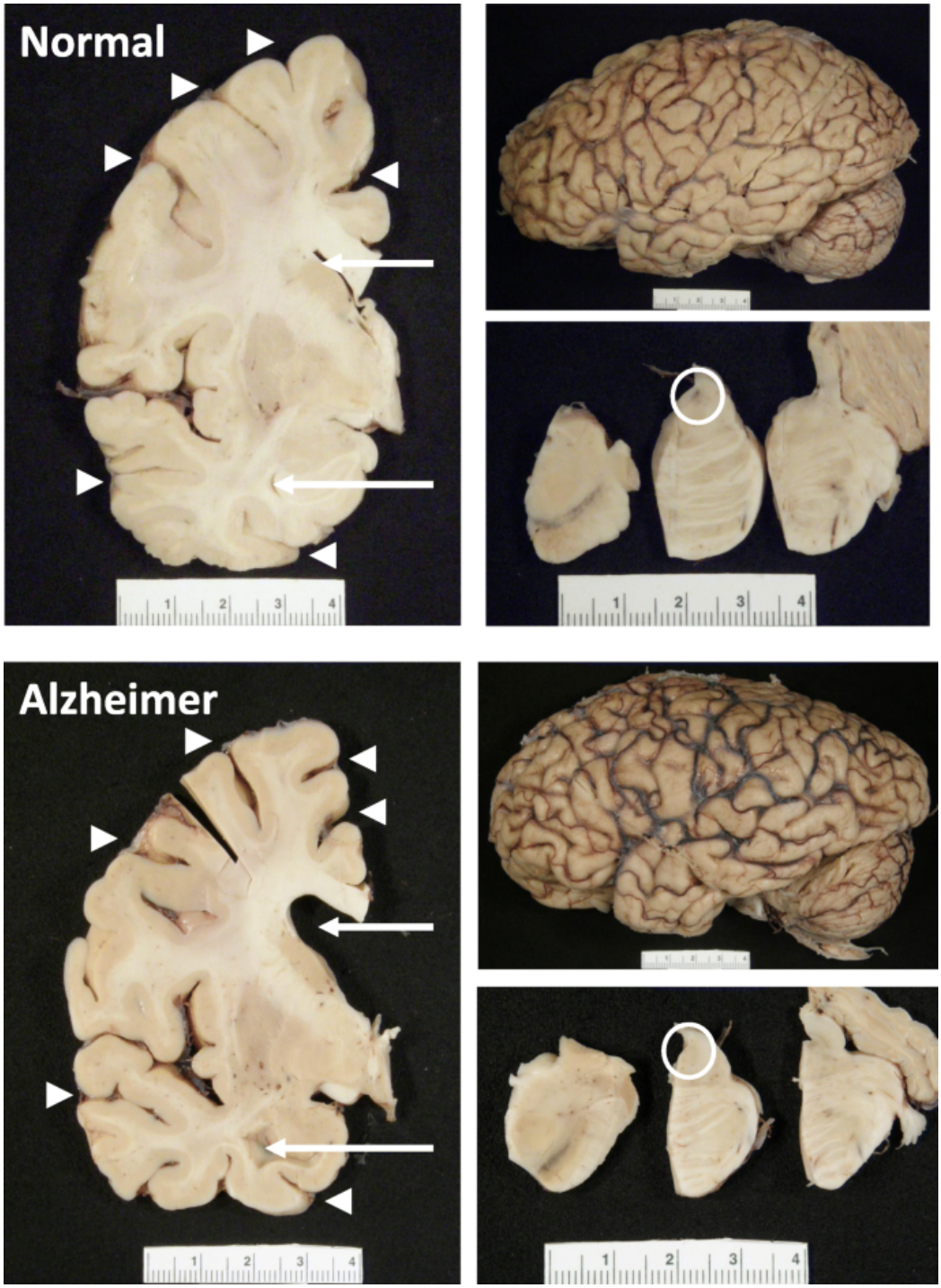


Figure 1.1.2.1: Gross anatomy of Alzheimer's brain
Lateral view of an Alzheimer's brain can show widening of sulcal spaces and narrowing of gyri compared to a normal brain. This may be more readily observed in coronal sections as indicated by the arrowheads, and this atrophy is often accompanied by enlargement of the frontal and temporal horns of the lateral ventricles as highlighted by the arrows. Additionally, loss of pigmented neurons in the locus coeruleus is commonly observed in the pontine tegmentum as shown with the open circle. Adapted without any changes except reformatting image captions from Deture *et. al.* [29] under the Creative Commons Attribution 4.0 licence detailed in https://creativecommons.org/licenses/by/4.0/.

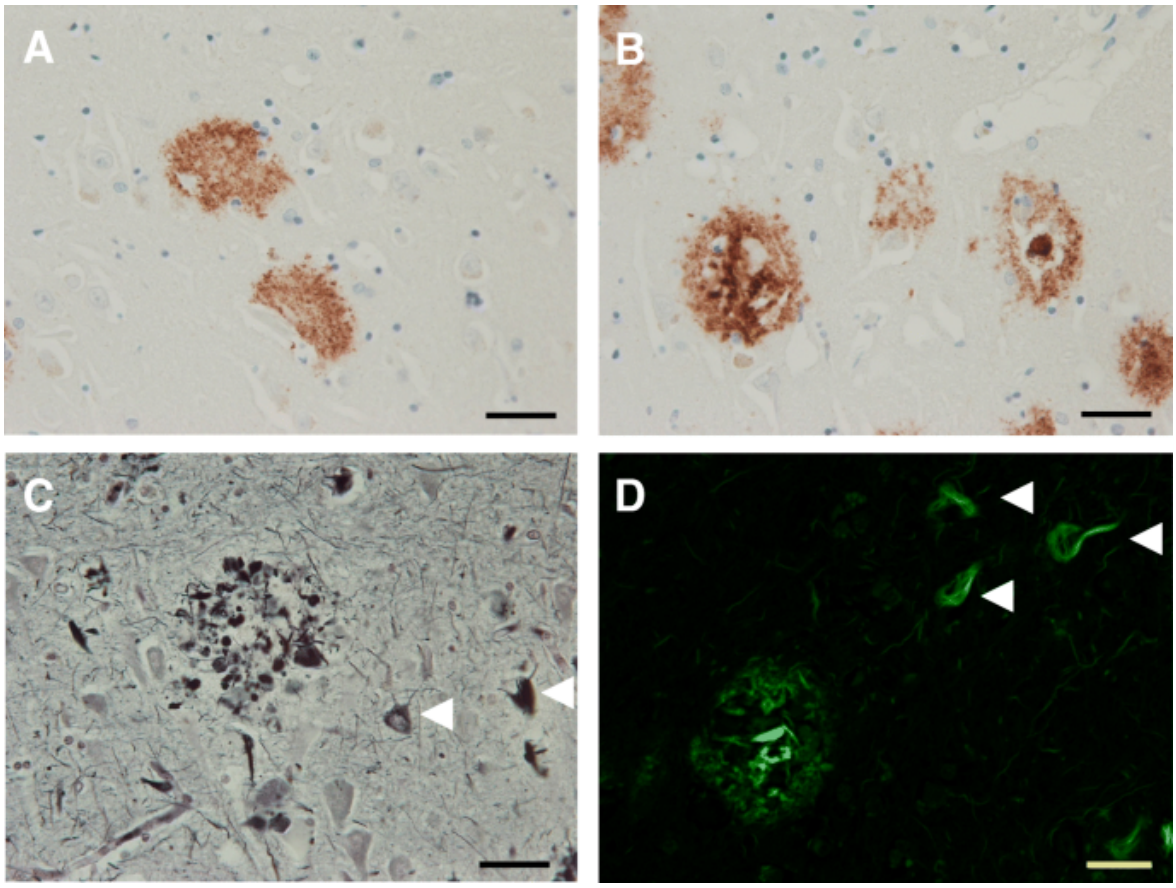


Figure 1.1.2.2: Amyloid plaques visualisation
Immunohistochemistry of affected Alzheimer's brain tissues using antibodies directed against Aβ peptides demonstrates the presence of both (A) diffuse and (B) dense core amyloid plaques. These dense core plaques are often associated with neuritic elements that can stain filamentous tau and correlate with disease severity. Neuritic AD plaques are readily observed using (C) Bielchowsky silver staining or (D) Thioflavin S staining. These stains can also label neurofibrillary tangles as shown by the arrowheads. Scale bars = 40 µm. Adapted without any changes except reformatting image captions from Deture *et. al.* [29] under the Creative Commons Attribution 4.0 licence detailed in https://creativecommons.org/licenses/by/4.0/.

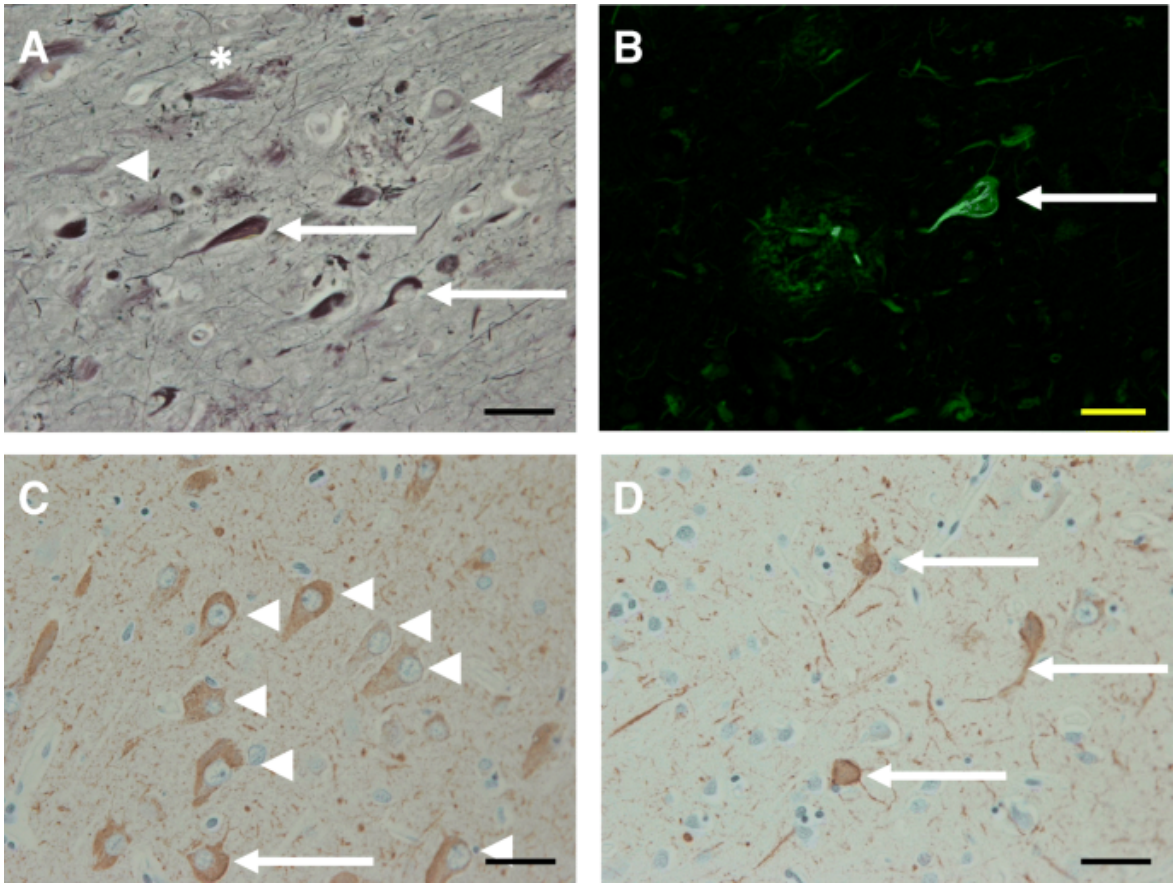


Figure 1.1.2.3: Neurofibrillary tangles (NFT) visualisation
NFT develop from intracellular pre-tangles containing misfolded tau and small tau aggregates to mature NFTs containing bundles of cross-linked tau filaments before the neuron dies and an extracellular ghost tangle (asterisk) remains. (A) Silver staining and (B) Thioflavin S capture many mature tangles (arrows) and some pre-tangles (arrowheads) along with amyloid plaques and tau neuropil threads. Development of NFTs from the pre-tangles is more easily visualized using tau immunohistochemistry (C, D). Scale bars = 40 µm. Adapted without any changes except reformatting image captions from Deture *et. al.* [29] under the Creative Commons Attribution 4.0 licence detailed in https://creativecommons.org/licenses/by/4.0/.

For the first century after the first AD case was described, post-mortem identification was the only conclusive method to diagnose AD and define disease propagation stage (i.e., Braak stage) of AD [33]. However, the advent of AD biomarkers in recent years has made it possible to visualise or detect neuropathology *in vivo*. This has led to another supplementary update in 2018 [34] on the NIA-AA guidelines mentioned in Chapter 1.1.1 that AD is "defined *in vivo* by biomarkers and by post-mortem examination, not by clinical symptoms"

but cognitive decline observed in the clinic is still the primary parameter to stage AD progression from preclinical to clinical dementia stages. The biological definition of AD applies only in the research context, such as cohort studies and interventional trials, but not formal diagnosis in a clinical setting. In this Chapter on AD neuropathology, I will mainly focus on the biomarkers included in the 2018 NIA-AA guidelines categorised under the AT(N) biomarker grouping to define AD (Table 1.1.2).

Table 1.1.2: AT(N) biomarker profiles and corresponding interpretations for AD
A: Aggregated Aβ; T: Aggregated tau; (N): Neurodegeneration. Adapted without any changes from Jack *et. al.* [34] under the CC BY-NC-ND 4.0 licence detailed in https://creativecommons.org/licenses/by-nc-nd/4.0/.

AT(N) profiles	Biomarker category	
A-T-(N)-	Normal AD biomarkers	
A+T-(N)-	Alzheimer's pathologic changes	Alzheimer's continuum
A+T+(N)-	Alzheimer's disease	
A+T+(N)+	Alzheimer's disease	
A+T-(N)+	Alzheimer's and concomitant suspected non-Alzheimer's pathologic change	
A-T+(N)-	Non-AD pathologic change	
A-T-(N)+	Non-AD pathologic change	
A-T+(N)+	Non-AD pathologic change	

A: Aggregated Aβ or associated pathological state

Aβ in *vivo* can be visualised by positron emission tomography (PET) brain imaging (Figure 1.1.2.4) where a radioisotope ligand that can bind to Aβ is injected intravenously into an individual before scanning, and that amyloid PET could detect Aβ accumulation in the brain as early as 20 years before the expected age of onset in fAD patients [35]. The first PET ligand developed for Aβ is a ^{11}C-labelled agent known as Pittsburgh Compound-B (PiB) [36] which could differentiate AD cases from healthy control (HC) subjects by showing

greater retention in the cortical areas. As the radioactive half-life of ^{11}C-labelled ligands is relatively short (20 min), ^{18}F-labelled radiotracers such as florbetapir (also ^{18}F-AV-45) later emerged as a better alternative with a 110-min half-life and could also distinguish AD patients from HC individuals [37,38]. The use of amyloid PET was further validated by the strong correlation between ante-mortem amyloid PET and post-mortem analysis of amyloid burden from the same individuals [39].

Apart from brain imaging, Aβ can also be detected in the cerebrospinal fluid (CSF) by immunoassays or mass spectrometry-based assays. Both $A\beta_{1\text{-}40}$ and $A\beta_{1\text{-}42}$ species (more on Aβ species in Chapter 1.2.1), as well as the resultant Aβ 1-42:1-40 ratio have been measured in AD CSF. $A\beta_{1\text{-}42}$ concentration was reported to be lower in AD patients compared to HC, most likely due to the aggregation of $A\beta_{1\text{-}42}$ preventing it from being transported into the CSF [40], whereas $A\beta_{1\text{-}40}$ concentration did not differ between the two groups [41–43]. When multiple studies on AD CSF are taken into account, Aβ 1-42:1-40 ratio generally demonstrates comparable if not better diagnostic accuracy including differentiating MCI from AD [44]. Importantly, detection of Aβ changes in the CSF was shown to precede Aβ accumulation identified by amyloid PET [45] making it one of the most sensitive methods to uncover brain changes long before AD symptom onset.

T: Aggregated tau (NFT) or associated pathologic state

Similar to Aβ biomarkers, tau pathology can be visualised and detected *in vivo* via the aforementioned methods (Figure 1.1.2.4). Tau PET detecting the accumulation of pathological NFT using flortaucipir (^{18}F-AV-1451; same as the one used in the analysis in

Chapter 6) radiotracer in the brain can distinguish AD from cognitively normal individuals [46,47]. In addition, concentration of phosphorylated tau (pTau) such as the one situated at the T181 [48] or T231 [49] residues that are elevated specifically in AD CSF samples. Compared to Aβ biomarkers, tau biomarkers emerge at detectable levels closer to symptom onset as cognitively normal individuals with Aβ pathology were identified to present without tau pathology measured by both PET and pTau concentration in the CSF [50,51]. Crucially, pTau in the CSF showed correlation with NFT pathology upon post-mortem analysis [52]. More recently, the capability to detect differential levels of Aβ and pTau in the plasma of AD patients [53,54], albeit at very low concentration, gave rise to the possibility to potentially scale up AD biomarker trials since blood samples are generally more readily available.

Correlation with cognitive decline

Despite the ability to detect specific AD pathology *in vivo* by differentiating AD from other types of dementia [55,56], Aβ and tau biomarkers differ in their correlation with cognitive outcomes in AD patients. There was no correlation between CSF concentration of $A\beta_{1-42}$ with duration and severity of dementia in one of the earliest studies on Aβ in the CSF [42] whereas pTau concentration in the CSF correlates with progression of cognitive decline in MCI subjects [49]. Furthermore, tau PET was found to be more superior than amyloid PET in determining prognostic cognitive decline [57] and overall the best predictor of cognitive decline in one study when taking both CSF and PET data into account [58]. In fact, Braak staging of AD propagation in the brain is based on the severity of widespread NFT pathology in the brain [33]. These results of CSF and PET measurements confirmed the early

neuropathological studies where NFT deposition was shown to correlate with AD severity measured by cognitive tests instead of amyloid plaques [59,60]. Nevertheless, Aβ biomarkers are more specific to AD and tau biomarkers alone cannot conclusively indicate AD pathology due to the potential implication of other tauopathies (i.e., neurological diseases exhibiting tau pathology). It was previously reported in a multi-centre study suggested that $A\beta_{1-42}$ concentration in the CSF alone, as opposed to CSF pTau, achieved the best differential diagnostic sensitivity and specificity for AD among other types of dementia including tauopathies such as FTD [61].

(N): Neurodegeneration or neuronal injury

Although neurodegeneration is not AD-specific, several concomitant biomarkers of neurodegeneration have been shown to accompany AD pathological markers mentioned above. In the AT(N) profile, the bracket around the (N) biomarkers was placed to indicate the supplementary nature of (N) biomarkers to define AD. Concomitant increase in concentration of total tau (tTau) in the CSF of AD patients is often observed with the rise of pTau, yet tTau is not as specific to AD as $A\beta_{1-42}$ or pTau. As such, CSF tTau has been used to improve diagnostic power of $A\beta_{1-42}$ or pTau but the increase in tTau alone overlaps significantly with other types of dementia including tauopathies [48,49,55]. CSF tTau is therefore thought to more likely reflect axonal degeneration (tau can be found in the axons of neurons, more in Chapter 1.2.2) and a state of neuronal injury [62,63].

Detecting brain atrophy using brain structural magnetic resonance imaging (sMRI) is another sensitive and cheaper biomarker for AD [64,65] (Figure 1.1.2.4). The rate of cortical

thinning and hippocampal atrophy has been shown to correlate well with disease progression and cognitive outcomes. Although brain atrophy detected by sMRI is not AD-specific, it is a powerful and non-invasive method to supplement the diagnosis of AD.

Apart from AD pathology-specific PET radiotracers like florbetapir or flortaucipir, PET imaging using ^{18}F-fluorodeoxyglucose (FDG) radiotracer has been used as a biomarker for hypometabolism in AD [66]. Like sMRI, FDG PET has displayed excellent diagnostic power for AD by identifying region-specific patterns of hypometabolism and particularly in differentiating AD from other dementias as well as early detection in the MCI stage [67,68].

Overall, identifications of Aβ and tau neuropathology especially in combination remain the most specific for AD but not exclusively as other brain imaging methods like sMRI and FDG PET can also offer comparable diagnostic value for AD. However, it is crucial to recognise that AD is not only a multi-factorial, progressive disease, but also a highly heterogeneous one [69] and misdiagnosing AD ante-mortem is not uncommon. Recently, it was found that 20-50% of older (> 80 years old) adults suffered from a newly coined limbic-predominant age-related TDP-43 encephalopathy [70] which very closely mimics AD clinical manifestations and pathology. This case exemplifies the need for a neuropathology-based biological definition of AD that will have downstream implications in accurate diagnosis and clinical trials.

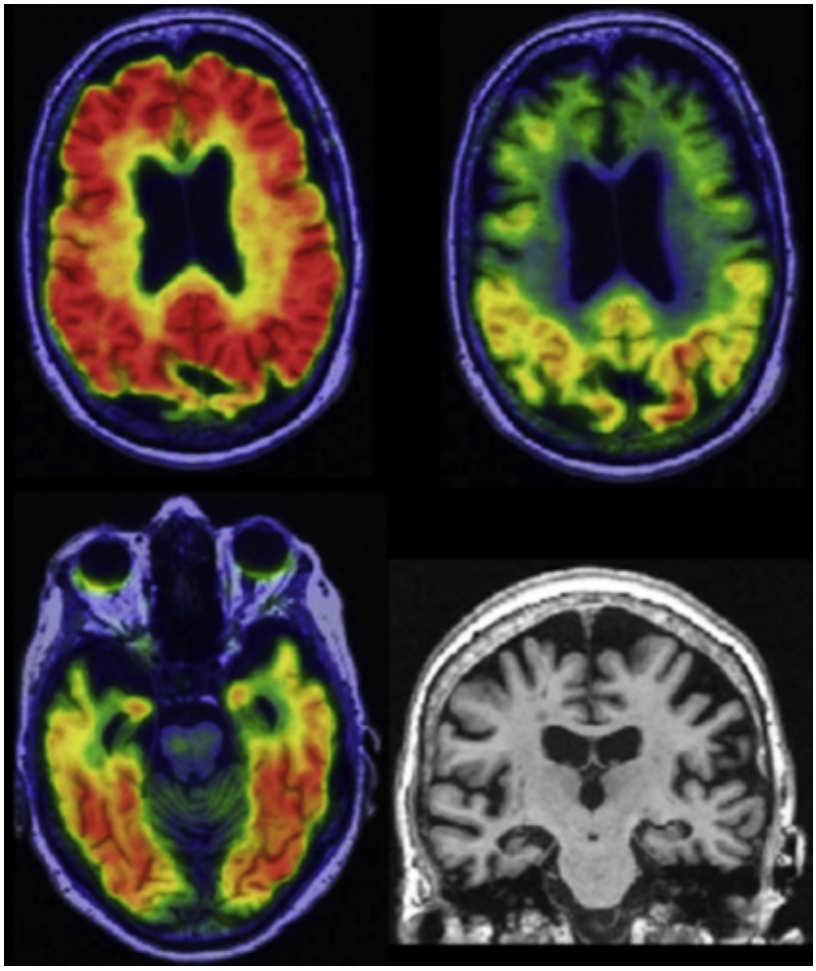


Figure 1.1.2.4: Brain imaging of AD with dementia
A 75-year-old woman with amnestic multidomain dementia. Participant in the Mayo Alzheimer's Disease Research Center. Abnormal amyloid PET with Pittsburgh compound B (top left), tau PET with flortaucipir (top right and bottom left), and atrophy on MRI (bottom right). Biomarker profile A+T+(N)+. Adapted without any changes from Jack *et. al.* [34] under the CC BY-NC-ND 4.0 licence detailed in https://creativecommons.org/licenses/by-nc-nd/4.0/.

1.1.3 Genetic and non-genetic aetiology

Genetic causes of fAD

Multiple mutations were identified in a gene coding for amyloid precursor protein (APP; Chromosome 21) [71–74] in fAD patients in 1991. This discovery prompted the suggestion of the "amyloid cascade hypothesis" [75,76] postulating that the deposition of Aβ, which is one of the cleaved products derived from APP (more in Chapter 1.2.1), is the causative agent

of AD pathology. The hypothesis was based partially on the fact that an additional chromosome 21, where *APP* is located, is the genetic cause of Down syndrome and adults with Down syndrome face increased risks of AD symptoms and neuropathology [77,78]. Subsequently, analyses in partial trisomy 21 individuals (i.e., with or without *APP* locus) revealed that increased *APP* dosage specifically is the cause of AD in adults with Down syndrome [79,80].

In 1995, mutations in two additional genes coding for presenilin-1 (*PSEN1*; Chromosome 14) [81] and presenilin-2 (*PSEN2*; Chromosome 1) [82,83] were found in fAD patients. Importantly, PSEN1 and PSEN2 are both subunits of γ-secretase complex which cleaves APP resulting in Aβ peptides (more in Chapter 1.2.1) and the mutations led to the inhibition of γ-secretase's ability to carry out normal cleavage of APP [84,85]. It was later confirmed that *APP*, *PSEN1* and *PSEN2* mutants led to the production of Aβ species found in amyloid plaques [86,87]. Notably, no mutations in the *MAPT* gene coding for tau protein have been implicated to cause fAD but instead are associated with other tauopathies like FTD and parkinsonism linked to chromosome 17 [88], corticobasal degeneration (CBD) [89], and Pick's disease [90].

The pathogenic fAD mutations act in an autosomal dominant manner and almost invariably cause AD. The age of AD symptom onset for fAD is usually below 65 years and lower than that of sAD, specifically in the forties for *PSEN1* mutation carriers and fifties for *APP* mutation carriers [12]. Several studies had shown that fAD and sAD manifest largely similar cognitive outcomes (based on family history of AD) and neuropathology [91–93] while fAD patients carrying a *PSEN1* mutation was found to exhibit faster cognitive decline as compared to sAD patients [94]. Yet, fAD patients, especially those with *PSEN1* mutation,

demonstrated longer survival and longer time before nursing home placement than sAD patients [95,96]. Earlier age of onset and hence less co-morbidity due to old age and greater cognitive reserve could potentially explain the better survival rate in fAD patients.

There are noteworthy, though extremely rare, exceptions when fAD mutations in the *APP* or *PSEN1* genes did not cause AD. A rare *APP* A673T mutation was discovered to protect against AD and cognitive decline in elderly populations [97]. The mutation is situated at the site of β-secretase cleavage (more in Chapter 1.2.1) and resulted in little Aβ pathology in one subject who lived until age 104.8 years [98]. Another documented case revealed an individual who is a carrier of pathogenic *PSEN1* E280A mutation had high levels of amyloid plaque but little tau pathology by PET imaging [99]. Crucially, she did not progress into the MCI stage until three decades after her expected age of symptom onset. Subsequent sequencing results showed that she carries two copies of the rare Christchurch (R136S) mutation in *APOE ε3* (the *APOE* gene will be elaborated later in this Chapter) [100] which might confer resistance to developing tau pathology.

Genetic risk factors of sAD

Although there are no causative gene mutations that are linked to sAD, many genetic risk variants are associated with sAD. *APOE ε4* was the first genetic risk variant identified by case-control studies and remains the strongest genetic risk factor associated with AD [101,102]. There are three variants of the *APOE* gene coding for a lipid-binding apolipoprotein namely *APOE ε2*, *ε3*, and *ε4* associated with the lowest to the highest risk of AD in that order [103]. As opposed to *APOE ε4, APOE ε2* demonstrated protective effects

against the risk of AD. Using *APOE ε3/ε3* (the most common genotype) as reference, having an *ε2* allele reduces the risk of AD by a factor of 4 whereas having one or two copies of the *ε4* allele significantly increases the risk of AD by a factor of 4 and 19, respectively (Figure 1.1.3.1). Subsequently, another study showed that *APOE ε4* carriers exhibited greater acceleration of cognitive decline as compared to noncarriers [104].

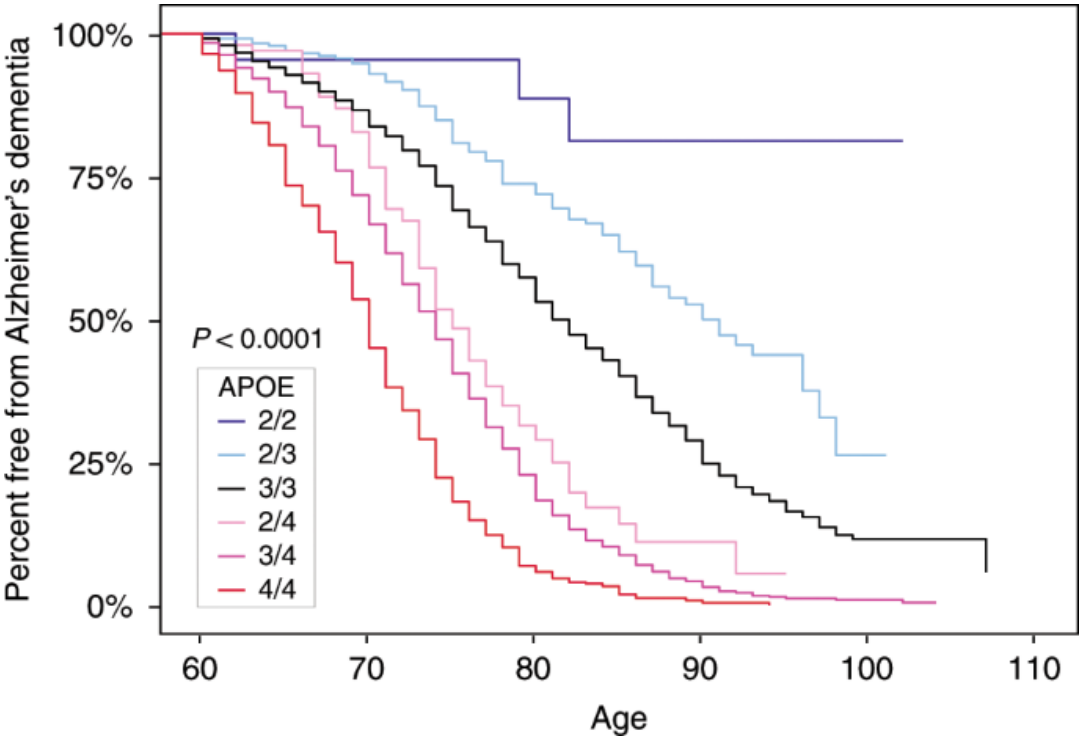


Figure 1.1.3.1: Kaplan–Meier curves were generated from Alzheimer's dementia cases and cognitively unimpaired non-AD controls in the neuropathologically confirmed group
***Y*-axis represents the percentage of persons with each *APOE* genotype in the neuropathologically confirmed group who remained free from Alzheimer's dementia. *X*-axis denotes age at death for controls and age at onset of cases, while replacing with age at death when age at onset was unavailable. Adapted without any changes except reformatting image captions from Reiman *et. al.* [105] under the Creative Commons Attribution 4.0 licence detailed in https://creativecommons.org/licenses/by/4.0/.**

Many additional genetic risk factors have been singled out by genome-wide association studies (GWAS) since the discovery of the *APOE ε4* genetic risk variant with varying, but mainly low (increment up to a factor of 2), levels of risks associated with developing AD

[106–113] (Figure 1.1.3.2). Overall, the genes are associated with pathways such as lipid-related processes, APP/amyloid degradation, astrocyte activation, immune cell recruitment, NFT-related processes, and microglia-mediated responses. It is also evident that rarer gene variants tend to have greater effect sizes especially for the fAD genes described above (Figure 1.1.3.2). Crucially, a rare genetic variant in the *MAPT* gene (A152T), which was originally known to be associated with PSP and PD risks, has also shown significant association with higher risks of AD and FTD from a case-control study (not shown in Figure 1.1.3.2) [114]. The carriers of the *MAPT* A152T variant (n = 7 for FTD and n = 2 for AD) were also found to exhibit neurodegenerative disease phenotypes [115]. None of these genes causes AD.

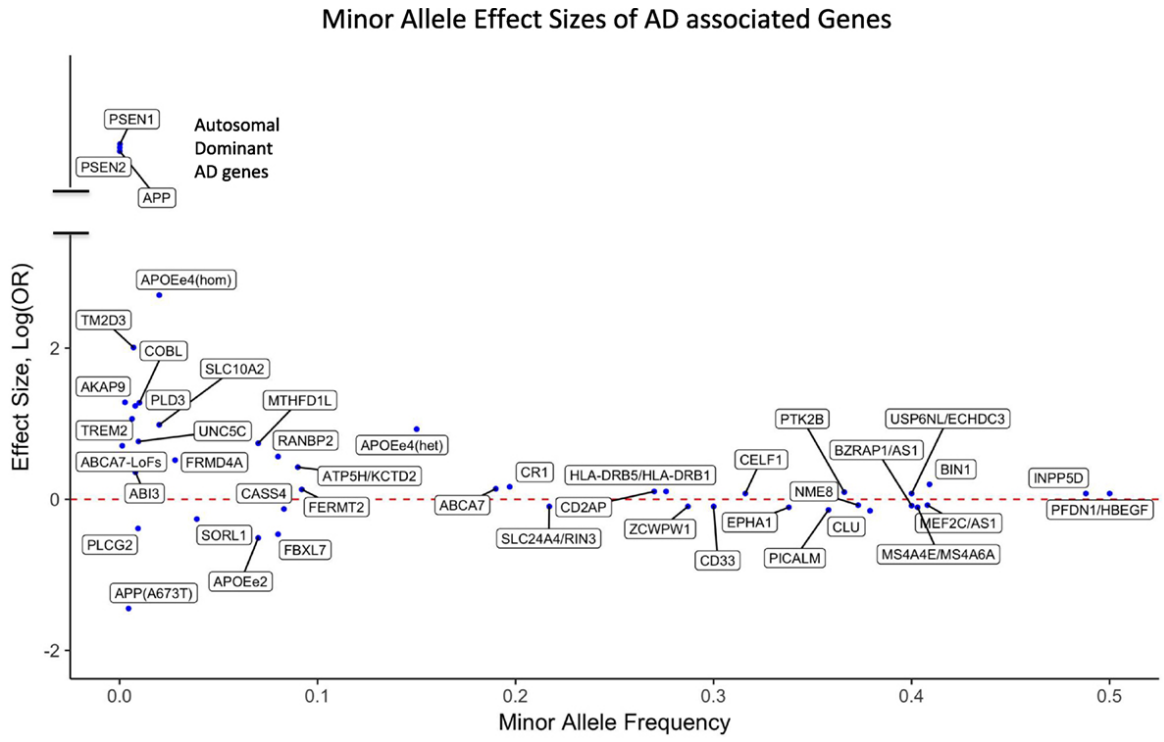


Figure 1.1.3.2: Effect sizes of AD associated variants for the respective minor alleles The red dotted line indicates OR = 1 [log(OR) = 0]. Minor alleles with log(OR) above the line are risk alleles and below the line are protective. Abbreviations: APOEe4(hom), homozygosity for the *APOE4* allele; APOEe4(het), heterozygosity for the APOE4 allele; ABCA7-LoFs, aggregated effects of loss-of-function variants in ABCA7; OR, odds ratio; AD, Alzheimer's disease. Adapted without any changes from Freudenberg-Hua *et. al.* [116] under the Creative Commons Attribution 4.0 licence detailed in https://creativecommons.org/licenses/by/4.0/.

The discovery of multiple risk loci for AD allows the computation of a polygenic risk score (PRS) by taking into account a combination of effects as each risk locus is given different weight contributing to the overall risk of AD explained by heritability. PRS was shown to predict AD by up to 90% accuracy and the *APOE* genotype is by far the main contributor to the PRS. The availability of PRS provides an opportunity to predict AD by categorising individuals into high or low risk groups, implicated in clinical trials or precision medicine [117,118]. It is however important to point out that discovering one's PRS or *APOE* genotype, though highly useful for research, has profound clinical and ethical implications for the individuals involved especially before symptom onset which is not guaranteed to happen.

Non-genetic risk factors

Not all sAD cases can be explained by heritability components alone as non-genetic risk factors also play a significant role linked to AD. These risk factors are considered potentially modifiable (i.e., lifestyle choices). The Lancet Commission reported 12 major potentially modifiable risk factors associated with AD in 2020 from over 10,000 adults in the UK and each of the factors represents different levels of population attributable fraction (PAF; i.e., proportion of AD incidents in a population attributed to a risk factor) [119]. In early life, less education is a major contributor to late-life AD risks measured by PAF (7%). This is followed by hearing loss (8%), traumatic brain injury (TBI; 3%), hypertension (2%), high alcohol consumption (1%) and obesity (1%) in midlife. Smoking (5%), depression (4%), social isolation (4%), physical inactivity (2%), air pollution (2%) and diabetes (1%) are also

linked to AD later in life and in total these potentially modifiable risk factors amount to approximately 40% of total PAF for AD.

While genetic risk factors are unavoidable by an individual and currently no treatment is available to modify the genetic makeup of an individual at risk of AD, the 12 potentially modifiable risk factors can be actively managed and prevented. This notion has led to the establishment of multidomain lifestyle interventional trials such as the Finnish Geriatric Intervention Study to Prevent Cognitive Impairment and Disability which first demonstrated beneficial effects in certain subgroups as compared to the control group and was later expanded worldwide [120,121]. Subsequently, the World Health Organisation developed the first guidelines for risk reduction of cognitive decline and dementia to manage some of the aforementioned modifiable risk factors [122].

1.2 Amyloid-β and tau proteins

1.2.1 Amyloid-β protein formation, functions, and disease associations

Formation of Aβ

Aβ is one of the by-products from the sequential cleavage of its much larger precursor APP which is a transmembrane protein [123] (Figure 1.2.1). APP can be processed in two alternative pathways involving different proteases [124]. In the amyloidogenic pathway, APP is first cleaved by β-secretase at the ectodomain and then by γ-secretase at the intramembrane region. These two cleavage events result in soluble APPβ, APP intracellular domain (AICD) and Aβ peptides. APP is first cleaved by α-secretase instead at a site close

to that of β-secretase (< 10 amino acid residues) in the non-amyloidogenic pathway and then by γ-secretase, producing soluble APPα, AICD and P3 peptides. Both β- and γ-secretases cleave APP at a range of cleavage sites, thus the resultant Aβ peptides can range between 37-49 amino acid residues in length. In AD, Aβ peptides secreted into the extracellular space aggregate to form higher order assemblies from oligomers, protofibrils, to insoluble mature fibrils and eventually deposits in amyloid plaques [125].

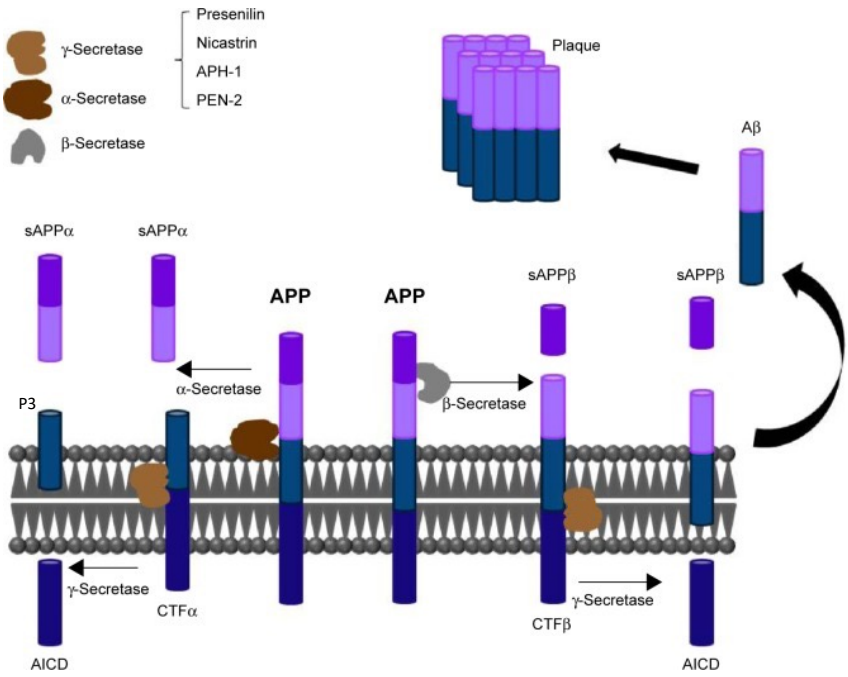


Figure 1.2.1: The process of APP processing and Aβ aggregation
APP is a transmembrane protein. APP processing includes non-amyloidogenic and amyloidogenic pathways. Non-amyloidogenic pathway (left): APP is cleaved by α-secretase in the middle of Aβ with production soluble APPα (sAPPα) and C-terminal fragment α (CTFα). Then CTFα is hydrolyzed by γ-secretase to generate APP intracellular domain (AICD). Amyloidogenic pathway (right): APP is cleaved by β-secretase resulting in N-terminal soluble APPβ (sAPPβ) leaving the C-terminal fragment β (CTFβ) which is hydrolyzed by γ-secretase to yield Aβ and AICD. Presenilin, nicastrin, anterior pharynx-defective 1 (APH-1) and presenilin enhancer 2 (PEN-2) are the parts of γ-secretase. *PSEN* mutation might increase γ-secretase activity to cause plaque forming. Adapted with the representation of presenilin mutation removed and annotation of P3 added from Cai *et. al.* [126] under the Creative Commons Attribution 3.0 Non-Commercial licence detailed in https://creativecommons.org/licenses/by-nc/3.0/.

Physiological functions and pathological forms of Aβ

The physiological functions of Aβ have been explored suggesting that Aβ presents antimicrobial activity, seals leaks in the blood-brain barrier (BBB), promotes recovery from brain injury, and regulates synaptic function [127]. The key in determining whether Aβ is present in a physiological or pathological context lies in the Aβ species involved. The primary Aβ species released from cells is the $A\beta_{1-40}$ peptide, but around 5-10% of the Aβ peptide extends into $A\beta_{1-42}$ peptide [128]. Indeed, the majority Aβ in early amyloid plaque deposits in AD patients belongs to the $A\beta_{1-42}$ species [129,130] suggesting that $A\beta_{1-42}$ is implicated in the formation of Aβ pathology in AD brains. Furthermore, cells and mice with fAD mutations in *APP*, *PSEN1* and *PSEN2* exhibited significant increase in Aβ production particularly $A\beta_{1-42}$ hence raising the Aβ 1-42:40 ratio [87,131,132]. Although both $A\beta_{1-40}$ and $A\beta_{1-42}$ can aggregate rapidly, $A\beta_{1-42}$ was shown to aggregate more quickly into oligomers and subsequently protofibrils as compared to $A\beta_{1-40}$ [133]. The aggregation-prone $A\beta_{1-42}$ is therefore thought to be the main pathological Aβ species in AD.

As mentioned in Chapter 1.1.2, insoluble Aβ fibril-rich amyloid plaques detected by PET imaging display weak association with cognitive decline. In fact, the majority of Aβ deposits are of the diffuse type which is not composed of fibrils [134]. Soluble Aβ, including Aβ oligomers, was then found to correlate well with cognitive decline and severity of neurodegeneration in individuals with dementia or AD [135,136]. This is also true in the CSF where Aβ oligomers were shown to differentiate AD from HC subjects [137,138]. The patient studies were supported by the data from AD mouse models where synaptic functions were inhibited before amyloid plaques formed in the brain [139,140]. Finally, direct

applications of Aβ oligomers derived from human AD brains caused long-term potentiation (LTP) impairment which disrupts memory formation and tau hyperphosphorylation in rat brains and hippocampal neurons, respectively [141,142]. These results indicate that Aβ oligomer-driven toxicity plays a central role in early AD pathogenesis leading to subsequent cognitive decline.

Precisely how extracellular Aβ oligomers elicit neuronal toxicity mediated via intracellular mechanisms is still an ongoing research question. It has been demonstrated that Aβ oligomers interact with a range of cell surface receptors, some of which are ion channels localised at postsynaptic terminals [125]. In particular, NMDAR has been implicated to mediate Aβ-driven tau hyperphosphorylation and excitotoxicity at synapses. Both phenotypes are highly relevant to the clinical manifestation of AD.

It was demonstrated in mouse primary neurons that NMDAR was activated by Aβ oligomers, leading to subsequent Ca^{2+} influx at synapses. This signalling cascade resulted in, but not exclusively, the activation of kinases such as cyclin-dependent kinase 5 (cdk5) or glycogen synthase kinase 3 β (GSK3β) both of which phosphorylate tau [143–146]. This sequence of events revealed one of the mechanisms linking the exposure to Aβ oligomers and eventual tau hyperphosphorylation and aggregation into NFTs [31].

Aβ oligomers emerged as the main culprit leading to synaptic dysfunction and loss before the formation of amyloid plaques as mentioned earlier in this Chapter. Direct exposure to Aβ oligomers led to synapse loss in neurons and this process is again NMDAR-dependent [147,148]. In addition to synapse loss, NMDAR-mediated influx of Ca^{2+} coupled with

excitotoxicity caused by Aβ oligomers can also lead to hyperactivation and eventually neuronal death [149,150].

1.2.2 Tau protein functions and disease associations

Physiological tau functions

The gene coding for microtubule-associated protein tau (*MAPT*; tau) is situated in Chromosome 17 [151] consisting of at least 16 exons, of which 8 of them are known to be alternatively spliced [152]. In the central nervous system (CNS), 6 major tau isoforms arise from alternative splicing events of exons 2, 3 and 10 [153]. These isoforms are assigned by their inserted regions (N-terminus inserts {N} or microtubule-binding domain tandem repeats {R}) corresponding to the exons included namely 2N4R (exon 2+3+10+), 2N3R (exon 2+3+10-), 1N4R (exon 2+3-10+), 1N3R (exon 2+3-10-), 0N4R (exon 2-3-10+), and 0N3R (exon 2-3-4-) in order of their molecular weight from the highest to the lowest (Figure 1.2.2.1). The 1N4R isoform is slightly longer than the 2N3R isoform, but lower in terms of its molecular weight. A tau peptide can be broadly divided into two functional domains from the projection domain at the N-terminus to the microtubule-binding domain, which consists of three or four highly conserved tandem repeats, closer to the C-terminus (Figure 1.2.2.1).

Tau isoform expression patterns are developmentally regulated [154] with human adult brains expressing all six isoforms whereas foetal brains express only the smallest 0N3R isoform. In mouse brain, all tau isoforms are expressed by 28 days postnatal [155]. The information on tau isoform expression patterns in human brain across early development is not available, although it could be broadly estimated that mice aged 28 days postnatal are

equivalent to the age of a human toddler/child [156]. In adult human brain, levels of 3R and 4R isoforms are roughly equal whereas the 0N, 1N and 2N tau isoforms make up ~37%, ~54%, and ~9% of total tau, respectively [157]. The alternative splicing pattern also exhibits regional specificity; for instance, the 0N3R isoform expression levels are lower in cerebellum as compared to other brain regions [158]. Furthermore, the expression levels of *MAPT* mRNA differ among brain regions such that the expression levels in the neocortex are double of those in cerebellum, for example. This observation on tau expression was replicated in rodent brains [159].

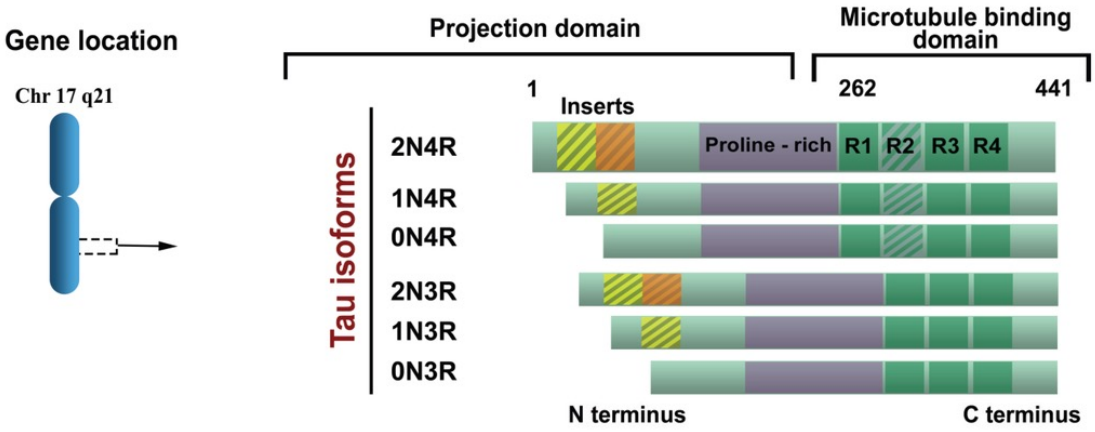


Figure 1.2.2.1: Chromosomal location of the gene and protein structure for microtubule-associated protein tau
Tau exons 2, 3 and 10 are alternatively spliced, giving rise to six different mRNAs, translated in six different tau isoforms. Tau isoforms differ by the absence or presence of one or two 29 amino acid inserts encoded by exon 2 (yellow) and 3 (orange) in the N-terminal part, in combination with either three (R1, R3 and R4) or four (R1-R4) repeat regions in the C-terminal part. The R2 repeat is encoded by exon 10. The longest 2N4R adult tau isoform (Exon 2+3+10+) has 441 amino acids (aa), followed by 1N4R isoform of 412 aa (2+3−10+), 2N3R isoform of 410 aa (2+3+10−), 0N4R isoform of 383 aa (2−3−10+), 2N3R isoform of 381aa (2+3−10−) and the shortest 0N3R isoform of 352 aa (2−3−10−). Adapted with the representation of tau extracted and figure caption reformatted from Šimić *et. al.* [160] under the Creative Commons Attribution 4.0 licence detailed in http://creativecommons.org/licenses/by/4.0/.

Tau is highly expressed in neurons and mostly localised in axons as a microtubule-binding protein [161] although somatodendritic and nuclear tau are also present [162,163]. Together with other microtubule-associated proteins (MAPs), tau is known to stabilise microtubules by directly binding to the microtubule surface and promote self-assembly from free tubulins [164]. Tau also regulates the dynamic instability of microtubule allowing reorganisation of cytoskeleton in a neuron [165]. As such, the involvement of tau in axons is important to the process of neurite outgrowth that requires extension and reorganisation of microtubules (to be further investigated in Chapter 4). On the other hand, tau regulates axonal transport by interacting with motor proteins such as kinesin-1 and dynein along axons but preferentially inhibits kinesin movements [166,167]. The regulatory function of tau for axonal transport affects the dynamics of transported cargoes in and out of distal synaptic terminals (to be further investigated in Chapter 4). Apart from its functions specifically in the axonal compartment, atypical tau functions such as maintaining genomic DNA integrity at the nucleus [163], binding to and regulating synaptic vesicle release at the presynaptic terminal [168,169], and ensuring proper localisation of Fyn kinase that in turn regulates NMDAR at the postsynaptic terminal [170,171] have all been reported previously [172].

Tau in NFT pathology

The fact that many atypical functions of tau (i.e., not related to its microtubule-binding premise) have been discovered suggests that tau is versatile and its pathological involvement in AD may implicate subcellular processes other than those confined within the axonal compartment. Tau pathology in AD brain requires the formation of intracellular NFTs which mainly comprise of hyperphosphorylated tau PHFs. Like Aβ aggregation described in

Chapter 1.2.1, tau monomers aggregate to form higher order oligomers and then PHFs before eventually accumulating into NFTs. However, unlike Aβ where the aggregation is in part driven by the amyloidogenic pathway of APP cleavage and overproduction of the $A\beta_{1-42}$ species, tau molecules first get hyperphosphorylated before detaching from microtubules thus allowing subsequent tau aggregation to take place [31,173–175]. This is further supported by the evidence showing that tau aggregation in AD depends on a sequence motif (^{306}VQIVYK^{311}, within the microtubule-binding domain) which is also essential for microtubule binding, suggesting that there is a competition between physiological interaction and pathogenic aggregation [176,177].

There are multiple putative phosphorylation sites along a tau peptide and more can be identified in AD (Figure 1.2.2.2). Normal tau carries on average 1.9 mol phosphate/mol of protein as opposed to that of AD brain at 8.1 mol phosphate/mol of protein [178]. Tau is a substrate of multiple kinases and several kinases have been identified to be activated downstream of extracellular challenge by Aβ as mentioned above [179]. These hyperphosphorylated tau molecules were shown to self-assemble into PHFs *in vitro*. However, certain phosphorylation sites have also been associated with protection against Aβ-driven toxicity and prevention from tau aggregation hence suggesting that tau phosphorylation alone is not purely pathogenic and not sufficient for its aggregation [180–182].

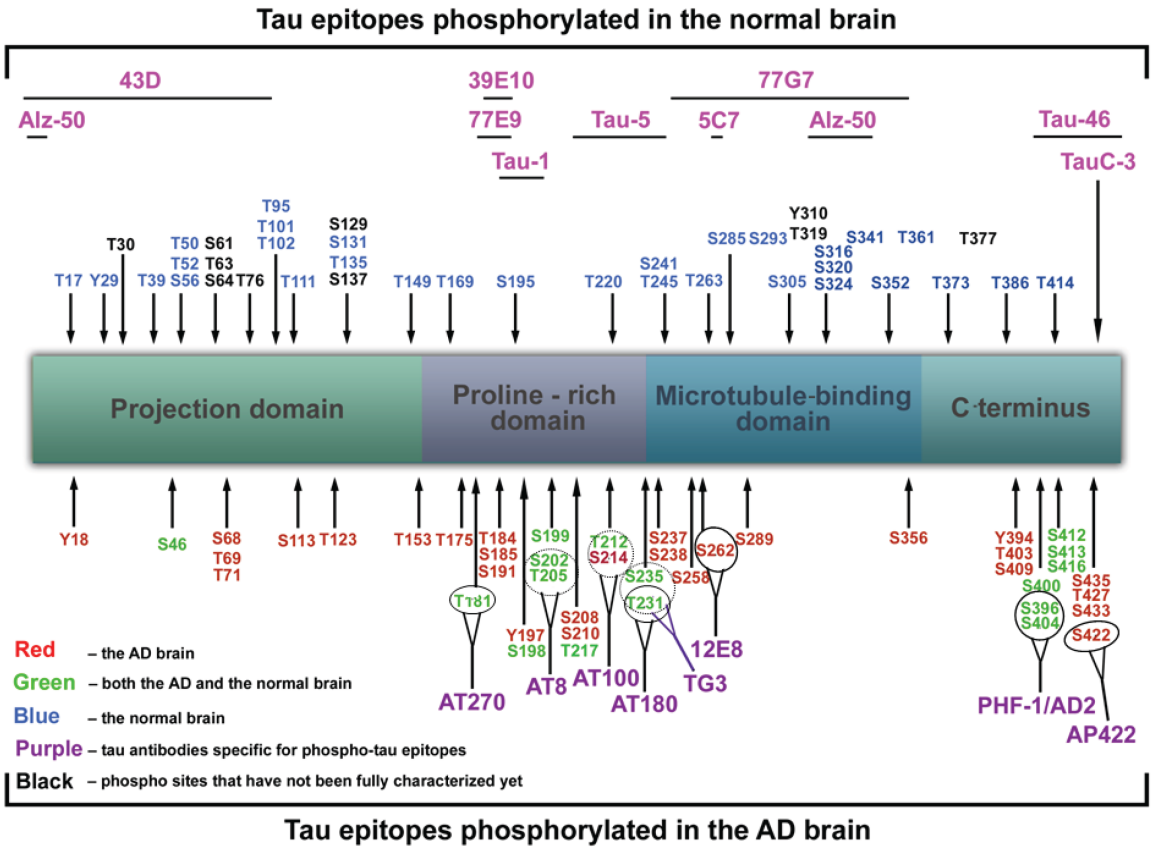


Figure 1.2.2.2: Putative phosphorylation sites on tau protein and epitopes specific for major tau antibodies
Red colour denotes amino acids phosphorylated in AD brain, green in both AD and normal brain, blue in normal brain, while black colour means that those phosphorylation sites have not been fully characterised yet. Tau antibodies specific for phospho-tau epitopes are given in purple, while pink colour denotes antibodies specific for non-phosphorylated tau epitopes: Alz-50 (aa 2–10, aa 312−342), 43D (aa 1–100), 77E9 (aa 185–195), 39E10 (aa 189–195), Tau-5 (aa 210–230), 5C7 (aa 267–278), Tau-1 (aa 195, 198, 199 and 202), 77G7 (aa 270–375), Tau-46 (aa 404–441), TauC-3 (tau cleaved on aa 421). Red—in the AD brain; Green—in both the AD and the normal brain; Blue—in the normal brain; Black—phosphorylation sites that have not been fully characterized yet; Purple—tau antibodies specific for phospho-tau epitopes; Pink—tau antibodies specific for unphosphorylated tau epitopes. Adapted without changes from Šimić *et. al.* [160] under the Creative Commons Attribution 4.0 licence detailed in http://creativecommons.org/licenses/by/4.0/.

More than 80 mutations have been found in human *MAPT* to date, but these mutations do not cause AD and instead are associated with other tauopathies (see Chapter 1.1.3). Several mutations associated with FTD with parkinsonism linked to chromosome 17 have gained particular interest because of their ability to cause tau aggregation *in vitro*. These mutant tau

proteins are more favourable substrates for kinases, and exhibit reduced binding to protein phosphatase 2A and microtubules [183–185]. Moreover, less phosphate groups per mutant tau molecule were needed to result in aggregation as compared to wild-type tau. Although these mutations are not linked to AD, they are highly relevant as they directly cause hyperphosphorylated tau aggregation. One particular missense *MAPT* mutation at the P301 amino acid residue (P301L [186] and P301S [187]) close to a microtubule-binding motif has been incorporated in transgenic mice expressing human P301L [188] or P301S [189] tau, resulting in NFT pathology and tau filaments which partially resemble the ones seen in AD brain as mouse does not naturally develop tau pathology (more in Chapter 1.3.1).

1.3 Animal models of Alzheimer's disease

1.3.1 Animal models mimicking Alzheimer's disease pathologies – focus on Amyloid-β-tau cooperation

Rodent models most widely used in research such as mice and rats do not naturally develop AD. Researchers have thus been relying on transgenic introduction of mutations in *APP*, *PSEN1* and/or *PSEN2* associated with fAD patients to induce amyloid pathology and its associated disease phenotypes [190]. However, unlike in human, fAD mutations are insufficient to cause NFT pathology in mice to recapitulate typical AD pathologies more appropriately. One of the strategies in fAD transgenic mice is to introduce another transgenic mutation in human tau such as P301L mentioned in Chapter 1.2.2 leading to NFT formation. Double transgenic mice with mutations in both human *APP* and *MAPT* could result in enhanced NFT pathology when aged for at least 9 months and exhibited comparable amyloid pathology as compared to single transgenic mice, suggesting that the amyloid pathology

exacerbated NFT pathology [191]. This agrees with another study replacing the *APP* mutation with $A\beta_{1-42}$ fibril injection causing a five-fold increase in NFT pathology [192].

A previous study has shown that double transgenic mice with *APP* mutations and wild-type human *MAPT* instead of human *MAPT* with a P301L mutation managed to accumulate NFT pathology though much later after 18 months of age [193]. These mice exhibited memory impairment at 6 months of age, earlier than that of the single transgenic *APP* mice used in this study to indicate synergistic toxic interaction between Aβ and tau pathologies. Importantly, the NFT composition in the double transgenic mice resemble the one in AD patients more closely as compared to the double transgenic mice with a P301L mutation in *MAPT* having PHF structure more relevant to other tauopathies.

Single transgenic mice such as the ones with APP mutations [194] are also widely used and often crossed with other mouse models to study Aβ-driven toxicity in different contexts. These mice display widespread amyloid pathology and associated cognitive impairment with age. Single transgenic mice with *PSEN1* [195] or *PSEN2* [196] mutations are less commonly adopted by research groups as they either incur significant neuronal loss much earlier than amyloid pathology that only appears after 17 months (*PSEN1*), or develop little to none amyloid pathology (*PSEN2*). Still, double transgenic mice with both *APP* and *PSEN1* mutations are widely adopted as they exhibit accelerated amyloid pathology and cognitive decline as compared to single *APP* transgenic mice [197]. Much like the mutant *APP*-wild-type *MAPT* or mutant *APP*-P301L *MAP*T transgenic mice, the *APP/PSEN1*-wild-type *MAPT* triple transgenic mice demonstrated that amyloid plaque size increased in the presence of wild-type human tau and that the Aβ-tau interaction led to downregulation of synaptic genes and marked behavioural hyperactivity [198,199] whereas *APP/PSEN1*-

P301L *MAPT* triple transgenic mice exhibited accelerated NFT propagation from the entorhinal cortex [200].

There are multiple limitations related to human transgene overexpression used in the aforementioned transgenic mouse models. One of the most significant shortcomings related to the overexpression of most likely multiple copies of transgenes, for *APP* transgenic mice specifically, is the overproduction of other cleaved APP fragments including Aβ itself such that they may interact unphysiologically with other cellular proteins [201]. It was also reported in a transgenic P301L tau mouse model that the mutant tau was not the only contributor to pathology [202]. One available option to address the issues associated with transgene introduction is the creation of knock-in mouse models. Human *APP* knock-in mouse model was later developed specifically and only with the mouse endogenous *App* replaced by human *APP* with fAD-linked mutations [203]. Crucially, depending on the combination of *APP* mutations included, amyloid plaque and memory impairment can be detected as early as 2 months and 6 months of age, respectively without an overexpression system. Tau pathology triggered by insoluble tau seeds derived from human AD brains was enhanced in these mutant *APP* knock-in mice, replicating the Aβ-tau cooperation seen in the mutant *APP*-overexpressing mice [204].

Subsequently, human wild-type *MAPT* knock-in mice were generated by humanising and replacing endogenous *Mapt* [205] and expressed all six isoforms as opposed to most transgenic P301L/S mice which express only the 2N4R isoform. However, the *APP-MAPT* double knock-in mice did not exhibit NFT pathology despite having increased tau phosphorylation caused by the presence of *APP* mutations. This indirectly indicates that the

NFT pathology seen in *APP*-wild-type *MAPT* transgene-overexpressing mice is partly influenced by the significant increase in expression levels.

In the past few years, the Model Organism Development and Evaluation for Late-onset Alzheimer's Disease consortium (MODEL-AD) was established with the aim to create next-generation mouse models that recapitulate late-onset sAD without relying on the expression of fAD-linked mutations [206]. A range of strategies from introducing genetic risk variants (see Chapter 1.1.3) to humanising endogenous mouse genes linked to APP processing have been employed. One of the sAD mouse models expressing both *APOE ε4* and *Trem2* R47H genetic risk factors, which are two of the strongest genetic risk factors of AD (Figure 1.1.3.2), did not develop amyloid plaques but demonstrated alterations in AD-related processes [207].

1.3.2 Knockout animal models – focus on tau-dependent Amyloid-β-driven toxicity

Knockout mouse models have been instrumental in elucidating the physiological functions and pathological associations of proteins involved in the amyloidogenic pathway of APP cleavage, in part to understand if removing or reducing any of these proteins might result in protective effects against AD by depleting Aβ. The observations on these knockout mouse models are summarised in Table 1.3.2. Overall, complete whole-body knockout of proteins involved in the amyloidogenic pathway of APP processing in mice appeared to be less favourable with overt neurological deficiencies or lethality. Conditional knockout mice offer an interventional window to effectively manage adverse neurological symptoms, reduce Aβ production, and protect against AD pathogenesis. This has profound implications in clinical

intervention targeting these proteins such that partial and localised inhibitions appear to be a viable strategy.

Table 1.3.2: Summary of phenotypes of germline and conditional knockout of proteins associated with the amyloidogenic pathway of APP processing in mouse

Protein	Germline knockout phenotypes	Conditional knockout phenotypes
APP	Fertile and viable; reduced weight; decreased locomotor activity; reactive gliosis; age-dependent cognitive deficits; impaired LTP; synapse loss [208,209].	Reduced grip strength, brain weight and body weight; APP family conditional knockout in either inhibitory or excitatory forebrain neurons led to cognitive deficit, impaired synaptic transmission, and impaired LTP [210–212].
β-secretase (BACE1)	Fertile and viable; initially determined to have normal phenotypes [213,214], subsequent further studies observed higher lethality, impaired synaptic plasticity, impaired cognitive function, axonal targeting errors, altered neurogenesis and astrogenesis, and schizophrenia-like and epilepsy-like phenotypes; no Aβ production [215].	Most adverse phenotypes seen in BACE1 germline knockout mice were absent, except LTP impairment (conflicting reports) and axonal organisation; BACE1 conditional knockout rescues pathological phenotypes in AD mice; no Aβ production [216,217]
PSEN1	Lethal shortly after birth; deformed skeleton, CNS haemorrhages, impaired neurogenesis, and neuronal loss [218].	Postnatal forebrain conditional knockout mouse is viable without gross abnormalities; reduced Aβ production; subtle cognitive deficit in long-term spatial memory only [219].
PSEN2	Viable and fertile; mild pulmonary fibrosis and haemorrhage; no change in APP processing	Single conditional knockout not available; PSEN1 and PSEN2 double conditional knockout in postnatal forebrain led to impairment in synaptic plasticity and NMDAR-mediated responses; aged mice exhibited neurodegeneration in cerebral cortex and increased Cdk5 and hyperphosphorylated tau levels; reduced Aβ production; increased inflammatory response; rescues AD phenotypes in mice carrying APP mutations [220–222].

In addition to the introduction of tau functions in Chapter 1.2.2, tau knockout (*Mapt-/-*) mice have been widely used to elucidate tau-dependent processes and toxicity in the context of AD. First generated almost 30 years ago in 1994 and subsequently several strains were generated by different groups [223–228], *Mapt-/-* mice are viable and by and large do not present overt cognitive or behavioural deficits. *Mapt-/-* mice do not exhibit learning and memory impairments, but it was also reported that these mice suffered from age-dependent motor dysfunctions in a subset of studies [229,230]. Upon closer examinations on *Mapt-/-* neurons, microtubule instability and axonal outgrowth impairment were observed both *in vitro* and *in vivo* [224,226]. More recent data suggest that *Mapt-/-* neurons showed less firing and more excitability in inhibitory neurons [231]. This is consistent with related studies demonstrating that *Mapt-/-* mouse was less prone to seizure episodes and the *Mapt-/-* background rescued autism mouse models from suffering adverse phenotypes like epilepsy [228,232–234]. Moreover, tau and its phosphorylation at S396 residue were shown to be essential for long-term depression (LTD) for neuronal plasticity [235,236], while conflicting reports have emerged regarding LTP impairment in *Mapt-/-* neurons [237,238]. Nevertheless, no long-term memory deficits have been reported in *Mapt-/-* mouse. Compensatory mechanism from other MAPs, specifically MAP1A, has been proposed to explain the general lack of deficits in cognitive functions in most of the *Mapt-/-* mouse strains. However, the elevation in MAP1A expression levels was not consistently observed and appeared to be relevant only in early development [223,224,226]. Like *Mapt-/-* mouse models, studies on *Drosophila* models of tau knockout (*dTau-/-*) have demonstrated inconsistent outcomes such that the removal of tau could either lead to no effects on motor and neuronal functions or developmental lethality [239,240]. *dTau-/-* flies were shown to exhibit no difference in synaptic transmission but another report proved altered neuroplasticity [168,241]. It remains unresolved in both vertebrate and invertebrate systems

how tau's functions are compensated in *Mapt-/-* neurons, and *Mapt-/-* phenotypes have been varied in an age-dependent and mouse strain-specific manner.

As extracellular Aβ challenge can result in tau pathology and associated toxic effects in various mouse models of AD as described in Chapter 1.3.1, it is then logical to establish whether any of the effects are tau-dependent by studying Aβ-driven phenotypes in the absence of tau using a *Mapt-/-* mouse. The first documented study 20 years ago on the necessity of tau in Aβ-driven toxicity demonstrated that mouse *Mapt-/-* primary hippocampal neurons were unaffected by the exposure to extrinsic Aβ fibrils whereas the *Mapt*+/+ neurons experienced widespread neuronal death and neurite degeneration [242]. By crossing mutant *APP* and *PSEN1* double transgenic mouse with *Mapt-/-* mouse, another group showed that the absence of tau reduced amyloid plaque burden coupled with suppressed Aβ overproduction, rescued motor and working memory deficits, improved survival, and prevented synapse and neuronal losses in the mutant *APP/PSEN1* double transgenic mice [243]. *Mapt-/-* primary forebrain neurons were also protected from cytotoxicity caused by a potent form of truncated Aβ oligomers [244].

Adverse cellular phenotypes, such as microtubule disassembly followed by neurite degeneration, preceding neuronal loss were also observed due to the exposure of extrinsic Aβ. It was demonstrated in primary mouse and rat neurons that microtubule severing was observed when the neurons were exposed to extrinsic Aβ insults [143,245]. This phenotype was coupled with tau phosphorylation and missorting of tau to dendrites. Localised Ca^{2+} influx and losses of spines and mitochondria were also detected in these dendrites where tau was missorted to. It was later found that Aβ-driven microtubule disassembly was also

protected in *Mapt-/-* mice, most likely explaining the lack of neurite degeneration seen with a higher dosage of extrinsic Aβ on *Mapt-/-* neurons [242,246].

Additionally, earlier subcellular events prior to neurons suffering from neurite degeneration and eventual neuronal loss due to the exposure to extrinsic Aβ could be observed *in vitro*. Significant anterograde mitochondrial transport deficits along axons were detected via live imaging in mouse hippocampal neurons caused by either extrinsic Aβ insult or overexpression of human *APP* mutant [247,248]. The axonal transport response is not specific to mitochondria but also neurotrophin receptor TrkA which is essential for neuronal function. Tau depletion again was sufficient to rescue the reduction in mitochondrial and TrkA cargo transport along axons.

The first evidence of cognitive decline reversal in AD mouse model due to the loss tau expression was documented where transgenic mutant APP mice were crossed with *Mapt-/-* mice [234]. The *Mapt-/-* background prevented memory loss caused by the overexpression of human *APP* mutant measured by Morris water maze, ameliorated a battery of behavioural deficits, and improved survival even though the amyloid plaque burden remained severe. Mechanistically, Aβ-induced LTP impairment in mouse hippocampal brain slices was abolished in the *Mapt-/-* background and it was later demonstrated that the LTP impairment could be reinstated when human *MAPT* expression was introduced to the *Mapt-/-* mice [237,249]. Inhibition of GSK3β, a major kinase capable of phosphorylating tau [250], was sufficient to block Aβ-induced LTP impairment in the *Mapt+/+* mice suggesting that the LTP impairment was dependent on tau phosphorylation specifically but not tau expression *per se*. Zooming in on postsynaptic terminals, tau ablation was sufficient to prevent excitotoxicity in human mutant *APP*-overexpressing transgenic mice without reducing

amyloid plaque burden [171]. The removal of tau prevented Fyn kinase from engaging with NMDAR, thus uncoupling the NMDAR-PSD95 interaction axis which leads to excitotoxicity in AD mice. The study also involved overexpressing only the projection domain of tau, which was designed to outcompete endogenous tau, to deplete tau in dendrites and postsynaptic terminals since the truncated tau is largely localised in the soma and cell membrane. The expression of the truncated tau achieved virtually the same, if not better, protective effects as tau knockout indicating the pivotal role of dendritic tau in mediating Aβ-driven toxicity.

There are several notable exceptions when it comes to the protective effects conferred by tau depletion against Aβ-driven toxicity. First of all, Drosophila models of tau depletion was not sufficient to prevent fly death caused by Aβ thus pointing to a potential species-specific function of tau in mediating Aβ-induced toxicity [239]. Another study reported that Aβ-driven LTP impairment in mouse hippocampal slices could not be ameliorated by tau ablation in direct contrast to the abovementioned paper [237], and that short-term memory was rescued instead [251]. Lastly, *Mapt-/-* mice seemed to exhibit exacerbated axonal degeneration under the background of human *APP* mutant overexpression [252]. Interestingly, these studies that failed to demonstrate tau's protective role against Aβ-driven toxicity employed the same *Mapt-/-* mouse strain used in the studies that showed reversals in cytotoxicity, memory deficits, LTP impairments, and axonal transport dysfunctions [234,237,242,247]. These inconsistent findings warrant additional tau knockout models to validate the role of tau in mediating Aβ-driven toxicity.

Finally, the amelioration of various adverse phenotypes caused by Aβ insults in *Mapt-/-* mice has been shown to be Aβ and AD-specific. It was reported previously that tau depletion

did not rescue transgenic mice expressing the G93A mutation in the *SOD1* gene associated with amyotrophic lateral sclerosis (ALS) from disease onset or reduced survival [253]. Mouse models of Parkinson's disease (PD), which is the second most common form of age-related neurodegenerative disease, could not have their motor deficits reversed when tau expression was removed [254]. As for the transgenic mice overexpressing the A53T mutation in human α-synuclein (*SNCA*) gene associated with familial PD, contradictory reports have emerged demonstrating that tau ablation could either exacerbate degeneration of parvalbumin-positive neurons or rescue memory and postsynaptic deficiencies in transgenic mice overexpressing human A53T *SNCA* [255,256]. Taken together, the protective effects due to the absence of tau appear to be AD-specific without sufficient evidence to suggest that tau ablation is beneficial in mouse models of other neurodegenerative diseases.

1.4 Human cellular models of Alzheimer's disease

Although mouse models have played an integral part in delineating the mechanisms of AD pathogenesis, distinct biological differences remain between human and mouse in the context of AD. As mentioned in Chapter 1.3, aged mice do not develop AD pathology without the introduction of disease-causing mutations indicating dissimilar disease susceptibility as compared to humans. Both 3R and 4R isoforms of tau can be found in NFTs from human AD brains [257], yet adult mouse almost exclusively expresses 4R isoforms while 3R isoforms are expressed transiently only in newborn neurons [154,155,258]. Additionally, removal of mouse endogenous tau in the presence of human *MAPT* transgene enhances tau pathology suggesting that mouse endogenous tau may interfere with tangle formation by human tau [259]. It has also been postulated that differences in brain ageing

and neuroinflammatory responses between human and mouse may underlie the observation where transgenic mice expressing human *APP* mutant fail to recapitulate both amyloid and tau pathologies despite reliably exhibiting amyloid plaque pathology and cognitive decline [260,261]. Indeed, it was reported that the *Trem2* R47H mutation, which is involved in immune response and one of the strongest genetic risk factors associated with sAD, impairs *Trem2* splicing and mRNA levels only in mice but not in humans [262]. It is therefore important to have AD experimental models representing human genetic and biological backgrounds, though restricted to cellular models *in vitro*, to complement existing AD models by accounting for the species difference between animal models and human.

1.4.1 Induced pluripotent stem cell and CRISPR/Cas9 technologies

Pluripotent stem cells, like embryonic stem cells derived from inner cell mass of a blastocyst, are undifferentiated and capable of self-renewal with a potential to become almost any cell types in a body under the right conditions. There had been successful past efforts in creating mammalian pluripotent stem cells *in vitro* by fusing embryonic stem cells with somatic cells or transferring nuclear materials into an oocyte [263]. Although these methods had underscored the possibility of making personalised stem cells, the potential use of human oocytes and embryonic stem cells have raised ethical concerns. Subsequently in 2006, Shinya Yamanaka and his colleagues demonstrated the creation of induced pluripotent stem cells (iPSCs) by reprogramming mouse skin fibroblasts and thereafter from adult human skin fibroblasts *in vitro* by overexpressing four defined transcription factors – OCT4, SOX2, MYC and KLF4 [264,265]. The reprogramming strategies have since evolved such that it is now possible to obtain human iPSCs from blood samples using non-integrating Sendai virus

to result in transient transcription factor overexpression, like some of the iPSC lines used in this thesis.

The ability to derive iPSCs from any individual, whether the person is healthy or a patient with or without any disease-associated genetic mutations, brings about the opportunity of personalised disease modelling *in vitro* among other applications [266]. The proliferative nature of iPSCs translates into virtually unlimited sources of cells for differentiation into specialised brain cells such as cortical neurons [267,268] (see Chapter 2.4), dopaminergic neurons [269], astrocytes [270], or microglia [271], all of which are inaccessible without invasive brain surgeries. For neuronal differentiation in particular, these directed differentiation strategies generally involve a combination of small molecule-mediated inhibitions, expression of transcription factors, introduction of growth factors, and exposure to suitable extracellular matrix guided by developmental neurobiology of specific neuronal lineages. The differentiated neurons have been shown to be functionally active measured by electrophysiology and express markers that are specific to the neuronal subtype. The advent of iPSC technologies therefore allows the derivation of patient-specific neurons from either fAD or sAD patients for experiments *in vitro*.

The fact that iPSCs are undifferentiated and mitotic offers an opportunity for genome engineering as the engineered iPSCs with intended genetic modifications can then be expanded and cryopreserved before being differentiated *in vitro* into any cell type of interest. Crucially, these edited and parental iPSC lines from which the edited lines are derived would be isogenic (i.e., sharing the same genotypes except the homozygous or heterozygous nature of the edited region) thus accounting for any effects on transcriptional variation or

differentiation propensity caused by a particular genetic background from the donor [272,273].

Several programmable nucleases have been discovered and utilised for precise gene editing in cells *in vitro* such as zinc finger nucleases (ZFN), transcription activator-like effector nucleases (TALEN), and more recently clustered regularly interspaced short palindromic repeats (CRISPR)-associated protein 9 (Cas9) nucleases used in the CRISPR/Cas9 gene editing system [274]. The CRISPR/Cas9 system in genome engineering has since been widely adopted for iPSC disease modelling including the iPSC lines used in Chapters 3 to 5 of this thesis [275,276] (Figure 1.4.1.1).

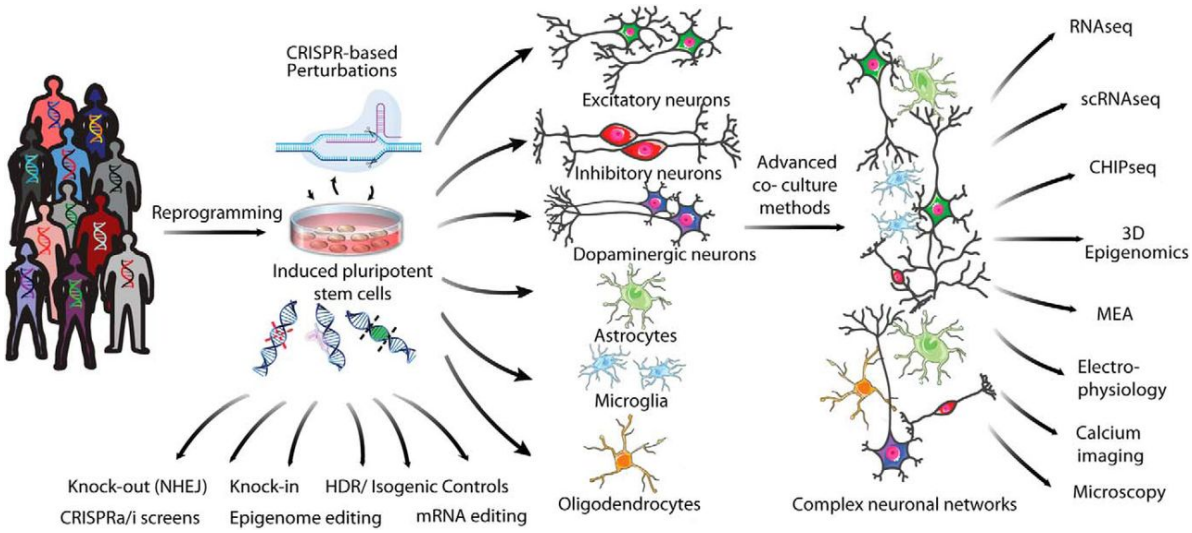


Figure 1.4.1.1: Approaching human iPSC disease modelling
The general human population exhibits high genetic variability, which can be overcome by stratification of the cohort or by CRISPR editing approaches. Generated iPSC lines can be differentiated or induced into several neural cell types, comprising neurons and glia, which can be modularly combined into cocultures for complex genetic, phenotypic, or functional analysis. Components of schematic were adapted from Servier Medical Art (https://smart.servier.com/#) and BioRender (created with www.BioRender.com). Adapted without changes from Rehbach *et. al.* [276] under the Creative Commons Attribution 4.0 licence detailed in http://creativecommons.org/licenses/by/4.0/.

The current CRISPR/Cas9 gene editing system is modified from a type of prokaryotic adaptive immune response against viral pathogens, and originally consists of a ribonucleoprotein complex containing two non-coding RNAs and a nuclease – CRISPR RNA (crRNA) containing a matching sequence to the target DNA sequence, trans-activating crRNA (tracrRNA) which pairs with crRNA to form a functional guide RNA (gRNA), and Cas9 nuclease that makes a double-stranded break (DSB) on the target DNA sequence [277]. The system was subsequently simplified by adding a linker between crRNA and tracrRNA to form a single modifiable gRNA (Figure 1.4.1.2) that can be designed to target any DNA region adjacent to a protospacer adjacent motif (PAM; 5'-NGG-3' for Cas9) [275,278]. Single gRNA can be introduced to create a DSB which is later repaired via the non-homologous end joining (NHEJ) mechanism. However, the NHEJ mechanism is error-prone and often introduces nucleotide insertions or deletions at the repair site thus potentially allowing a frame-shift mutation to arise leading to abolished gene expression [279]. Alternatively, two gRNAs targeting two different DNA sites flanking a defined sequence can be introduced simultaneously to result in a sequence deletion event which can also lead to gene expression ablation. Both strategies are employed in this thesis to generate gene expression knockout iPSC lines (see Chapter 3).

A range of adaptations and improvements has emerged since the simplified CRISPR/Cas9 system was used for gene editing in human cells *in vitro*. Instead of delivering plasmids that contain the sequences necessary for Cas9 and gRNA expressions within the target cells, the Cas9 and gRNA ribonucleoprotein complex can be hybridised first before carrying out direct cytosolic delivery of the ribonucleoprotein complex, often by electroporation, to eliminate the need for transcription and translation and improve CRISPR/Cas9 targeting efficiency [280]. On the other hand, the Cas9 protein can be mutated on either of its nuclease domains

to create a Cas9 “nickase” which executes single-stranded DNA breaks instead of DSB [281]. Combining two gRNAs flanking a specific DNA sequence with Cas9 nickase improves gene editing specificity and gives rise to an opportunity to knock-in any sequence of interest into the repair region with the single-stranded overhangs (Figure 1.4.1.2). The two Cas9 nuclease domains could also be mutated concurrently such that DNA targeting can take place without any nuclease activities. The resultant dead Cas9 nuclease has been used in a CRISPR interference technique where the CRISPR/Cas9 complex interferes with gene transcription mechanisms leading to silencing [282]. Taken together, the iPSC and CRISPR/Cas9 technologies are powerful tools that offer great versatility allowing AD researchers to generate patient-specific iPSC lines and edit genes that are associated with AD in human cells which can then be differentiated into neurons *in vitro*.

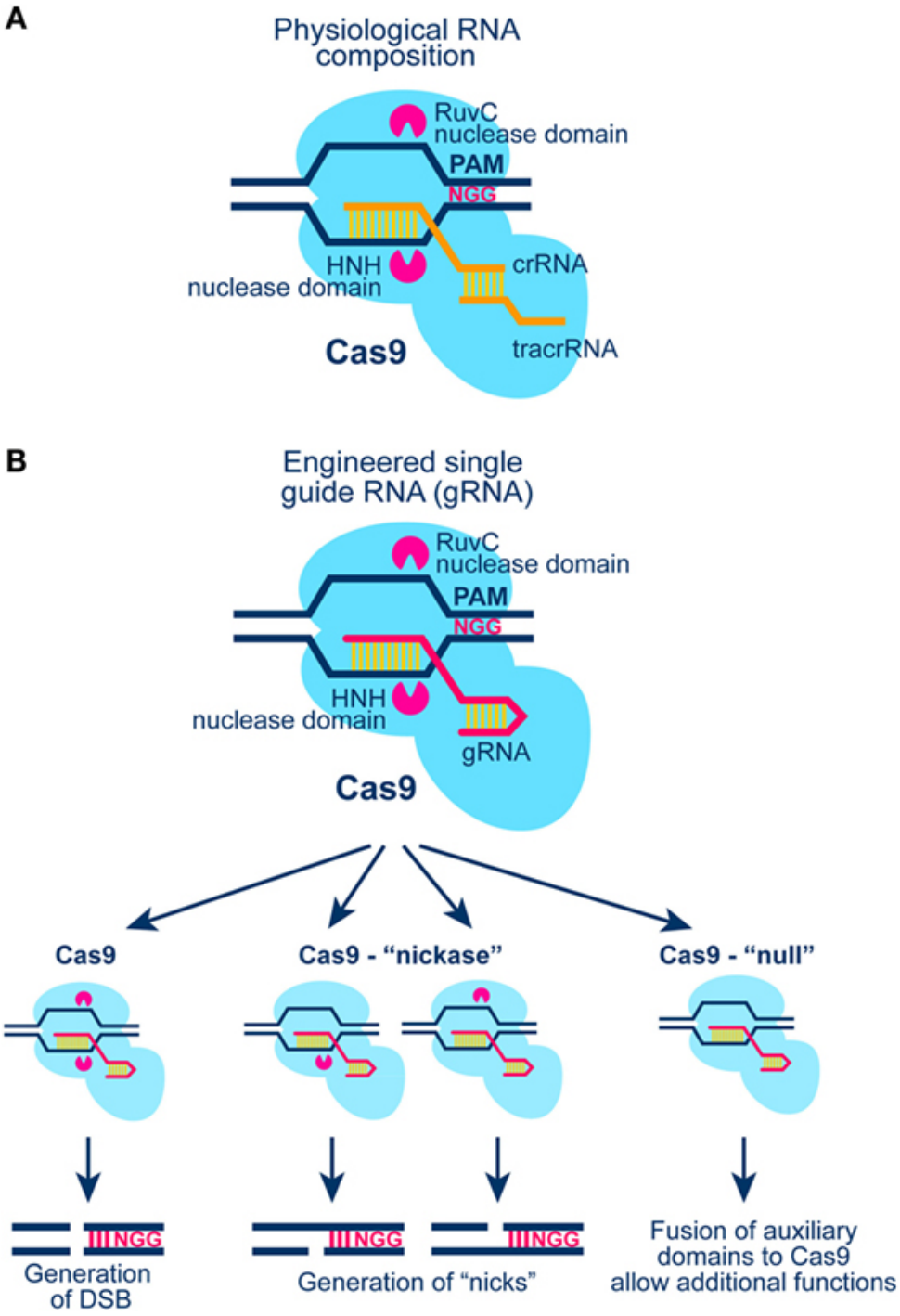


Figure 1.4.1.2: Schematic representation of the CRISPR/Cas9 gene editing system (A) Schematic representation of the CRISPR/Cas9 system in *S. Pyogenes*. Cas9 generates blunt ends by cutting 3 bp downstream the PAM region of the target DNA molecule. (B) Schematic representation of Cas9 activation with a chimeric gRNA combining crRNA and tracrRNA. Cas9 nuclease harbours two nuclease domains: HNH and RuvC-like; mutation of one or both nuclease domains results in Cas9 enzymes with "nickase" properties, or with null nuclease activity. The latter form of Cas9 can be tethered to other proteins for gain-of-function DNA sequence-specific operations. Adapted without changes except reformatting the figure caption from Mladenova *et. al.* [283] under the Creative Commons Attribution 4.0 licence detailed in http://creativecommons.org/licenses/by/4.0/.

1.4.2 Induced pluripotent stem cell models of Alzheimer's disease

iPSC lines derived from fAD patients

Most studies using iPSC derived from either fAD or sAD patients have focused on differentiation into cortical neurons which are excitatory *in vitro* for disease modelling [284], as the cortices are one of the most affected brain regions with abundant amyloid and tau pathologies. The first iPSC models of fAD harbouring *PSEN1* (A246E) and *PSEN2* (N141I) mutations were described 10 years ago in collaboration with the Yamanaka lab [285]. It was demonstrated that all fAD iPSC-derived neurons secreted greater levels of Aβ and Aβ 42:40 ratio in the conditioned media. This was subsequently confirmed in several independent studies using iPSC lines derived from fAD patients with various presenilin gene mutations (*PSEN1* G384A [286]; *PSEN1* intron 4 deletion (int4del) [287]; *PSEN1* skipped exon 9 (ΔE9) [288]; *PSEN2* N141I [289]). Crucially, corrections of the *PSEN1* mutations to wild type using the ZFN, TALEN, or CRISPR/Cas9 systems reversed the secreted Aβ phenotype in these iPSC-derived neurons. One of the studies further demonstrated that electrophysiological deficits caused by a *PSEN2* mutation in iPSC-derived neurons were ameliorated by eliminating the mutation via gene editing [289].

In parallel, iPSC lines derived from fAD patients with a mutation in *APP* V717I or duplication of the *APP* gene similarly demonstrated increased Aβ 42:40 ratios in the iPSC-derived neurons [290,291]. These neurons also secreted increased levels of tTau and pTau which were not observed in iPSC-derived neurons with *PSEN1* mutations (Y115C and int4del) [290,292,293] whereas the rest of the studies mentioned using *PSEN1* mutant iPSC lines did not specifically report any changes in tau expression or phosphorylation. Importantly, it was shown that CRISPR/Cas9-mediated correction of *APP* dosage down to

wild-type levels could suppress the increase in Aβ, tau and pTau levels in the iPSC-derived neurons with a duplication in *APP* proving that the AD phenotypes were caused specifically by the mutation [290]. Depleting *APP* expression levels further by knocking out APP however led to altered cholesterol metabolism and impaired lipoprotein and Aβ endocytosis in iPSC-derived astrocytes [294].

Apart from the differential effects on tau expression and phosphorylation, secreted Aβ profiles also vary significantly between *APP* and *PSEN1* mutant iPSC-derived neurons [295]. Secreted $A\beta_{1-38}$ levels were elevated in the *APP* mutant lines but not in the *PSEN1* mutant lines, though both lines showed greater Aβ 42:40 ratios. The conditioned media containing secreted Aβ from either *APP* or *PSEN1* mutant iPSC-derived neurons were both capable of eliciting LTP impairments in rat hippocampal brain slices [296]. Beyond Aβ and tau pathophysiology, the fAD iPSC-derived neurons were also shown to cause differential effects in early endosome abnormalities (particularly in *APP* mutants) and premature terminal differentiation (particularly in *PSEN1* mutants) while enlargement and axonal transport of lysosomes measured by probing LAMP1 (including late endosomes) were seen in both fAD neurons [297,298]. As mentioned in Chapter 1.1.3, the A637T mutation in *App* was shown to be a protective mutation in a mouse model. This phenotype was reproduced in human iPSC lines harbouring the said mutation such that the A637T mutation in *APP* resulted in reduced amyloidogenic processing of APP in iPSC-derived neurons, providing evidence that not all mutations in *APP* are pathogenic [299].

iPSC lines derived from sAD patients

The first documented iPSC models of sAD followed soon after the first iPSC models of fAD were published. With the iPSC line with *APP* duplication as reference, one of the two sAD iPSC lines exhibited comparable elevations in $A\beta_{1-40}$ levels and pTau:tTau ratios [300]. Subsequent studies using sAD iPSC lines echoed the lack of pathological Aβ and tau phenotype by further showing that none of the sAD iPSC-derived neurons experienced increased Aβ 42:40 ratios while only one study reported increased pTau levels as opposed to *APP* (V717L) and *PSEN1* (A246E, V89L, and L150P) mutant iPSC-derived neurons which reproducibly produced greater Aβ 42:40 ratios and pTau levels [301–303]. Moreover, contradictory results of neuronal vulnerability to extrinsic $A\beta_{1-42}$ were demonstrated in sAD iPSC-derived neurons as compared to the ones with *PSEN1* mutations [302,303]. Taken together, it is evident that iPSC models of sAD could not reliably recapitulate typical AD pathophysiology without the presence of mutations in fAD genes involved in APP processing.

The use of iPSC models of sAD was later refined to account for the genetic risk factors (see Chapter 1.1.3) associated with sAD. Human iPSC-derived neurons with the *APOE ε4* variant, the strongest genetic risk factor, exhibited increases in Aβ 42:40 and pTau/tTau ratios as compared to those with the *APOE ε3* variant [304–306]. Furthermore, the *APOE ε4* iPSC-derived microglia and astrocytes both displayed reduced ability of Aβ uptake, leading to impaired clearance of extracellular Aβ. Importantly, these pathological phenotypes could all be effectively reversed when the *APOE ε4* variant was corrected to *APOE ε3* by gene editing as isogenic controls making it evident that the observed phenotypes were specifically caused by the *APOE ε4* risk factor. It is noteworthy that the *APOE-/-* iPSC-derived neurons did not

lead to any phenotype changes seen in the *APOE ε4* neurons, and that re-introducing *APOE ε4* expression restored the pathological phenotypes indicating a gain of toxic effects caused by the *APOE ε4* variant [306].

In contrast to the *APOE* risk factor, *TREM2 R47H* variant which is also associated with AD and involved in microglial functions, conferred subtle reduction in phagocytosis efficiency in iPSC-derived microglia as compared to the significant inhibition in phagocytosis seen in *TREM2-/-* iPSC-derived microglia [307,308]. Further analysis showed that both *TREM R47H* and *TREM2-/-* genotypes resulted in similar transcriptional changes in iPSC-derived microglia. Therefore, unlike the gain-of-function effects observed in iPSC models harbouring the *APOE ε4* variant, the *TREM2 R47H* variant is associated with loss-of-function effects in iPSC-derived microglia as supported by the results in the *TREM2-/-* background.

Research into human iPSC models of AD has made considerable progress in the past 10 years, proving their effectiveness, versatility, and relevance to AD pathogenesis in the context of human genetic background whether it is a knockout model or patient-specific line with a defined genotype. Although most studies on iPSC models of AD investigated the involvement of tau expression and phosphorylation, iPSC models for studying tau-dependent processes are not currently available. Additionally, iPSC models of sAD without defined categorical influences from genetic risk factors do not consistently produce pathological phenotypes *in vitro* as opposed to fAD models. This observation may prompt a change in approach to studying sAD using patient-derived iPSC lines. Instead of asking whether these patient-derived neurons produce significant increases in pathological Aβ or tau levels, which can vary tremendously in sAD patients, one could explore if sAD patient-

derived iPSC lines reflect clinical symptoms or present comparable levels of vulnerability taking their range of neuropathological status into account. In this thesis, I will further investigate these knowledge gaps using human iPSC-derived neuronal models of AD.

1.5 Aims of the thesis

- Generate tau-deficient human iPSC models in collaboration with the Cowley group, and characterise tau-deficient iPSC-derived neurons alongside their isogenic controls
- Elucidate the effects of tau depletion in iPSC-derived cortical neurons by comparing to their isogenic controls
- Determine whether tau is essential in Aβ-driven toxicity *in vitro*
- Establish the correlations between cellular vulnerability to extrinsic Aβ insults and clinical vulnerability to Aβ burden using AD patient iPSC-derived neurons and clinical outcome data of the same patients from the Deep and Frequent Phenotyping pilot cohort

Chapter 2: Methods and Materials

All reagents were purchased from Sigma-Aldrich (now Merck) and all cell cultures were incubated at 37 °C and 5% CO_2 level unless stated otherwise.

2.1 Generation of *MAPT* knockout induced pluripotent stem cell lines

Two strategies targeting either Exon 1 or Exon 4 of the *MAPT* gene were employed in two separate iPSC lines from healthy individuals – the SBAd-03-01 (Exon 1 targeted; 36 years old female) and SFC856-03-04 (Exon 4 targeted; 76 years old female) lines. The excisions of *MAPT* gene were achieved by using the Alt-R CRISPR/Cas9 System (IDT) following manufacturer's protocol by Ms Jane Vowles and Dr Sally Cowley of the Oxford Stem Cell Institute. The Cas9 Nuclease V3 was used with a single gRNA to result in a DSB in Exon 1, whereas Exon 4 was targeted with a pair of gRNAs to create a 25 bp deletion (Table 2.1). To deliver hybridised Cas9-gRNA ribonucleoprotein into the iPSCs, a Neon Transfection System was used in a suspension of 220,000 iPSCs with a single pulse at 1400 V with 20 ms pulse width.

Table 2.1 List of gRNAs used in CRISPR/Cas9 system targeting *MAPT* gene

gRNA (as DNA sequence) for targeting *MAPT* gene with CRISPR/Cas9 system	
Target	**Sequence (5' – 3')**
MAPT Exon 1	CACCATGCACCAAGACCAAG
MAPT Exon 4 (forward)	CATACACCAGCTGAAGAAGC
MAPT Exon 4 (reverse)	GCAGCTTCGTCTTCCAGGCT

The transfected iPSCs were then plated onto a well in a 24-well plate for recovery until they became confluent. Thereafter, the cells were singularised before plating 2,000 cells per well in a 6-well plate on irradiated mouse embryonic fibroblast feeder cell line CF1. Ninety-six separate iPSC colonies were picked and transferred into a 96-well plate before they were lysed for DNA extraction. All the DNA samples were then amplified and sequenced. Afterwards, I selected candidate iPSC clones that showed the expected genetic modifications for sub-cloning into a plasmid to confirm successful gene knockout at the allele level (Chapter 2.2). Finally, I differentiated the confirmed iPSC clones into neural progenitor cells (NPCs) (Chapter 2.4.1) and collected cell lysate to determine the absence of tau protein expression by Western blot (Chapter 2.7). Human OmniExpress v1.2 BeadChip array (Illumina) was used post-editing to check for any karyotype abnormalities, which were not present in all iPSC lines used in this study.

2.2 DNA sequencing, polymerase chain reaction and molecular cloning

To determine if the intended *MAPT* genetic modification was successful in a particular iPSC clone, I first prepared 50 ng of the whole-cell DNA samples for sequencing by conducting polymerase chain reaction (PCR) (Table 2.2.1) with primers (IDT) flanking the targeted regions (single primer per reaction) in either *MAPT* Exon 1 or 4 (Table 2.2.2). The DNA regions of interest were amplified with the BigDye™ v3.1 reagent (purchased from the Department of Zoology) before precipitation.

Table 2.2.1: Reagents and conditions of sequencing PCR with BigDye™ v3.1

Reaction constituents		
Reagents	**Volume (µL)**	
BigDye v3.1	0.25	
Sequencing buffer	1.75	
Primer (10 µM)	1	
DNA template (50 ng)	3	
Water	Top up	
Total volume	10	
Sequencing PCR thermocycling conditions		
Temperature	**Duration**	**Cycles**
96 °C	60 s	1
96 °C	10 s	30
50 °C	5 s	
60 °C	240 s	
16 °C	Hold	1

Table 2.2.2: List of primers targeting *MAPT* in PCR for DNA amplification prior to sequencing

Target	Sequence (5' – 3')
MAPT exon 1 (forward)	AATATGGAGCACGGGATGAG
MAPT exon 1 (reverse)	CCGTGTCTGGCCATTATCTC
MAPT exon 4 (forward)	AGAGCTGAGGCACCTTGGTA
MAPT exon 4 (reverse)	CCCGGCCTAGAGTTTCTGTT
T7 (pGEM-T Easy vector)	TAATACGACTCACTATAGGG
SP6 (pGEM-T Easy vector)	TATTTAGGTGACACTATAG

Thereafter, the resultant DNA was precipitated by first adding 2 μL of 125 mM EDTA, 2 μL of 3 M sodium acetate and 50 μL of 100% ethanol to each sample. This was briefly vortexed before centrifugation at 3,000 g at 4 °C for 30 min. After removing the supernatant by centrifugation at 185 g for 15 s, the DNA precipitates were washed with 70 μL of 70% ethanol per sample. Finally, the supernatant was removed again before the DNA precipitate samples were sent to the Department of Zoology for sequencing.

The sequencing results were visualised with the SnapGene® Viewer v5.2.4 and BLAST® [309] to identify candidate iPSC clones that appeared to have undergone successful genetic modifications at the targeted regions. The targeted regions were then sub-cloned into the pGEM®-T Easy Vectors (Promega) to reveal allele-specific genotypes of the candidate iPSC clones. The targeted regions first underwent PCR for amplification with the AmpliTaq Gold™ polymerase (Thermo; Table 2.2.3). The resultant DNA molecules had a single 3' adenine overhang added by the *Taq* polymerase, and the overhang is compatible with the

pGEM®-T Easy Vectors that have a single 3' thymine overhang when digested. The circular pGEM®-T Easy Vectors were digested with NotI-HF restriction enzyme (New England Biolabs) for 1 h at 37 °C (Table 2.2.4), followed by 1% agarose gel (dissolved in TBE buffer containing 100 mM Tris, 100 mM boric acid and 2 mM EDTA) electrophoresis at 85 mA for 90 min. I extracted the linear pGEM®-T Easy Vectors from the agarose gel using the QIAquick PCR Purification Kit (Qiagen). The linear pGEM®-T Easy Vectors were then ligated with the PCR products encompassing the *MAPT* regions of interest overnight at 4 °C (Table 2.2.5).

The next step was to transform the ligated vectors into the One Shot™ TOP10 Chemically Competent *E. coli* (Thermo) by heat shock at 42 °C for 45 s for plasmid transformation. The cells were then plated onto a Luria-Bertani broth (LB) agar plate containing 100 μg/ml of ampicillin and incubated at 37 °C overnight. Subsequently, at least 6 clones (so that the chance of picking all 6 bacterial clones with the same *MAPT* allele insert was 1.6%) were picked for overnight growth in LB plus ampicillin shaking at 37 °C. I then extracted the plasmids with *MAPT* inserts by using the QIAprep Spin Miniprep Kit (Qiagen) and used the T7 and SP6 primers (Table 2.2.2) for DNA sequencing to confirm *MAPT* knockout in both alleles.

Table 2.2.3: Reagents and conditions of PCR with AmpliTaq Gold™

Reaction constituents		
Reagents	**Volume (µL)**	
Amplitaq Gold™	0.08	
10X Gold Buffer	2	
Primer (1:1 mixture of forward and reverse) (1 µM; IDT)	5	
DNA template (50 ng)	5	
dNTPs (2.5 mM each; Thermo)	0.5	
$MgCl_2$ (25 mM; Thermo)	1.2	
Water	Top up	
Total volume	20	
PCR thermocycling conditions		
Temperature	**Duration**	**Cycles**
95 °C	15 min	1
95 °C	30 s	35
60 °C	30 s	
72 °C	30 s	
72 °C	10 min	1
16 °C	Hold	1

Table 2.2.4: Reagents of restriction enzyme digest reaction

Reagents	Volume (μL)
DNA (μg)	Variable
10X CutSmart Buffer	1
NotI-HF restriction enzyme	0.1
Water	Top up
Total volume	10

Table 2.2.5: Reagents of DNA ligation reaction

Reagents	Volume (μL)
PCR product (100 ng)	Variable
Linear pGEM®-T Easy Vectors (25 ng)	0.5
2X Rapid Ligation Buffer	5
T4 DNA Ligase (3 Weiss units/μL)	1
Water	Top up
Total volume	10

2.3 Deep and Frequent Phenotyping pilot cohort and patient derived induced pluripotent stem cells

The Deep and Frequent Phenotyping (DFP) cohort pilot study protocol was detailed in Koychev *et al.* [310] and a subset of the clinical data and study participants (13 early symptomatic AD cases) was used for analyses (Table 2.3.1). The AD patients were aged

between 56 and 82 years old and 5/13 were female. In the study protocol, both amyloid and tau PET imaging with [^{18}F] AV45 (0–60 min, 150 ± 24 MBq; 9/13 participants) and [^{18}F]AV1451 (0–120 min, 163 ± 10 MBq; 8/13 participants), respectively, and MEG recordings (7/13 participants) were conducted once. Global efficiency metric from the γ-band (32-100 Hz) of the MEG raw data was used for analysis as it is the oscillation range linked to cognitive function and local connectivity [311]. Lumbar puncture was performed over two visits 169 days apart in 11/13 of the study participants for CSF collection. $A\beta_{1-42}$ peptide concentration was quantified by electrochemiluminescence in 96-well plates from Meso Scale Discovery (Aβ peptide panel 1 with 6E10 antibody) whereas total tau (tTau) and phospho-tau at Thr181 (pTau181) concentrations were quantified by the INNOTEST enzyme-linked immunosorbent assays (Fujirebio Europe), before deriving the average values from the two visits for downstream analyses. All pilot study participants underwent cognitive testing including a Mini Mental State Examination (MMSE; Mean = 25.2) and a MMSE score loss rate measuring cognitive decline was derived by dividing the MMSE score differences between the baseline visit and symptom onset with the time difference in days. I then calculated an arbitrary 'clinical vulnerability quotient' ranging from 0 (least vulnerable or most resilient) to 1 (most vulnerable, least resilient) by deriving and rescaling within the pilot cohort the clinical outcomes as a function of that individual's CSF $A\beta_{1-42}$ levels or PET standard uptake value ratios (SUVR). The patient-derived iPSC lines were reprogrammed from erythroblasts using Sendai virus via a StemBANCC effort. Prior to neuronal differentiation, the patient lines were transduced with Ngn2 and rtTA lentiviruses (Chapter 2.5) before cryopreservation. The patient iPSC line identification numbers are listed in Table 2.3.2 corresponding to individual cohort participants.

Table 2.3.1: Characteristics of the DFP pilot cohort participants

			AD biomarkers					Clinical outcomes	
Patients	***MMSE score (Baseline visit)***	***APOE genotype***	***Cortical amyloid PET (SUVR)***	***Tau PET (SUVR)***	***CSF $A\beta_{1-42}$ concentration[§] (pg/ml)***	***CSF tTau concentration[§] (pg/ml)***	***CSF pTau181 concentration[§] (pg/ml)***	***MMSE score loss rate[§§] (per day)***	***Global MEG recording[§§§]***
1	22	ε4/ε4	1.60	1.38	298	611	60	1.5×10^{-3}	0.974
2	24	ε2/ε3	1.21	1.32	269	861	103	8.4×10^{-3}	0.983
3	23	ε4/ε4	1.28	N/A	344	1024	119	6.3×10^{-3}	0.985
4	27	ε3/ε4	N/A	N/A	395	251	40	0.2×10^{-3}	N/A
5	25	ε3/ε4	1.60	1.32	450	1233	122	3.9×10^{-3}	0.979
6	22	ε3/ε3	1.28	1.33	252	753	80	3.7×10^{-3}	0.966
7	27	ε3/ε3	N/A	N/A	236	445	71	1.2×10^{-3}	N/A
8	29	ε3/ε4	N/A	N/A	262	1162	140	3.0×10^{-3}	N/A
9	26	ε4/ε4	N/A	N/A	164	555	65	2.9×10^{-3}	N/A
10	24	ε3/ε4	1.30	0.91	414	460	56	1.9×10^{-3}	N/A
11	24	ε3/ε4	1.62	1.09	287	687	95	10.5×10^{-3}	0.944
12	26	ε3/ε4	1.56	1.18	N/A	N/A	N/A	3.1×10^{-3}	N/A
13	29	ε3/ε4	1.18	1.11	N/A	N/A	N/A	0.5×10^{-3}	0.961

[§] Average value between two visits which were 169 days apart

[§§] Derived from two MMSE measurements between the baseline visit and onset of symptoms

[§§§] Global efficiency metric from the γ-band (32-100 Hz)

Note: N/A – not available

Table 2.3.2: DFP pilot cohort patient-derived iPSC identification numbers

Patient #	iPSC ID
1	BPC-927 03-01
2	BPC-928 03-07
3	BPC-929 03-07
4	BPC-932 03-03
5	BPC-934 03-02
6	BPC-936 03-07
7	BPC-937 03-01
8	BPC-939 03-01
9	BPC-940 03-08
10	BPC-943 03-03
11	BPC-944 03-04-01A
12	BPC-946 04-10
13	BPC-947 04-09

2.4 Induced pluripotent stem cell culture and differentiation into cortical neurons

All iPSC lines were seeded on Matrigel® (Corning)-coated plates and cultured in mTeSR™ medium (STEMCELL Technologies) which was replaced daily. Fully confluent iPSC culture was passaged at a 1:6 ratio with TrypLE™ (Thermo) for 5 min in the incubator and pelleted by centrifugation at 400 g for 5 min.

I used two variations of cortical neuron differentiation protocols which were adapted from Shi *et al.* (pharmacologically directed) [268] and Zhang *et al.* (transcription factor directed) [267]. All media were filtered through a polyethersulfone (PES) membrane with a 0.22 μm pore size (Millipore). All cortical neuron cultures were seeded in co-culture with a confluent layer of rat astrocytes except for harvesting cell lysate or live assays in with dyes such as JC-10. For the neuronal monoculture without rat astrocytes, the end point of differentiation was generally set to be Day 50 or before to make sure that the culture remained relatively homogeneous without any contamination with non-neuronal cells that might emerge sporadically.

2.4.1 *MAPT* knockout lines

The first 25 days of cortical neuron differentiation was adapted from Shi et al. [268] (Figure 2.4.1). The *MAPT*+/+, *MAPT*+/- and *MAPT*-/- iPSC lines were first seeded on Geltrex™ (Thermo)-coated plates at 105,000 cells/cm^2 (1,000,000 cells in a well of a six-well plate) in mTeSR™ medium supplemented with 10 μM Y-27632 (Tocris). The Y-27632 compound was removed from the medium the next day and subsequently the medium was replaced daily. When the iPSC culture became confluent, it was washed once with PBS before changing to neural induction medium (NIM) which is neural maintenance medium (NMM) supplemented with 10 μM SB-431542 (Tocris) and 1 μM Dorsomorphin. NMM contains two types of media at 1:1 ratio: **(1)** Neurobasal™ medium (Thermo) supplemented with 1X B-27™ supplement (Thermo), 25 U/ml Penicillin-Streptomycin (Thermo) and 1 X GlutaMAX (Thermo) **(2)** DMEM/F12 medium (Thermo) supplemented with 1X N-2 supplement (Thermo), 50 μM non-essential amino acid (Thermo), 50 μM 2-

mercaptoethanol (Thermo), 2.5 μg/ml insulin, 1 mM sodium pyruvate (Thermo) and 2 mM L-glutamine (Thermo). The NIM was subsequently replaced daily until Day 12.

I passaged the cells on Day 12 with 1 mg/ml dispase (10 mg/ml dispase dissolved in PBS and added directly to the cell culture media), for approximately 10 to 30 min in the incubator. The sheet of cells was then broken up by pipetting once before transferring to 10 mL of NIM. The cell aggregates were allowed to settle by gravity before I washed the cell aggregates with 10 mL of NIM twice. Finally, the cell aggregates were seeded onto 15 μg/ml fibronectin-coated plates at a 1:2 ratio in NIM.

On Day 13 and 15, the cells were provided with NMM supplemented with 20 ng/ml FGF2. On Day 17, I passaged the cultures as on Day 12 except that the cells were washed and plated in NMM. The cell aggregates were seeded onto 100 μg/ml poly-L-ornithine plus 10 μg/ml laminin (PO/L)-coated plates at a 1:3 ratio. Finally, the NMM was replaced every two days until Day 25 where the NPCs were lifted by incubating with Accutase® and cryo-preserved at 2,000,000 cells/vial in NMM supplemented with 20 ng/ml FGF2.

The second part of the differentiation protocol beyond Day 25 was modified from Zhang *et al.* and the protocol relies on the doxycycline-inducible overexpression of a transcription factor Ngn2 to result in an excitatory cortical neuronal identity [267]. Each vial of NPCs was thawed, spun down, and plated into a single well in a twelve-well plate (Day 25). Ngn2 and rtTA lentiviruses (Chapter 2.5) (25 μL each) were added into the cell suspension in NMM as the NPCs settled onto PO/L-coated plates. The cell culture medium was replaced 8 h later. On Day 28, the NMM was replaced by neuronal medium consisting of Neurobasal™ medium (Thermo) supplemented with 1X B27™ (Thermo), 1X GlutaMAX™

(Thermo), 25 U/ml Penicillin-Streptomycin (Thermo), 10 ng/ml neurotrophin-3, 10 ng/ml BDNF (Peprotech), 1 µg/ml doxycycline, 200 ng/ml laminin and 200 µM ascorbic acid. On Day 30, the neuronal medium was replaced and supplemented with 1 µg/ml puromycin. On Day 32, the neurons were passaged with Accutase® and seeded in co-culture with a confluent monolayer of primary rat cortical astrocyte seeded onto 10 µg/ml poly-D-lysine-coated plates at its third passage (Thermo). On Day 40, the co-culture was treated with 100 nM Ara-C which was gradually removed over subsequent feedings.

When co-culture was not suitable for a particular experiment such as biochemical analysis, the neurons were seeded onto PO/L-coated plates. I maintained the rat cortical astrocyte culture in DMEM with high glucose supplemented with 15% foetal bovine serum (FBS) (Thermo), 2 mM L-glutamine (Thermo) and 50 U/ml Penicillin-Streptomycin (Thermo). After the neurons were seeded onto the astrocyte, the co-culture was maintained in the neuronal medium only.

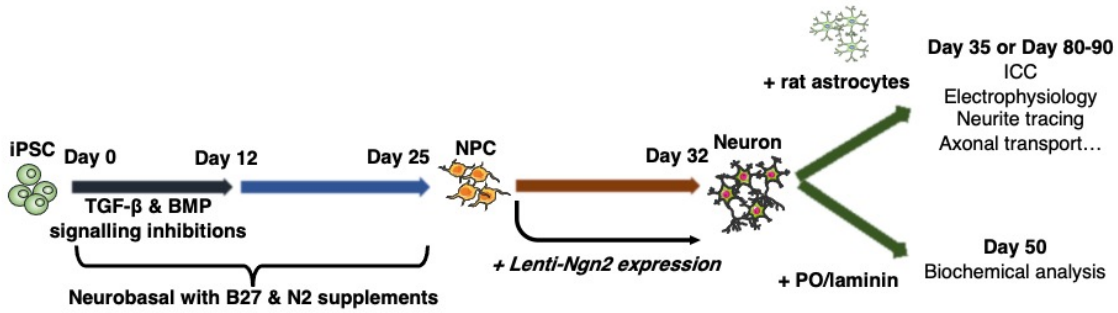


Figure 2.4.1: Schematic of the cortical neuron differentiation protocol used for the *MAPT* knockout lines

2.4.2 Deep and Frequent Phenotyping pilot cohort lines

As compared to Chapter 2.4.1, this protocol involved overexpressing Ngn2 starting from Day 0 of the differentiation process. The iPSC lines were thawed and seeded between 60,000 to 90,000 cells/cm^2 onto PO/L-coated plates in mTeSR^{TM} medium supplemented with 10 µM Y-27632 (Figure 2.4.2). The mTeSR^{TM} medium was replaced with the neuronal medium 5 h later as described in Chapter 2.4.1. On Day 2, the neuronal medium was replaced and supplemented with 1.5 µg/ml puromycin. On Day 4, similar to Day 32 in Chapter 2.4.1, the neurons were lifted and seeded onto a confluent layer of rat cortical astrocytes in 96-well plates at 25,000 cells/cm^2. The DFP cohort patient-derived neurons were treated with 100 nM Ara-C on Day 10, 20, 40 and 60 before treatments with extrinsic Aβ insults on Day 80.

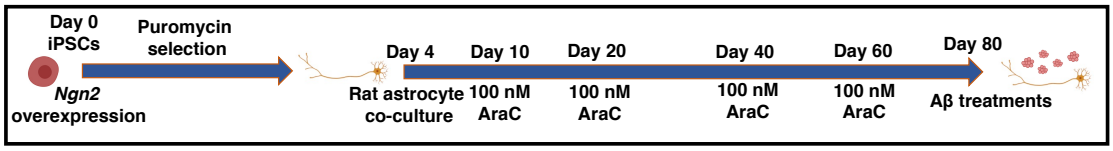


Figure 2.4.2: Schematic of the cortical neuron differentiation for the iPSC lines derived from the DFP pilot cohort

2.5 Packaging of lentiviral plasmids

I generated lentiviral particles carrying plasmids that express genes of interest by expressing lentiviral proteins in HEK293T cells which were grown in DMEM/F12 medium supplemented with 10% FBS, 2 mM L-glutamine, 100 µM non-essential amino acids and 50 U/ml Penicillin-Streptomycin (all from Thermo). The cells were passaged with TrypLE^{TM} (Thermo) and seeded at 80,000 cells/cm^2 (1,000,000 cells in a T75 flask) 24 h before plasmid transfection.

The following protocol describes the reagents used for a single T75 flask of HEK293T cells. The Lipofectamine™ 3000 transfection reagent (Thermo) was used to deliver plasmids into HEK293T cells. 40 µL Lipofectamine™ 3000 transfection reagent was first mixed with 50 µL of P3000 reagent (also from the same kit) in 1 mL of Opti-MEM™ medium (Thermo) for at least 5 min. Meanwhile, various plasmids expressing lentiviral proteins were mixed with plasmids expressing genes of interest in equimolar ratio in 1 mL of Opti-MEM™ medium in another tube. I used second-generation lentiviral packaging plasmids psPAX2 (#12260; 10 µg) and pMD2.G (#12259; 5.65 µg) to produce lentiviral particles. These plasmids were mixed with FUdeltaGW-rtTA (rtTA; #19780; 9.6 µg), pTet-O-Ngn2-puro (Ngn2; #52047; 9.6 µg) or pLV-TetO-hNGN2-eGFP-Puro (Ngn2-GFP; #79823; 9.6 µg) individually. All plasmids were purchased from Addgene. Finally, the plasmid tube was added to the Lipofectamine tube dropwise before adding the mixture to the cells now grown in 13 mL of the above-mentioned medium without Penicillin-Streptomycin. The transfection reagents were left overnight and replaced with fresh medium the following day with Penicillin-Streptomycin.

I collected the lentivirus-containing cell supernatant 48 h after the last medium change and it was centrifuged at 400 g for 5 min to remove any cells before filtering through a cellulose acetate membrane with 0.45 µm pore size (Millipore). The supernatant was snap-frozen in dry ice before storing it at -80 °C. For the pLV-TetO-hNGN2-eGFP-Puro virus, the aliquots were thawed once and sub-aliquoted in small volume to keep the lentivirus titre consistent since a small amount of this particular lentivirus was needed per transduction.

2.6 Harvesting cell lysate and quantifying protein concentration

The NPCs were seeded on PO/L-coated plates on Day 25 and maintained until Day 30 for harvesting NPCs or the Day 25 NPCs were transduced with the *Ngn2* lentivirus and final plated on Day 32 for harvesting neurons on Day 50. The cells were washed once with PBS before they were lysed on ice in radioimmunoprecipitation assay (RIPA) buffer containing 50 mM Tris-HCl, 150 mM NaCl, 1% (v/v) Triton X-100, 1% (w/v) sodium deoxycholate and 0.1% (w/v) sodium dodecyl sulphate (SDS) at pH 7.4. The RIPA buffer was supplemented with cOmplete™ mini EDTA-free protease inhibitor cocktail (Roche). The lysate was then transferred into a tube on ice and left incubating for at least 15 min. Finally, the lysate was centrifuged at 20,000 g for 30 min at 4 °C before the supernatant was frozen at -80 °C.

To quantify protein concentration in the lysates, I used the Pierce™ BCA Protein Assay Kit (Thermo) following manufacturer's instructions. Briefly, 12.5 µL of either bovine serum albumin (BSA) standards or cell lysates were added into a 96-well plate followed by 100 µL of the BCA reagent. The plate underwent incubation at 37 °C for 30 min before I read it for BCA absorbance at 562 nm wavelength in a PHERAstar® microplate reader (BMG Labtech). Protein concentration was determined by comparing to a BSA standard curve.

2.7 SDS-PAGE and immunoblot

Cell lysates were denatured by heating at 95 °C for 10 min with sample loading dye containing (final concentration in the mixture) 2% SDS, 5% 2-mercaptoethanol, 10% glycerol, 0.002% bromophenol blue and 375 mM Tris at pH 6.8. For immunoblots probing for tau protein, the cell lysates underwent dephosphorylation with (final concentration in the

mixture) 10% $MnCl_2$, 10% reaction buffer and 0.38 µL lamda-phosphatase (New England Biolab; sufficient for up to 10 µg of cell lysate) for 1 h at 30 °C prior to adding the sample loading dye for denaturation.

Denatured samples were loaded into precast 4-15% gradient polyacrylamide gels (Bio-Rad) submerged in SDS-PAGE running buffer consisting of 25 mM Tris base, 192 mM glycine and 0.1% SDS. I ran the SDS-PAGE at 100 V for 3.5 h and the gel underwent semi-dry transfer by the Trans-Blot® Turbo™ Transfer System (Bio-Rad) onto a 0.2 µm PVDF membrane at 1.3 A for 11 min. The resultant blot was washed once in tris-buffered saline with 0.1% Tween-20 (TBST) and blocked in 5% milk dissolved in TBST shaking for 1 h at room temperature. The blot was then incubated with primary antibodies (Table 2.6) diluted in 1% milk in TBST shaking overnight at 4 °C.

The blot was washed with TBST shaking for 10 min at room temperature three times prior to incubation with secondary antibodies (Table 2.6) diluted in 1% milk in TBST for 1 h at room temperature. Thereafter, I washed the blot for three more times before adding Immobilon® Western Chemiluminescent HRP Substrate (Millipore) to the blot. The blot was imaged in the ChemiDoc™ Imager (Bio-Rad) and analysed in the Image Lab v6.1 (Bio-Rad) software.

Table 2.7: List of primary and secondary antibodies used for immunoblotting

Primary antibodies	Host species	Dilution	Supplier
Tau-1	Mouse	1:1,000	Millipore
Tau-5	Mouse	1:500	Abcam
Tau-46	Mouse	1:500	Santa Cruz
Actin-HRP conjugate	Mouse	1:10,000	Abcam

Secondary antibodies	Dilution	Supplier
Goat anti-mouse IgG-HRP	1:5,000	Bio-Rad
Goat anti-rabbit IgG-HRP	1:5,000	Bio-Rad

2.8 RNA extraction and quantitative polymerase chain reaction

iPSC-derived cortical neurons were seeded on PO/L-coated plates and maintained until Day 30 before lysing with the TRIzol™ reagent (Thermo) to extract total RNA. The lysate was phase-separated by mixing vigorously with chloroform equivalent to 10% of the lysate volume and spinning at 4 °C at 10,000 rpm for 10 min. I then transferred the transparent aqueous layer and added an equal volume of 70% ethanol prior to column extraction using the RNeasy Mini Kit (Qiagen). The resultant RNA samples were quantified using the Qubit™ RNA Assay Kit (Thermo). For reverse transcription, 1 µg of RNA was converted to cDNA using the SuperScript™ III Reverse Transcriptase System (Table 2.6.1) and 5 ng of cDNA was used per quantitative PCR (qPCR) reaction per well. The TaqMan Gene Expression Master Mix (Table 2.6.2) was used for qPCR assays and the plates were read on the StepOnePlus System (Applied Biosystems) equipment. The FAM-labelled TaqMan Expression Assays for *MAPT* were multiplexed with VIC-labelled equivalents for control

housekeeping genes. The qPCR primers I used are listed in Table 2.6.3. *MAPT* expression levels were determined by normalising to the geometric means of the three housekeeping genes used.

Table 2.8.1: Conditions of SuperScript™ III Reverse Transcriptase System

Reagents	**Volume per reaction (µL)**
Total RNA (1 µg)	11 in total
Water	
dNTP mix (10 mM; Thermo)	1
Random primers (150 ng/µL; Thermo)	1
Sub-total	13
Reaction conditions: 65 °C for 5 min, on ice for 1 min	
5X First-Strand Buffer	4
DTT (0.1 M)	1
RNaseOUT™ ribonuclease inhibitor (40 U/µL; Thermo)	1
SuperScript III (200 U/µL)	1
Total	20
Reaction conditions: 25 °C for 5 min, 55 °C for 60 min then 70 °C for 15 min	

Table 2.8.2: Conditions of qPCR with TaqMan Expression Assays

Reagents		**Volume per reaction (µL)**
cDNA (1 ng/ml)		5
TaqMan Gene Expression Master Mix (2 X)		10
MAPT probe primer mix (20 X) FAM		1
Housekeeping gene probe primer mix (20 X) VIC		1
Water		3
Total		20
Thermocycling conditions		
Temperature (°C)	**Duration**	**Cycles**
50	2 min	1
95	10 min	1
95	15 s	40
60	1 min	

Table 2.8.3: List of TaqMan qPCR primers used to quantify *MAPT* transcripts

TaqMan Gene Expression Assay	**Assay ID**
MAPT Exon 3+ Transcripts (Exon 3-4)	Hs00902315_m1 FAM/MGB/NFQ
MAPT Exon 10+ Transcripts (Exon 9-10)	Hs00902312_m1 FAM/MGB/NFQ
MAPT Total (Exon 12-13)	Hs00902194_m1 FAM/MGB/NFQ
GAPDH	Hs02758991_g1 VIC/MGB/NFQ
HPRT1	Hs02800695_m1 VIC/MGB/NFQ
ACTIN	Hs01060665_g1 VIC/MGB/NFQ

2.9 Extraction of brain homogenate from human Alzheimer's disease post-mortem cortical tissues

The AD post-mortem brain homogenate extraction protocol was modified from Jin *et al*. [312]. To elaborate, 1 g of AD cortical tissue was thawed on ice prior to homogenisation in a Dounce homogeniser for 25 strokes in 4 mL of cold artificial CSF (aCSF; 124 mM NaCl, 2.8 mM KCl, 1.25 mM NaH_2PO_4 and 26 mM $NaHCO_3$, pH = 7.4) supplemented with a panel of protease inhibitors (5 mM EDTA, 1 mM EGTA, 5 ug/ml leupeptin, 5 µg/ml aprotinin. 2 µg/ml pepstatin, 120 µg/ml Pefabloc and 5 mM NaF). I then performed ultracentrifugation at 200,000 g for 110 min at 4 °C with a SW-41 Ti rotor (Beckman Coulter) and transferred the supernatant into a Slide-A-Lyzer™ G2 Dialysis Cassettes 2K MWCO (Thermo) in a 100X volume of aCSF without the protease inhibitors swirling for 72 h. The aCSF bath was replaced every 24 h. The resultant brain homogenate was frozen at -80 °C.

I obtained the AD cortical tissues from the Oxford Brain Bank and temporal cortices from a patient and healthy control (73 years old, female, Braak stage VI, 75 h delay post-mortem, *APOE* ε3/ε3; 70 years old female healthy control, Braak stage I, 81 h delay post-mortem, *APOE* ε3/ε3) were used for the *MAPT* knockout project. Frontal cortices from two patients and a healthy control (#1: The same 73-year-old female, #2: 81 years old, male, Braak stage VI, 26 h post-mortem delay, *APOE* ε4/ε4; and the same 70-year-old female healthy control) were used for the DFP cohort project. The brain homogenates from both frontal cortices were pooled together for experiments.

2.9.1 Isolating human brain-derived amyloid-β

Immunodepleted controls were included in a subset of the experiments using AD brain homogenate as Aβ insult. First, Protein A (if the host species is rabbit) or Protein G (if the host species is mouse) agarose beads (Abcam) were washed three times in aCSF and centrifuged at 400 g for 5 min at 4 °C. The beads were then resuspended in 50% slurry with aCSF. At the same time, the brain homogenate aliquots were thawed on ice and centrifuged at 16,000 g at 4 °C for 2 min. The agarose beads were then added to the brain homogenate at 3% v/v. Thereafter, 3 mg/ml of S97 anti-amyloid antibody (gifted by Dominic Walsh; host species: rabbit) at 1:100 dilution (for the *MAPT* knockout project) or 1 mg/ml of each 4G8 and 6E10 anti-amyloid antibodies (Biolegend) at 1:500 dilution (for the DFP cohort project) was added to the brain homogenate-agarose beads mixture. I also performed mock immunodepletion on the AD and healthy control brain homogenates with normal rabbit or mouse IgG antibodies (Abcam).

The mixture was left rotating at 4 °C for 12 h before it was centrifuged at 400 g for 5 min at 4 °C. The supernatant was transferred for another two rounds of mock or actual immunodepletion whereas the beads were kept in PBS at 4 °C for the brain-derived Aβ isolation process later. Finally, the supernatant was mixed with Protein A or G agarose beads only (at 2% v/v) for 2 h before the brain homogenate was used for treatments on iPSC-derived cortical neurons.

The antibody-coated agarose beads that pulled down Aβ were washed 3 times with 1 ml of PBS, each time settling the beads by centrifugation at 400 g for 5 min at 4 °C. I then eluted Aβ bound to the antibodies by adding 0.1 M glycine (pH 2.8) that was equivalent to 3 times in volume of the beads. The tube was left rotating at room temperature for 10 min and the

eluate was transferred to an equal volume of 1 M Tris (pH 8.0). This elution step was repeated for another two times on the same beads before the eluate was transferred to a centrifuge filter protein concentrator (3K MWCO). The concentrators underwent centrifugation at 14,000 g for 2 h at 4 °C and the Aβ solution that remained above the filter was diluted in PBS before storing at -80 °C. The overall elution efficiency is listed in Table 2.9.1.

Table 2.9.1: Calculations of elution efficiency for brain-derived Aβ enrichment over 7 attempts

Attempt	Amount of $A\beta_{1-40}$ pulled-down in theory (pg)	Amount of $A\beta_{1-40}$ eluted in practice (pg)	Elution efficiency (%)	Remarks
1 (New concentrator columns)	1085	246	22.7	Temporal 2 ml S97
2 (Reused columns)	328	105	32	Temporal 2 ml S97
3 (Reused columns)	402	16	4	Temporal 1 ml commercial
4 (Reused columns)	23486	74	0.32	Frontal 8 ml commercial
5 (Reused columns)	8260	21	0.25	Frontal 3 ml commercial
6 (New concentrator columns)	23694	641	3	Frontal 12 ml commercial
7 (New concentrator columns)	31333	953	3	Frontal 12 ml commercial

2.9.2 Soluble amyloid-β immunoassay

I quantified Aβ in/from brain homogenate using the V-Plex Plus Aβ Peptide Panel 1 (6E10) Kit from Meso Scale Discovery (MSD) according to the manufacturer's instructions. The samples of interest were diluted 1:2 (for brain homogenate) or 1:8 (for brain-derived Aβ) in the assay buffer for quantification. The MSD Workbench 4.0 software was used to analyse Aβ levels via electrochemiluminescence from antibodies bound to Aβ.

I replaced the MSD kit with a Cisbio $A\beta_{1-40}$ kit in 2020 (Cisbio $A\beta_{1-42}$ kit was not available yet) as the Cisbio kit was more cost-effective if I only needed to determine Aβ depletion in

the AD brain homogenate. The Aβ levels were detected via homogeneous time-resolved fluorescence from a pair of antibodies. The samples were also diluted in the same ratios as in the MSD kit. After mixing the kit reagents and Aβ samples and leaving the plate to incubate overnight at 4 °C, I read the Cisbio plate in a PHERAstar® microplate reader (BMG Labtech) to detect fluorescence signals at wavelengths 665 and 620 nm. The data were represented as ΔF which is a relative value to the 665/620 nm signal ratio of the negative control.

The overall quantification of AD brain homogenate, immunodepleted homogenate and isolation of AD brain-derived Aβ is represented in Figure 2.9.2. Both $A\beta_{1-40}$ and $A\beta_{1-42}$ were present in the AD brain homogenate derived from both temporal and frontal cortices (approx. 2,000-3,000 pg/mL of $A\beta_{1-40}$ and 200-300 pg/mL of $A\beta_{1-42}$), but only at low levels in both Aβ immunodepleted (ID) AD brain homogenate (up to 78 pg/mL of $A\beta_{1-40}$ and 3.5 pg/mL of $A\beta_{1-42}$) and healthy brain homogenate (up to 125 pg/mL of $A\beta_{1-40}$ and 21 pg/mL of $A\beta_{1-42}$) (Figure 2.9.2A). Approximately 200 pg/mL of $A\beta_{1-40}$ managed to be isolated per mL of AD brain homogenate, making it around 10% of antibody-captured Aβ that was successfully eluted and concentrated via the isolation procedure (Chapter 2.9.1).

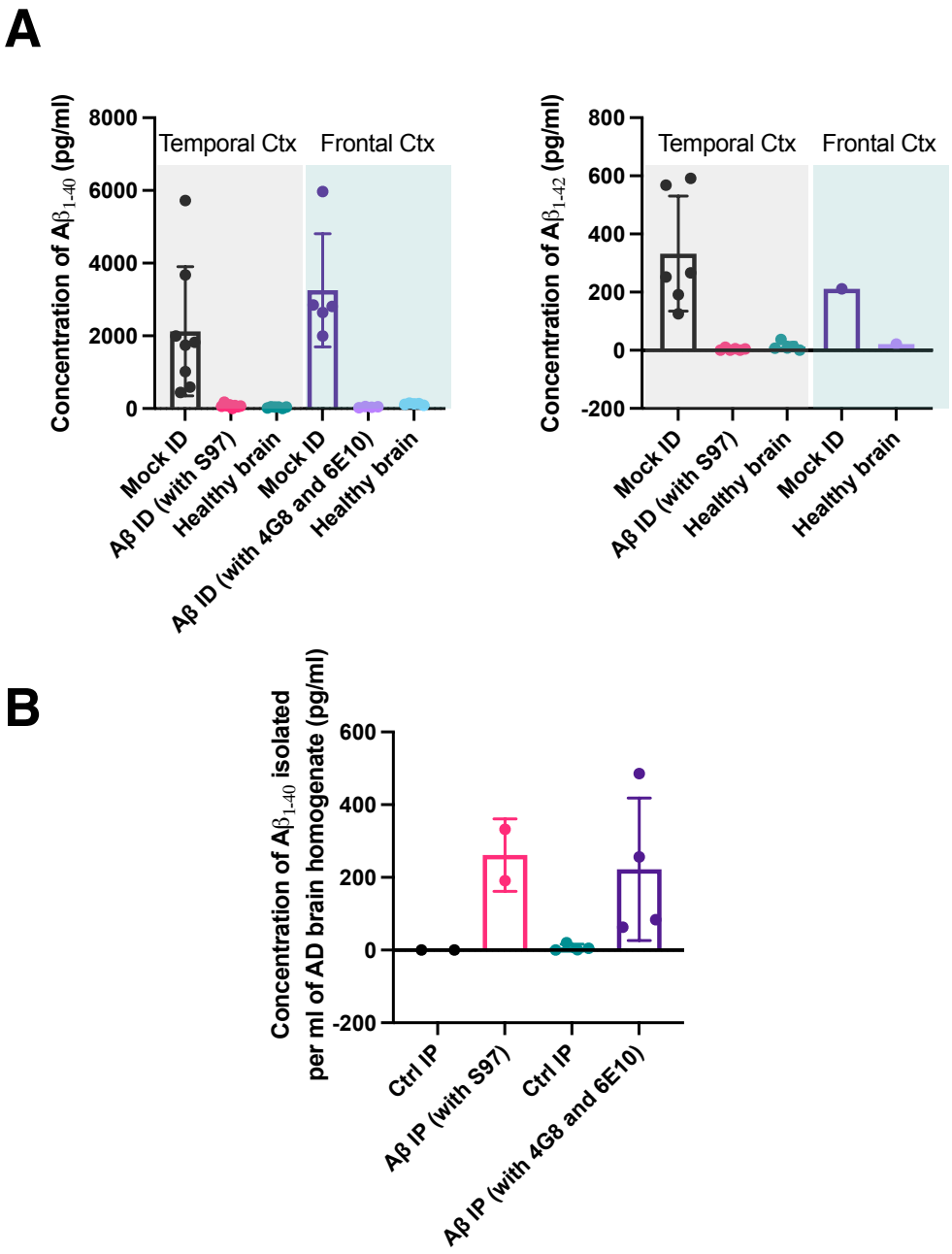


Figure 2.9.2: Quantification of Aβ in AD brain homogenate and isolated brain-derived Aβ

(A) $A\beta_{1-40}$ and $A\beta_{1-42}$ measured in various brain homogenates. All readings for the temporal cortex $A\beta_{1-40}$ were measured using the MSD assay except one with the Cisbio assay; all readings for the frontal cortex $A\beta_{1-40}$ were measured using the Cisbio assay except one with the MSD assay; all readings for $A\beta_{1-42}$ were recorded using the MSD assay. N = 7 (temporal cortex $A\beta_{1-40}$) or 6 (frontal cortex $A\beta_{1-40}$ and all $A\beta_{1-42}$ readings) independent repeat measurements.

(B) $A\beta_{1-40}$ measured in Aβ isolated from AD brain homogenate via IP adjusted per mL of brain homogenate using the Cisbio assay. N = 2 (IP with the S97 antibody) or 4 (IP with the 4G8 and 6E10 antibody mixture) independent repeat measurements.

No statistical analysis was performed for this figure on the data derived from the post-mortem brain tissue of a single individual of each disease status.

2.10 Synthetic Amyloid-β oligomerisation

2.10.1 Amyloid-β_{1-42}

Both lyophilised $A\beta_{1-42}$ and treatment control scrambled $A\beta_{1-42}$ peptides (Bachem, H-1368 and H-7406) were resuspended to 1 mM in Hexafluoro-2-propanol (HFIP). The tubes were vortexed and left sitting at room temperature for 30 min, before they were aliquoted and dried in a Speed-Vac concentrator for 30 min (Thermo) and stored at -80 °C. To oligomerise the $A\beta_{1-42}$ peptides, I first resuspended the Aβ film in dimethyl sulfoxide (DMSO) to 5 mM before sonicating them in a water bath at room temperature for 10 min. I then added PBS to dilute the peptides to 100 μM and the tubes were left stationary at 4 °C for 24 h. Just before treating the cells with Aβ oligomers, the solution was centrifuged at 14,000 g for 10 min at 4 °C to remove any precipitate/fibrils. The $A\beta_{1-42}$ oligomers were used at a concentration range from 2 to 20 μM.

2.10.2 Amyloid-β_{25-35}

Both lyophilised $A\beta_{25-35}$ and treatment control $A\beta_{35-25}$ reversed peptides (Bachem, H-1192 and H-2964) were resuspended to 2 mg/ml in deionised water and vortexed before incubating at 37 °C for 2 h for oligomerisation. The vial was then aliquoted and frozen at -80 °C. The $A\beta_{25-35}$ oligomers were used at a concentration of 20 μM.

2.11 Transmission electron microscopy

$A\beta_{1-42}$ oligomer samples were first applied onto a carbon-coated 3 mm copper grid (TAAB), which underwent glow discharge for 20 s, by adding 10 μL of 100 μM samples. The samples

incubated for 2 min at room temperature on the copper grid, before staining with 2% uranyl acetate for 10 s. The grid was washed once with water and stored at room temperature.

Transmission electron microscopy (TEM) images were acquired using a Tecnai 12 TEM microscope (120 kV) with a Gatan US1000 camera.

2.12 Thioflavin T assay

I dissolved lyophilised Thioflavin T (ThT) in PBS to 2 mM before filtering with a PES membrane with a 0.22 μm pore size (Millipore). The ThT stock solution was added to Aβ samples to result in 50 μL of reaction mix with 20 μM ThT per well in a 96-well plate. The plate was subsequently sealed and left incubating for 30 min at 37 °C shielded from light. I read the plate in in a PHERAstar® microplate reader (BMG Labtech) to detect fluorescence at a wavelength of 520 nm (4.1 mm focal plane and 500 units of gain). The fluorescence intensity readings were subtracted by those of negative control (ThT only) for analysis.

2.13 High-content imaging and analysis

Punctate staining such as synaptic, lysosomal, and mitochondrial markers: Neurons seeded in 96-well plates were imaged on a Perkin Elmer Opera Phenix high-content imager. I captured 15 images per well with a 43X objective at +1 μm focus level with a binning value of 1. I then analysed the images with the Harmony software v4.9 from Perkin Elmer with a customised pipeline. The MAP2-positive neurites were identified with a 0.5-unit overall threshold as the region of interest and resized by expanding outwards by 5 px to

cover synaptic signals which lay slightly above the MAP2 signals. For synaptic markers, both presynaptic (SYNAPSIN I/II) and postsynaptic (HOMER1) signals were then identified with the Method A of the "Find spots" function with threshold values of 0.17 and 0.14, respectively, with spots larger than 100 px^2 filtered away. Finally, the synapses were ascertained by finding HOMER1 signals in the vicinity of SYNAPSIN I/II signal regions which had been resized by expanding outwards by 5 px. The absolute number of synapses was then normalised to the total MAP2-positive area to derive synaptic density which was used for all downstream analyses. Synapse loss was achieved by adding the following Aβ insults to the neurons: (1) 10 μM of $A\beta_{1-42}$ oligomers for 24 h, (2) 20 μM of $A\beta_{25-35}$ for 24 h, (3) 25% (v/v) of AD brain homogenate for 72 h, and (4) 12.5% (v/v) of AD brain homogenate for 5 days.

Nuclear staining such as cortical markers and cleaved caspase 3 (CC3): I captured 15 images at -1, 0 and +1 and μm focus levels per well with a 20X objective and binning value of 2. I analysed the images on the same Harmony software by first identifying human nuclei among the co-culture with rat astrocytes and filtering away the nuclei with circularity less than 0.6 units. The percentage of signal-positive cells was calculated by selecting the human nuclei with mean signal intensity greater than a threshold which was determined as the mean intensity across all human nuclei identified plus two standard deviations. To induce cytotoxicity and CC3 overexpression, I treated the neurons with either 10 or 20 μM of $A\beta_{1-42}$ oligomers for 5 days.

2.13.1 Immunocytochemistry

Adherent neurons were fixed in 4% paraformaldehyde for 5 min (for synaptic staining) or 20 min (for every other marker), followed by treating with 0.05% saponin in PBS for 20 min for permeabilisation. To block the samples, I treated the plates with 10% normal goat serum (NGS) with 0.01% tween-20 in PBS for 30 min. Primary antibodies were then left incubating with the samples at 4°C overnight with 1% NGS and 0.01% tween-20, before washing 3 times with PBS. Secondary antibodies were then applied in 1% NGS and 0.01% tween-20 at room temperature for 1 h before washing for another 4 times before imaging on the same day. The primary and secondary antibodies used are listed in Table 2.11.1.

Table 2.13.1: List of primary and secondary antibodies used for immunocytochemistry

Primary antibodies	Host species	Dilution	Supplier (Catalogue #)
Synapsin I/II	Guinea pig	1:500	Synaptic Systems (106004)
Homer1	Rabbit	1:500	Synaptic Systems (160003)
vGLUT1	Rabbit	1:500	Synaptic Systems (135303)
MAP2	Chicken	1:1,000	Abcam (ab92434)
Human nuclear antigen	Mouse	1:200	Abcam (ab191181)
Cleaved caspase 3	Rabbit	1:500	Abcam (ab2302)
CUX2	Rabbit	1:200	Abcam (ab130395)
TBR1	Rabbit	1:200	Abcam (ab31940)
CTIP2	Rat	1:500	Abcam (ab18465)
Secondary antibodies		**Dilution**	**Supplier (Catalogue #)**
Goat anti-guinea pig Dylight 488		1:1,000	Abcam (ab96959)
Goat anti-mouse Alexa Fluor 488			Thermo (A11001)
Goat anti-rabbit Alexa Fluor 555			Thermo (A27039)
Goat anti-chicken Alexa Fluor 555			Thermo (A21437)
Goat anti-rabbit Alexa Fluor 647			Thermo (A21245)
Goat anti-rat Alexa Fluor 647			Thermo (A21247)

2.13.2 Live neurite tracing

To accurately trace neurite with live imaging, I transduced a low titre of lentivirus (Ngn2-GFP; Chapter 2.5) that led to the expression of green fluorescent protein (GFP) in approximately 1% of the neuronal population. The Ngn2-GFP virus was introduced at the same time as the regular Ngn2 virus on Day 25 of the cortical neuron differentiation (Chapter 2.4.1) when the NPCs were thawed. I added 0.25 μL (0.025% v/v in the neuronal media) of the Ngn2-GFP virus per well in a 12-well plate per vial of NPCs thawed, and the rest of the differentiation protocol remained the same. The neurons were seeded in co-culture with rat astrocytes on Day 32 at 25,000 cells/cm^2, and the live imaging session started on Day 35 and the neurons were imaged daily. For neurite tracing experiments with extrinsic Aβ insults, I added either 5 or 10 μM of $A\beta_{1-42}$ oligomers and traced the neurites over the next 5 days. The whole well was imaged with a 20X objective with 1% overlap between the fields of view to ensure neurite continuity between images.

The images were analysed with the Harmony software with a customised pipeline. Both nuclei and neurites could be identified with the same GFP signal which is stronger at the nuclei. I first identified the nuclei with the "Find nuclei" function with Method B and filtered away the identified nuclei with circularity less than 0.6, length greater than 10 μm and width to length ratio greater than 0.3 to remove false positives. The neurites were then traced from the nuclei with the "Find neurite" function. Four parameters were selected in this study: (1) Total neurite length per neuron, (2) maximum neurite length per neuron, (3) ramification index per neuron and (4) neurite branch length per branch.

2.14 Cytotoxicity assay measured by adenylate kinase

I used the ToxiLight™ Non-Destructive Cytotoxicity BioAssay Kit (Lonza) to quantify levels of cytotoxicity in neuronal culture supernatant by measuring the release of adenylate kinase (AK). The AK detection reagent was made by mixing the lyophilised reagent with the AK assay buffer supplied in the kit at room temperature. The AK detection reagent was left for 15 min at room temperature shielded from light. I then added 100 µL of the AK detection reagent to 25 µL of cell supernatant per well before incubating for 5 min at room temperature. The plate was read in a PHERAstar® microplate reader (BMG Labtech) by detecting the levels of fluorescence intensity. Higher fluorescence intensity indicates greater amount of AK released into the neuronal culture supernatant i.e. higher cytotoxicity levels. The AK assay was not performed for the experiments that involved brain homogenate treatments as the soluble factors interfered with the AK detection reagent.

2.15 Mitochondrial axonal transport live imaging in microfluidic devices

I used MitoTracker™ Deep Red FM (Thermo) dissolved in DMSO at 100 nM to label mitochondria for axonal live imaging on a NIKON Eclipse TE-2000-U fluorescent microscope. The MitoTracker was removed by replacing the staining media with Hank's balanced salt solution (HBSS) supplemented with 5 mM glucose and 10 mM HEPES. The automated microscope manoeuvre and imaging parameters were controlled by the Volocity® v6.3.1 (Perkin Elmer) software. I took an image every second for the live imaging with a 20X air objective at 37 °C. For the Aβ insult experiments, I first took baseline images in HBSS before treating the neurons with 2 µM $A\beta_{1-42}$ oligomers for 1 h and imaging again

post-treatment. For the positive control of mitochondrial transport inhibition, 10 µg/ml of nocodazole was used instead for 1 h. The time course images were then exported as .tiff files to be analysed with Fiji [313] using a macro called TrackMate [314] to track moving mitochondria along axons. The Laplacian of Gaussian filter was applied for the spot detector, and I set the estimated blob diameter to be 6 px. The quality threshold was selected to be 5 units and sub-pixel localisation was applied. The number of stationary spots were determined by the median value of all images and the moving spots were determined by subtracting every image in the time course to the median image. A moving mitochondrion was defined by having travelled continuously for at least 10 s and for more than 2 µm in displacement over 150 s of time lapse imaging. I selected motile mitochondria ratio, mean speed, and displacement of mitochondrial axonal transport as the readouts of interest.

I used the AXIS^{TM} microfluidic devices (Millipore, discontinued in 2018) and those from XONA Microfluidics to isolate axons and establish directionality for live imaging. Both types of devices had multiple 450-µm long microgrooves between two chambers and the cell bodies were separated by the microgrooves within each chamber. iPSC-derived cortical neurons were seeded at 100,000 cells/cm^2 according to Chapter 2.4.1 in co-culture with rat astrocytes on one side (soma chamber) of the microfluidic device. The other side of the device (distal chamber) was filled with the same neuronal media (maintained a volume gradient with less volume on the distal side) with BDNF and NT-3 10 times more concentrated to encourage axonal outgrowth towards the distal chamber. Mitochondrial axonal transport live imaging took place on Day 80, but the timepoint ranges from Day 70 to 95 due to technical issues and lab closure during the COVID-19 pandemic. To label mitochondria, the MitoTracker dye was added to the device and left incubating in the dark

at 37 °C for 3 h. The live imaging per field of view lasted for 150 s and at least 20 axons were imaged per device.

2.16 Mitochondrial membrane potential measurement with JC-10

The iPSC-derived neurons seeded at 50,000 cells/cm^2 in monoculture were aged until Day 50. The neurons were then stained with a JC-10 dye before having their mitochondrial membrane potential measured by detecting signals in two wavelengths emitted by the JC-10 dye. For the Aβ insult experiments, I treated the neurons with 2 μM of $A\beta_{1\text{-}42}$ oligomers for 1 h before removing the oligomers and replaced the medium with DMEM basal medium without phenol red (Thermo) with JC-10 (AAT Bioquest) added at 1:1,000 dilution. The plate incubated at 37 °C for 1 h while shielded from light, before JC-10 was removed by aspiration and the neuronal culture was replenished with fresh dye-free medium.

To quantify mitochondrial membrane potential, the JC-10-treated plates were read in a PHERAstar® microplate reader (BMG Labtech) by detecting the ratios of fluorescence intensity at wavelengths 520 and 590 nm. Higher 590/520 ratios indicate greater mitochondrial membrane potential with more JC-10 in aggregated form within mitochondria as compared to the monomeric form outside of mitochondria. The plate was read at baseline for 3 cycles each 13 min apart before adding 10 μM of carbonyl cyanide m-chlorophenyl hydrazone (CCCP) to completely depolarise mitochondrial membrane and the plate was read for another 2 cycles. The change in mitochondrial membrane potential ($\Delta\psi_m$) is defined as the difference in 590/520 fluorescence ratio between the baseline and depolarised mitochondria caused by CCCP.

2.17 Multi-electrode array assays

I performed multi-electrode array (MEA) experiments using the MEA system from Axion Biosystems. The iPSC-derived cortical neurons were seeded in the CytoView 48-well MEA plates (16 electrodes per well) on Day 32 (Chapter 2.4.1) as a droplet in the middle of a well to prevent the neurons coming in contact with the grounding electrodes. I coated the plates with PO/L in a droplet and subsequently seeded 15,000 neurons per well in a 5 µL droplet. The neurons were allowed to settle for at least 30 min before I added 5,000 rat astrocytes in 3 µL directly into the existing droplet on the plate. Finally, all cells were allowed to settle for at least 1 h before the wells were filled with 200 µL of neuronal medium.

On Day 90, I first measured baseline neuronal firing activities in the iPSC-derived cortical neurons in a Maestro Pro MEA equipment at 37 °C and 5% CO using the AxIS Navigator™ v2.0.4 by recording for 6 min. I then treated the neurons with Aβ insults which were either AD brain homogenate at 25% (v/v) or 10 µM of $A\beta_{1-42}$ oligomers. Neuronal activities were measured every hour by recording for 2 min each time for the first 18 h and afterwards daily for five days from the baseline. The MEA data were analysed in the AxIS Navigator™ and Neuro Metric Tool v2.5.1 software. All recordings were normalised to the baseline of individual well of neurons (e.g., well A1 on Day 1 to 5 of recording was normalised to the recording of well A1 at baseline).

2.18 Patch-clamp electrophysiology

iPSC-derived cortical neurons were seeded on Day 32 (Chapter 2.4.1) in co-culture with a confluent layer of rat astrocytes on the Nunc™ Thermanox™ (Thermo) plastic coverslips

at 100,000 cells/cm^2. I performed patch-clamp experiments on these neurons around Day 80-100 of neuronal differentiation.

During the whole-cell patch-clamp procedure, the coverslips were continuously (1 mL/min) perfused with extracellular solution at 30 °C containing (in mM): 5 KCl, 140 NaCl, 10 HEPES, 10 glucose, 2 $MgCl_2$ and 2 $CaCl_2$ adjusting to pH 7.36 with NaOH and osmolarity to 290 mosm. Whole-cell patch-clamp recordings were performed with a MultiClamp 700B amplifier-Digidata 1550A series interface board using Clampex 10.6 software (Molecular Devices). Pulled glass electrodes had final resistance at 5-9 MΩ and infused with intracellular solution containing (in mM): 140 K-gluconate, 6 NaCl, 1 EGTA, 1 HEPES, 4 MgATP, 0.4 Na_3GTP adjusting to pH 7.3 with KOH and osmolarity to 290 mosm. Data were analysed using the Clampfit v10.7 software (Molecular Devices). Bipolar and multipolar cells with long axons were chosen and cells with access resistance greater than 50 MΩ were omitted in data analyses.

For spontaneous miniature excitatory postsynaptic current measurement (mEPSC) derived from 5 min of recordings, 1 μM of tetrodotoxin (TTX) (bio-techne) was perfused to the coverslip to inhibit spontaneous action potentials (AP) by blocking sodium channels and the neuron was held at – 70 mV.

2.19 Statistical analysis

All datasets were subject to D'Agostino-Pearson normality test and none of the datasets presented in this thesis passed the normality test, thus non-parametric statistical tests were chosen by default for all data analyses, except the correlation analyses (Chapter 6) by simple

linear regression line fittings where I reported Pearson's coefficient of correlation and two-tailed p-values to indicate statistical significance. Pearson's coefficient (parametric) of correlation was chosen even though the datasets did not pass the normality test because (1) the data points represent different human participants and (2) the distributions were more likely to be normal as opposed to lognormal when both normality and lognormality tests were considered.

For every other dataset, I used two-tailed Mann-Whitney test for statistical analysis to compare between two groups. For one-way ANOVA test comparing a single readout across multiple cell lines or conditions, I used Kruskal-Wallis test with the Dunn's multiple comparison correction. To compare among different conditions/time points and cell lines, I used ordinary two-way ANOVA test with Šídák's (single parameter per variable) or Tukey's (multiple parameters per variable) multiple comparison correction. The Kolmogorov-Smirnov test was used to compare between two cumulative frequency distributions. All statistical tests were two-tailed and performed by the GraphPad Prism v9.2.0 software. NS stands for "not significant". * $p < 0.05$, ** $p < 0.01$, *** $p < 0.001$, **** $p < 0.0001$ for all statistical analyses.

Chapter 3: Identification and characterisation of *MAPT-/-* iPSC lines

3.1 Introduction

Although *MAPT-/-* mouse models have been extensively studied, human *MAPT-/-* neuronal models have not been available at the point of writing. *MAPT-/-* model *in vitro* with a human genetic background would be useful not only because of the species relevance but also because it would be an important complement to the existing *in vivo MAPT-/-* mouse models. The differences in *MAPT* transcript and tau protein expression between mouse and human plus the inconsistent results reported from various *MAPT-/-* mouse strains (Chapter 1.3.2), further highlight the need for a human model to clarify the effects of tau ablation and its implication in AD.

Since the advent of using the CRISPR/Cas9 system for genome editing [275], many researchers have been taking advantage of this novel gene targeting system. The simple yet efficient system involving only two readily available components – the Cas9 nuclease for making DNA cuts and gRNA for targeting the Cas9 nuclease to the intended gene locus – has made gene editing relatively more versatile where multiple gRNAs targeting different genes/loci can be introduced simultaneously with the same Cas9 nuclease.

3.1.1 Aims of this chapter

In this chapter, I will describe the process of generating human *MAPT-/-* iPSC lines (Chapter 2.1) from two healthy individuals using the CRISPR/Cas9 system in collaboration with the

Cowley group from the Dunn School of Pathology, University of Oxford. I will also provide evidence on tau protein knockout validation in NPCs. The aims are to

- Establish isogenic *MAPT-/-* iPSC lines and validate the absence of tau protein expression
- Establish cortical neuron differentiation *in vitro* and characterise *MAPT-/-* iPSC-derived cortical neurons

3.2 Rationale of knockout strategies

At the beginning of my DPhil studies, Dr. Cowley and her colleagues had already designed the gRNAs for targeting the *MAPT* gene. Knowing that the *MAPT* gene locus was especially difficult to target from past experiences, she chose to directly introduce the hybridised Cas9-gRNA ribonucleoproteins into healthy iPSC lines by electroporation instead of using a system based on plasmid delivery and expression. Two different strategies were also used on two parental iPSC lines (known to be capable of differentiating into cortical neurons) to diversify the *MAPT* targeting options. Exons 1 and 4 were selected as the target loci to cause DSBs relatively upstream in the *MAPT* gene and Exons 2 and 3 were not targeted because they undergo alternative splicing at the mRNA level [153]. Furthermore, a single gRNA was used to target Exon 1 (in the SBAd-03-01 iPSC line) with a single intended DSB whereas a pair of gRNAs flanking 19 bp within Exon 4 were used to result in a 25-bp excision since the DNA cut happened 3 bp upstream from the 3' end (in the SFC856-03-04 iPSC line). In short, two iPSC lines, targeting strategies and target loci were included to maximise the chances of achieving homozygous *MAPT* knockout.

3.3 Results

3.3.1 DNA sequencing to identify successful *MAPT-/-* iPSC clones

As mentioned in Chapter 3.2, the Cowley group employed two strategies targeting either Exon 1 or 4 of *MAPT* separately in two parental iPSC lines from healthy individuals (herein referred to as Exon 1 or Exon 4 lines). The gRNAs were situated immediately upstream of a PAM which is a 3-nucleotide sequence (5'-NGG-3') required for the nuclease function of Cas9 (Figure 3.3.1A).

After obtaining the whole cell DNA samples from the Cowley lab, I prepared the DNA precipitates for sequencing (Chapter 2.2) from all 96 Exon 1-targated iPSC clones and 72 Exon 4-targeted iPSC clones to screen for successful gene knockout events (Figure 3.3.1B). A total of 13 candidate clones from both knockout strategies subsequently underwent sub-cloning to verify homozygous *MAPT* knockout genotypes, and that resulted in 7 candidate clones based on their DNA sequences. Interestingly, not all the iPSC clones exhibiting the expected genetic changes in both alleles of *MAPT* ended up with the absence of tau protein expression (Chapter 3.3.2). This has eventually resulted in two *MAPT*-/- Exon 1 lines and a single *MAPT*-/- Exon 4 line, effectively giving rise to 2.1% and 1.4% in knockout efficiency, respectively. A *MAPT*+/- and *MAPT*+/+ line each was also selected for each isogenic panel for downstream experiments (Table 3.3.1).

Table 3.3.1: List of genotype-confirmed iPSC lines of the *MAPT* knockout isogenic panels
These lines were later confirmed by their tau expression levels on a immunoblot (Chapter 3.3.2).

SBAd-03-01 Exon 1 single gRNA targeting				
Well position	**Allele 1 (no. of bacterial clones)**	**Allele 2 (no. of bacterial clones)**	***MAPT* genotype**	**Symbol**
A1	1 bp insertion (4)	1 bp insertion with 1 bp mutation next to it (2)	Homozygous knockout	*-/- #1*
B3	Wild-type	Wild-type	Wild-type	+/+
F5	1 bp insertion (6)	Same as Allele 1	Homozygous knockout	*-/- #2*
G9	1 bp deletion (2)	3 bp in-frame insertion and several mutations around the cut site (3)	Heterozygous knockout	+/-
SFC856-03-04 Exon 4 double gRNA targeting				
Well position	**Allele 1 (no. of bacterial clones)**	**Allele 2 (no. of bacterial clones)**	**Genotype**	**Symbol**
A12	25 bp deletion (4)	Wild-type (1)	Heterozygous knockout	+/-
B7	Wild-type	Wild-type	Wild-type	+/+
E1	25 bp deletion (8)	Same as Allele 1	Homozygous knockout	-/-

The Exon 1 knockout strategy produced a range of genetic alterations due to a DNA DSB caused by targeting with a single gRNA. In one of the confirmed Exon 1 *MAPT-/-* lines (*MAPT-/-* #1), one allele carries a 1-bp insertion whereas the other allele has a single-nucleotide mutation in addition to the insertion. Both genetic alterations resulted in a single-nucleotide frame shift and gave rise to a stop codon within Exon 1 (Figure 3.3.1C; *MAPT-/-* Allele #1 and #2). The other Exon 1 *MAPT-/-* line (*MAPT-/-* #2) has a single-nucleotide insertion as in *MAPT-/-* Allele #1 in both alleles. In the Exon 1 *MAPT+/-* line, one of the alleles sustained a 1-bp deletion, similarly giving rise to a frame shift and a stop codon within Exon 1. The other allele experienced a 3-bp in-frame insertion, coupled with several mutations around the insertion site, and caused changes in five amino acid residues without

producing a stop codon. On the other hand, the Exon 4 *MAPT-/-* and *MAPT+/-* lines both carry the same 25-bp deletion and that led to a frame shift plus a stop codon within Exon 4 (Figure 3.3.1C).

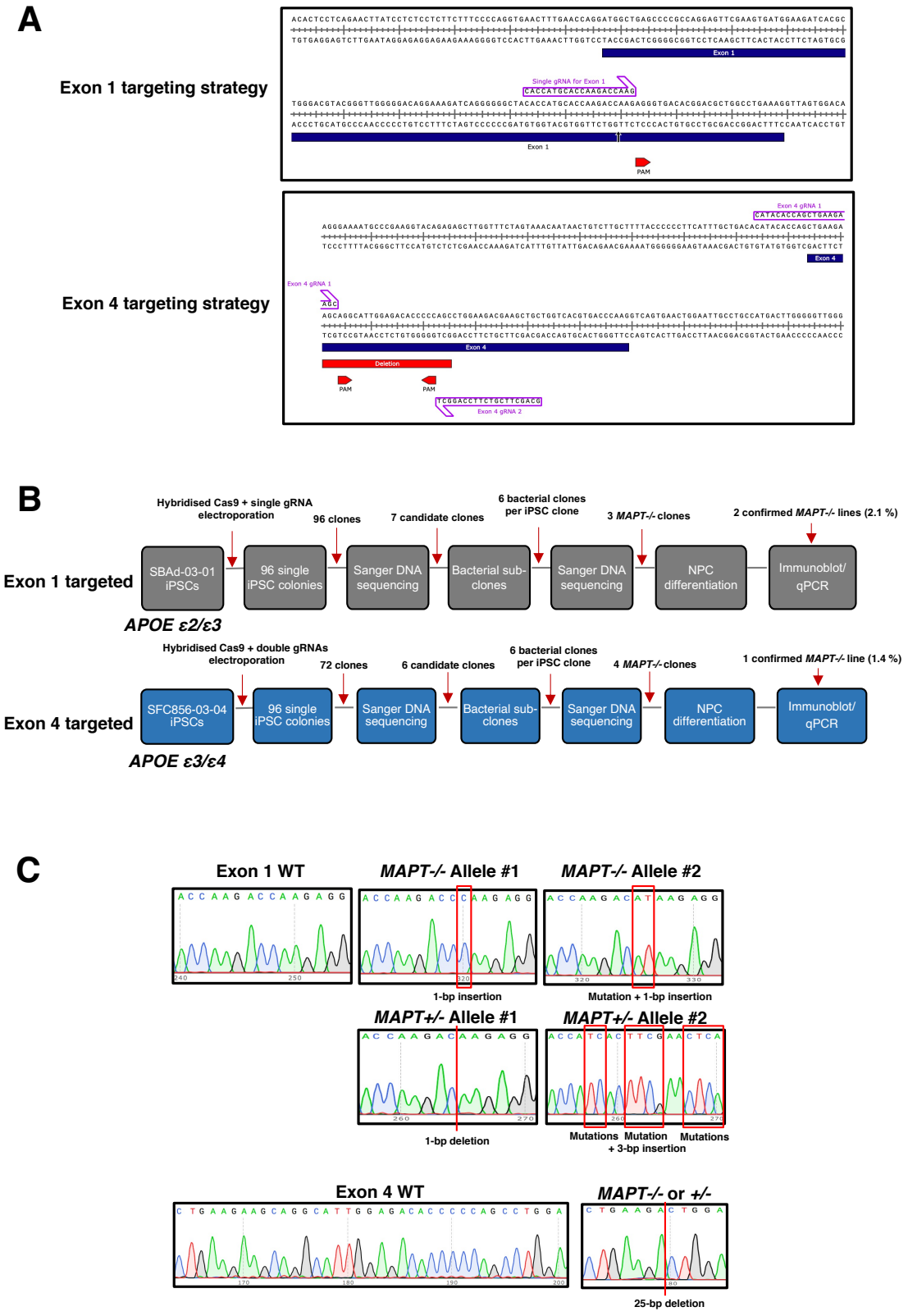


Figure 3.3.1: *MAPT* CRISPR/Cas9 system-mediated knockout strategies and outcomes
(A) Schematic on gRNA positions and target regions in Exon 1 and 4 of the *MAPT* loci.
(B) Schematic on the workflow of identifying successful *MAPT* knockout candidate iPSC clones.
(C) DNA sequencing results of the homozygous and heterozygous *MAPT* knockout in their respective exons.

3.3.2 *MAPT* transcript and tau protein expression validation

After confirming *MAPT* knockout based on DNA sequences, I conducted qPCR (Chapter 2.8) and Western blot (Chapter 2.7) assays to validate the absence of *MAPT* expression both at the transcript and protein levels. The *MAPT*+/+, +/- and -/- iPSC lines were differentiated concurrently into NPCs/neurons until Day 30 or Day 50 of the differentiation and the cell lysates were harvested for biochemical analyses.

All candidate *MAPT*-/- iPSC clones were first differentiated into NPCs to reach detectable levels of tau expression in either the *MAPT*+/+ lines that underwent the same CRISPR/Cas9 system-mediated knockout process or the parental iPSC lines for comparison. At this stage, the NPCs expressed only the shortest 0N3R tau isoform. Three *MAPT*-/- lines successfully demonstrated the absence of tau expression as indicated by their genotypes but 4 out of 7 candidate *MAPT*-/- clones failed to show complete ablation of tau expression (Figure 3.3.3A). A single *MAPT*+/- line from each parental iPSC line was also selected to be used in experiments based on their expression levels being approximately half of that in the *MAPT*+/+ lines. Finally, both *MAPT*+/+ lines (one from each knockout strategy) exhibited similar levels of tau expression to those in the parental lines as expected from their genotypes.

I then focused on the 7 selected iPSC lines grouped as two isogenic panels of *MAPT* knockout lines and asked if the *MAPT* transcript expression levels matched the tau protein expression levels seen in Figure 3.3.3A. Unexpectedly, Exon 4 *MAPT*+/- line showed more than 50% reduction in *MAPT* transcript expression levels whereas Exon 1 *MAPT*-/- lines continued to express significant levels of *MAPT* transcripts (Figure 3.3.3B).

As the qPCR primers used to detect total *MAPT* transcripts recognise the region close to the 3' end (Exon 12-13) while the anti-tau antibody (Tau-1) used in Figure 3.3.3A targets the mid-region (amino acid 192-204) of tau peptide [315], there was insufficient evidence to rule out the possibility that part of the tau protein close to the C-terminus was expressed despite the genetic modifications. Therefore, in addition to using Tau-1 antibody, I further validated the absence of tau expression by employing Tau-5 (also targeting the mid-region between amino acid 218-225) [316] and Tau-46 (targeting the C-terminus between amino acids 404-441) [317] antibodies. Cell lysates from older neurons up to Day 50 of the cortical neuron differentiation were also included. Immunoblots probed with these antibodies all conformed to the same 0N3R tau isoform expression patterns seen in the Tau-1 blot, confirming the genotypes of the selected isogenic panels of *MAPT* knockout lines (Figure 3.3.3C). A band corresponding to the 2N3R tau isoform was also noticeable in Tau-5 and Tau-46 blots across all lines, but the band was considered unspecific. Since tau isoform expression is developmentally regulated (Chapter 1.2.2) i.e., expressing progressively from the shortest isoform in foetus to eventually including the full-length 2N4R tau isoform in adults, it is unlikely that the NPCs were expressing a more mature tau isoform without expressing the 0N3R isoform first. Moreover, the iPSC-derived NPCs 30 days into neuronal differentiation are immature neuronal cells thus unlikely to be expressing mature 2N tau isoforms.

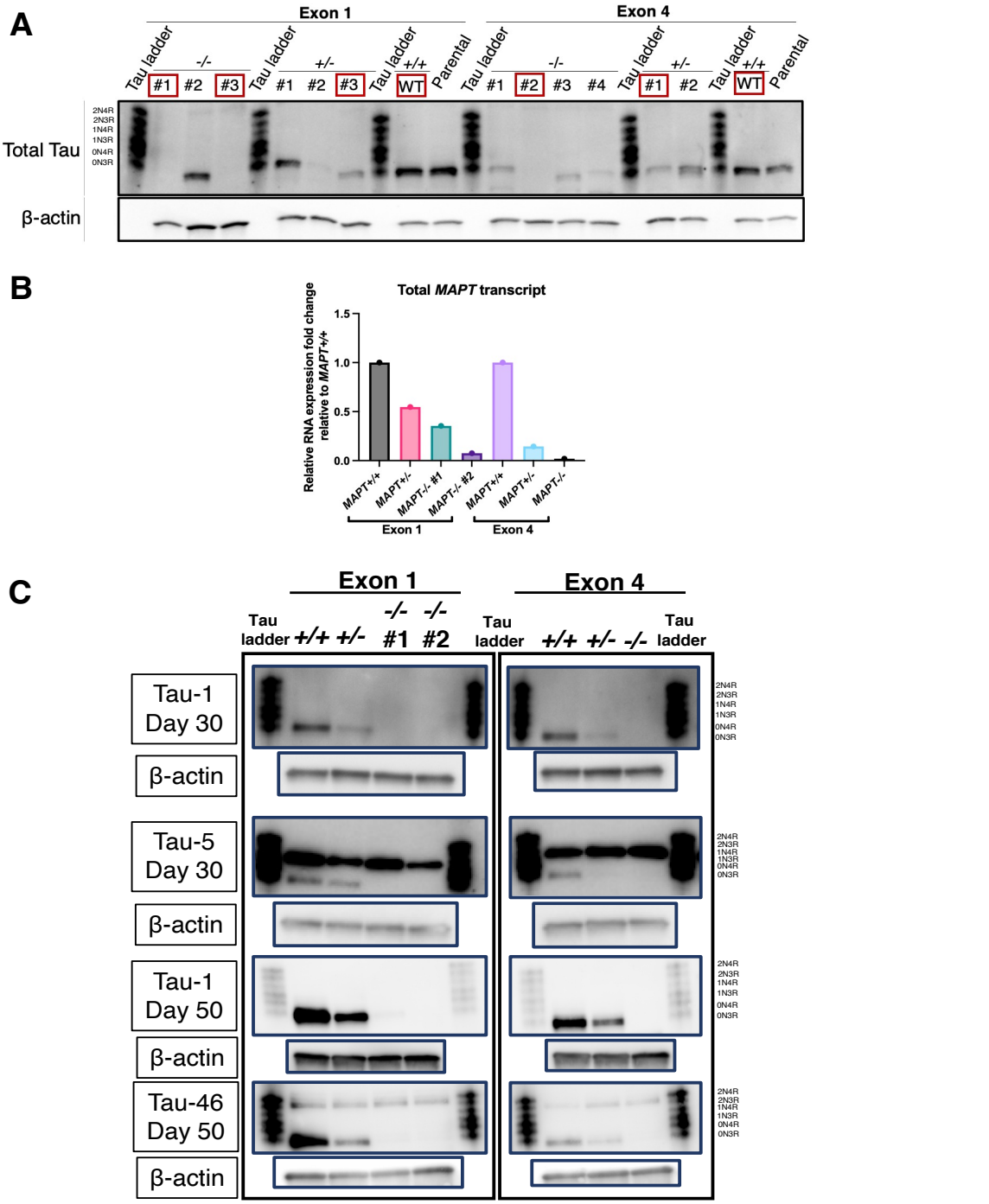


Figure 3.3.2: *MAPT* knockout validation

(A) Confirmation of the absence of tau expression in DNA sequence-validated candidate iPSC-derived NPCs on Day 30 of differentiation by Western blot using Tau-1 antibody. 5 µg of cell lysate was loaded into the gel. iPSC lines which were selected for all downstream experiments are highlighted in red boxes.

(B) Quantification of total *MAPT* transcripts by qPCR in Day 30 iPSC-derived NPCs from both isogenic panels of *MAPT* knockout lines from one differentiation repeat. No statistical analysis was performed as the data were derived from a single differentiation.

(C) Further validation of the absence of tau expression in both isogenic panels of *MAPT* knockout lines by Western blot with three antibodies targeting different regions of tau peptides from Day 30 and Day 50 iPSC-derived NPCs/neurons. 5 µg of cell lysate was loaded into the gel except for the Tau-46 blot (10 µg).

3.3.3 Characterisation of iPSC-derived cortical neurons

The two validated isogenic panels of *MAPT* knockout lines were subsequently differentiated into aged cortical neurons as described in Chapter 2.4.1 for basic cellular and functional (Chapter 5) characterisations.

I first set out to confirm that the differentiation protocol succeeded in making neurons of cortical lineage by staining for deeper layer (layer V-VI) cortical markers such as CTIP2 [318] and TBR1 [319] as well as superficial layer (layer II-IV) cortical marker CUX2 [320] by immunocytochemistry. Moreover, MAP2 was used as the dendritic marker to label neuronal morphology whereas the human nuclei of the iPSC-derived neurons were specifically labelled by an antibody recognising human nuclear antigen due to the presence of rat astrocytes in the co-culture (Chapter 2.13.1). The iPSC-derived neurons were positive for MAP2 and the selected cortical markers identified to be co-staining with human nuclei on Day 80 of cortical neuron differentiation (Figure 3.3.3A). The percentages of cortical markers-positive neurons did not differ among all the *MAPT* knockout lines, indicating similar differentiation propensities into cortical lineage despite the absence of tau expression (Figure 3.3.3B). Notably, a greater proportion of neurons expressed superficial cortical layer marker CUX2 as compared to deeper layer markers CTIP2 and TBR1 regardless of their *MAPT* genotypes. The iPSC-derived cortical neurons were also stained positive for presynaptic markers such as Synapsin I/II, Synaptotagmin and vGLUT1 which is a voltage-gated glutamate transporter responsible for the accumulation of glutamate in secretory vesicles [321] (Figure 3.3.3C), suggesting the presence of glutamatergic (excitatory) synaptic connections (more on Chapter 5).

As the aim of the thesis is to understand the effects of tau deletion in iPSC-derived cortical neurons, it is important to first elucidate the expression profile of tau isoforms in these neurons. The iPSC-derived cortical neurons from the parental lines were aged for 100 days or more and probed for the presence of the six known tau isoforms. The expression levels of *MAPT* transcripts increased until Day 50, where the neurons appeared to have formed a stable network of extensive neurites *in vitro*, before decreasing thereafter (Figure 3.3.3D). The expression levels of Exon 3 (2N isoforms) and Exon 10 (4R isoforms) also escalated along the chronological age of the neurons *in vitro* especially upon 100 days into neuronal differentiation (Figure 3.3.3D). In terms of protein translation, the 0N3R peptide was expressed when the cells began to adopt the neuronal fate on Day 30 (Figure 3.3.2C) and the 0N3R peptide continued to be expressed as the neurons aged (Figure 3.3.3E). From Day 50 of the neuronal differentiation, the 0N4R isoform was detectable by immunoblot probed with Tau-1 antibody but the 2N isoforms, as demonstrated to be detectable on the transcript level approximately 30-fold above the levels in iPSCs (Figure 3.3.3D), were not visible by immunoblot in neurons up to 150 days into differentiation (Figure 3.3.3E).

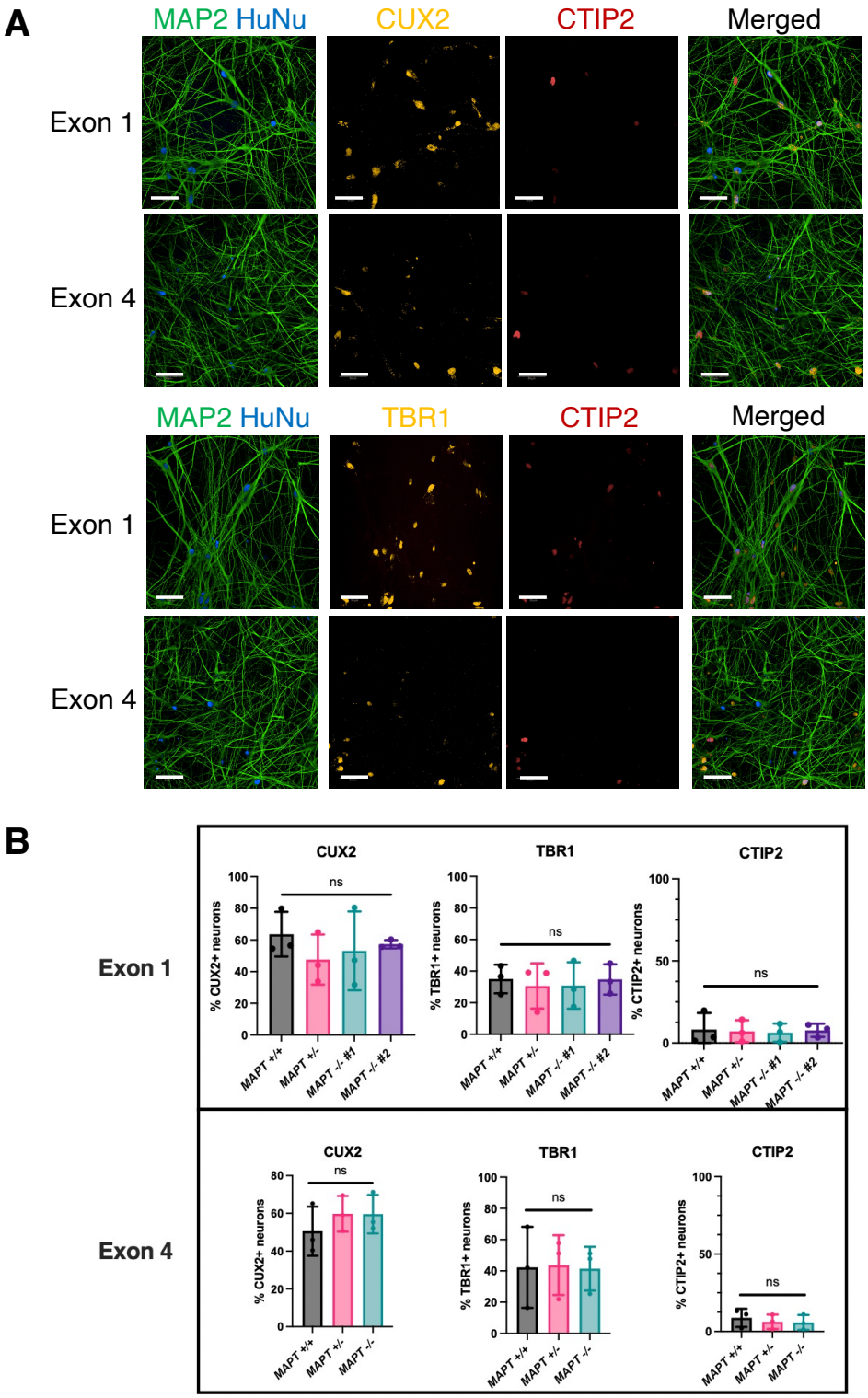
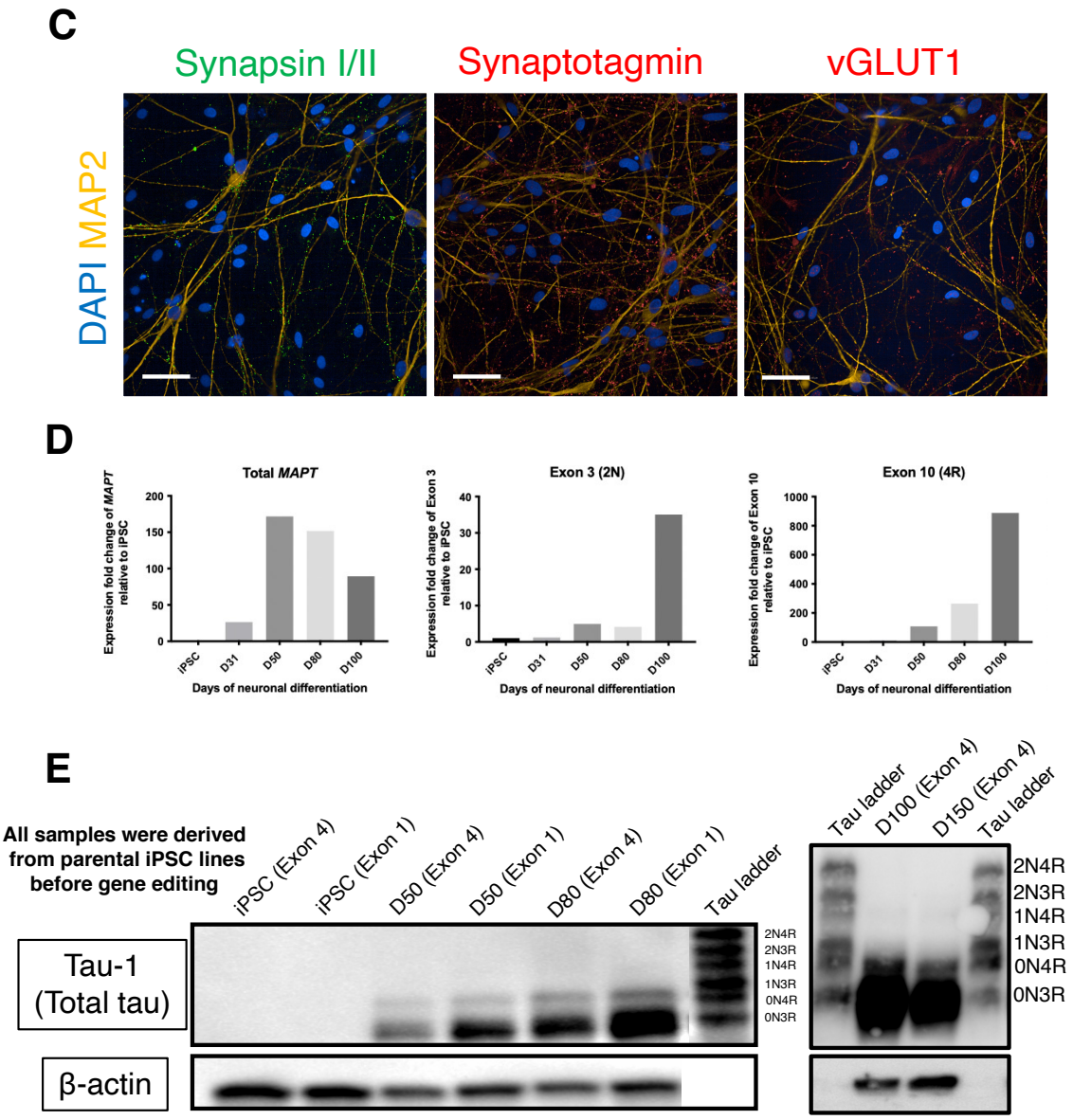


Figure 3.3.3: Characterisation of iPSC-derived cortical neurons
(A) Representative images of cortical marker (CUX2, TBR1 and CTIP2) staining in Day 80 iPSC-derived cortical neurons in co-culture with rat astrocytes from the *MAPT*+/+ lines. Scale bar = 50 µm.
(B) Quantification of cortical marker expression in iPSC-derived cortical neurons from both isogenic panels of *MAPT* knockout lines. Exon 1: Day 73-80; Exon 4: Day 80-84 of cortical neuron differentiation. N = 3 independent differentiation repeats. Mean ± SD. Kruskal-Wallis test with Dunn's multiple comparison correction was used for the statistical analysis.



(C) Representative images of presynaptic marker (Synapsin I/II, Synaptotagmin and vGLUT1) staining in Day 84 iPSC-derived cortical neurons from Exon 4 parental line. Scale bar = 50 μm.

(D) Quantification of total *MAPT*, Exon 3 and Exon 10 transcripts relative to the expression levels in iPSCs in the Exon 4 parental line from one differentiation repeat up to Day 100. No statistical analysis was performed as the data were derived from a single neuronal differentiation.

(E) Immunoblots probed with Tau-1 (total tau) in iPSC-derived cortical neurons from Exon 1 and Exon 4 parental lines aged up to Day 150 of differentiation from one differentiation repeat. 5 μg of cell lysate was loaded into the gel.

3.4 Discussion

Discordance of MAPT knockout validations from genetic sequences to protein translation

In Chapter 3, I successfully identified the isogenic *MAPT* knockout panels from two parental iPSC lines in collaboration with the Cowley group who generated the CRISPR/Cas9-targeted iPSC clones. The candidate iPSC clones were filtered through various steps of validations to confirm the loss of tau protein expression. Based on the whole-cell DNA sequences, 13 iPSC clones were identified to be potential *MAPT-/-* lines. However, the subsequent allele sub-cloning revealed that 6 of the candidate clones possessed one allele with wild-type *MAPT* sequence at the intended cut sites, suggesting that it is possible that the sequence on one of the alleles was not detected during whole-cell sequencing.

Thereafter, 4 of the 7 remaining *MAPT-/-* candidate clones appeared to be expressing tau when they were differentiated into NPCs indicating that sequence confirmation alone was insufficient to verify protein ablation. Clone heterogeneity could potentially explain the observation where the cut sites were undetected by chance while tau expression persisted in the minority of the iPSC clone population. Moreover, the majority of the *MAPT* locus was not sequenced after the CRISPR/Cas9-mediated knockout procedure since only Exon 1 and Exon 4 were targeted. Off target effects from the Cas9-gRNA ribonucleoprotein [322] elsewhere could potentially disrupt the frame-shift effects created by the genetic changes shown in Figure 3.3.1C. Overall, the homozygous knockout efficiency sits at merely 1-2% and that might be attributed to the fact that tau expression is silenced in iPSCs such that the *MAPT* locus is less accessible to transcriptional mechanisms as well as the CRISPR/Cas9 ribonucleoprotein introduced for gene editing.

It is worth noting that the Exon 1 *MAPT-/-* lines still expressed detectable levels of *MAPT* transcripts (Figure 3.3.2B) even though the absence of tau protein was confirmed (Figure 3.3.2C). In theory, the premature stop codon created due to the 1-bp insertion should trigger the mechanism of nonsense-mediated decay (NMD) of *MAPT* mRNAs although that is not a perfectly efficient process. The differences in exon lengths, mRNA decay rates and distances to stop codon could each influence NMD efficiencies for the *MAPT-/-* Exon 1 and 4 [323]. Ultimately, the slight change in the *MAPT* gene sequence should not affect the transcriptional mechanism since no premature transcriptional terminator would be generated. It is also evident that the *MAPT* transcript detected is not translated into tau protein and the presence of which is the primary outcome used to determine the genotypes of the iPSC lines.

Maturation in iPSC-derived cortical neurons

Defining and achieving neuronal maturity in iPSC-derived cortical neurons from undifferentiated and immature stem cells remains a challenge in the field of age-related neurodegenerative diseases where the cellular models should ideally recapitulate not just neuronal maturity but also aged phenotypes [324,325]. In the *MAPT* knockout studies, I aimed to generate mature cortical neurons which were functionally active (more in Chapter 5) and expressing mature tau isoforms like those in the adult brain *in vivo*.

In terms of cortical markers, a higher percentage of superficial cortical layer marker (CUX2) was observed as compared to that of deeper layer cortical markers (TBR1 and CTIP2) (Figure 3.3.3B). This indicates that there was a mixed cortical population across cortical layer identities in the iPSC-derived neurons in co-culture with rat astrocytes and that more

than half of the neurons began to adopt the identity of superficial cortical layer, which forms at the later stage of cortical development in the brain [326].

Since tau isoform expression is developmentally regulated [154], the expression pattern can be used as a proxy to gauge the maturity of a neuronal culture *in vitro* and the ultimate goal is to demonstrate the expression of the full-length 2N4R isoform as is the case in adult human brains. I showed in Figure 3.3.3D that the 2N and 4R transcript expression levels increased with time in iPSC-derived cortical neurons as well as total *MAPT* transcript levels decreasing after the neurons formed a morphologically stable network *in vitro* approximately from Day 50 of the neuronal differentiation. This *MAPT* isoform expression pattern is consistent with the observation in iPSC-derived dopaminergic neurons [327].

Immunoblots probed with Tau-1 antibody in Figure 3.3.3E demonstrated that the 0N4R isoform was indeed translated in addition to the foetal 0N3R band from Day 50 onwards. As compared to a previous study on iPSC-derived cortical neurons [328], the neuronal culture described in this thesis exhibited earlier emergence of 4R tau isoform on and before Day 100 of the neuronal differentiation. The overexpression of *Ngn2* (Chapter 2.4.1) included in the present study likely contributed to the acceleration of 4R tau isoform expression at the protein level. According to the study reported previously, it was also confirmed that prolonging the neuronal culture up to Day 365 *in vitro* was sufficient to result in the expression of both 0N and 1N isoforms although the full-length 2N4R isoform was still untranslated [328].

Overall, the iPSC-derived cortical neurons described in this thesis were a heterogeneous neuronal population from different cortical layers and achieved the expression of the 0N4R

tau isoform at the protein level in addition to the foetal 0N3R isoform. Furthermore, the qPCR analyses revealed that the neurons began to considerably raise the expression levels of Exon 3 (2N) and Exon 10 (4R) *MAPT* isoforms from Day 100 of the neuronal differentiation. However, the lack of expression of any 1N and 2N isoforms in iPSC-derived cortical neurons at the protein level up to five months into the neuronal differentiation reveals the immaturity of these neurons. The lack of mature tau isoforms also raises the issue of potential differences in tau-mediated cellular processes and responses to exogenous Aβ between iPSC-derived models and relatively more mature neurons *in vivo*. It was previously reported that tau's N-terminus interacts with neuronal plasma membrane [329] and Fyn kinase, which mediates tau-dependent excitotoxicity caused by exogenous Aβ [171]. Furthermore, 1N tau was found to be enriched in the nucleus whereas 2N tau is comparatively more highly expressed in axons in mice [330]. The iPSC-derived models used in this thesis thus might not accurately capture the phenotypes associated with 1N and 2N tau isoforms which are expressed in mature neurons. It is important to highlight however that the cell lysates used in the Western blots were derived from neuronal monoculture while most experiments done in Chapters 4 to 6 involved co-culture with rat astrocytes which facilitate functional maturation of iPSC-derived cortical neurons [331,332]. As such, the assumption was that the neurons in astrocyte co-culture were expected to have either the same or more mature tau isoform expression pattern as compared to their age-matched monoculture counterparts. To improve neuronal maturity further in addition to co-culture with glial cells, one could extend the duration of differentiation for up to a year or more to ensure neuronal maturity in terms of tau isoform expression patterns [328]. It would be however logistically challenging to maintain such cultures for a prolonged period and assays compatible with long-term cultures are limited as it is challenging to preserve neuronal morphology suitable for imaging experiments over a year.

Chapter 4: Cellular phenotypes of *MAPT-/-* iPSC-derived cortical neurons

4.1 Introduction

Having generated two panels of *MAPT* knockout isogenic lines, I then investigated a select set of cellular phenotypes which were previously reported to exhibit differential outcomes in *Mapt-/-* primary neurons derived from animal models.

Dystrophic neurites have been observed in post-mortem AD brains, indicating that neurite degeneration precedes neuronal death which eventually leads to brain atrophy [333]. Neurite outgrowth deficit has also been shown in *Mapt-/-* mouse primary neurons [226], while Aβ-induced neurite degeneration could be prevented in *Mapt-/-* neurons but not in *Mapt*+/+ neurons [242]. Furthermore, *Mapt-/-* mouse primary neurons were protected from Aβ-induced cytotoxicity *in vitro* [242–244]. These results suggest that tau plays an important role in establishing neuronal morphology and its expression levels are relevant in the context of AD pathology.

On the other hand, it has been demonstrated that mitochondrial transport along axons in mouse primary neurons was hindered by acute exposure to extrinsic Aβ insults or expression of mutant *APP* [247,248]. *Mapt-/-* background again exhibited protective effects against Aβ-driven mitochondrial transport deficits both in the anterograde (i.e., towards distal/synaptic terminals) and retrograde (i.e., towards cell soma) directions although the absence of tau expression itself did not elicit a change in mitochondrial transport in terms of percentage of motile mitochondria and movement velocity both *in vitro* [247,248] and *in vivo* [334]. Apart from mitochondrial shuttling to and from distal synapses to support the bioenergetic demand

that is essential for neuronal function [335] and affected early in AD pathogenesis [336], reduced mitochondrial membrane potential which is indicative of poorer mitochondrial function has been implicated in AD as well [337]. It has been reported that mitochondrial membrane potential deficit caused by $A\beta_{1-42}$ oligomers was prevented in *Mapt*-/- mouse neurons [338], while tau ablation in mice did not alter mitochondrial membrane potential in another study [339]. These prior experiments in animal models of AD provided the basis which shaped the aims and designs of the experiments in this thesis.

Experiments done in animal models are often not directly transferrable to iPSC-derived neuronal models *in vitro* due to a range of technical challenges and inherent biological differences between primary neurons and neurons differentiated from pluripotent stem cells. As such, several experiments described in this chapter had been adapted to the iPSC-derived neuronal culture including the use of rat astrocyte co-culture detailed in Chapter 2.4 to improve neuronal morphology, maturation, and adherence.

4.1.1 Aims of this chapter

- Establishing the effects of tau depletion in neurite outgrowth, axonal mitochondrial transport, and mitochondrial membrane potential
- Elucidating the deleterious effects of extrinsic Aβ insults on these cellular phenotypes as well as Aβ-driven cytotoxicity
- Determining if the absence of tau expression is protective against extrinsic Aβ insults

4.2 Results

4.2.1 Experimental design- neurite tracing by live imaging

To accurately trace individual neurite outgrowth over time, I adopted a strategy to label a subset of neurons with lentivirus which expresses NGN2 and GFP under the same promoter at low titre (MOI ± 0.01) so that most neurons could be imaged separately from each other while being seeded at a sufficient density to ensure survival (Figure 4.2.1). To avoid transducing the rat astrocytes in the co-culture, the lentivirus was introduced on Day 25 of the neuronal differentiation (see Chapter 2.4.1) a week before the neurons were replated onto a monolayer of rat astrocytes. The neurons were plated at a relatively low density at 25,000 cells/cm^2 (as compared to ICC imaging at 50,000 cells/cm^2) to prevent the neurites from intersecting to improve neurite identification with the Harmony® software. Both the neuronal nuclei and neurites were imaged under the same 488 nm channel, yet the nuclei could be singled out by filtering for GFP signal contrast and morphology as the nuclei displayed greater signal intensity and rounder morphology (Chapter 2.13.2). The whole well was covered in the imaging pipeline to ensure every GFP+ neuron was captured.

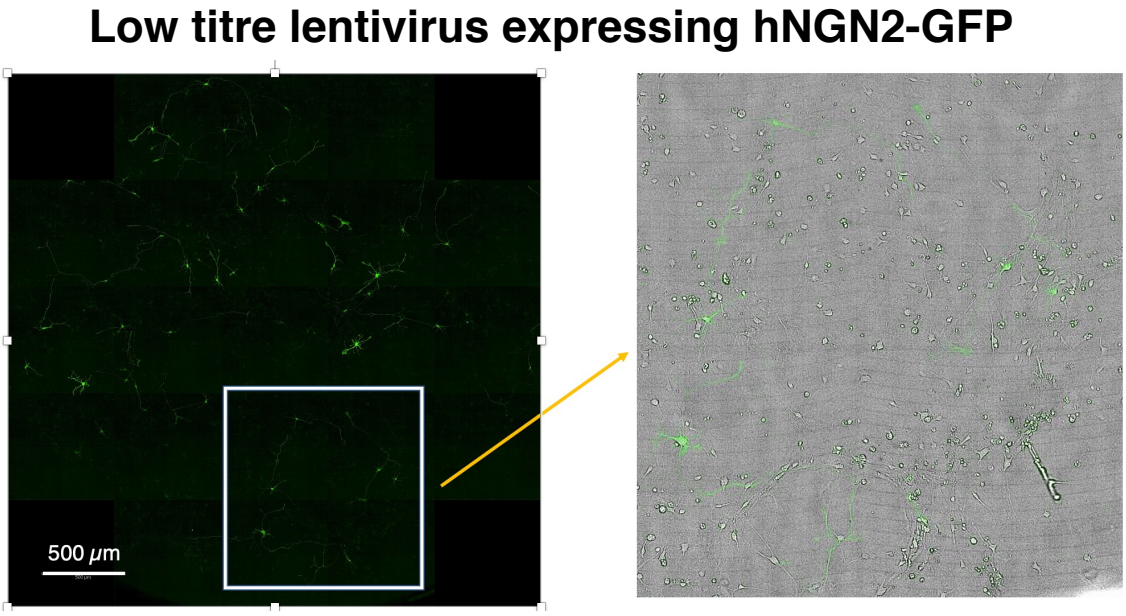


Figure 4.2.1: Representative image of the neurite tracing experiment design
The images show a subset of iPSC-derived cortical neurons expressing GFP on Day 35 of the neuronal differentiation, and a representative image in the Harmony® software analysis pipeline identifying GFP+ nuclei and neurites stemming from those nuclei.

4.2.2 Neurite outgrowth of *MAPT-/-* iPSC-derived neurons

Before examining whether the loss of tau expression affects neurite outgrowth in human iPSC-derived cortical neurons, the absolute baseline (i.e., 0 h of live imaging, on Day 35) neurite outgrowth parameters were first quantified to ensure that all lines, regardless of their genotypes, underwent neurite tracing from similar starting points. There was no difference in baseline neurite outgrowth readouts due to the levels of tau expression within each isogenic panel (Figure 4.2.2A). Equal baseline among the neuronal lines is required for reliable quantifications in neurite outgrowth as the neurite tracing data are normalised to the baseline to facilitate comparisons among variables such as the *MAPT* genotypes and extrinsic $A\beta_{1\text{-}42}$ oligomer insults.

As the neurons were subject to various control conditions, it was also important to ensure that none of the treatment controls led to significant neurite outgrowth impairment over the course of live imaging. In both *MAPT*+/+ lines, there was significant neurite outgrowth measured by neurite length, maximum neurite (axon) length and ramification index which is a readout for branching complexity defined as the number of neurite branches per primary root from each neuron (Figure 4.2.2B). The neurite branch length and the number of neurons did not change over time, indicating constant branch length during outgrowth and the lack of cell proliferation over 5 days. Moreover, both vehicle (PBS) and scrambled $A\beta_{1\text{-}42}$ oligomer treatments did not lead to any deviation from the outgrowth trajectory in the untreated samples, or cytotoxicity (Figure 4.2.2B).

Next, I asked if the loss of tau expression results in changes in neurite outgrowth in the iPSC-derived cortical neurons (Figure 4.2.2C). In both isogenic panels, there was marked neurite outgrowth impairments measured by neurite length and maximum neurite (axon)

length in the *MAPT*+/- and *MAPT*-/- lines (Figure 4.2.2D) revealing that partial depletion of tau expression was sufficient to cause neurite outgrowth impairment. The extent of impairments as compared to the *MAPT*+/+ lines was less pronounced measured by ramification index, and there were no changes in neurite branch lengths over 5 days regardless of the *MAPT* genotypes. Unexpectedly, one of the Exon 1 *MAPT*-/- clones deviated from the rest of the *MAPT*+/- and *MAPT*-/- lines by having similar neurite outgrowth trajectories as compared to the Exon 1 *MAPT*+/+ line. Comparing between the Exon 1 and Exon 4 lines, it was noticeable that the Exon 1 *MAPT*+/- and *MAPT*-/- lines started diverging towards outgrowth impairments from the *MAPT*+/+ line earlier around the third day of neurite tracing as compared to the Exon 4 lines where the divergence could manifest as late as the last day of neurite tracing. These results suggest that tau ablation alone can but does not necessarily lead to neurite outgrowth impairment and that neurite outgrowth can vary considerably among neurons derived from different iPSC clones or parental lines.

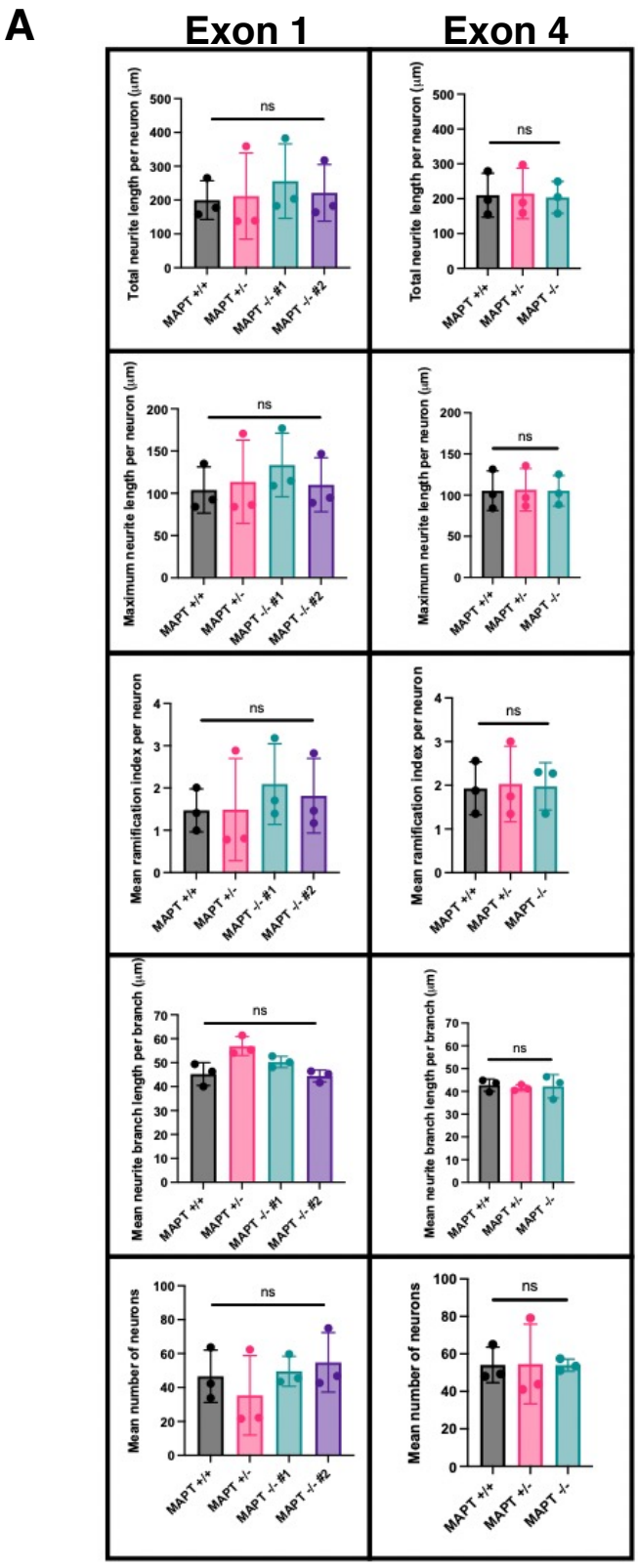
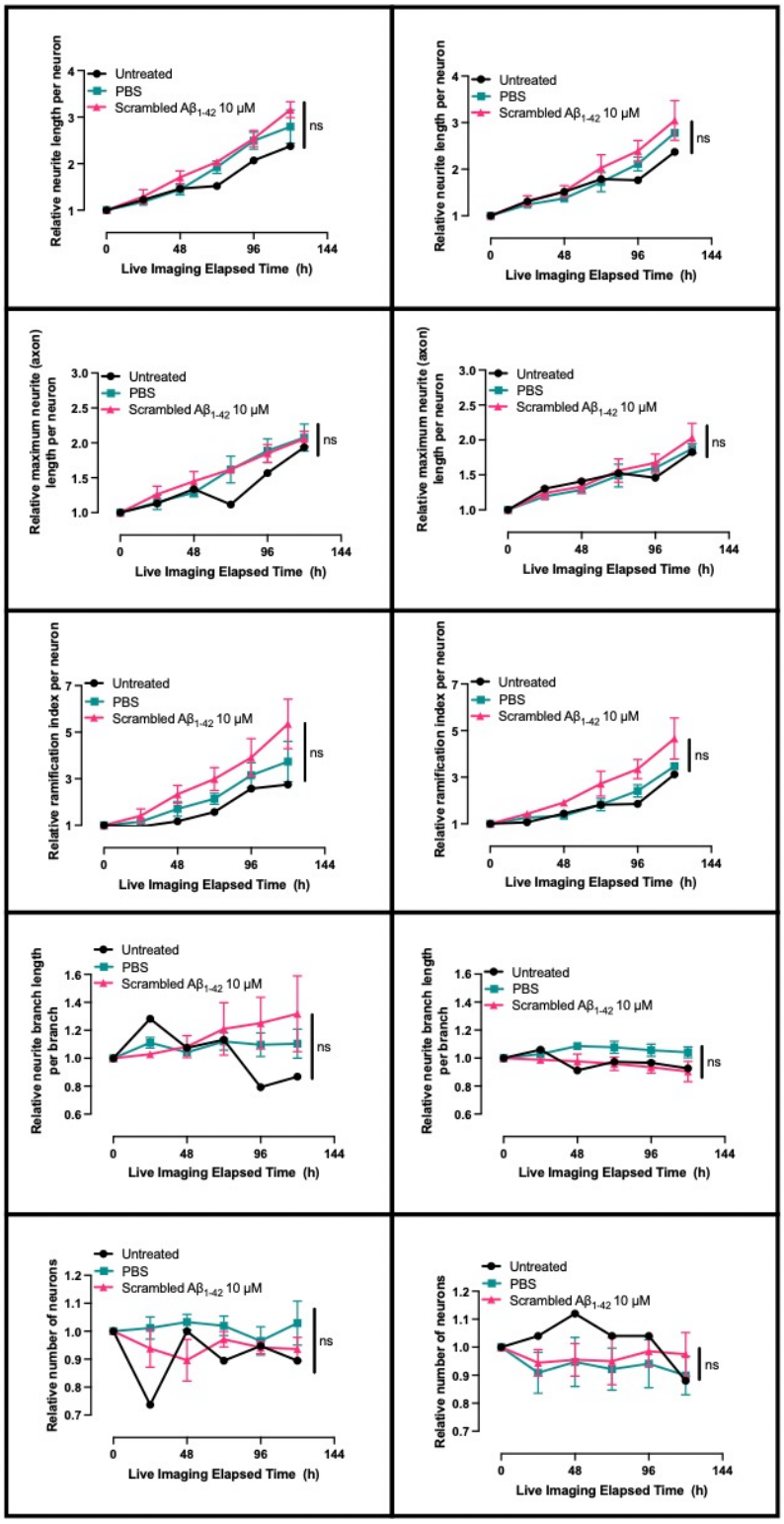
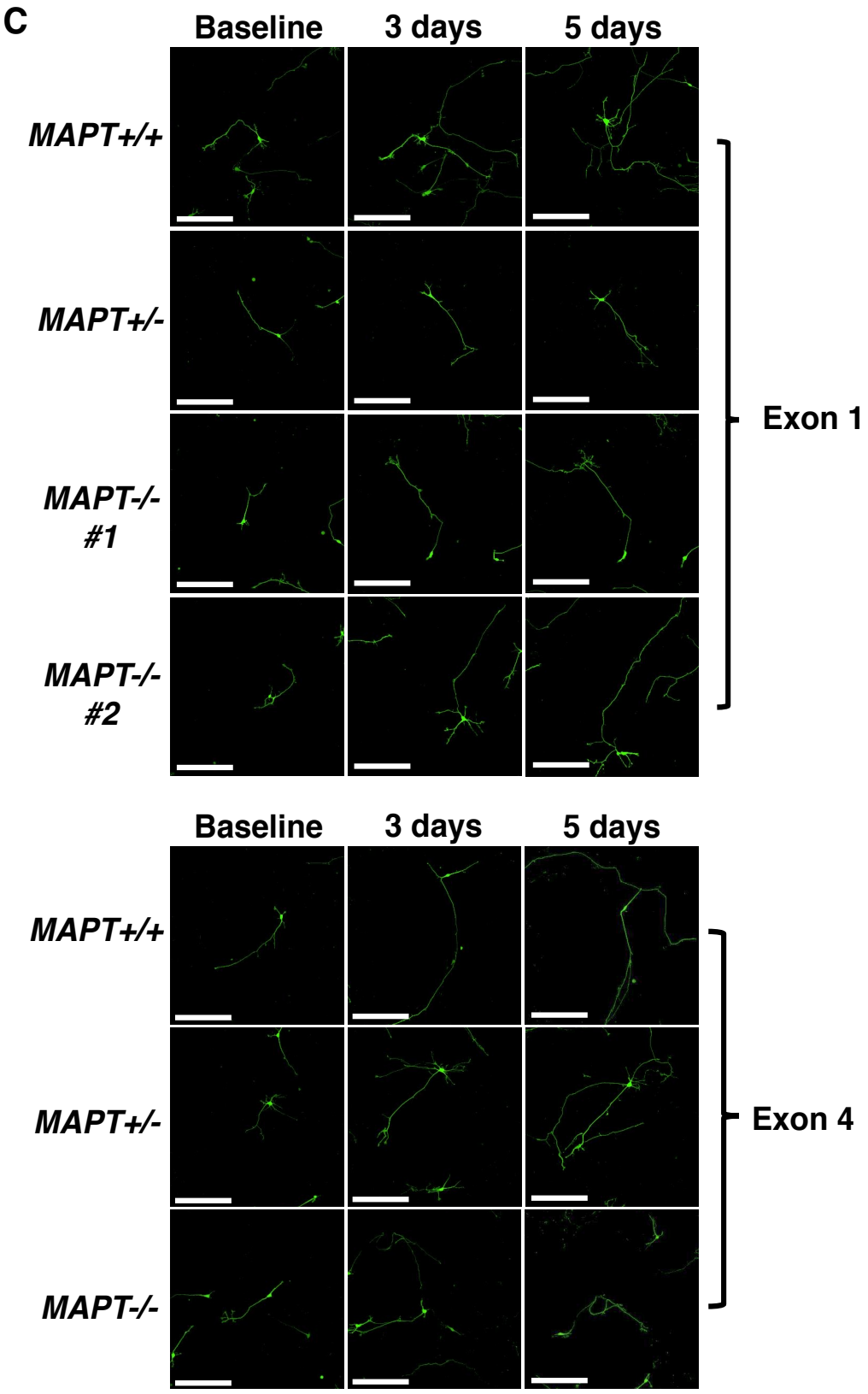


Figure 4.2.2: Neurite outgrowth quantification in Day 35-36 iPSC-derived cortical neurons of the isogenic *MAPT-/-* lines.
(A) Absolute values of neurite outgrowth parameters at baseline (i.e., 0 h of live imaging). Mean ± SD. N = 3 independent differentiation repeats. Kruskal-Wallis test with Dunn's multiple comparison correction was used for the statistical analysis.

B

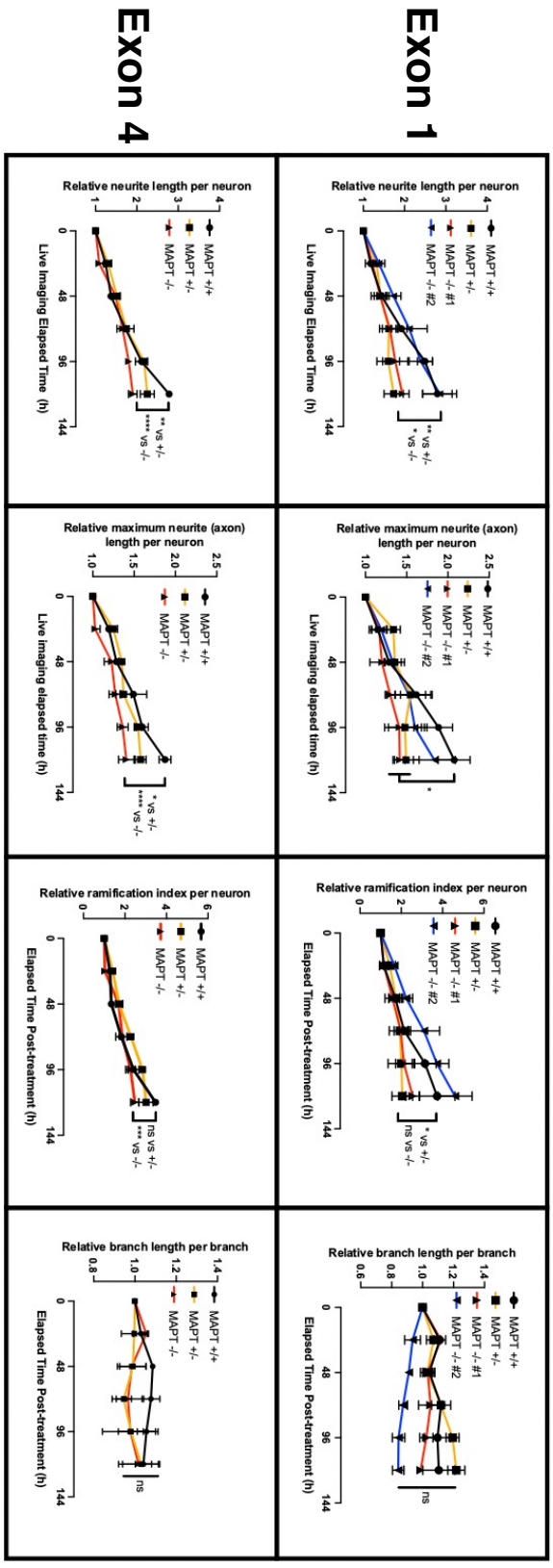


(B) Neurite outgrowth parameters relative to baseline (i.e., 0 h of live imaging) over 5 days with control treatments namely untreated, vehicle (PBS) and 10 μM of scrambled $A\beta_{1-42}$ peptides in the *MAPT*+/+ lines only. Mean ± SEM. N = 3 independent differentiation repeats except for the untreated sample where N = 1. Two-way ANOVA with Tukey's multiple comparison correction was used for statistical analysis. Statistical significance of the 120 h-elapsed data was marked on the figure.



(C) Representative images of neurite tracing at baseline, 3 days, and 5 days post-tracing of Day 35 neurons. Scale bar = 200 μm.

D



(D) Neurite outgrowth parameters relative to baseline (i.e., 0 h of live imaging) over 5 days with vehicle (PBS) treatment in all isogenic lines. Mean ± SEM. N = 3 independent differentiation repeats. Two-way ANOVA with Tukey's multiple comparison correction was used for the statistical analysis. Statistical significance of the 120 h-elapsed data was marked on the figure.

4.2.3 Neurite outgrowth impairment caused by extrinsic Aβ insults

I then investigated whether the loss of tau expression alters neuronal responses to extrinsic $A\beta_{1-42}$ oligomer insults. Over the course of 5 days subject to the exposure of 10 μM $A\beta_{1-42}$ oligomers, there were clear neurite outgrowth impairments in the iPSC-derived neurons (Figure 4.2.3A) in terms of their neurite lengths, maximum neurite (axon) lengths, and ramification indexes (Figure 4.2.3B; statistical analysis relative to the treatment control not shown on the graphs). The neurite branch lengths were unaffected by the Aβ insult, overall indicating that neurite branches do not change in length during outgrowth (Figure 4.2.2B), are not dependent on the presence of tau protein (Figure 4.2.2D), and do not shorten in the presence of an Aβ insult even when the total neurite length decreases (Figure 4.2.3B). Interestingly, the Aβ insult was also capable of causing considerable loss of neurons (~ 25% loss after 5 days).

However, no differential responses were observed among the *MAPT* genotypes measured by the neurite parameters suggesting that the loss of tau expression was not enough to prevent neurite outgrowth impairments caused by Aβ. There were some indications that the *MAPT-/-* neurons were less susceptible to cell death and these data prompted the follow-up experiments in Chapter 4.2.5.

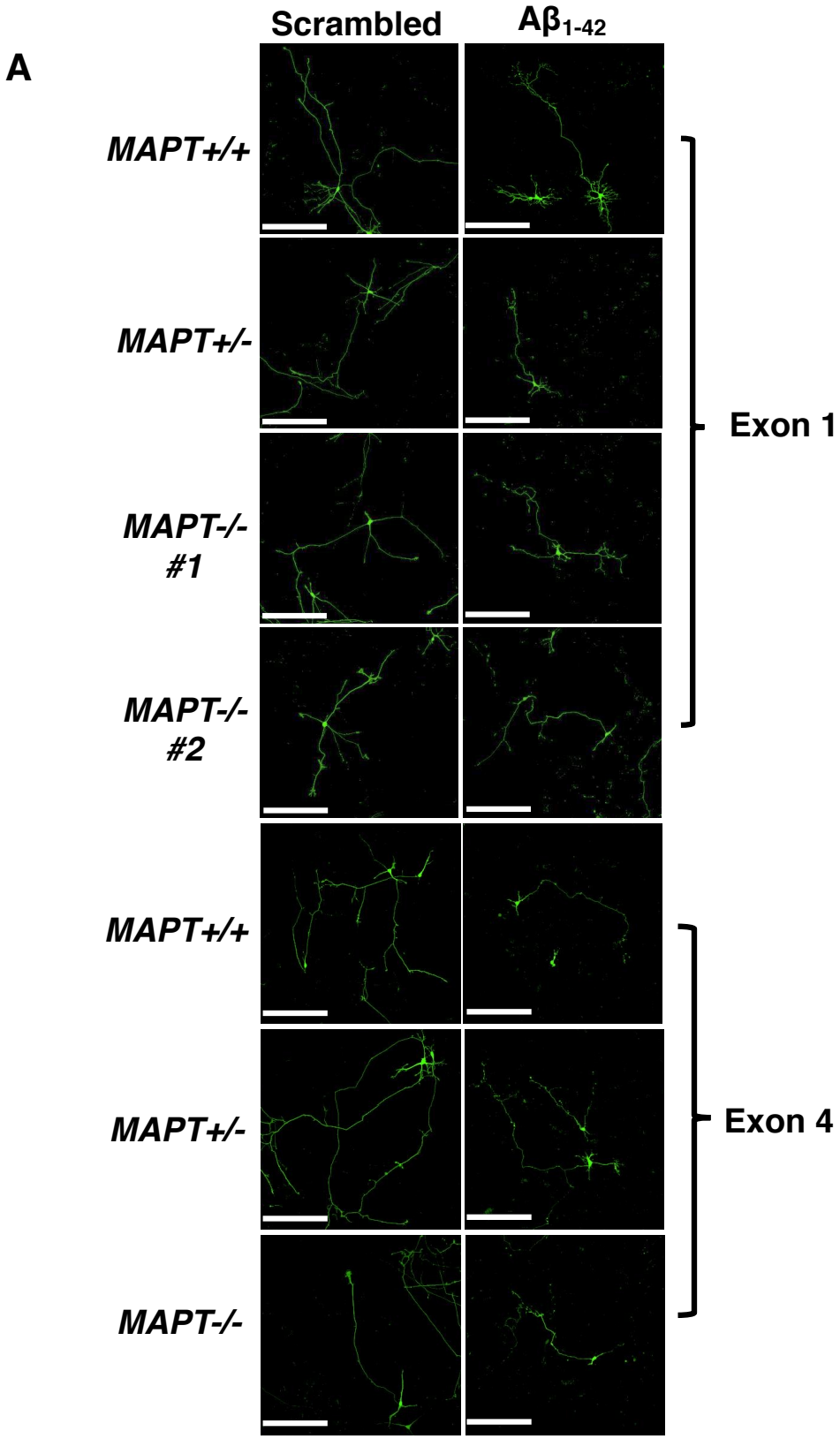
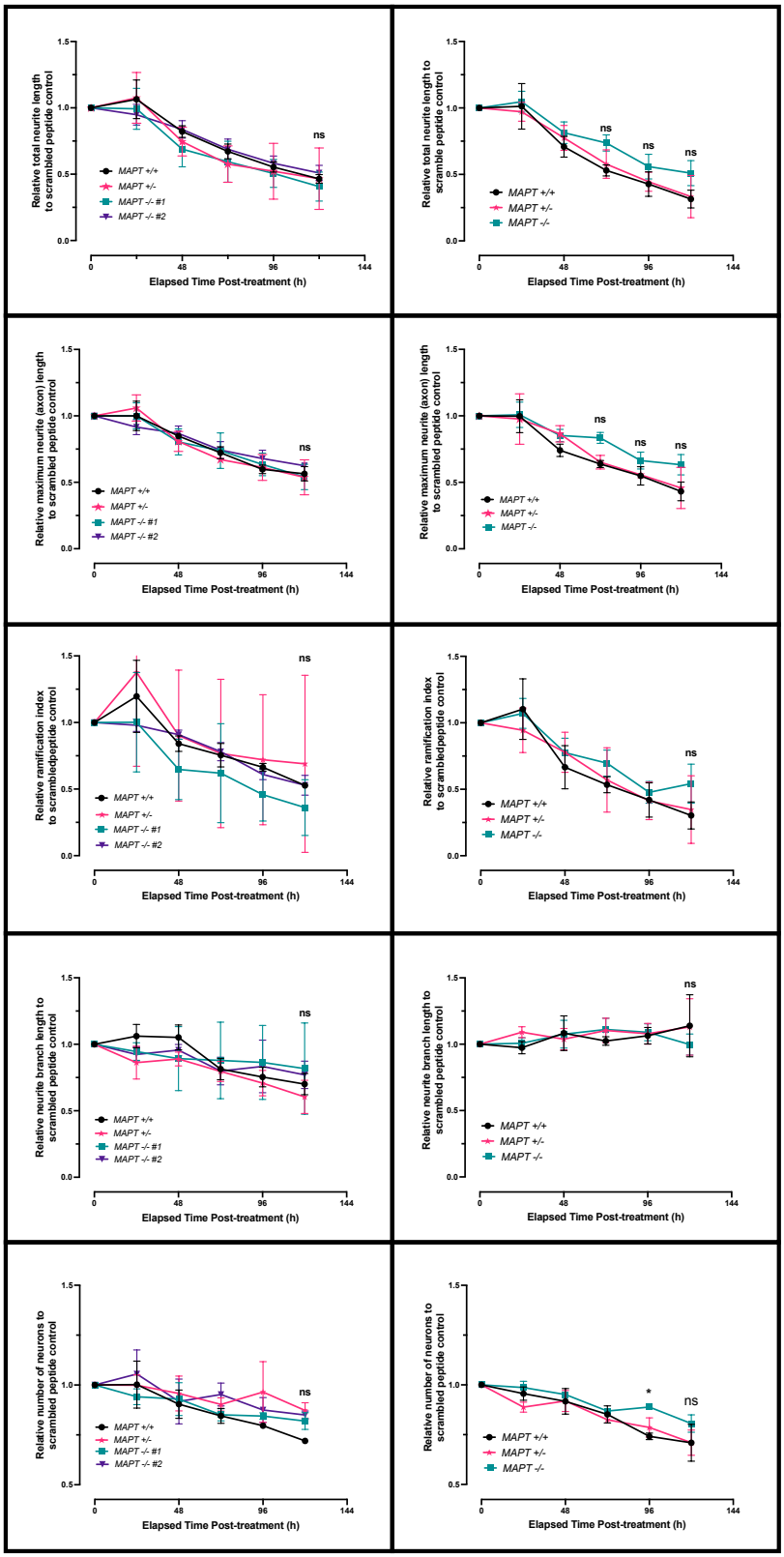


Figure 4.2.3: Quantifications of neurite outgrowth impairment caused by 10 μM of $A\beta_{1-42}$ oligomer in the Day 35-36 iPSC-derived cortical neurons of the *MAPT-/-* isogenic lines

(A) Representative images of neurite outgrowth impairments caused by 10 μM of $A\beta_{1-42}$ oligomer 5 days post-treatment. Scale bar = 200 μm.

B **Exon 1** **Exon 4**



(B) Relative neurite outgrowth parameters to the 10 μM scrambled $A\beta_{1-42}$ oligomer treatment (relative value of 1) over 5 days of neurite tracing. Mean ± SEM. N = 3 independent neuronal differentiation repeats. Two-way ANOVA with Tukey's multiple comparison correction was used for the statistical analysis.

4.2.4 Experimental design - cytotoxicity assays

Cleaved caspase-3 (CC3) was chosen to be the apoptotic marker for cytotoxicity in the iPSC-derived cortical neurons around 80 days into neuronal differentiation because activated (cleaved) caspase-3 was shown to be elevated in AD brains either in a more widespread manner or localised in the hippocampus [340,341]. Since the human neurons were seeded in co-culture with rat astrocytes, a human nucleus-specific antibody was used to mark the regions of interest co-stained with CC3 for downstream quantifications (Figure 4.2.4A). CC3 overexpression could be observed in the neurons (including the rat astrocytes in co-culture) after 5 days of exposure to $A\beta_{1-42}$ oligomers. The definition used in this study of an apoptotic CC3+ neuron due to Aβ-driven cytotoxicity is a neuron displaying CC3 signal intensity level that is two SD above the mean across all human nuclei identified in the scrambled $A\beta_{1-42}$ peptide-treated group. Finally, the percentage of CC3+ neurons could be calculated over the total number of human nuclei as a normalised readout. The dosage of 10 μM $A\beta_{1-42}$ oligomers was chosen instead of 20 μM because of the consistency across replicate wells, sufficient response to the Aβ insult (2- to 5-fold) (Figure 4.2.4B) and the consideration to not cause overt rat astrocyte death as the neurons depend on the astrocytes for adhesion to the plate.

Additionally, the cell supernatant was collected for a cell viability assay by measuring AK (Chapter 2.14) just before the neurons were fixed for ICC. The AK detection assay served as a complementary cytotoxicity readout on top of the CC3 measurements.

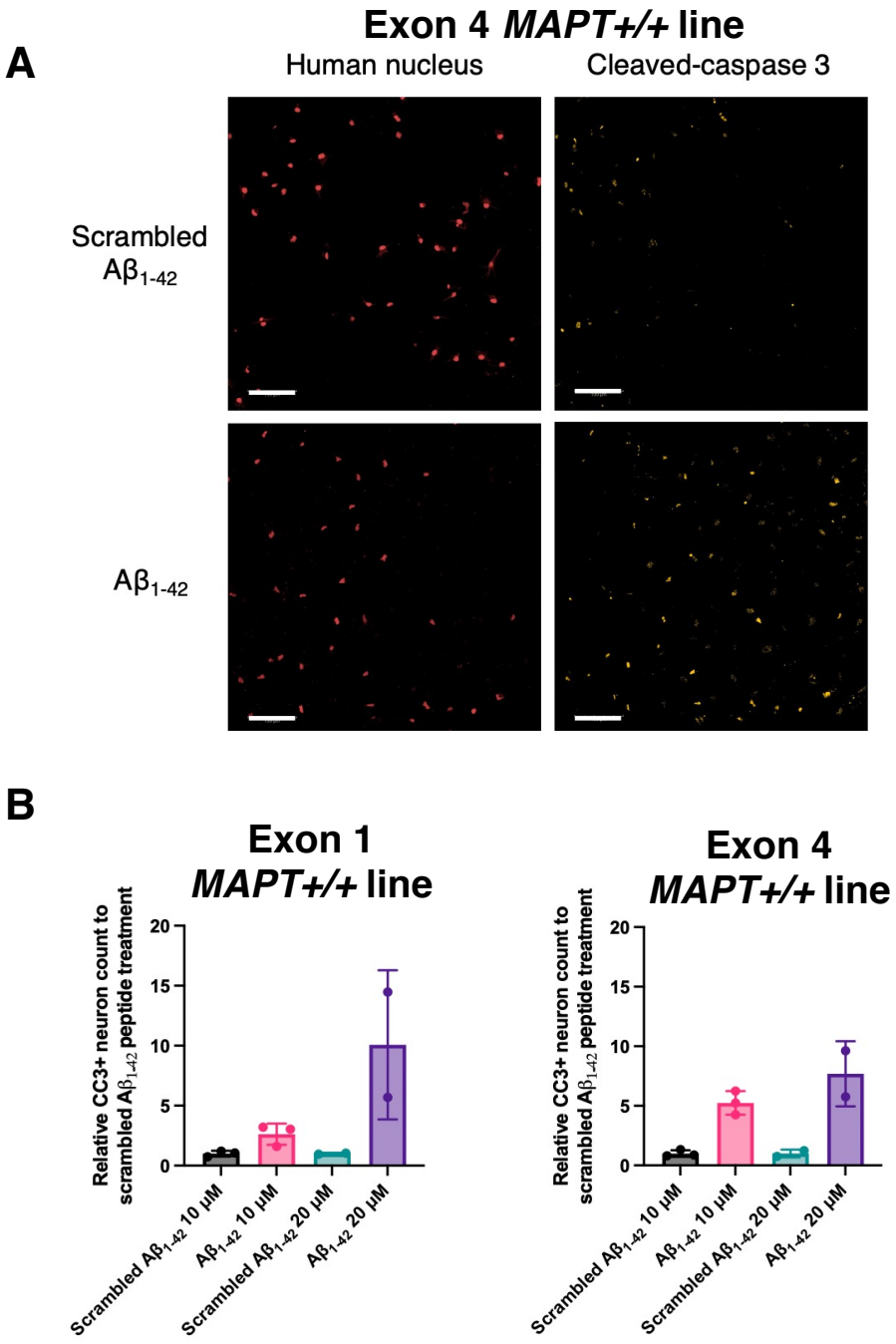


Figure 4.2.4: Quantification of cytotoxicity measured by CC3 ICC
(A) Representative images of Day 83 iPSC-derived neurons from the Exon 4 *MAPT*+/+ line stained with anti-human nuclear antigen and anti-CC3 antibodies in both scrambled $A\beta_{1-42}$ and $A\beta_{1-42}$ oligomers-treated samples. Scale bar = 100 μm.
(B) Quantification of CC3 overexpression caused by 5 days of exposure to $A\beta_{1-42}$ oligomers relative to the scrambled peptide control in Day 83 *MAPT*+/+ iPSC-derived cortical neurons. N = 2 (20 μM) or 3 (10 μM) technical replicate wells from one differentiation repeat. Mean ± SD. No statistical analysis was performed as the data were derived from a single neuronal differentiation.

4.2.5 Aβ-driven cytotoxicity in iPSC-derived neurons

To assess whether the *MAPT-/-* background is protective against Aβ-driven cytotoxicity in human iPSC-derived cortical neurons, I treated the neurons (around Day 80 of neuronal differentiation) with extrinsic $A\beta_{1-42}$ oligomers before fixing the cells 5 days later for ICC (Figure 4.2.5A) while the cell supernatant from the same samples was frozen for an AK detection assay (Chapter 2.14). Both *MAPT+/+* lines from the isogenic panels exhibited increased number of CC3+ neurons by approximately 5-fold (Exon 1) and 12-fold (Exon 4) post-treatment with 10 μM of $A\beta_{1-42}$ oligomers, whereas the *MAPT+/-* and *MAPT-/-* neurons did not demonstrate significant increases in the number of CC3+ neurons as compared to the scrambled $A\beta_{1-42}$ peptide-treated samples (Figure 4.2.5B). It is also worth noting that the Exon 4 lines appeared to be more susceptible to the Aβ insult as compared to the Exon 1 lines with greater CC3 upregulation overall. The data suggest that partial or total loss of tau expression was sufficient to protect the neurons against Aβ-driven cytotoxicity.

Similarly, significant levels of AK upregulation were observed in the cell supernatant from the *MAPT+/+* neurons due to the extrinsic Aβ insult (Figure 4.2.5C). This corroborates that there was pronounced cytotoxicity in the neurons in co-culture with rat astrocytes. In the Exon 1 panel, the AK luminescence results did not fully agree with the CC3 measurements (Figure 4.2.5B) as there was also apparent AK upregulation noticeable from the *MAPT+/-* and one of the *MAPT-/-* clones though at lower levels as compared to that from the *MAPT+/+* neurons. On the other hand, the data from the Exon 4 lines mirrored more closely with the CC3 measurements supported by statistical analyses thus suggesting protective effects in the *MAPT-/-* neurons.

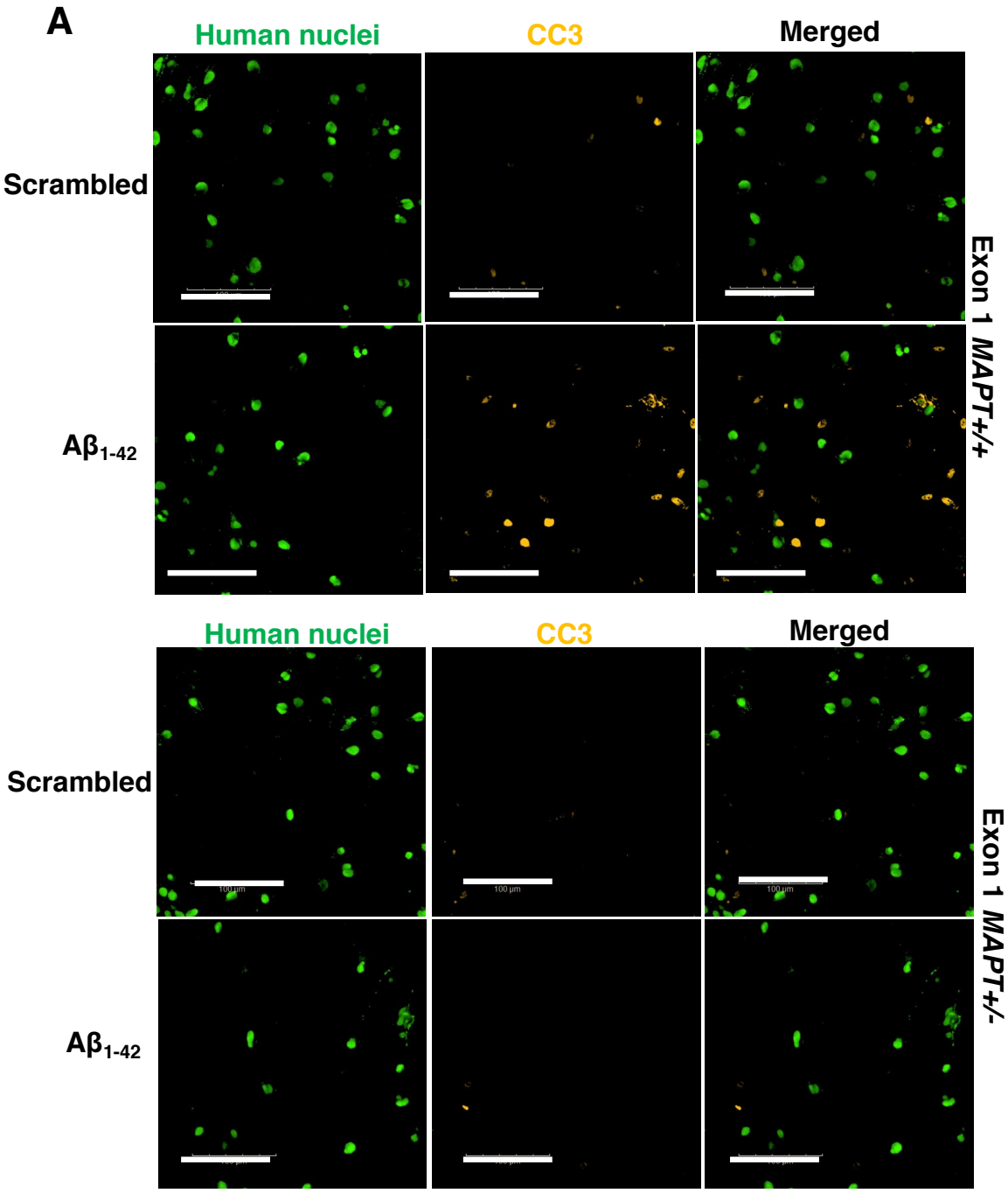
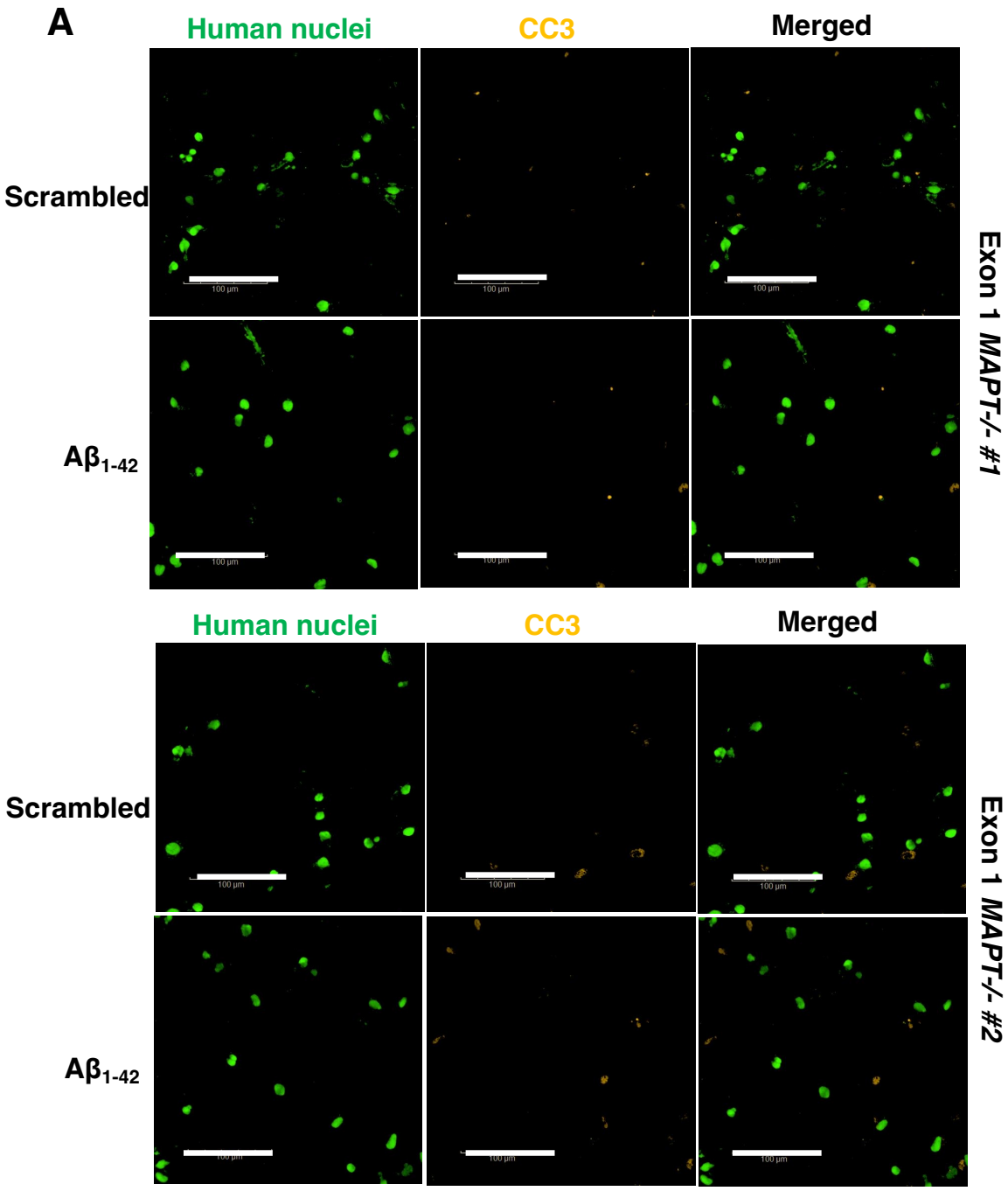
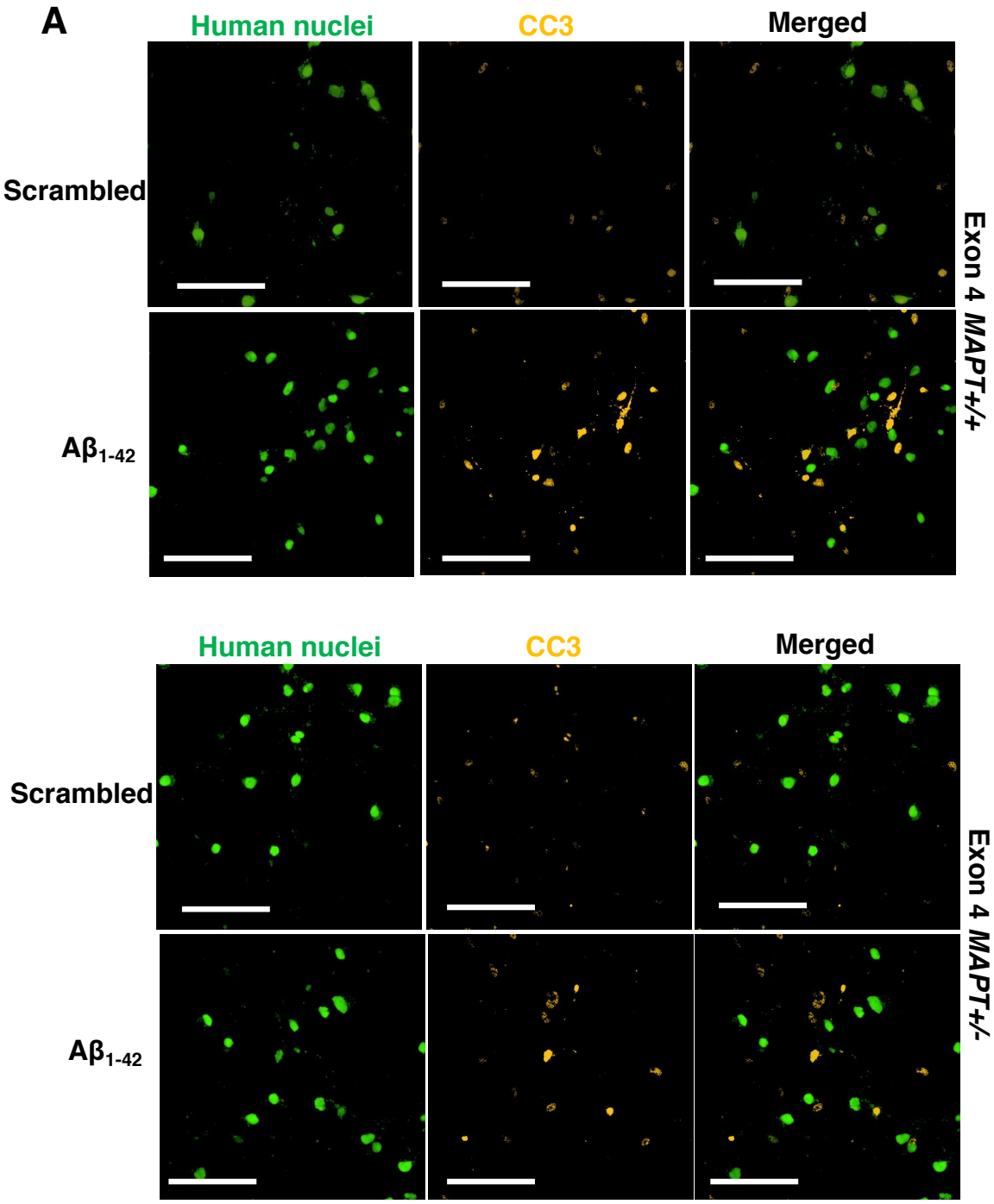
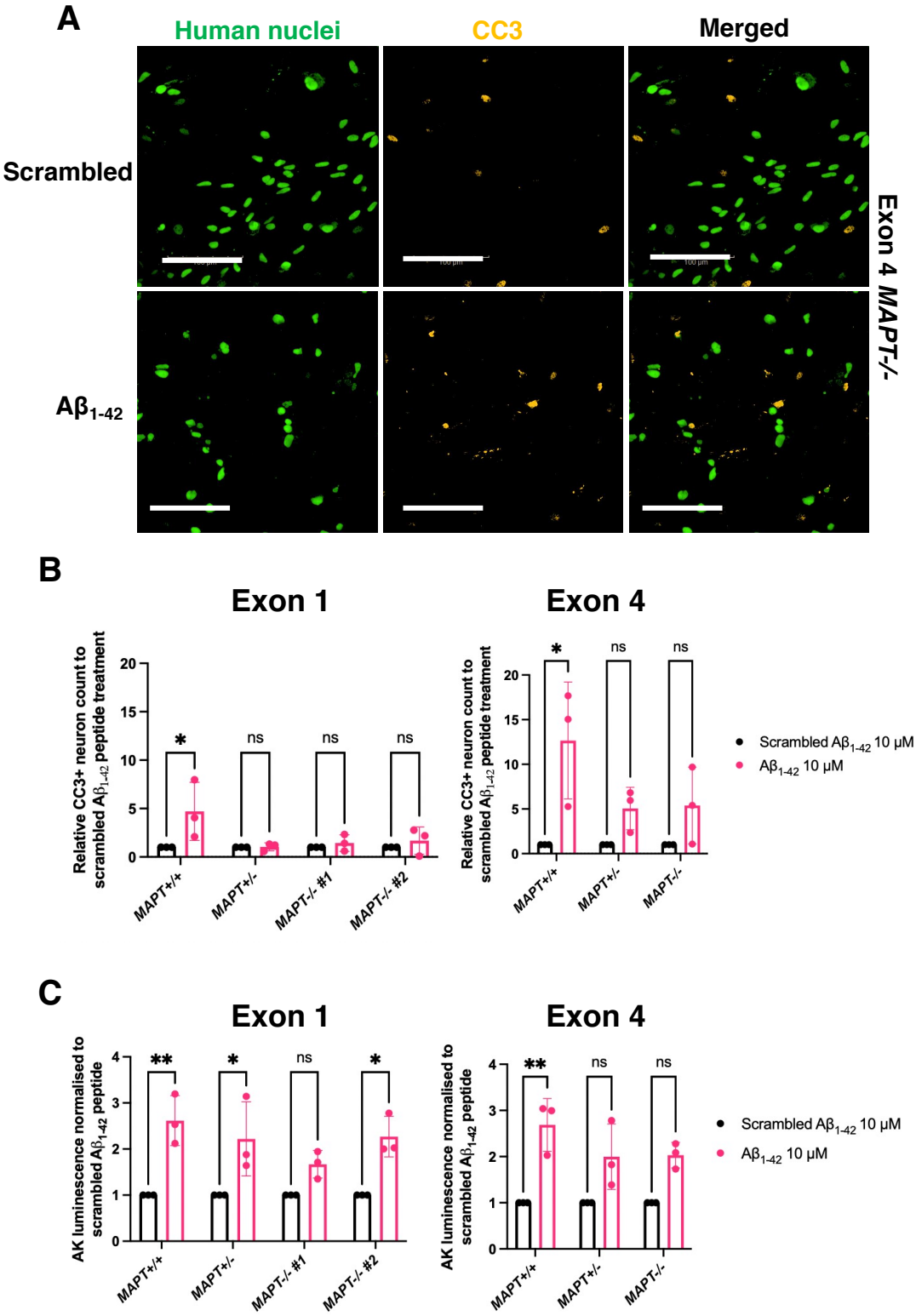


Figure 4.2.5: Quantifications of cytotoxicity caused by 5-day exposure to 10 μM of $A\beta_{1-42}$ oligomers in Day 79-83 (Exon 1) or Day 79-86 (Exon 4) iPSC-derived cortical neurons from the *MAPT-/-* isogenic lines.
(A) Representative images of iPSC-derived cortical neurons treated with either 10 μM of scrambled $A\beta_{1-42}$ peptide or 10 μM of $A\beta_{1-42}$ oligomers for 5 days. The neurons were probed with antibodies against human nuclei (green) and CC3 (yellow). Scale bar = 100 μm.


A
Human nuclei
CC3
Merged
Scrambled
Aβ1-42
Exon 1 MAPT-/- #1
Human nuclei
CC3
Merged
Scrambled
Aβ1-42
Exon 1 MAPT-/- #2


A
Human nuclei
CC3
Merged
Scrambled
Aβ1-42
Exon 4 MAPT+/+
Human nuclei
CC3
Merged
Scrambled
Aβ1-42
Exon 4 MAPT+/-



(B) Relative number of CC3+ neurons to the scrambled Aβ1-42 peptide-treated samples (black bars) measured by ICC. Mean ± SD. N = 3 independent neuronal differentiation repeats. Two-way ANOVA with Tukey's multiple comparison correction was used for the statistical analysis.

(C) Relative AK luminescence to the scrambled Aβ1-42 peptide-treated samples (black bars). Mean ± SD. N = 3 independent neuronal differentiation repeats. Two-way ANOVA with Tukey's multiple comparison correction was used for the statistical analysis.

4.2.6 Experimental design - mitochondrial transport by live imaging

The microfluidic devices used in this study were designed to have cell-seeding compartments connected by microgrooves which are just large enough for neurites to grow through yet too small for fluid exchange or cell migration to be permitted. These microfluidic devices were used to precisely discern the direction of mitochondrial transport by allowing axons to grow along the microgrooves with the neuronal soma restricted within the cell seeding chamber (Figure 4.2.6A). To promote axonal outgrowth towards the distal side of the microfluidic device, a volume as well as concentration gradient was maintained (i.e., lower volume and higher growth factor concentration at the distal side) throughout the neuronal differentiation process until around Day 80 where time lapse images (1 image/s for 150 s) were captured before and after treating the neurons with either $A\beta_{1\text{-}42}$ oligomers or nocodazole.

To assess if the TrackMate analysis pipeline used could correctly detect mitochondrial movements, I used nocodazole, which is a small molecule capable of inhibiting microtubule polymerisation, as a positive control to eliminate axonal transport. The loss of motile mitochondria and decreasing movement speed and displacement were evident upon quantification with the TrackMate analysis pipeline (Figure 4.2.6B).

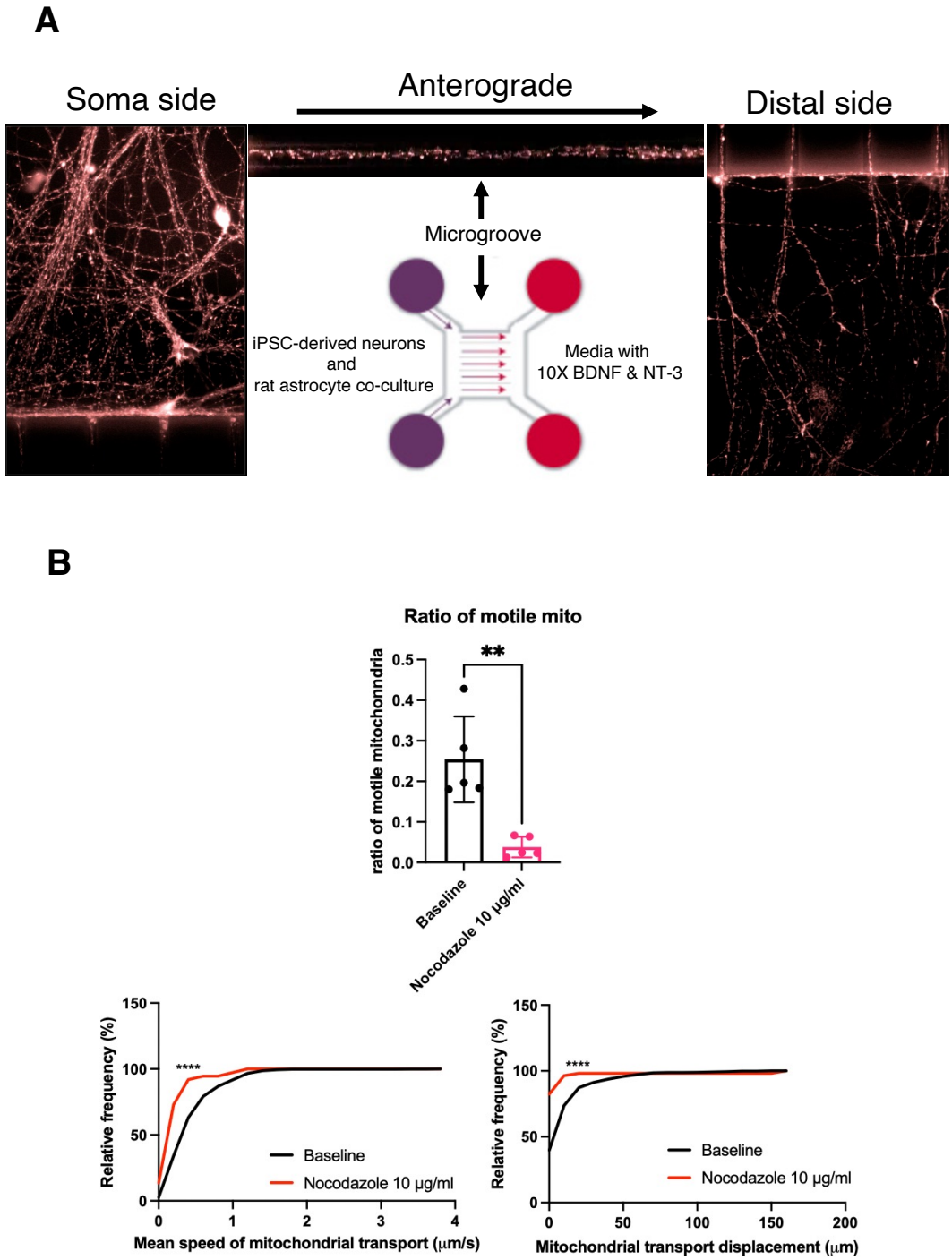


Figure 4.2.6: Mitochondrial transport along axons organised in microfluidic chambers (A) Schematic of iPSC-derived neuronal culture in a microfluidic device setup for mitochondrial imaging labelled with 100 nM of the MitoTracker™ Deep Red FM dye. Time lapse images were captured within the microgrooves for downstream analysis. (B) Quantification of mitochondrial transport along axons using the TrackMate analysis pipeline in the Fiji software. Baseline measurements were first recorded before treating the Exon 4 *MAPT*+/+ neurons (Day 83-90) with 10 µg/ml nocodazole for 1 h as a positive control for inhibiting mitochondrial transport. N = 5 microfluidic devices for the ratio of motile mitochondria; N = 913 (baseline) or 37 (nocodazole) motile mitochondria tracks for the cumulative frequency graphs. Mann-Whitney test was used for the bar graph and Kolmogorov-Smirnov test was used for the frequency distribution graphs for the statistical analyses.

4.2.7 Mitochondrial transport along axons in *MAPT-/-* iPSC-derived neurons

I then asked whether the absence of tau protein, which is a microtubule-binding protein, affects mitochondrial transport along axons in aged human iPSC-derived cortical neurons. The Exon 4 lines were tested and the *MAPT*+/+ and *MAPT*-/- neurons showed no difference in the ratio of motile mitochondria between the genotypes (Figure 4.2.7A). However, the *MAPT*-/- neurons exhibited lower mean speed and greater displacement of mitochondrial movements along axons indicating that the absence of tau protein led to overall slower yet more uninterrupted (i.e., more continuous despite lower speed) axonal transport of mitochondria.

The changes in mitochondrial transport shown in Figure 4.2.7A were statistically significant yet small in effect sizes. I next re-analysed the same dataset to differentiate the directionality of the motile mitochondria to resolve in more detail whether there was a bias in either anterograde or retrograde mitochondrial transport along axons due to the loss of tau expression. The *MAPT*-/- neurons exhibited greater ratio of anterograde motile mitochondria as compared to the retrograde ratio yet there still was no statistical difference between the *MAPT*+/+ and *MAPT*-/- neurons in either direction (Figure 4.2.7B). In terms of moving speed, retrograde mitochondrial movement in the *MAPT*-/- neurons was significantly slower as compared to the anterograde movement and to the retrograde movement in the *MAPT*+/+ neurons. In addition, both *MAPT*+/+ and *MAPT*-/- neurons demonstrated greater anterograde mitochondrial displacements as opposed to the retrograde ones and there was greater anterograde displacement in the *MAPT*-/- neurons as compared to that in the *MAPT*+/+ neurons. All in all, there appeared to be a deficiency specifically in the retrograde mitochondrial transport in comparison to the anterograde direction due in the *MAPT*-/-

neurons with fewer and slower mitochondria moving in the retrograde direction while covering less displacement. Additionally, the data in Figure 4.2.7B explain the observations in Figure 4.2.7A in more detail with regards to the effects of tau ablation; the slower moving speed in the *MAPT-/-* neurons was attributed mainly to the retrograde movement whereas the greater displacement of mitochondria was attributed mainly to the anterograde movement.

A

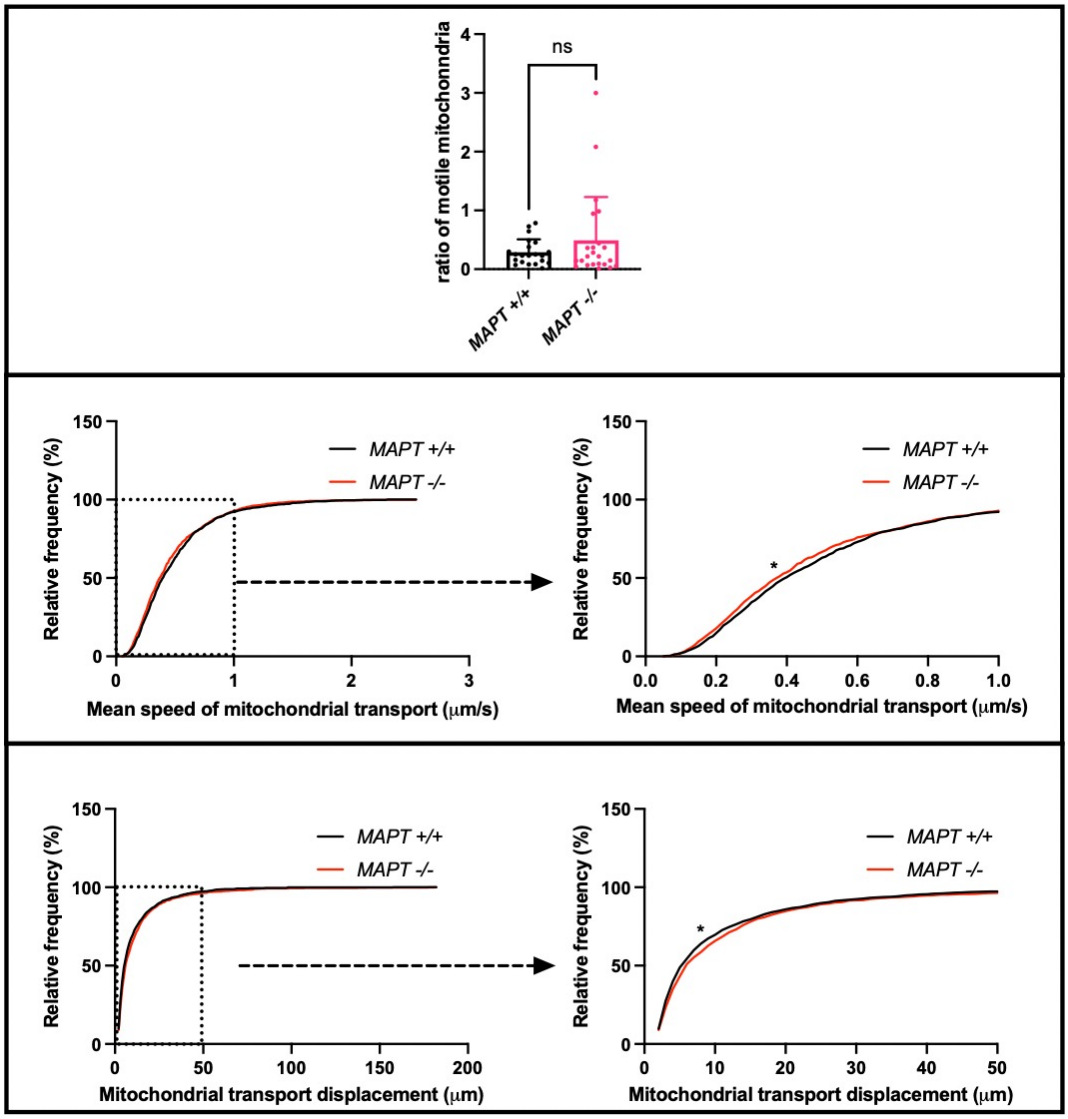
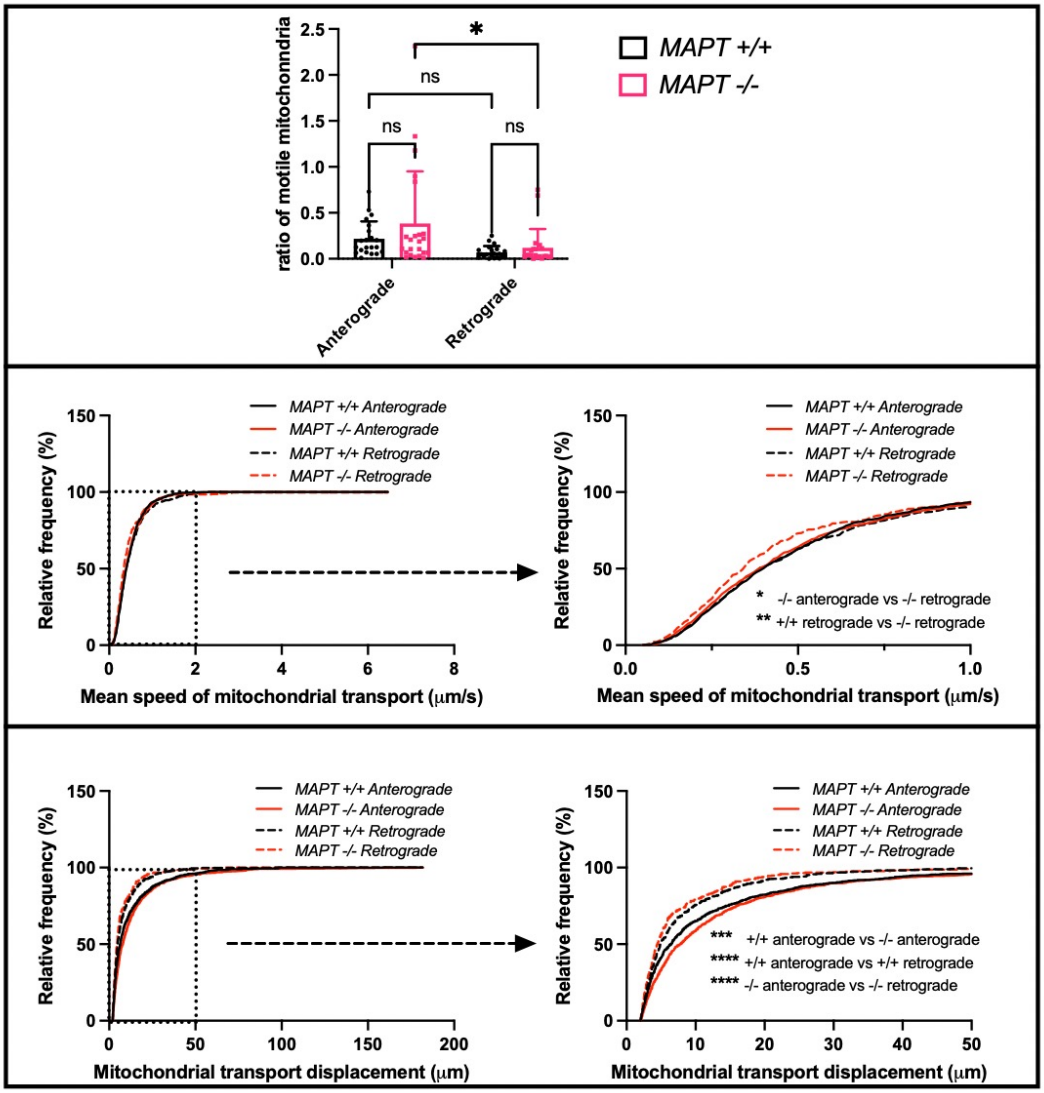


Figure 4.2.7: TrackMate analysis of baseline mitochondrial transport along axons in Day 70-95 iPSC-derived cortical neurons from the Exon 4 lines seeded in microfluidic chambers

(A) Total ratios of motile mitochondria; N = 21 (*MAPT*+/+) or 23 (*MAPT*-/-) microfluidic chambers imaged from 5 independent neuronal differentiation repeats. Cumulative frequency graphs of mean speed and displacement of mitochondrial transport; N = 1492 (*MAPT*+/+) and 1243 (*MAPT*-/-) moving tracks of mitochondria from 5 independent neuronal differentiation repeats. The duplicate graphs on the right side depict the enlarged regions of interest at lower x-axis values. Mann-Whitney test was used for the bar graph and Kolmogorov-Smirnov test was used for the frequency distribution graphs for the statistical analyses.

B



(B) Ratios of motile mitochondria with directionality; N = 21 (*MAPT*+/+) or 23 (*MAPT*-/-) microfluidic chambers imaged from 5 independent neuronal differentiation repeats. Cumulative frequency graphs of mean speed and displacement of mitochondrial transport with directionality; N = 1492 (*MAPT*+/+) and 1243 (*MAPT*-/-) moving tracks of mitochondria from 5 independent neuronal differentiation repeats. The duplicate graphs on the right side depict the enlarged regions of interest at lower x-axis values. Two-way ANOVA with Šídák's multiple comparison correction was used for the bar graph and Kolmogorov-Smirnov test was used for the frequency distribution graphs for the statistical analyses.

4.2.8 Mitochondrial transport deficits caused by extrinsic Aβ insults

Having established the baseline differences due to the absence of tau, I then moved on to study the effects on mitochondrial transport along axons caused by an extrinsic Aβ insult

and probe if there are differential responses to Aβ in the *MAPT-/-* neurons. After the 1 h treatment with 2 μM of $A\beta_{1\text{-}42}$ oligomers, there was significant decrease (~ 50%) in the ratio of motile mitochondria of the *MAPT+/+* neurons, but such decrease was absent in the *MAPT-/-* neurons (Figure 4.2.8A). There was a considerable reduction in the speed of mitochondrial transport due to the extrinsic Aβ insult regardless of the *MAPT* genotypes, while the mitochondrial displacement was unaffected post-treatment in the *MAPT+/+* neurons. Unexpectedly, there was an increase in the mitochondrial displacement only in the *MAPT-/-* neurons post-treatment although the effect size was notably smaller than what was observed in the readout for speed.

Upon distinguishing the directionality of mitochondrial transport, it became evident that the decrease in the ratio of motile mitochondria due to the extrinsic Aβ insult seen in Figure 4.2.8A was largely attributed to the mitochondria moving in the anterograde direction in the *MAPT+/+* neurons (Figure 4.2.8B) although the noticeable decrease in the retrograde direction was close to statistical significance ($p = 0.064$). The ratios of motile mitochondria remained unchanged post-treatment in either direction in the *MAPT-/-* neurons. Like the data in Figure 4.2.8A, the speed of mitochondrial transport was greatly diminished post-treatment in either direction regardless of the *MAPT* genotypes. The mitochondrial transport displacement remained unaffected post-treatment in the *MAPT+/+* neurons in either direction whereas the surprising increase in displacement in the *MAPT-/-* neurons post-treatment described in Figure 4.2.8A was specific to the retrograde movement. Altogether, the data suggest that extrinsic Aβ insult could lead to a reduction in the number of motile mitochondria even though the remaining motile mitochondria would eventually be transported over the same displacement within the same time frame despite the curtailment in the speed of mitochondrial transport along axons. The *MAPT-/-* background is protective

against extrinsic Aβ insult by ensuring that the number of moving mitochondria remained constant post-treatment.

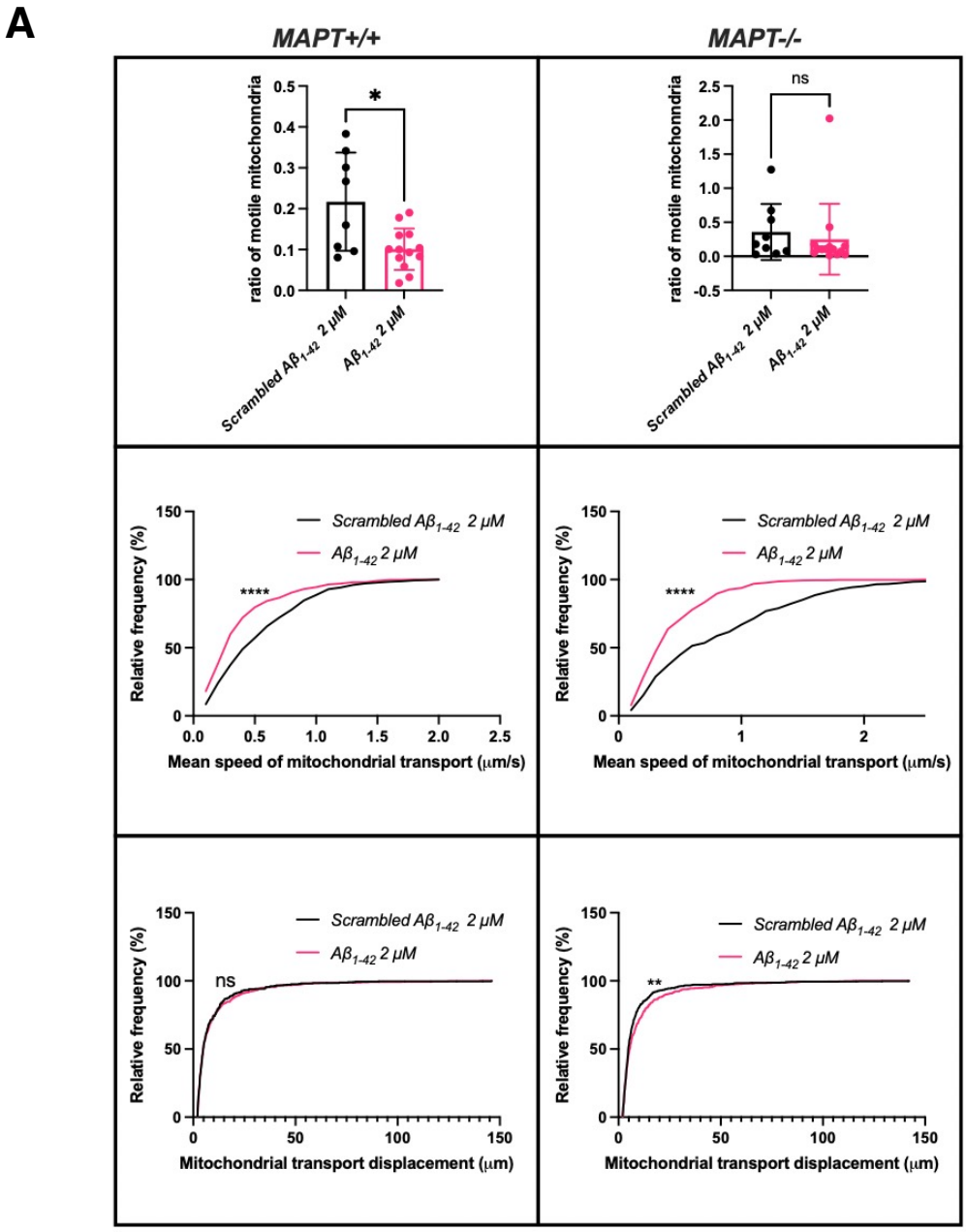
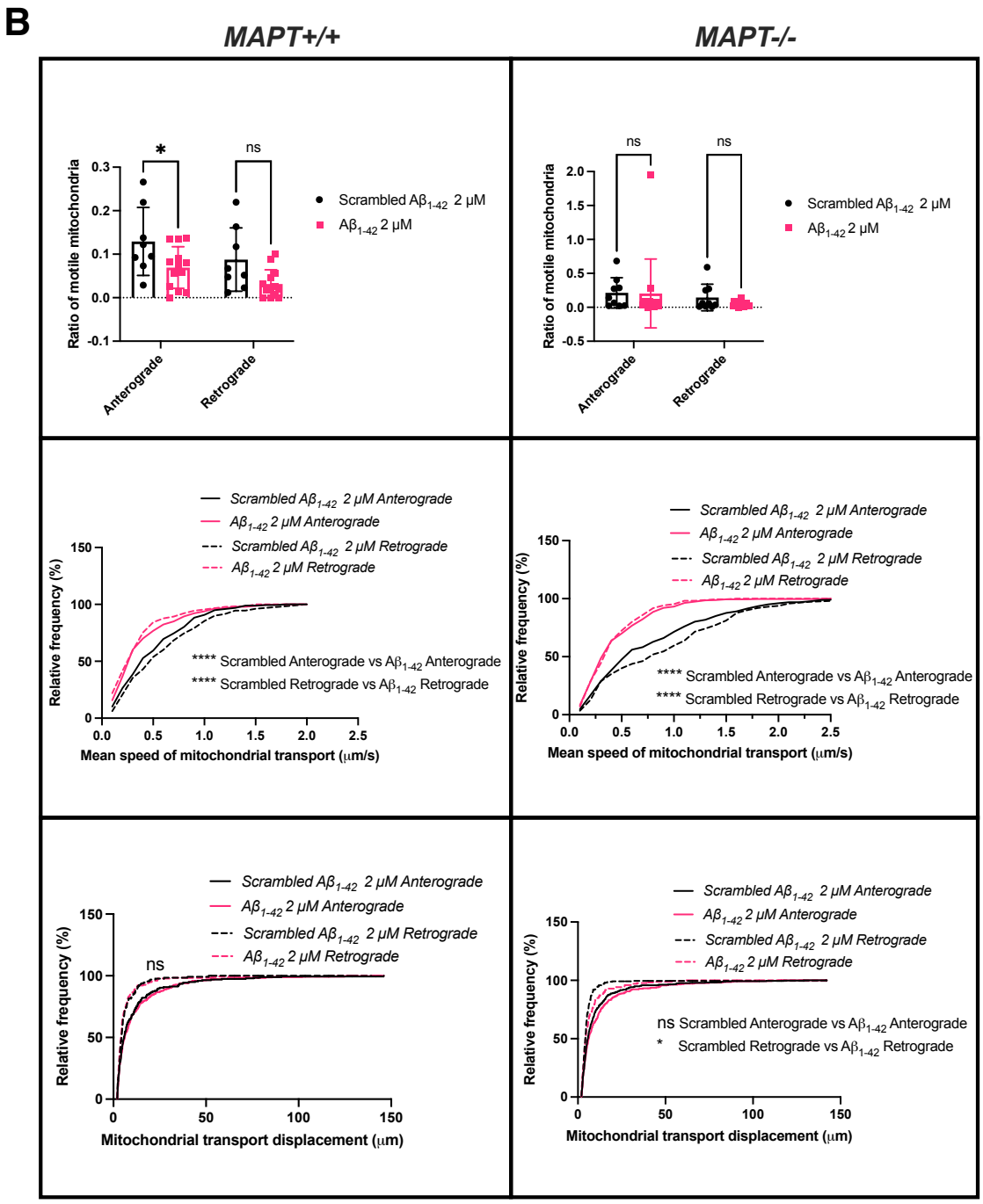


Figure 4.2.8: TrackMate analysis of mitochondrial transport along axons 1 h post-treatment with 2 μM of Aβ1-42 oligomers in Day 70-95 iPSC-derived cortical neurons from the Exon 4 lines seeded in microfluidic chambers
(A) Total ratios of motile mitochondria; N = 8 (*MAPT+/+;* Scrambled), 13 (*MAPT+/+;* Aβ), 9 (*MAPT-/-;* Scrambled) or 14 (*MAPT-/-;* Aβ) microfluidic chambers imaged from 5 independent neuronal differentiation repeats. Cumulative frequency graphs of mean speed and displacement of mitochondrial transport; N = 327 (*MAPT+/+;* Scrambled), 472 (*MAPT+/+;* Aβ), 690 (*MAPT-/-*; Scrambled) and 521 (*MAPT-/-*; Aβ) moving tracks of mitochondria from 5 independent neuronal differentiation repeats. Mann-Whitney test was used for the bar graphs and Kolmogorov-Smirnov test was used for the frequency distribution graphs for the statistical analyses.



(B) Ratios of motile mitochondria <u>with directionality</u>; N = 8 (*MAPT+/+;* Scrambled), 13 (*MAPT+/+;* Aβ), 9 (*MAPT-/-;* Scrambled) or 14 (*MAPT-/-;* Aβ) microfluidic chambers imaged from 5 independent neuronal differentiation repeats. Cumulative frequency graphs of mean speed and displacement of mitochondrial transport <u>with directionality</u>; N = 327 (*MAPT+/+;* Scrambled), 472 (*MAPT+/+;* Aβ), 690 (*MAPT-/-*; Scrambled) and 521 (*MAPT-/-*; Aβ) moving tracks of mitochondria from 5 independent neuronal differentiation repeats. Two-way ANOVA with Šídák's multiple comparison correction was used for the bar graph and Kolmogorov-Smirnov test was used for the frequency distribution graphs for the statistical analyses.

4.2.9 Mitochondrial membrane potential in the *MAPT-/-* iPSC-derived neurons and effects caused by extrinsic Aβ insults

To examine whether the changes in mitochondrial transport caused by the loss of tau expression and/or extrinsic Aβ insult are due to perturbations in mitochondrial functions, I conducted mitochondrial membrane potential assay by measuring JC-10 fluorescence (Chapter 2.16) in iPSC-derived cortical neurons from both isogenic panels around Day 50 of the neuronal differentiation. There were no consistent differences in the JC-10 signal ratios at baseline as well as the mitochondrial membrane potential ($\Delta\psi_m$) readout among the *MAPT* genotypes in both isogenic panels (Figure 4.2.9A). After treating the neurons with 2 μM of $A\beta_{1\text{-}42}$ oligomers (the same dosage used in Chapter 4.2.8), both *MAPT*+/+ neurons appeared to experience a reduction in mitochondrial membrane potential, yet the potential sustained at the original levels in the *MAPT*+/- and *MAPT-/-* neurons post-treatment in both isogenic panels (Figure 4.2.9B). The mitochondrial membrane potential experiment was only completed over two independent differentiation repeats, but the preliminary data suggest that there was no observable difference in baseline mitochondrial functionality among the *MAPT* genotypes while the *MAPT-/-* neurons demonstrated a consistent trend in both isogenic panels of preserving mitochondrial function post-treatment with extrinsic Aβ insult.

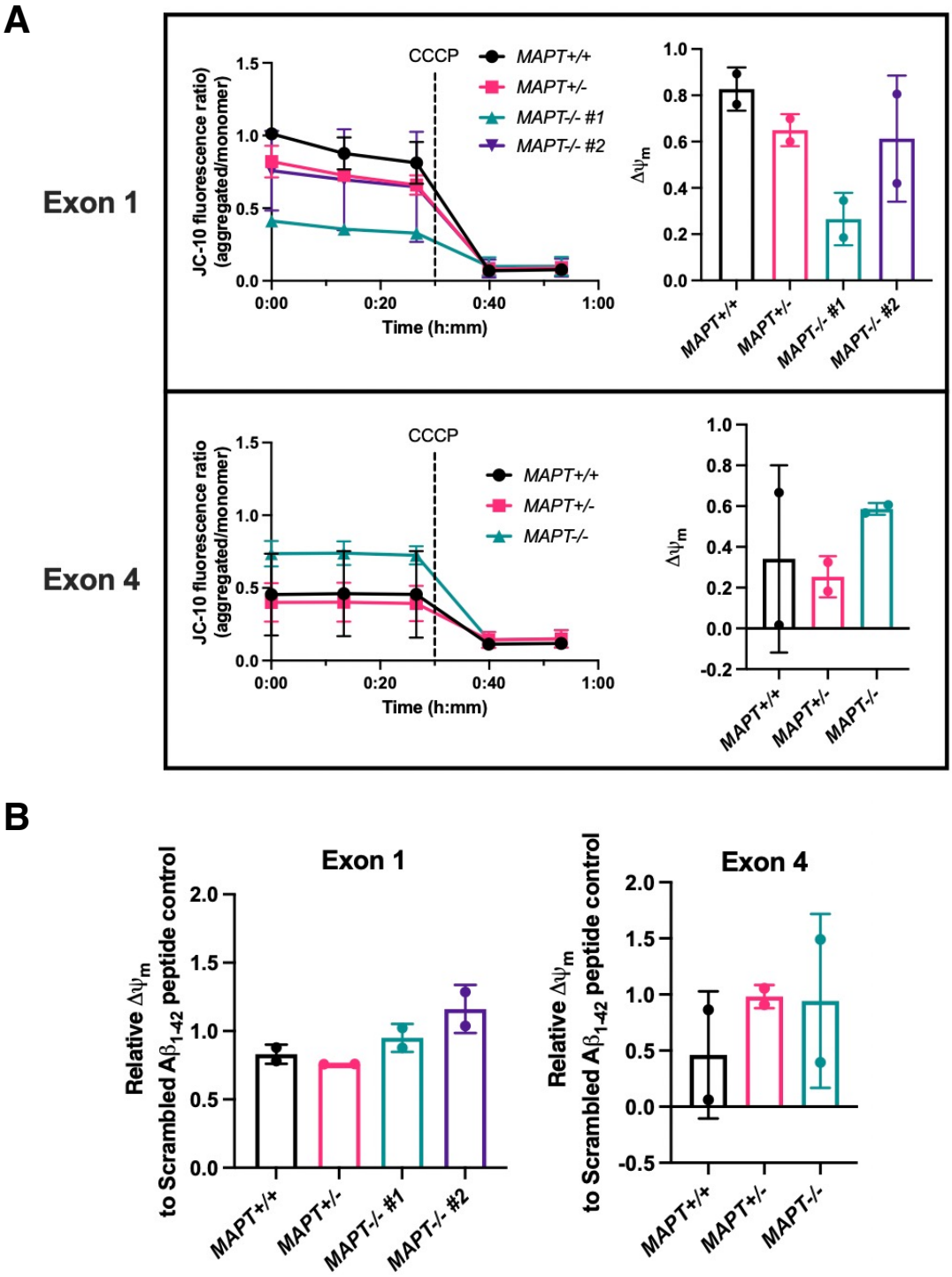


Figure 4.2.9: Quantification of mitochondrial membrane potential by measuring JC-10 fluorescence in Day 52-56 iPSC-derived cortical neurons from both *MAPT* isogenic panels

(A) Baseline JC-10 fluorescence ratio tracing (Mean ± SEM) pre- and post-treatment with 10 μM of $A\beta_{1-42}$ oligomers CCCP as well as mitochondrial membrane potential ($\Delta\psi_m$) in bar graphs (Mean ± SD). N = 2 independent neuronal differentiation repeats. (B) Bar graphs of mitochondrial membrane potential ($\Delta\psi_m$) post-treatment with 2 μM of $A\beta_{1-42}$ oligomers relative to the samples treated with 2 μM of scrambled $A\beta_{1-42}$ oligomers. Mean ± SD. N = 2 independent neuronal differentiation repeats. No statistical analysis was performed for this figure because the data were derived from less than three independent neuronal differentiation repeats.

4.4 Discussion

Not all MAPT-/- lines demonstrated neurite outgrowth impairments

In Figure 4.2.2D, the neurite tracing data established that tau ablation could result in neurite outgrowth impairments in human iPSC-derived cortical neurons thus agreeing with the previously published data in mouse primary hippocampal neurons [226]. However, one of the Exon 1 *MAPT-/-* lines (#2), which had the same frame-shift mutations as the other Exon 1 *MAPT-/-* line (#1), appeared to be uninfluenced by the lack of tau in terms of neurite outgrowth.

The Exon 1 *MAPT-/-* line (#2) in question behaved differently in culture apart from the rest of the iPSC lines in the sense that it did not present sufficient levels of proliferation both in the iPSC and NPC stages and displayed overt cell death during the first 25 days of neuronal differentiation (not quantified). The surviving neurons of the *MAPT-/-* line were otherwise normal ultimately in aged neurons in terms of cortical marker (Figure 3.3.3B) and synapse (Figure 5.2.2A) expressions.

This variability among *Mapt-/-* lines/strains was also evident in mice where the first *Mapt-/-* mice generated did not exhibit any outgrowth abnormalities [224]. Since then, several *Mapt-/-* mice had been generated with various gene-targeting techniques and mouse strains [223,225,226,228] but they manifested different characterisation results. Compensatory expression from other MAPs had been shown in a subset of the studies mentioned and could potentially explain the contradictions between the two Exon 1 *MAPT-/-* lines.

On the other hand, the data in Figure 4.2.3 contradicted a previous finding in mouse hippocampal neurons [242] by demonstrating that tau depletion was insufficient to prevent neurite degeneration in human iPSC-derived neurons after extrinsic Aβ insult. Other studies had reported that microtubule disassembly caused by extrinsic Aβ insult is tau-dependent in mice [245,246], indirectly suggesting that tau ablation should stop axonal degeneration under the exposure to Aβ. However, it was also reported that loss of tau elicited axonal degeneration in the presence of an *APP* mutation in mice [252].

Another potential cause of inconsistent neurite readouts between mouse models and human iPSC-derived models is the immaturity of the iPSC-derived neurons imaged for the neurite tracing experiments detailed in this Chapter. It was essential to image the GFP+ neurons within a few days after they were plated to accurately distinguish individual neurons using the analysis pipeline in the Harmony® software before the neurites intertwined with each other. It was also not possible to passage much older neurons after the neuronal network became well-connected as they would not survive. As such, neurite outgrowth was chosen to be the readout for neurite tracing even though it reflects more of developmental processes of the neurons as opposed to neurite degeneration experienced by AD animal models or patients.

It is also worth noting that the extrinsic Aβ used in these limited studies were different (20 μM $A\beta_{1-40}$ fibrils in [242], up to 3 μM of $A\beta_{1-40}$/$A\beta_{1-42}$ mixture in [246] and 1 μM prefibrillar $A\beta_{1-42}$ in [245]) from what was described in this thesis (10 μM $A\beta_{1-42}$ oligomers), hence further experiments such as one involving a lower concentration of $A\beta_{1-42}$ oligomers and longer exposure might be needed to understand the effects of tau knockout in human iPSC-derived neurons.

Taken together, given the marked neurite outgrowth impairments confirmed in not only the *MAPT-/-* neurons but also the *MAPT+/-* neurons from both isogenic panels, it can be concluded that tau depletion can result in neurite outgrowth impairments. However, the phenotype is also contingent on other factors not explored in this thesis and tau depletion alone is inadequate to consistently lead to neurite outgrowth impairments. Based on the data presented in Figure 4.2.3, the presence of tau is not essential for Aβ-induced neurite outgrowth impairments in human iPSC-derived cortical neurons.

Inconsistencies among the cytotoxicity readouts

Three types of Aβ-driven cytotoxicity readouts subject to the same dosage of $A\beta_{1\text{-}42}$ oligomers were presented in Chapters 4.2.3 and 4.2.5: (1) Decreasing number of neurons seen in the neurite tracing data on Day 35, (2) increasing AK luminescence from the iPSC-derived neurons in co-culture with rat astrocytes on Day 80 and (3) increasing number of CC3+ neurons on Day 80. In general, all three experiments concurred with the results in *Mapt-/-* mouse models [242–244] and suggested that the *MAPT-/-* background is also protective of Aβ-driven cytotoxicity in human iPSC-derived cortical neurons albeit with inconsistencies among the readouts.

There were several caveats associated with experiments (1) and (2). In experiment (1), only a subset of neurons were imaged thus the data were accompanied with reduced sample size (< 100 neurons per well). Since the neurite tracing experiment was designed to measure outgrowth, the images were captured soon after final plating with relatively immature

neurons. Neuronal loss based on the GFP expression is also considered an acute phenotype without taking the rest of the neurons, which might still be undergoing apoptosis, into account. In experiment (2), the AK luminescence readout was derived from the entire well including the confluent layer of rat astrocytes which existed in a larger number as compared to the neurons (4,000 neurons vs more than 8,000 astrocytes). The data in Figure 4.2.5C therefore appeared less distinct among the *MAPT* genotypes, most likely due to the presence of AK released from rat astrocytes masking the differential effects of the *MAPT* genotypes from the smaller population of neurons. As such, experiment (3) emerged as the most sensitive readout among the three and the ability to differentiate distinct levels of Aβ-driven cytotoxicity was reflected in Figure 4.2.5B. Experiment (3) involved aged iPSC-derived neurons, apoptosis-specific marker, and human neuron-specific regions of interest to accurately capture the neurons undergoing apoptosis without including the rat astrocytes surrounding them.

Mechanisms of mitochondrial transport along axons

There were no differences in the ratios of motile mitochondria shown in Figure 4.2.7 between the Exon 4 *MAPT*+/+ and *MAPT*-/- neurons in agreement with previous reports on mouse primary hippocampal neurons [247,248]. Additionally, the loss of tau was sufficient to prevent Aβ-induced reduction in the ratios of motile mitochondria (Figure 4.2.8) in human iPSC-derived neurons like what was observed in mouse primary hippocampal neurons.

Contrary to those studies, the *MAPT*-/- neurons displayed reduced retrograde speed as well as greater anterograde displacement of mitochondrial transport along axons as compared to

the *MAPT+/+* neurons. It is worth noting that the mean speed of mitochondrial movement presented in Figures 4.2.7 and 4.2.8 does not entail directionality as mitochondria often change their directions of movement and halt their movements intermittently along axons. The differences in mean speed hence do not necessarily translate into mitochondrial displacement which is a unidirectional measure between the beginning and the end of transport of a motile mitochondrion. Therefore, mitochondrial displacement is considered the primary outcome of mitochondrial transport in this study as mitochondrial displacement describes whether a mitochondrion ultimately arrives at its intended destination despite any fluctuations in speed.

Kinesin and dynein protein families are two main motor proteins involved in anterograde and retrograde axonal transport, respectively [342,343]. In axons, kinesin-1 and cytoplasmic dynein had been implicated specifically for mitochondrial transport [344] while it has been demonstrated before that tau preferentially inhibits kinesin instead of dynein [166] and hinders anterograde axonal transport [345,346]. The results presented in Figure 4.2.7 demonstrating that tau depletion led to an increase in anterograde mitochondrial displacement go in line with the view that the presence of tau inhibits kinesin function and thus anterograde axonal transport. Moreover, the preliminary data in Figure 4.2.9A suggest that the changes in mitochondrial transport due to tau ablation are linked primarily to the transport mechanisms instead of mitochondrial function. However, it remains unresolved if the reduction in the number of motile mitochondria caused by extrinsic Aβ directly resulted in decreasing mitochondrial membrane potential seen in Figure 4.2.9B or vice versa and if the protective effects in mitochondrial transport in the *MAPT-/-* neurons directly influence mitochondrial functions or vice versa.

Chapter 5: Synaptic and electrophysiological phenotypes of *MAPT*-/- iPSC-derived cortical neurons

5.1 Introduction

Neuronal functionality involves a network of cells capable of generating electrical currents and performing inter-neuronal signal transmission via synapses. As such, active neurons differentiated *in vitro* are deemed capable of generating action potentials (AP), forming synapses, and receiving presynaptic inputs from neighbouring neurons. Apart from being implicated in the cellular phenotypes discussed in Chapter 4, tau is also required in various electrophysiological aspects as in the capability to generate and relay electrical signals in neurons.

The localisation of endogenous tau in synapses is disputed with conflicting prior reports demonstrating that tau could not be found in synapses in mouse brains [347] while others proved that endogenously phosphorylated tau could physically interact with synaptic proteins [348]. Yet, a considerable number of studies have indicated that tau is heavily involved in neuronal and synaptic functions. Both wild-type and pathogenic tau bearing mutations can physically bind to synaptic vesicles [168] and the association with the latter causes presynaptic dysfunction mediated by synaptogyrin-3 [169] which is a protein localised in synaptic vesicle membrane. Acute downregulation of tau expression in mouse hippocampal neurons reduced synaptic density [349] and caused memory and learning deficits [350], all in all indicating tau's presence in synapses. Furthermore, alterations in BDNF-induced plasticity [349], long-term depression (LTD) [236], and AP firing [231] were observed in *Mapt-/-* mice.

Similar to the cellular phenotypes discussed in Chapter 4, differential responses in functional activities to Aβ due to the absence of tau expression had been demonstrated before in *Mapt-/-* animal models. Aβ and tau cooperate to result in hyperactivity and downregulation of synaptic genes that were reversed by lowering tau expression [198]. This interaction extends to their pathogenic mutant forms where crossing mice with mutations in *APP* and *PSEN1* genes and mice with a P301L mutation in *MAPT* compounded both amyloid plaque pathology and tau propagation in the brain [200]. However, tau depletion protected the mice from excitotoxicity [171], long-term potentiation (LTP) impairment [237], synapse loss [246], and finally memory deficits [234].

5.1.1 Aims of this chapter

In Chapter 5, I aim to:

- Establish the effects of tau ablation in synapse formation and electrophysiological activities
- Determine if the *MAPT-/-* background is protective against Aβ-induced synapse loss and electrophysiological alterations

5.2 Results

5.2.1 Experimental design - synapse imaging by ICC

To measure synaptic density in iPSC-derived cortical neurons, I probed the fixed samples with a presynaptic (Synapsin I/II) and a postsynaptic (Homer1) marker each to identify a

synapse when both markers exist in apposition within the regions of interest labelled by a dendritic marker (MAP2) (Figure 5.2.1A; Chapter 2.13). The total number of synapses was then normalised to the total MAP2+ area to derive synaptic density or more literally as the number of synapses per MAP+ area.

The Exon 1 *MAPT*+/+ line was used to trial for the toxic effects by $A\beta_{1-42}$ oligomers on synaptic density since the Exon 1 isogenic panel was generally less susceptible to extrinsic Aβ insult seen in Chapter 4. There was consistent synapse loss when the neurons were exposed to 10 μM of $A\beta_{1-42}$ oligomers relative to the scrambled $A\beta_{1-42}$ peptides at the same concentration for 24 h (Figure 5.2.1B). Other types of extrinsic Aβ insults derived from post-mortem AD brain tissue (AD brain homogenate and AD brain-derived Aβ) were also used in Chapter 5.2.2 and the exposure time was maximised to 5 days without a media change since the concentration of Aβ was relatively low as compared to synthetic Aβ peptide-derived oligomers.

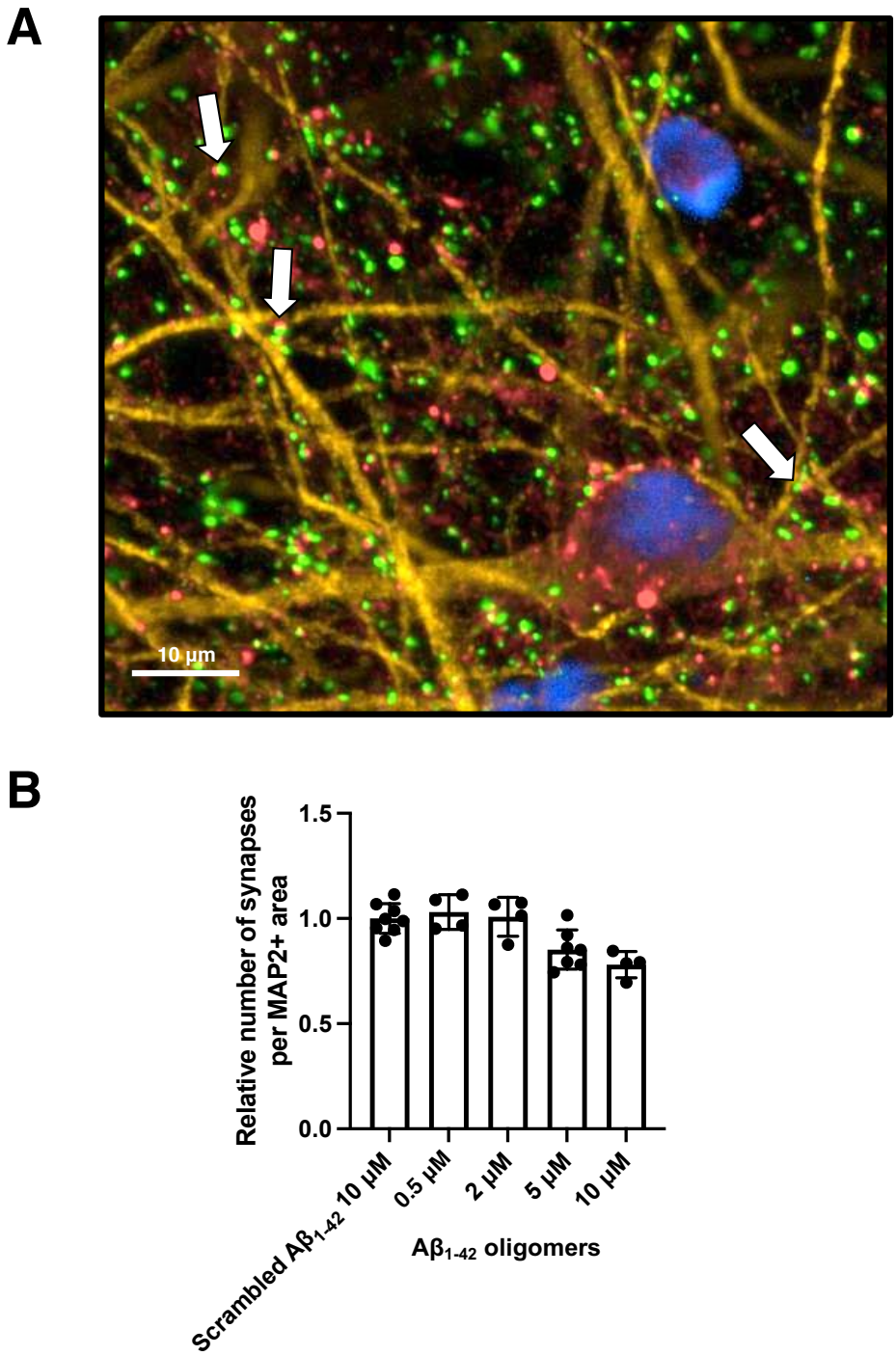


Figure 5.2.1: Synapse imaging by ICC
(A) Representative image of Day 84 iPSC-derived cortical neurons from the Exon 4 *MAPT*+/+ line probed with a presynaptic (Synapsin I/II; green), postsynaptic (Homer1; red), dendritic (MAP2; yellow) and human nucleus (blue) markers. White arrows indicate the identification of synapses with both Synapsin I/II and Homer1 markers existing in apposition within proximity.
(B) Quantification of synapse loss in Day 89 iPSC-derived cortical neurons from the Exon 1 *MAPT*+/+ line subject to 24 h of $A\beta_{1-42}$ oligomers treatment at a range of concentration relative to 10 µM of scrambled peptide treatment. Mean ± SD. N = 4 to 8 replicate wells. No statistical analysis was performed as the data were derived from a single neuronal differentiation.

5.2.2 Synaptic density and loss in *MAPT-/-* neurons caused by extrinsic Aβ insults

Before assessing electrophysiological properties in both isogenic *MAPT-/-* panels of iPSC-derived cortical neurons, I first investigated synapse formation in these neurons by imaging after conducting ICC with both pre- and postsynaptic markers. No differences in synaptic densities were observed among the *MAPT* genotypes in aged iPSC-derived cortical neurons (Figure 5.2.2A). Next, the neurons were treated with 5 or 10 μM of $A\beta_{1-42}$ oligomer for 24 h to elicit synapse loss. The *MAPT*+/+ neurons in both isogenic panels experienced significant decreases (20 to 30% reduction) in synaptic density relative to the scrambled peptide control with 10 μM of $A\beta_{1-42}$ oligomer but not with the 5 μM group (Figure 5.2.2B). However, both *MAPT*+/- and *MAPT-/-* neurons also underwent marked synapse losses treated with 10 μM of $A\beta_{1-42}$ oligomer in both isogenic panels indicating that the absence of tau could not protect the neurons from $A\beta_{1-42}$ oligomer-induced synapse losses.

I then opted for a more physiological/pathological source of extrinsic Aβ insult by deriving AD brain homogenate from post-mortem temporal cortical tissues. Both $A\beta_{1-40}$ and $A\beta_{1-42}$ were present in the AD brain homogenate, but only at low levels in Aβ immunodepleted (ID) and healthy brain homogenates (Chapter 2.9) which were potential alternatives as treatment controls. Contrary to the synapse losses elicited by $A\beta_{1-42}$ oligomers, AD brain homogenate at 1-in-8 dilution (approx. 58 pM of $A\beta_{1-40}$ and 8 pM of $A\beta_{1-42}$) was less consistent in causing synapse loss in the *MAPT*+/+ neurons relative to the aCSF (vehicle) control (Figure 5.2.2C). The removal of Aβ was insufficient to rescue the synapse losses caused by the AD brain homogenate in the *MAPT*+/+ neurons. Conversely, the healthy brain homogenate did not result in significant decreases in synaptic density in the *MAPT*+/+ neurons from both

isogenic panels. The results in the *MAPT*+/+ neurons suggest that all the soluble factors combined present in the AD brain homogenate other than Aβ itself might have a more dominant role in eliciting synapse loss. When the *MAPT*+/- and *MAPT*-/- neurons are considered, there is no discernible trend in synapse loss or protection compared to the *MAPT*+/+ neurons within or across the isogenic panels.

The variability in the synapse loss results due to the AD brain homogenate treatment prompted further validations on Aβ-induced synapse loss with or without the presence of tau expression. The Aβ captured during the immunodepletion procedure (Chapter 2.9.1) was eluted and concentrated to obtain AD brain-derived Aβ, with which the neurons were treated for 5 days before probing for synapses. Consistent, though relatively subtle (< 20% reduction), synapse loss was recorded over three differentiation repeats treated with 200 pg/mL (approx. 45 pM of Aβ) of AD brain-derived Aβ in the Exon 4 *MAPT*+/+ neurons however synapses in both the *MAPT*+/- and *MAPT*-/- neurons were not affected by the extrinsic Aβ insult (Figure 5.2.2D). Similarly, the preliminary results over two differentiation repeats in the Exon 1 panel indicated comparable trend resembling the data from the Exon 4 panel. The Exon 1 *MAPT*+/+ neurons incurred a subtle but consistent synapse loss (10% reduction) over two differentiation repeats whereas the Exon 1 *MAPT*-/- and *MAPT*+/- lines were unaffected by the AD brain-derived Aβ insult relative to the control treatment in two independent experiments. Taken together, various types of extrinsic Aβ insult could cause synapse losses in aged iPSC-derived cortical neurons. Yet, the AD brain-derived Aβ, which is the closest form of Aβ insult *in vitro* to the pathological Aβ species in an AD brain, was the only type of extrinsic Aβ insults tested that could demonstrate protection in the *MAPT*-/- neurons from Aβ-driven synapse loss.

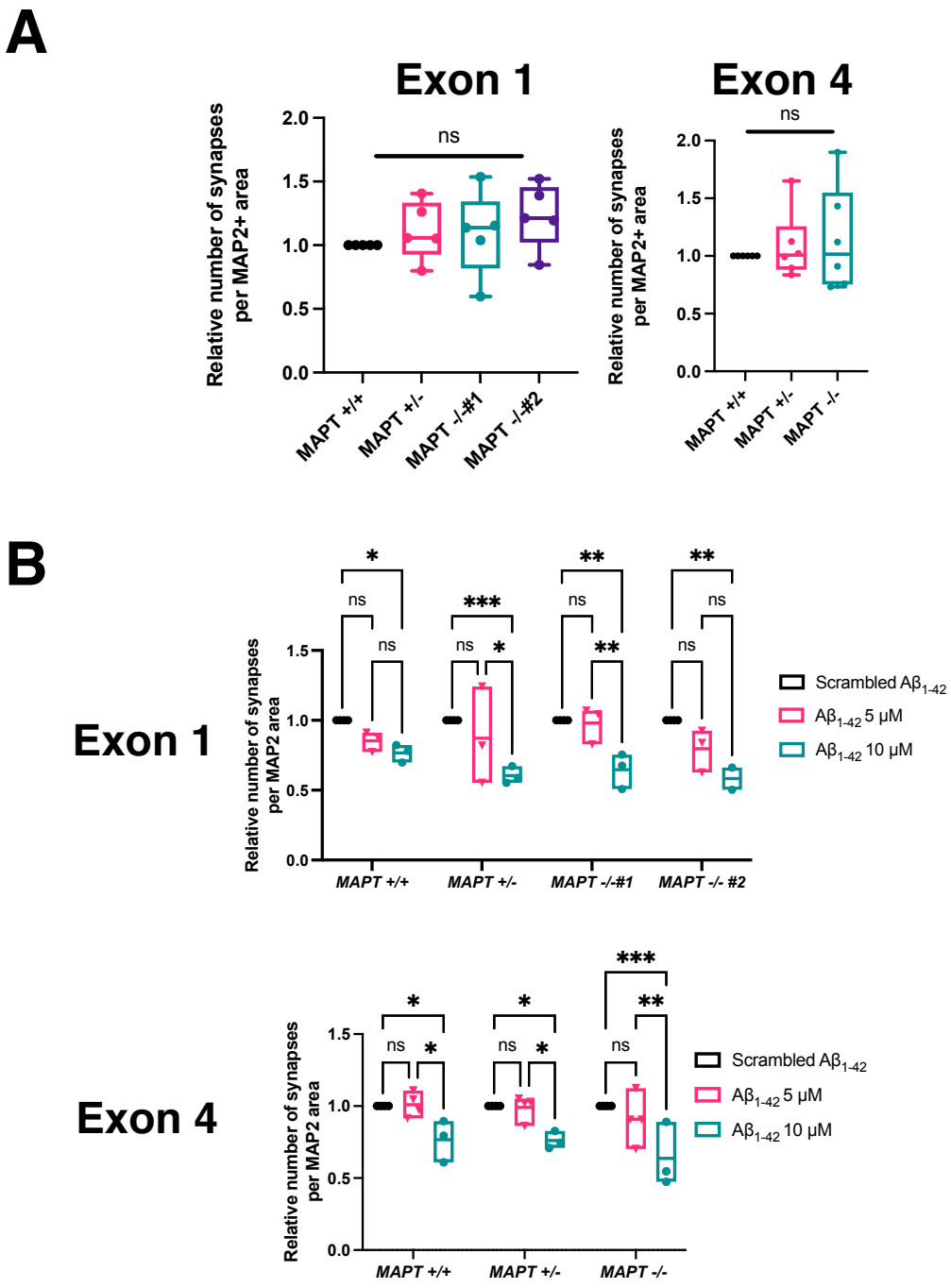
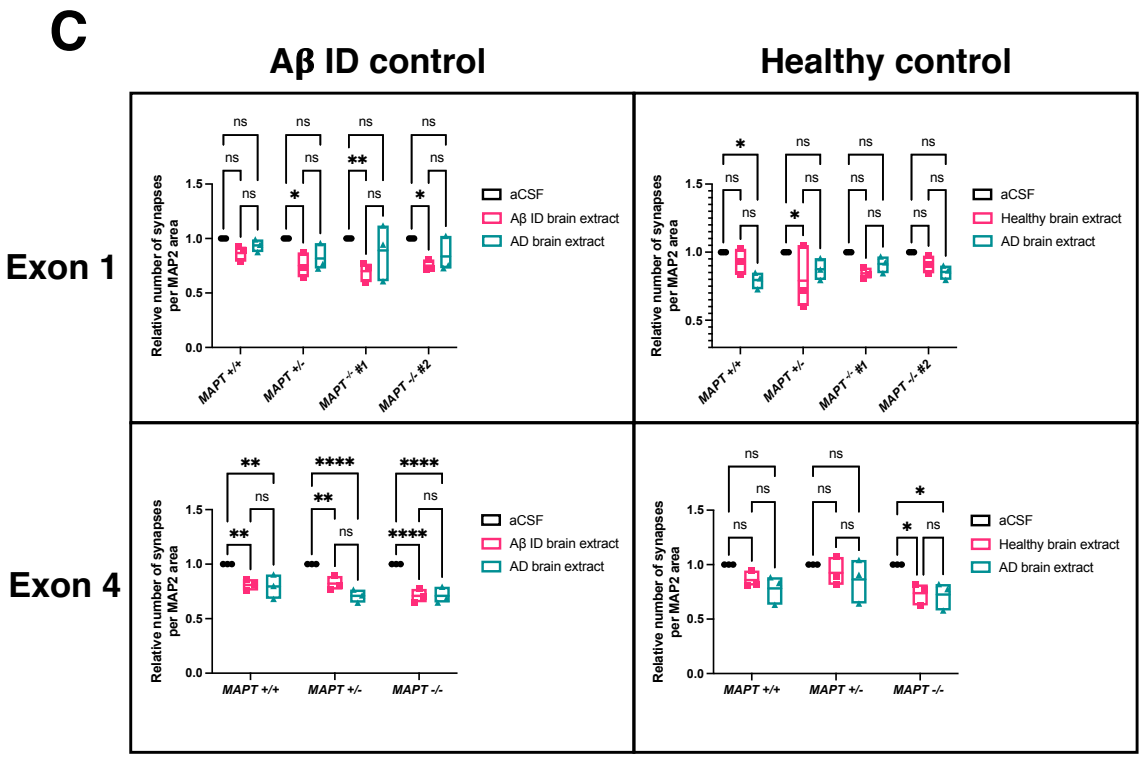
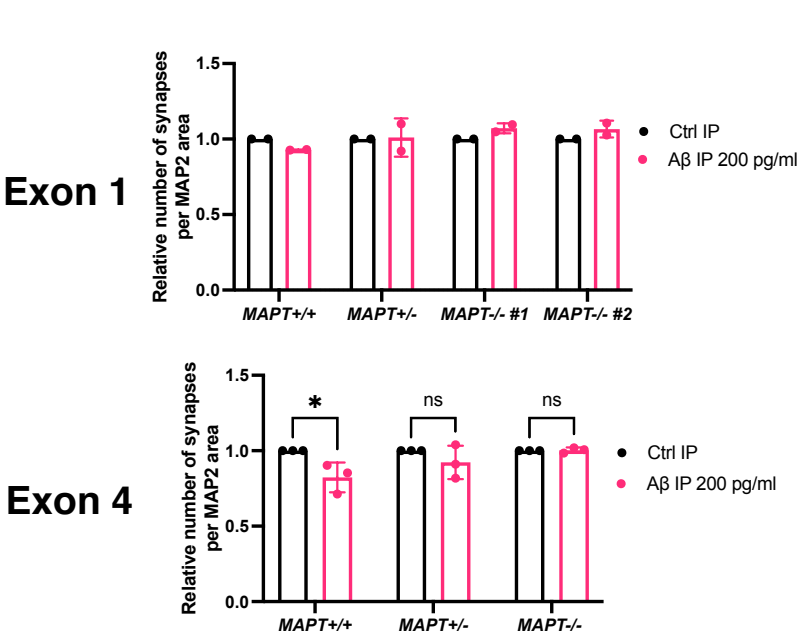


Figure 5.2.2: Quantifications of synaptic density and synapse loss in both isogenic panels of *MAPT-/-* iPSC-derived cortical neurons

(A) Boxplots of relative synaptic density at baseline to the respective *MAPT+/+* line in Day 74-89 iPSC-derived cortical neurons. Median ± range and box boundaries denote interquartile range. N = 5 independent neuronal differentiation repeats. Kruskal-Wallis test with Dunn's multiple comparison correction was used for the statistical analysis.

(B) Relative synapse loss due to 24 h of 5 and 10 µM of $A\beta_{1-42}$ oligomer treatments relative to the scrambled peptide treatment within each line in Day 74-89 iPSC-derived cortical neurons. Mean ± range. N = 3 independent neuronal differentiation repeats. Two-way ANOVA with Tukey's multiple comparison correction was used for the statistical analysis.





(C) Relative synapse loss due to 1-in-8 (i.e., 12.5% v/v) AD brain, Aβ immunodepleted (ID) brain and healthy brain homogenates for 5 days relative to the aCSF (vehicle) treatment in Day 74-89 iPSC-derived cortical neurons. Mean ± range. N = 3 independent neuronal differentiation repeats. Two-way ANOVA with Tukey's multiple comparison correction was used for the statistical analysis.

(D) Relative synapse loss due to 5 days of 200 pg/ml of AD brain-derived Aβ treatment in Day 79-86 iPSC-derived cortical neurons relative to the same volume of eluate using control immunoprecipitation with normal mouse IgG. Mean ± SD. N = 2 (Exon 1) or 3 (Exon 4) independent neuronal differentiation repeats. Two-way ANOVA with Šídák's multiple comparison correction was used for the statistical analysis for the Exon 4 panel only as there were three independent neuronal differentiation repeats.

5.2.3 Experimental design - electrophysiology by MEA

To measure electrophysiological activities in aged iPSC-derived cortical neurons, I seeded the neurons in MEA plates as depicted in Figure 5.2.3. The neurons were first seeded as a droplet on Day 32 (Chapter 2.4.1) at high density onto the electrodes (15,000 neurons per 5 µL droplet: approximately 200,000 neurons/cm^2) before settling and rat astrocytes were then added into the droplet directly to prevent the seeded cells from having contact with the ground electrodes. The neurons were then aged until around Day 90 of the neuronal differentiation where the baseline recording was taken without any treatments, before the neurons were treated with extrinsic Aβ insults and their functional activities measured over 5 days. Due to the well number constraint, only one of the Exon 1 *MAPT-/-* lines (*-/- #1*) was selected for the MEA experiments.

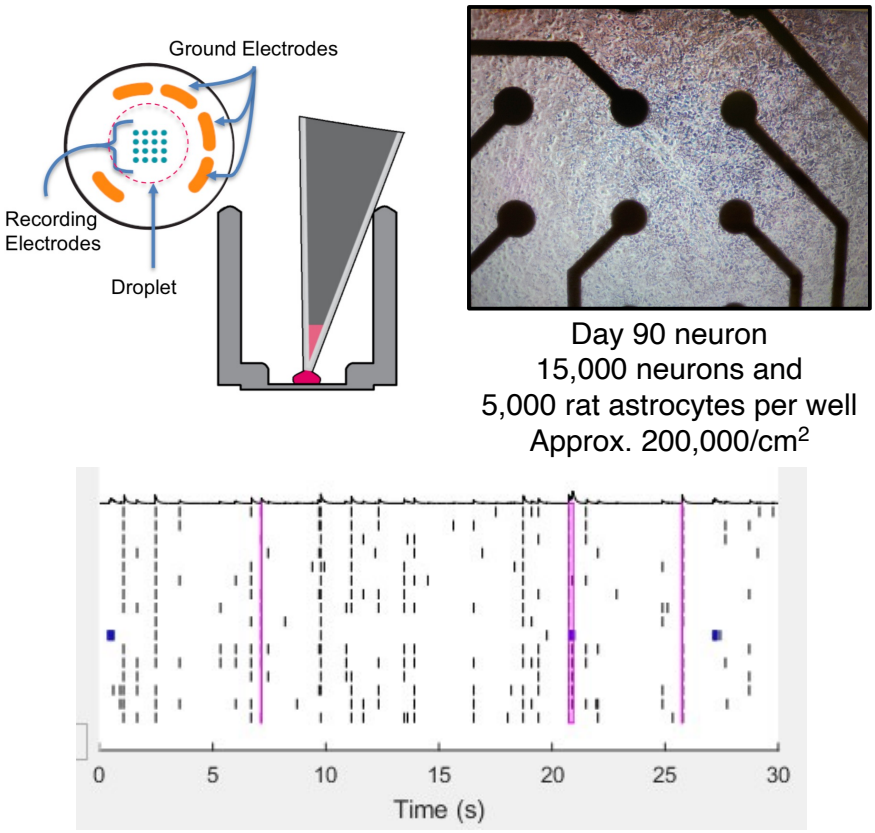


Figure 5.2.3: Representative images of the MEA system
MEA plate well format extracted from the equipment manual from Axion Biosystems, iPSC-derived cortical neurons seeded in a MEA well under brightfield and an example raster plot depicting a 30-second trace of spike detections.

5.2.4 Action potential firing in *MAPT-/-* neurons measured by MEA

Having established that synapse formation is unaffected by the lack of tau expression, I then measured the levels of electrophysiological activity in aged iPSC-derived cortical neurons using an MEA system in a multi-well format. The electrodes embedded in the wells of the MEA plates detect extracellular field potentials in the form of spiking events which are considered putative AP from the neurons in contact with the electrodes. In this thesis, those spiking events are referred to as putative AP generated from the iPSC-derived neurons, but it is essential to discern the MEA system used in the experiments does not directly measure AP. Four AP parameters were chosen for investigation, namely the (1) amplitude indicating the strength of AP, (2) firing frequency indicating AP recurrence, (3) synchrony index indicating the closeness in AP timing among the electrodes within a 20-ms window and (4) network burst frequency indicating the recurrence of repetitive (at least 50 spikes across all electrodes with inter-spike intervals less than 100 ms) and coordinated AP firings among the electrodes. Network activity is defined by the proprietary AxIS software (Axion Biosystems) as the functional activity with at least 6 participating electrodes.

In the *MAPT*+/+ neurons from both isogenic panels, spike amplitudes between 21.5 and 24.5 μV were recorded (Figure 5.2.4A) and they were considerably lower (approximately 1,000-fold lower) than a typical AP recorded intracellularly. The *MAPT*+/+ neurons also displayed AP firing frequency at around 2 Hz and synchrony index between 0.5 and 0.75 with the value of 1 denoting a perfectly synchronous firing pattern among the electrodes. The network burst frequency recorded was noticeably lower than the AP firing frequency in individual electrodes, suggesting that most spiking events were sporadic and a coordinated network activity only occurred on average every 12.5 to 16.7 s.

All AP parameters recorded were markedly lower in the *MAPT-/-* neurons from both isogenic panels (Figure 5.2.4A), indicating that tau deletion leads to lower functional activities in iPSC-derived cortical neurons with weaker propensity to generate AP. When the data were plotted relative to the *MAPT*+/+ neurons to normalise across the AP parameters, it became evident that the suppressed levels of functional activity due to the absence of tau expression were significantly more pronounced in the Exon 1 *MAPT-/-* neuron as compared to that of the Exon 4 line (Figure 5.2.4B). Overall, the results showed that the iPSC-derived cortical neurons aged until Day 90-100 of the neuronal differentiation were electrophysiologically active by generating AP and the capability of which was considerably dampened in the *MAPT-/-* neurons.

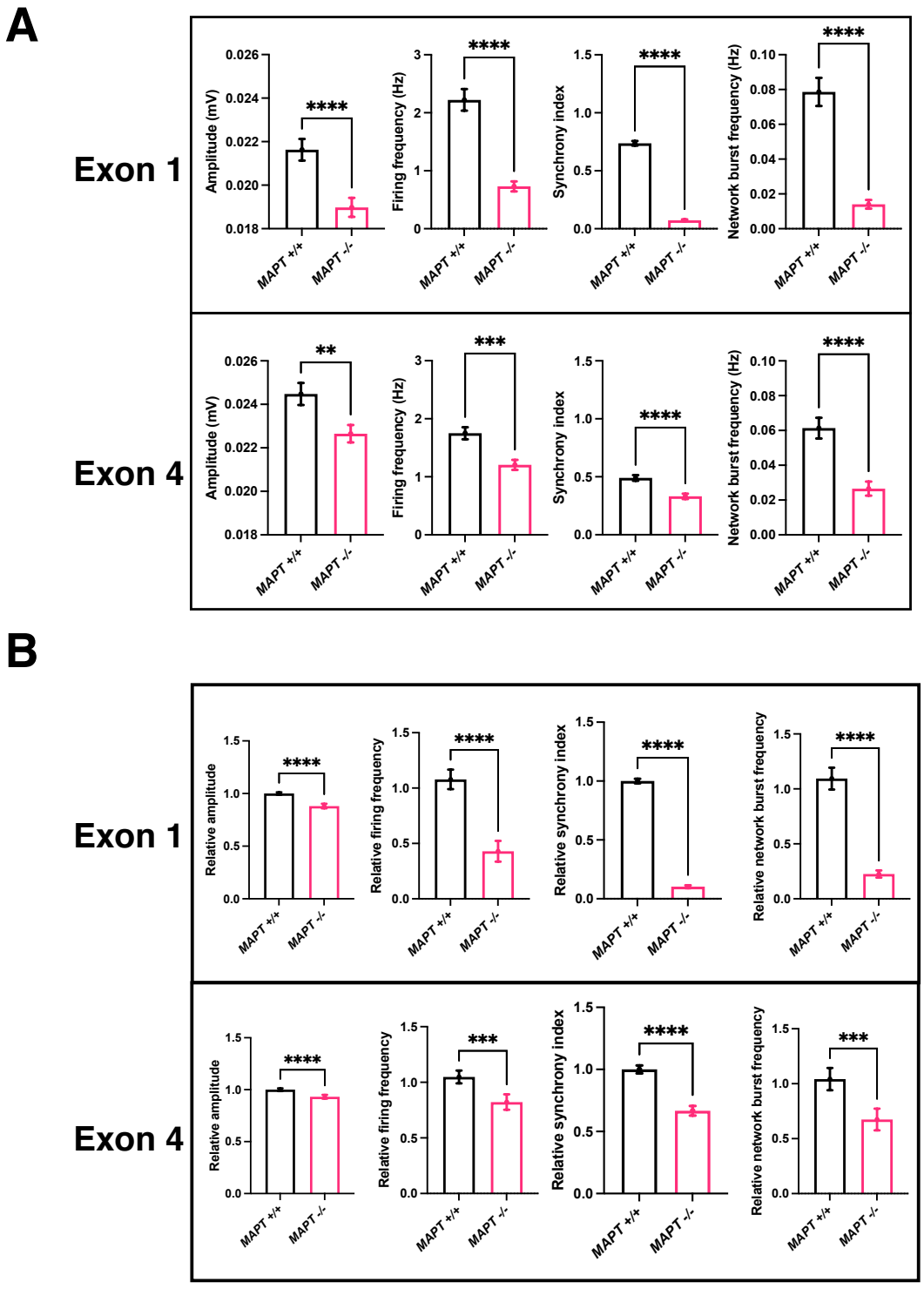


Figure 5.2.4: Quantification of baseline AP parameters measured by MEA assay in Day 90-100 iPSC-derived cortical neurons from both *MAPT*-/- isogenic panels
(A) Absolute readouts of baseline AP parameters.
(B) Relative readouts of baseline AP parameters to individual *MAPT*+/+ lines.
Mean ± SEM. N = 53-55 (Exon 1 *MAPT*+/+) or 51-53 (Exon 1 *MAPT*-/-) wells across 3 independent neuronal differentiation repeats; 101-105 (Exon 4 *MAPT*+/+) or 103-114 (Exon 4 *MAPT*-/-) wells across 6 independent neuronal differentiation repeats. Mann-Whitney test was used for the statistical analysis for all bar graphs in this figure.

5.2.5 Action potential firing changes caused by extrinsic Aβ insults

Next, I asked if the lack of tau expression could result in protection against extrinsic Aβ in aged iPSC-derived cortical neurons. It was previously reported that AD brain homogenate like the one used in Chapter 5.2.2 could lead to LTP impairment in mouse hippocampal slices, and that Aβ immunodepletion could effectively rescue the LTP deficit [351]. The study proved that Aβ in the AD brain homogenate played a dominant role in plasticity in mice. Hence, I first set out to examine if the AD brain homogenate could likewise result in functional changes measured by the MEA assay, and if there are differential responses in the *MAPT-/-* neurons.

The *MAPT+/+* neurons experienced close to a 3-fold increase in AP firing frequency and 8-fold increase in network burst frequency relative to the aCSF (vehicle) treatment control (Figure 5.2.5A) when they were treated with AD brain homogenate at 1-in-4 dilution (approximately 117 pM of $A\beta_{1-40}$ and 17 pM of $A\beta_{1-42}$) for 5 days, causing the neurons to be hyperactive. Importantly, the removal of Aβ in the immunodepleted AD brain homogenate was sufficient to abolish the increases down to a level equivalent to the aCSF (vehicle) treatment control thus preventing the neurons from becoming hyperactive due to the AD brain homogenate treatment. The AP amplitude and synchrony index remained relatively stable regardless of the presence of Aβ in the AD brain homogenate. The same AD brain homogenate treatments, on the other hand, did not result in any increments in AP firing frequency or network burst frequency in the *MAPT-/-* neurons over 5 days (Figure 5.2.5A). Taken together, the data in Figure 5.2.5A demonstrate that Aβ in the AD brain homogenate caused the iPSC-derived cortical neurons to be hyperactive and the phenotype was dependent on tau expression.

To further validate the effects of extrinsic Aβ insult on functional activities, I treated the iPSC-derived cortical neurons with 10 μM of $A\beta_{1-42}$ oligomers and measured the changes in AP over 5 days post-treatment. Contrary to the effects caused by the AD brain homogenate, $A\beta_{1-42}$ oligomers generally led to downregulation of AP parameters in the neurons over 5 days of exposure (Figure 5.2.5B). The $A\beta_{1-42}$ oligomers treatment resulted in decreasing AP firing frequency in the *MAPT*+/+ neurons relative to the scrambled peptide control (up to 30% and 70% decreases in the Exon 1 and 4 lines, respectively). There were indications of protective effects in the Exon 4 *MAPT*-/- neurons especially around 3 days post-treatment where the AP firing frequency did not drop below the levels seen in the scrambled peptide control, but the differential responses in the Exon 1 line was more modest and not statistically significant. Overall, the $A\beta_{1-42}$ oligomers treatment caused the neurons to lose network activity and synchronicity but not AP amplitude. There was otherwise no consistent trend of differential responses to $A\beta_{1-42}$ oligomers due to the loss of tau expression.

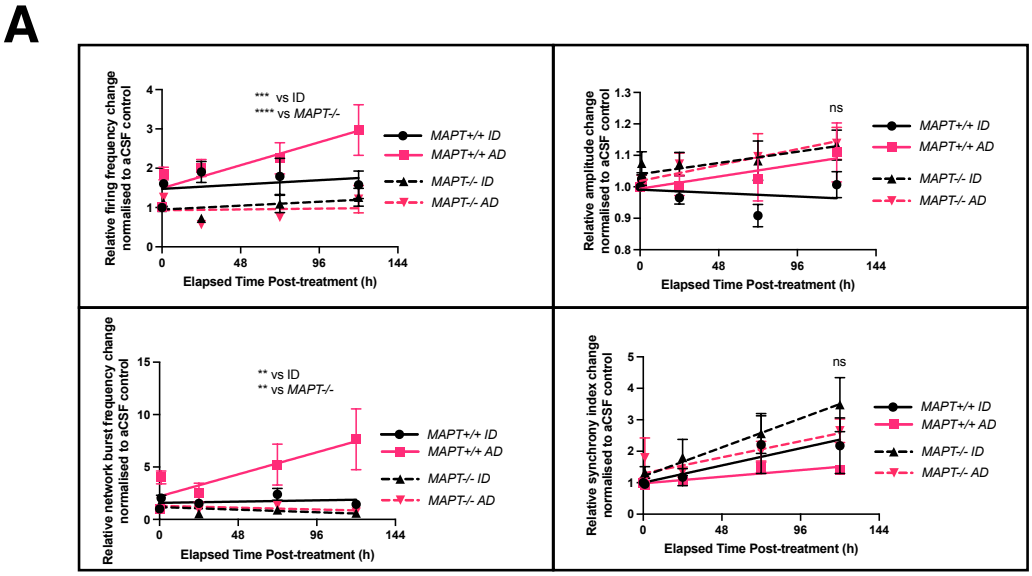
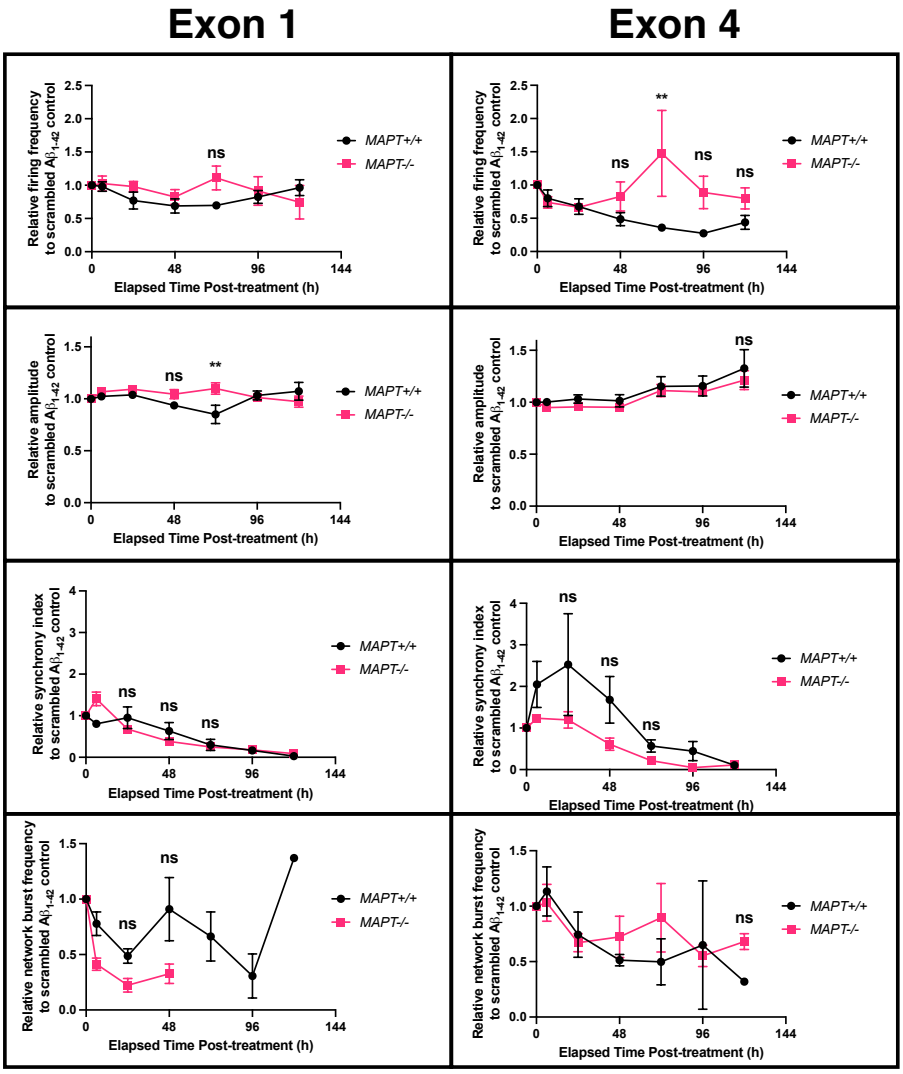


Figure 5.2.5: Quantification of AP parameters under the exposure to extrinsic Aβ insults in Day 90-100 iPSC-derived cortical neurons
(A) Time course quantification of AP parameters in neurons treated with 1-in-4 (i.e., 25% v/v) dilution of the AD and Aβ ID brain homogenates relative to the aCSF (vehicle) treatment control over 5 days in the Exon 4 isogenic panel. Mean ± SEM. N = 3 independent neuronal differentiation repeats. Two-way ANOVA with Tukey's multiple comparison correction was used for statistical analysis. Statistical significance of the 120 h-elapsed data was marked on the figure.

B



(B) Time course quantification of AP parameters in neurons treated with 10 μM of $A\beta_{1\text{-}42}$ oligomer relative to 10 μM of scrambled $A\beta_{1\text{-}42}$ peptide treatment control over 5 days from both *MAPT-/-* isogenic panels. Mean ± SEM. N = 3 independent neuronal differentiation repeats. Two-way ANOVA with Šídák's multiple comparison correction was used for the statistical analysis.

5.2.6 Electrophysiological properties in *MAPT-/-* neurons by patch-clamp

To obtain electrophysiological data at a single-cell level, I conducted patch-clamp experiments on the iPSC-derived cortical neurons. There was no observable difference in resting membrane potential between the Exon 1 and 4 *MAPT*+/+ neurons, as well as among the *MAPT* genotypes in the Exon 1 isogenic panel (Figure 5.2.6A). The resting membrane potentials were recorded on average at -50 mV, which was higher than the expected -70 mV *in vivo* but consistent with what was reported using similar neuronal culture systems [332]. The neurons were then held at – 70 mV and subject to 1 μM TTX for the measurement of spontaneous mEPSC. The preliminary data from one differentiation showed that there was higher mEPSC frequency recorded in the *MAPT-/-* neurons as compared to the *MAPT*+/+ neurons without concomitant changes in amplitude (Figure 5.2.6B). The current observation suggests that tau depletion can result in higher presynaptic vesicle release probability [352] given that the lack of tau expression does not alter synapse formation (Figure 5.2.2A).

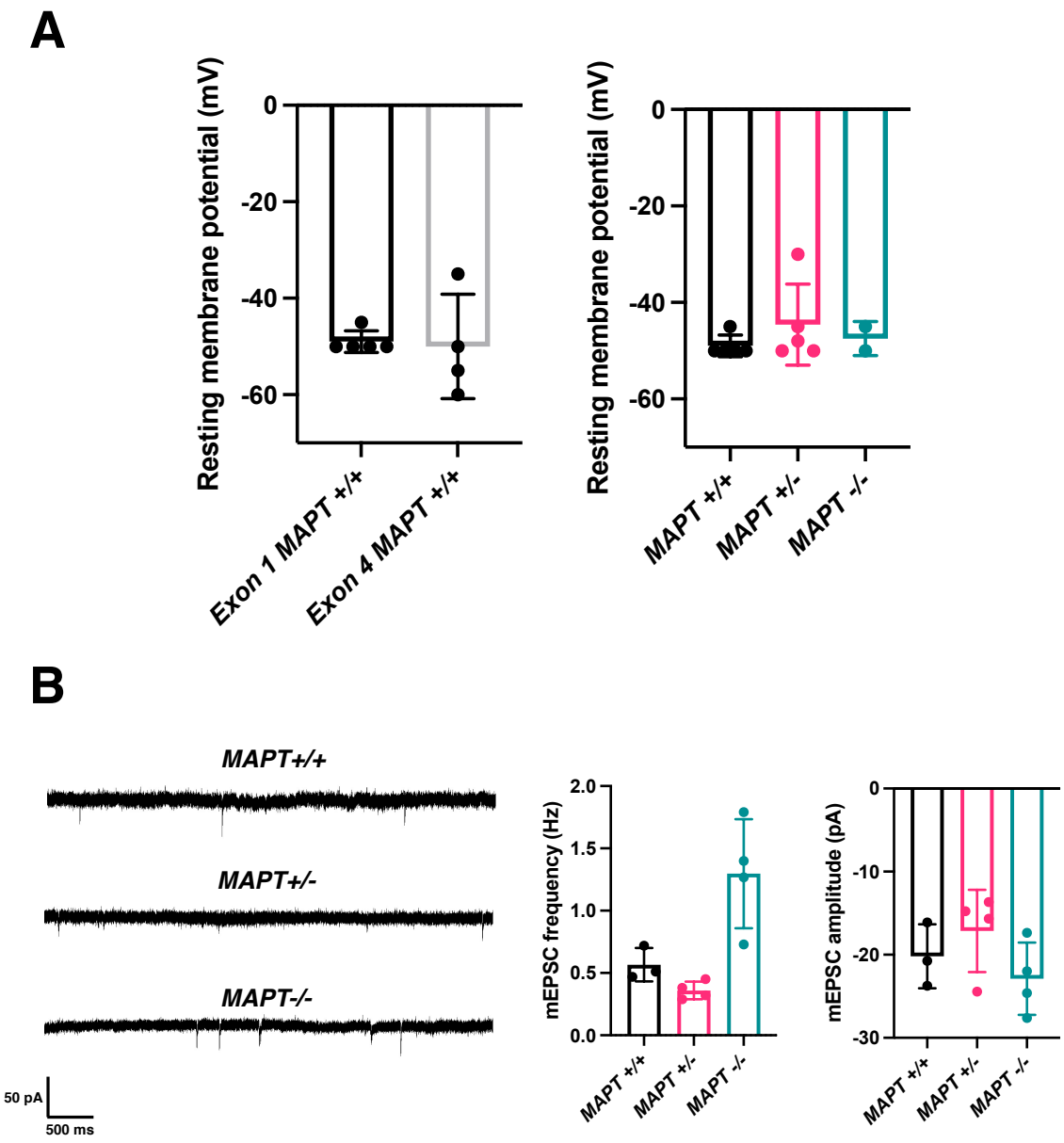


Figure 5.2.6: Electrophysiological properties by patch-clamp in aged iPSC-derived cortical neurons from the *MAPT-/-* isogenic panels
(A) Resting membrane potential quantification comparison between the Exon 1 (Day 96-104) and 4 (Day 83-104) *MAPT*+/+ iPSC-derived cortical neurons, as well as among the *MAPT* genotypes in the Exon 1 isogenic panel. N = 4 (Exon 4 *MAPT*+/+), 5 (Exon 1 *MAPT*+/+ and *MAPT*+/-) or 2 (Exon 1 *MAPT-/-*) neurons from 1 neuronal differentiation repeat. Mean ± SD.
(B) Representative traces and quantification of mEPSC in Day 83-104 iPSC-derived cortical neurons from the Exon 4 isogenic panels. N = 3 (*MAPT*+/+) or 4 (*MAPT*+/- and *MAPT-/-*) neurons from 1 neuronal differentiation repeat. Mean ± SD. No statistical analysis was performed as the data were derived from a single neuronal differentiation in this figure.

5.3 Discussion

Evaluating electrophysiological properties in the MAPT-/- neurons

The results in Chapter 5 reveal that removing tau expression from aged iPSC-derived neurons leads to reductions in AP firing both in amplitude and frequency, network activity and synchronicity among the population of neurons *in vitro* while expressing similar number of synapses. Furthermore, the preliminary data from the patch-clamp experiment indicate that tau depletion leads to an increase in presynaptic vesicle release frequency without a change in postsynaptic responses while the levels of resting membrane potential remained comparable regardless of the *MAPT* genotypes.

Consistent with the data presented in Chapter 5.2.4, the reduction in AP frequency was recently described in a *Mapt-/-* mouse model [231]. The reduction in axon initial segment (AIS) length and shift in AIS location further from the soma in the pyramidal cells were demonstrated in the *Mapt-/-* mice as the mechanism underlying the drop in AP frequency. There were also evidence in the same report suggesting that the *Mapt-/-* neurons were less prone to hypersynchrony after artificially eliciting over-excitation in the neurons. This observation led to the proposal explaining why *Mapt-/-* mice were shown to be protected from seizure occurrence and epilepsy [234,353,354], which were evident in an AD mouse model displaying early hypersynchronous network activity [355]. Indeed, the human *MAPT-/-* iPSC-derived cortical neurons displayed lower synchrony readouts at baseline in agreement with the phenotypes seen in the mouse studies. It is therefore debatable if the diminished AP readouts are considered as functional deficits since many electrophysiological abnormalities caused by Aβ in mice could be rescued by the *Mapt-/-* background [356]. Generally, tau ablation in mice does not lead to any overt cognitive

deficits [224,227,234,252] unless the mice have been aged for at least 12 months [229,230,357].

Recordings from both MEA and patch-clamp experiments were included in Chapter 5 and these two electrophysiological assays are distinct from each other in the readouts they deliver. MEA system detects field potentials from multiple neurons at once with higher throughput and temporal information is available from the same neurons. However, as compared to patch-clamp experiments, MEA does not offer single-cell resolution and is limited with a single type of electrophysiological property derived from extracellular field potentials.

In Chapter 5.2.6, spontaneous mEPSC was deliberately selected to be the AP-independent electrophysiological property of interest by patch-clamp to avoid data duplication with the MEA results as the mEPSC data were recorded while the sodium channels were blocked by TTX. The increase in mEPSC frequency observed in the human *MAPT-/-* iPSC-derived cortical neuron contradicts previous reports in *Mapt-/-* hippocampal brain slices/neurons between 1-6 months of age where both mEPSC frequency and amplitude remained unchanged regardless of the *Mapt* dosage [171,253,256,358] except for one study [359]. However, the said study demonstrated hyperpolarised resting membrane potential and reduced mEPSC frequency instead in *Mapt-/-* hippocampal granule cells. Taken together, the results from prior *Mapt-/-* mouse studies do not agree with the current findings and further experiments will be needed to validate (1) if the observed discrepancies are reproducible and thus represent a genuine feature particularly in the relatively immature cortical neurons with human genetic background and (2) if they can be potentially explained

by tau's interaction with synaptic vesicle to regulate presynaptic vesicle release mediated by synaptogyrin-3 shown in animal models [168,169].

Divergent effects from various sources of extrinsic Aβ insults

A couple of different sources of extrinsic Aβ insults were used to treat aged iPSC-derived cortical neurons in Chapters 5.2.2 and 5.2.5 and varying conclusions regarding the effects of tau depletion were drawn depending on the type of Aβ insult. In general, no differential responses were observed among the *MAPT* genotypes when more acute and toxic synthetic $A\beta_{1-42}$ oligomers were used at a relatively high concentration. On the other hand, protective effects due to the loss of tau expression could be distinguished when more chronic and milder AD brain-derived treatment options were used with a much lower Aβ concentration. Based on the data, it is likely that synapse loss and AP changes are comparatively more sensitive to Aβ exposure with more subtle phenotypes when tau's involvement is concerned as opposed to harsher subcellular events like apoptosis.

It was demonstrated in Chapter 5.2.2 that $A\beta_{1-42}$ oligomers, AD brain homogenate, Aβ immunodepleted AD brain homogenate, and healthy brain homogenate could all result in synapse loss regardless of tau expression levels in aged iPSC-derived cortical neurons. These results suggest that while synthetic $A\beta_{1-42}$ oligomers could elicit synapse loss, soluble factors other than Aβ in the brain homogenates were dominant in leading to the synapse loss observed. Although the immunodepletion procedure removed almost all the Aβ (and proteins bound to it) present in the AD brain homogenate (Figure 2.9.2), it is important to consider that Aβ is merely ~ 0.08% of the total protein in the AD brain homogenate (based

on the AD brain homogenate protein concentration at around 3 mg/ml measured by BCA assay). Yet, synapse loss was again evident when the isolated AD brain-derived Aβ was used to treat the neurons indicating that both brain-derived and synthetic Aβ could effectively and consistently elicit synapse loss albeit at a drastically different concentration (pM vs. μM range, respectively). It is possible but unclear as to why that only the Aβ composition more closely resembling AD pathological environment could demonstrate a rescue from synapse loss in the *MAPT-/-* neurons. Another synapse imaging experiment involving lower dosage of $A\beta_{1-42}$ oligomers treatment over 5 days could partially elucidate if the differential responses in the *MAPT-/-* neurons were dependent on the concentration of Aβ although $A\beta_{1-42}$ oligomer treatment at lower concentration might not achieve any synapse loss at all (I speculate that high nM range would be the minimum; Figure 5.2.1B). In fact, a protracted Aβ exposure assay at lower dosage over multiple re-treatments would be ideal in reproducing the typical chronic Aβ-induced toxicity that an AD brain undergoes even though it will be logistically challenging to perform.

On the other hand, the AD brain homogenate treatment caused the neurons to become hyperactive over 5 days of exposure and the Aβ species present in the homogenate appeared to be the dominant factor instead (as opposed to the synapse loss observation) in causing the increase in AP firing since the removal of Aβ abolished the phenotype (Figure 5.2.5A). Indeed, it was previously reported that neighbouring neurons experienced hyperactivity around Aβ plaques in a double transgenic APP23xPS45 AD mouse model expressing both *APP* and *PSEN1* mutants [360]. The current observation with the AD brain homogenate treatment mirrors the data from the laboratory from which the brain homogenate extraction protocol in this thesis is based. It was shown that functional changes (LTP in this case) in

mouse brain slices caused by an AD brain homogenate could be reversed by removing Aβ via immunodepletion [351].

The MEA experiments likewise yielded divergent results with regards to the effects of tau depletion in aged human iPSC-derived cortical neurons depending on the type of extrinsic Aβ used. Like the synapse imaging experiment, the Aβ species which mimic AD pathological environment more closely managed to demonstrate differential responses to Aβ in the *MAPT-/-* neurons i.e., the *MAPT-/-* neurons did not become hyperactive upon the treatment with the AD brain homogenate. However, the $A\beta_{1-42}$ oligomers at 10 μM caused rather aggressive functional deficits in the neurons regardless of their *MAPT* genotypes by reducing AP firing frequency and network activities suggesting that the dosage might be too toxic for more sensitive readouts such as electrophysiology. The high dosage was determined based on the initial MEA assay optimisation data from our laboratory and another local collaborator where $A\beta_{1-42}$ oligomer concentration ranging from 500 nM to 5 μM did not result in any noticeable changes in any AP parameters over 5 days of exposure. Based on the current data, it can be concluded that chronic Aβ treatment with the Aβ species closely mimicking AD pathological context might be the most suitable experimental strategy to cause relevant synaptic and functional responses to Aβ while teasing out subtle differences due to the involvement of tau seen in Figures 5.2.2D and 5.2.5A.

Chapter 6: AD patient iPSC-derived cortical neurons from the DFP pilot cohort

6.1 Introduction

The Deep and Frequent Phenotyping (DFP) study is a multi-centre clinical cohort for prodromal AD participants defined as individuals above 60 years of age displaying mild cognitive impairment with evidence of AD pathology [310]. As the name suggests, a wide range of clinical assessments and biomarker measurements were conducted over multiple time points within a relatively short period (i.e., approximately 10 visits over 12-14 months for various assessments). The DFP cohort is the most detailed clinical outcome and biomarker study to date involving assessments ranging from gait to brain imaging. Prior to the full-scale DFP study recruitment, a pilot cohort involving 20 (after screening and drop-outs) participants with early symptomatic AD was established from December 2014 with the last clinical assessment completed in January 2016. From the pilot cohort, iPSC lines from 13 participants were successfully reprogrammed and used in the experiments described in this Chapter (Table 2.3.2). Accompanying clinical data from the same participants were also available and only a subset of the DFP pilot cohort clinical data relevant to the experiments was used in this thesis as listed in Table 2.3.1.

Modelling AD with patient-derived iPSC lines has been an ongoing effort as elaborated in Chapter 1.4. A number of studies have been published since 2012 utilising sAD patient-derived iPSCs but most of them did not have an emphasis on the clinical outcomes of the patients from whom the iPSC lines were derived [284]. Recently, it was reported that sAD patient-derived neurons could reflect neuropathology and cognitive outcomes of their donors [361]. The study involved 53 iPSC lines and 16 of which were reprogrammed from participants diagnosed with LOAD. The authors demonstrated that cellular phenotypes from

the patient-derived neurons themselves (e.g., levels of secreted Aβ) directly reflect clinical features (e.g., amyloid plaques) of the iPSC donors.

The Experimental Medicine arm of the DFP study aims to integrate cellular and clinical phenotypes by using patient iPSC-derived neurons and taking advantage of the wealth of clinical information from the same patients. The iPSC work involves the DFP study clinical leads and three local research groups focusing on a range of cellular phenotypes *in vitro*, although this thesis includes only the experimental results of the DFP project obtained in our lab. Our hypothesis is that cellular vulnerability in patient iPSC-derived neurons can reflect clinical vulnerability of the same patients. During the first phase of experiments involving the iPSC lines from the DFP pilot cohort, I investigated cellular and clinical vulnerabilities specifically to Aβ.

6.1.1 Aims of this chapter

In this Chapter, I aim to elucidate if:

- The iPSC-derived neurons display vulnerability to extrinsic Aβ insults to different extents among the patient lines
- The genetic factor (e.g., *APOE* variants) or tau biomarker data of the patient donors are associated with the data on cellular vulnerability to Aβ *in vitro*
- Clinical vulnerability to Aβ burden in the brain correlates with cellular vulnerability to extrinsic Aβ insults

6.2 Results

6.2.1 Experimental design

Three collaborating groups taking on different experiments meant that we needed a simplified cortical neuron differentiation protocol that is associated with minimal number of variables to effectively harmonise the differentiation steps among the laboratories. This is particularly pertinent as it was shown previously that just two iPSC lines could exhibit substantial cross-site variability [362]. To maximise differentiation reproducibility among the laboratories, together we chose the one-step cortical neuron differentiation protocol involving overexpressing *Ngn2* in the iPSCs to drive neuronal differentiation (Chapter 2.4.2). The iPSC lines were first transduced (by Dr Anne Hedegaard) with lentiviruses carrying a doxycycline-inducible system of *Ngn2* overexpression (Chapter 2.5) before expansion. The cells from the same passage were then cryopreserved and distributed among the laboratories to ensure that we start the differentiation from the same iPSC source. From that point, the inclusion of doxycycline to induce and maintain the overexpression of *Ngn2* was the main factor leading to the cortical neuron differentiation. All patient iPSC lines underwent neuronal differentiation concurrently until Day 80 for extrinsic Aβ treatments.

Dysregulation, and eventually loss, of synapses is one of the earliest pathological phenotypes of AD and leads to cognitive decline and memory loss [363,364]. I therefore focused on synapse loss due to extrinsic Aβ insults in Chapter 6 obtained in the same way as it is described in Chapter 2.13. Three sources of Aβ insults were used: (1) 25% (v/v) of AD brain homogenate (aCSF as control) for 72 h, (2) 10 μM of $A\beta_{1\text{-}42}$ oligomers (scrambled $A\beta_{1\text{-}42}$ as control) for 24 h, and (3) 20 μM of $A\beta_{25\text{-}35}$ ($A\beta_{35\text{-}25}$ as control) for 24 h.

6.2.2 Characterisation and synapse loss caused by extrinsic Aβ insults of the DFP cohort patient-derived neurons

I first set out to determine if the DFP pilot cohort patient iPSC-derived neurons express cortical markers on around Day 80 of neuronal differentiation driven by the overexpression of *Ngn2* alone from the iPSC stage. The neurons expressed both upper layer cortical marker CUX2 as well as deeper layer cortical marker CTIP2 co-localising with human nuclei (Figure 6.2.2A). The expression levels of these cortical markers exhibited no significant differences across all patient lines. The patient iPSC-derived cortical neurons also stained positive for synapses and displayed no differences in synaptic density across all patient lines at untreated baseline (Figure 6.2.2B). The neurons however, demonstrated varying levels of vulnerability to the extrinsic Aβ insults in the patient lines. The synapse loss caused by the synthetic Aβ oligomers was greater (up to 55% for $A\beta_{1-42}$ and 65% for $A\beta_{25-35}$) and statistically significant across the patient lines whereas the effect size of the AD brain homogenate was smaller (up to 40%) hence the limited range of responses to the Aβ insult from the most resilient to the most vulnerable.

It is important to establish if the synapse loss due to extrinsic Aβ insults in individual patient lines was reproducible over multiple independent differentiation and experimental repeats. By comparing the extents of synapse loss among three differentiation repeats, I confirmed that the specific levels of vulnerability in each line of iPSC-derived neurons in response to Aβ insults remained consistent across all 3 differentiation repeats (Figure 6.2.2C). In other words, the vulnerable patient lines remained vulnerable to Aβ at comparable levels across 3 differentiation repeats. Consistent patient line-specific vulnerability measured by synapse loss was also evident regardless of the types of Aβ insults used although the reproducibility was clearer in the Aβ oligomer-treated neurons as compared to the ones treated by the AD

brain homogenate. It is also worth mentioning that the levels of synapse loss caused by the two types of Aβ oligomers displayed significant and positive correlation with each other (Figure 6.2.2D), suggesting that Aβ-induced synapse loss was not dependent on specific Aβ sequences. Additionally, the vulnerability to extrinsic Aβ insults measured by synapse loss in the patient lines could not be explained by their *APOE* variant genotypes in this pilot cohort (Figure 6.2.2E). Taken together, the vulnerability in extrinsic Aβ-driven synapse loss is patient line-specific and not dependent on the types Aβ insults used. The vulnerability also could not be explained by experimental variability across differentiation repeats or *APOE* variants of individual patients in this pilot cohort.

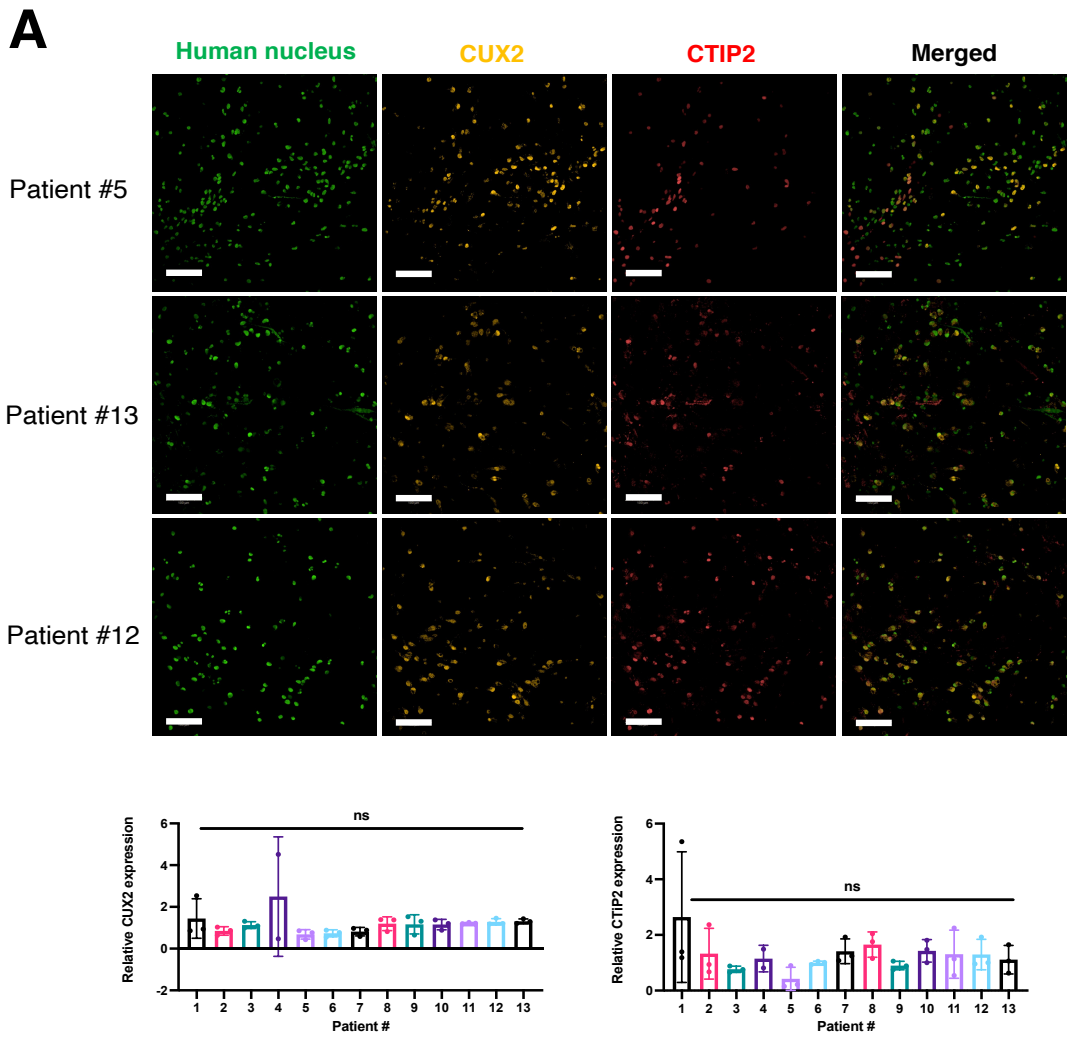
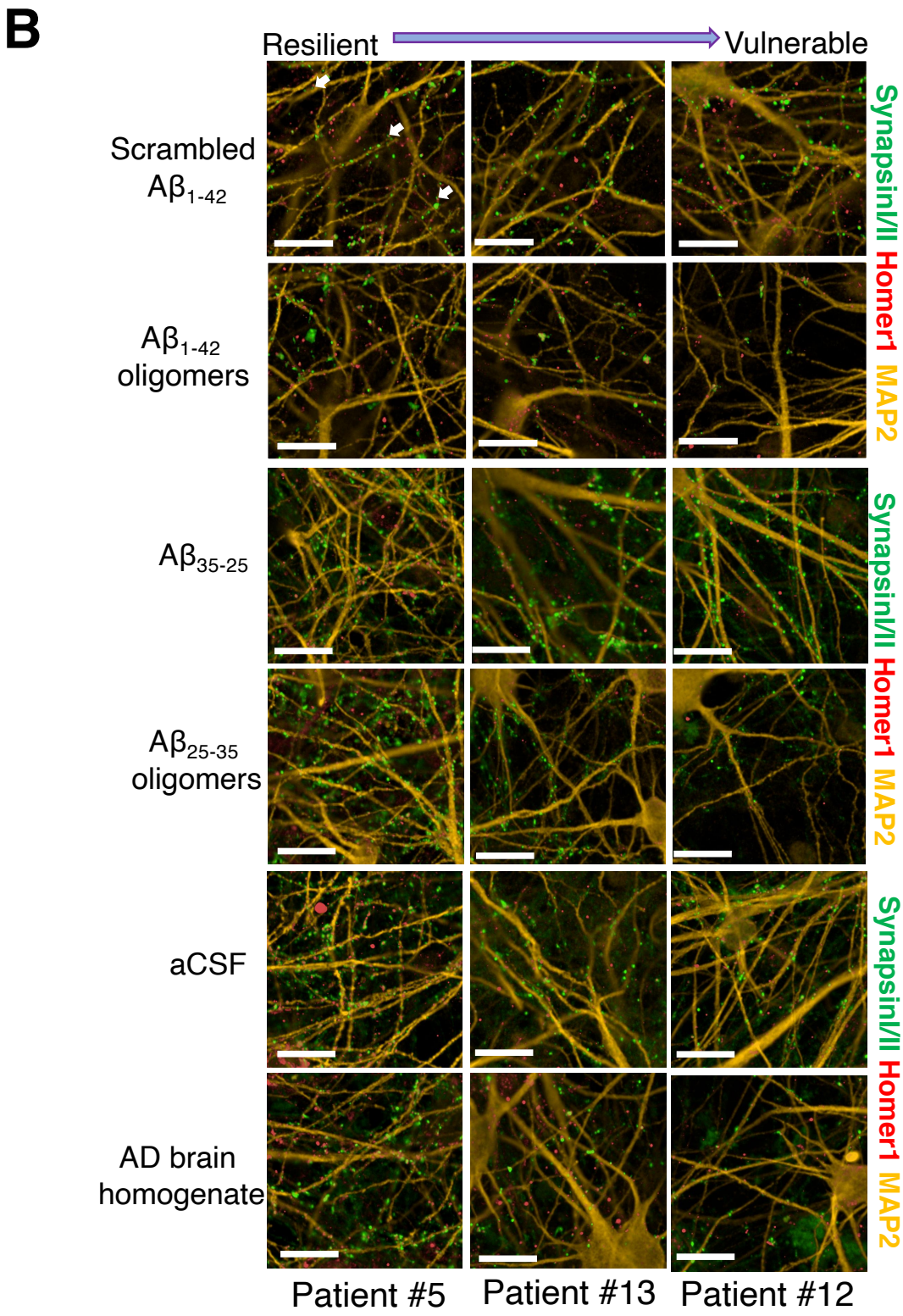
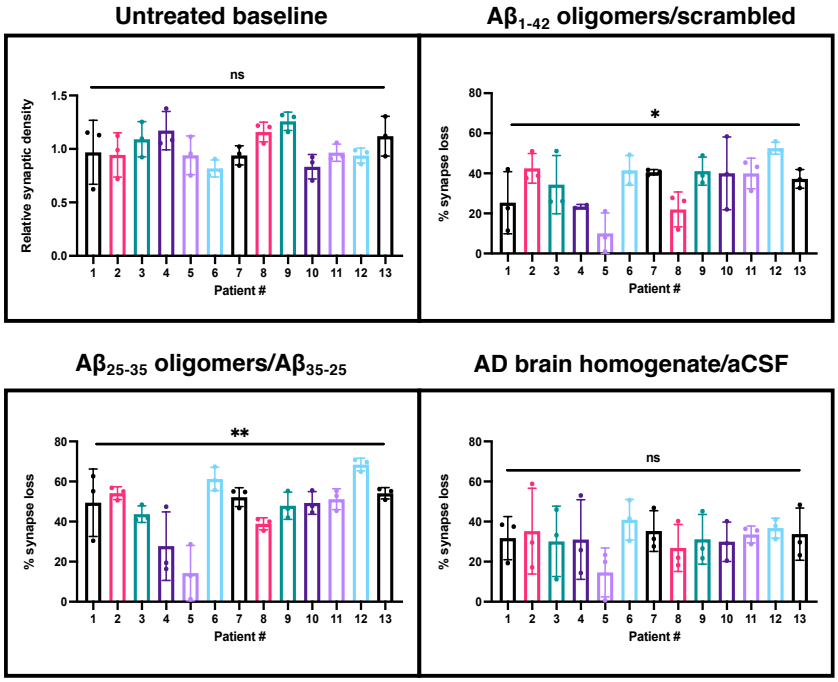


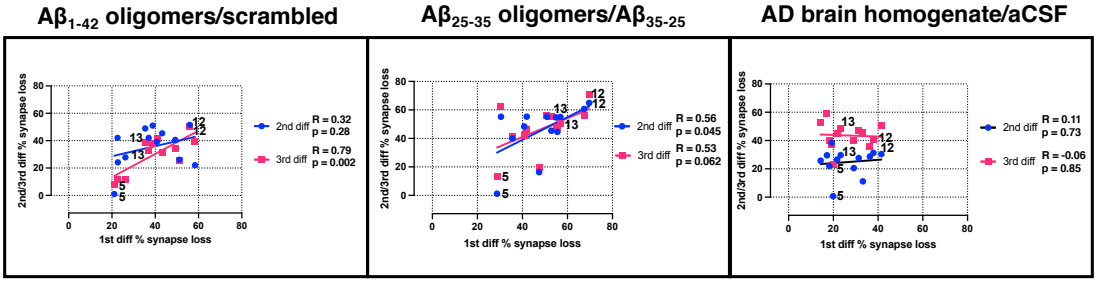
Figure 6.2.2: Characterisation of iPSC-derived neurons from the DFP pilot cohort and synapse loss caused by various sources of extrinsic Aβ insults
(A) Representative images of Day 83 iPSC-derived neurons from three select patient lines expressing cortical markers CUX2 (upper layer) and CTIP2 (deeper layer) co-localised with human nuclei. Scale bar = 100 μm; Quantification of relative cortical marker expression across all 13 lines. Mean ± SD. N = 3 independent neuronal differentiation repeats. Kruskal-Wallis test was used for the statistical analysis.



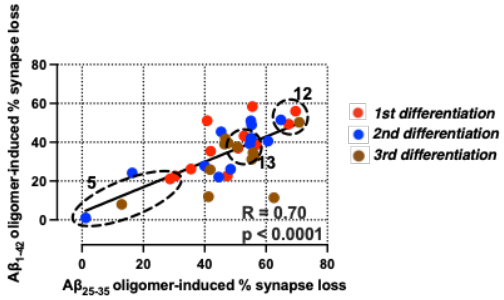
(B) Representative images of Day 80 iPSC-derived neurons from three select patient lines ranging from the most resilient to the most vulnerable to different extrinsic Aβ insults and probed for a presynaptic (Synapsin I/II), postsynaptic (HOMER1) and dendritic (MAP2) marker. Scale bar = 50 µm; Quantification of relative synaptic density at untreated baseline and synapse losses from all lines treated with different extrinsic Aβ insults. Mean ± SD. N = 3 independent neuronal differentiation repeats.



C



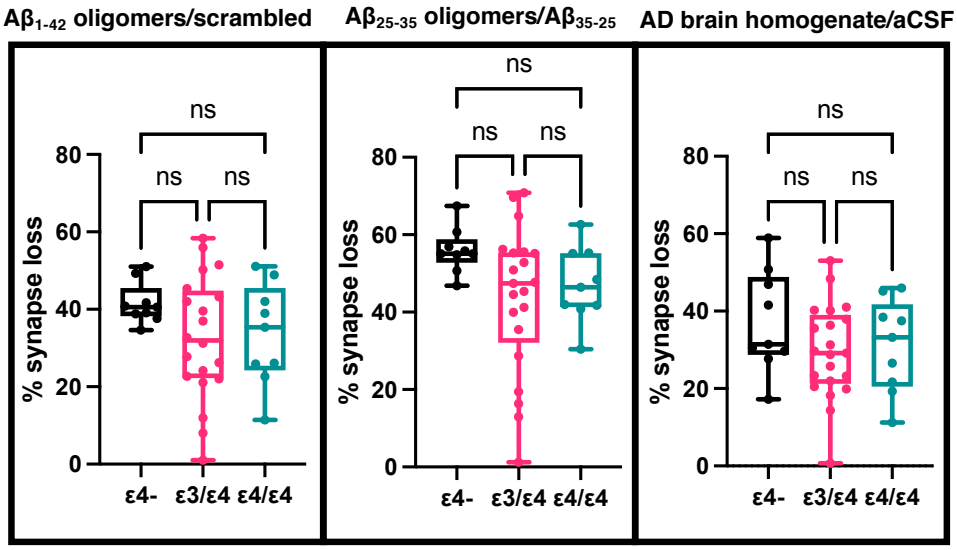
D



(C) Pairwise comparisons of the degrees of synapse loss between neuronal differentiation repeats, caused by different extrinsic Aβ insults. The three select patient lines along the spectrum of vulnerability to Aβ are indicated in the graphs. N = 13 patient lines per neuronal differentiation. Simple linear regression was performed for the statistical analysis and Pearson's coefficient of correlation was reported.

(D) Pairwise comparisons of the degrees of synapse loss between the two types of synthetic Aβ oligomers. The three select patient lines along the spectrum of vulnerability to Aβ are indicated in the graphs. N = 38 independent neuronal differentiation repeats across all patient lines. Simple linear regression was performed for the statistical analysis and Pearson's coefficient of correlation was reported.

E



(E) Boxplots of synapse losses from the DFP pilot cohort patient iPSC-derived cortical neurons categorised according to their *APOE* variant genotypes. Median within the box bordered by interquartile range with the whiskers representing the range of data. N = 9 (ε4-), 20 (ε3/ε4) and 9 (ε4/ε4) independent neuronal differentiation repeats across all patient lines. Kruskal-Wallis test with Dunn's multiple comparison correction was used for the statistical analysis.

6.2.3 Correlation of synaptic vulnerability in patient-derived neurons with clinical outcomes of the same patients

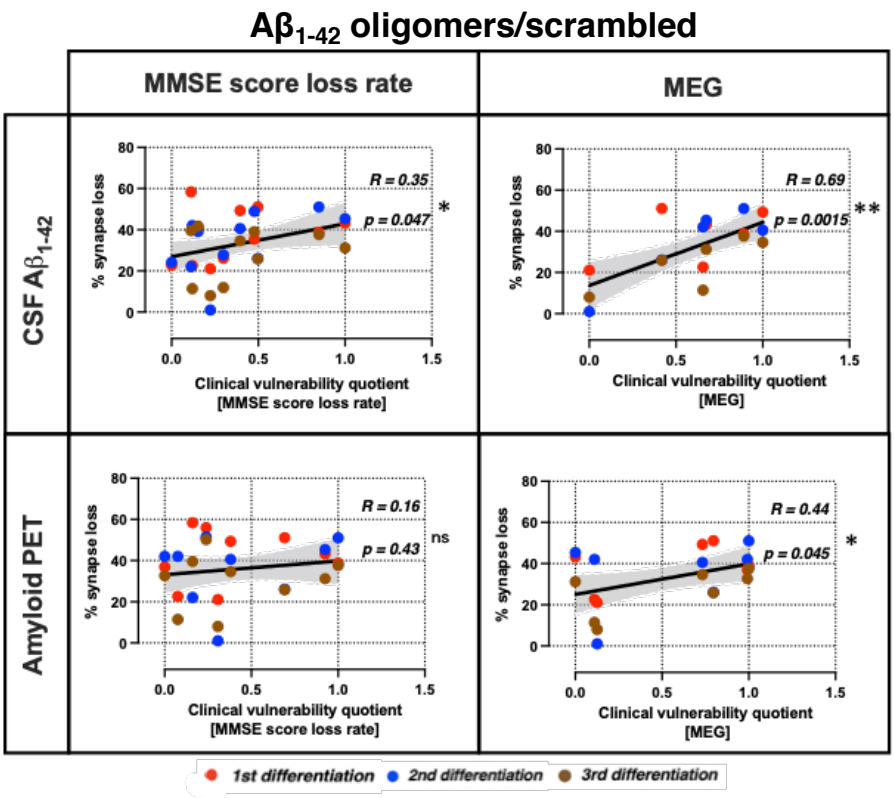
The synapse loss data from the iPSC-derived neurons presented in Chapter 6.2.2 were then used for correlation analyses with clinical outcomes from the donors to address the question whether cellular vulnerability to extrinsic Aβ insults *in vitro* can recapitulate clinical vulnerability to Aβ burden *in vivo*. Both MMSE score loss rate, which is a cognitive test that has been used to measure cognitive decline in AD [365,366], and MEG, which detects magnetic field generated by electrical activity in the brain and has been used to measure brain activity changes in AD [367,368], were chosen as broadly analogous clinical

assessments to synaptic health in the patient iPSC-derived neurons (Chapter 2.3). To determine clinical vulnerability, I calculated a "clinical vulnerability quotient" by first normalising the raw clinical outcome values with Aβ burden estimated by amyloid PET imaging or $A\beta_{1\text{-}42}$ concentration in the CSF to derive clinical outcome measures per unit of Aβ burden for each cohort participant, then the normalised data were rescaled to result in a range between 0 and 1 within the pilot cohort. The quotient was created to facilitate comparisons between clinical outcomes as a function of Aβ burden by having a more intuitive scale instead of the raw values and units (e.g., 0.000,005 MMSE score difference • mL/day • pg).

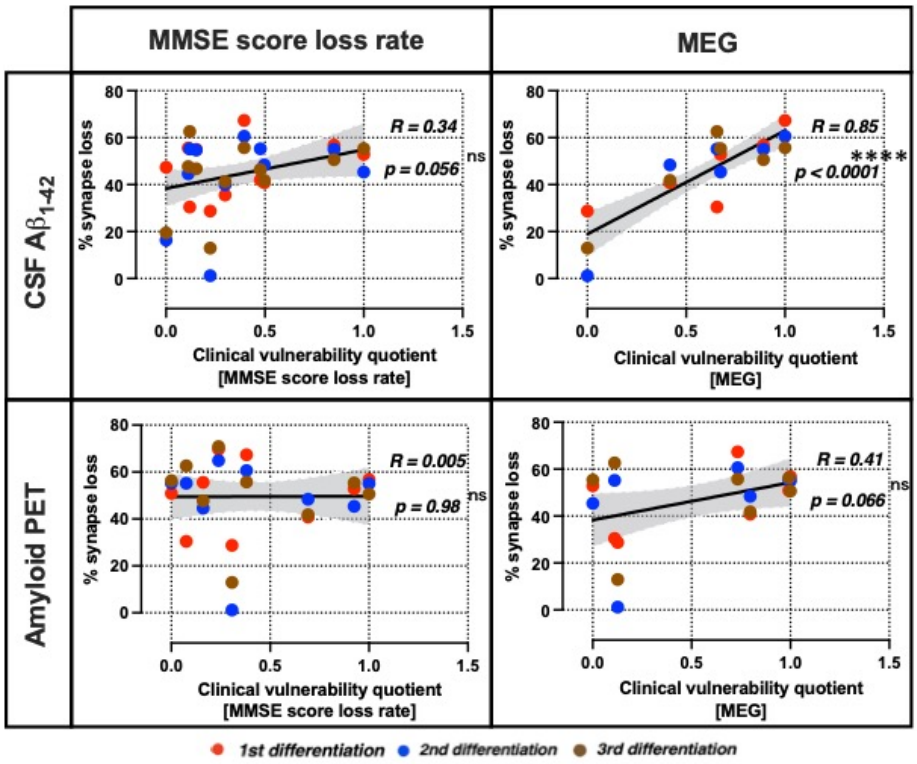
Among all the pairwise correlations between the synapse losses caused by three different extrinsic Aβ insults and two clinical outcomes as a function of two measures of Aβ burden in the brain, clinical vulnerability in terms of MEG as a function of $A\beta_{1\text{-}42}$ concentration in the CSF emerged as the most consistent readout regardless of the extrinsic Aβ insults used *in vitro* (Figures 6.2.3.1A, B and C). The data analyses demonstrated that greater global MEG signals in the AD brain (i.e., greater levels of brain activity) per unit of Aβ burden measured by the concentration of $A\beta_{1\text{-}42}$ in the CSF correlate positively with Aβ-driven synapse loss in the patient iPSC-derived cortical neurons. Meanwhile, the MMSE score loss rates as a function $A\beta_{1\text{-}42}$ concentration in the CSF also correlate well with the synapse loss due to the treatment with Aβ oligomers. The data showed that higher MMSE score loss rates (i.e., faster cognitive decline) correlate positively with synaptic vulnerability to Aβ oligomers, but the correlation was not observed in the synapse loss data involving the AD brain homogenate treatment (Figure 6.2.3.1C). In general, an increase in clinical vulnerability quotient that is adjusted with $A\beta_{1\text{-}42}$ concentration in the CSF is associated with more severe synaptic vulnerability in the iPSC-derived neurons from the same patients. On

the other hand, the correlations between Aβ-driven synapse losses *in vitro* and clinical outcomes as a function of Aβ burden *in vivo* measured by amyloid PET imaging appeared weaker than the ones adjusted for $A\beta_{1\text{-}42}$ concentration in the CSF with the majority of pairwise cellular-clinical comparisons unsupported by statistical significance (Figures 6.2.3.1A, B and C). Overall, the data from the DFP pilot cohort revealed that clinical vulnerabilities to Aβ burden measured by cognitive decline and levels of brain activity adjusted for $A\beta_{1\text{-}42}$ concentration in the CSF can reflect cellular vulnerability to extrinsic Aβ insults measured by synapse loss in individual patient iPSC-derived cortical neurons.

A


Aβ1-42 oligomers/scrambled
MMSE score loss rate
MEG
CSF Aβ1-42
Amyloid PET
% synapse loss
Clinical vulnerability quotient
[MMSE score loss rate]
[MEG]
R = 0.35
p = 0.047
*
R = 0.69
p = 0.0015
**
R = 0.16
p = 0.43
ns
R = 0.44
p = 0.045
*
1st differentiation
2nd differentiation
3rd differentiation

B


Aβ25-35 oligomers/Aβ35-25
MMSE score loss rate
MEG
CSF Aβ1-42
Amyloid PET
% synapse loss
Clinical vulnerability quotient
[MMSE score loss rate]
[MEG]
R = 0.34
p = 0.056
ns
R = 0.85
p < 0.0001
****
R = 0.005
p = 0.98
ns
R = 0.41
p = 0.066
ns
1st differentiation
2nd differentiation
3rd differentiation

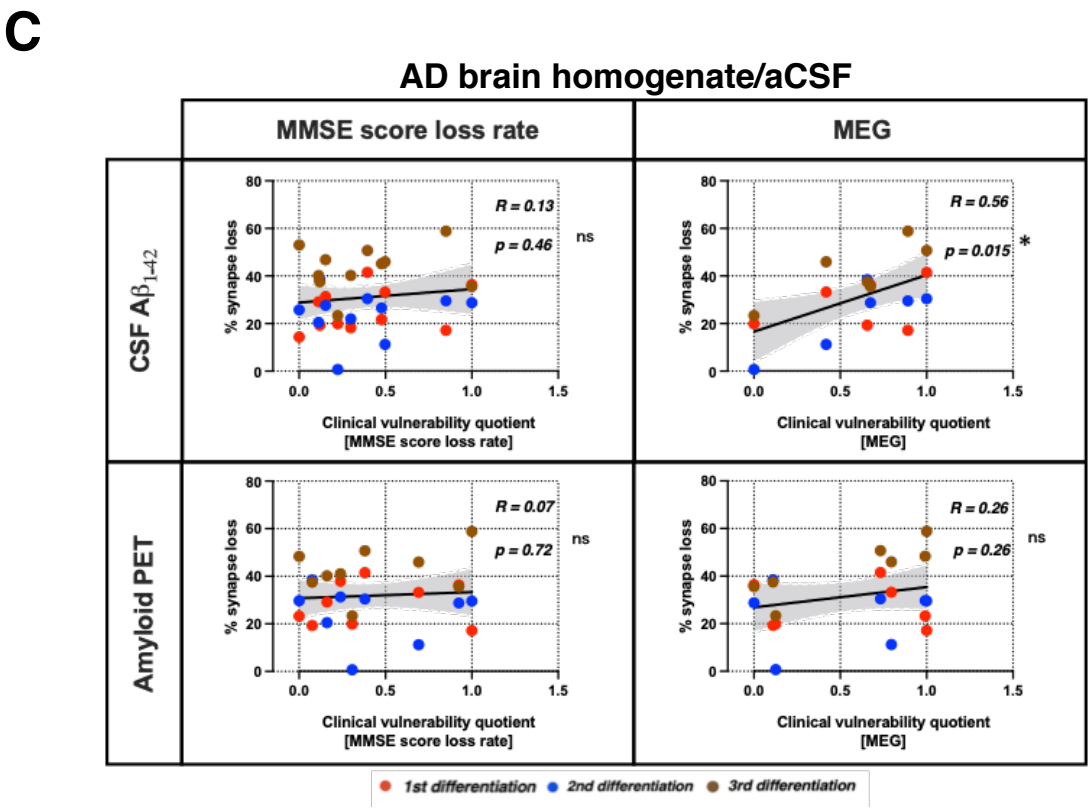
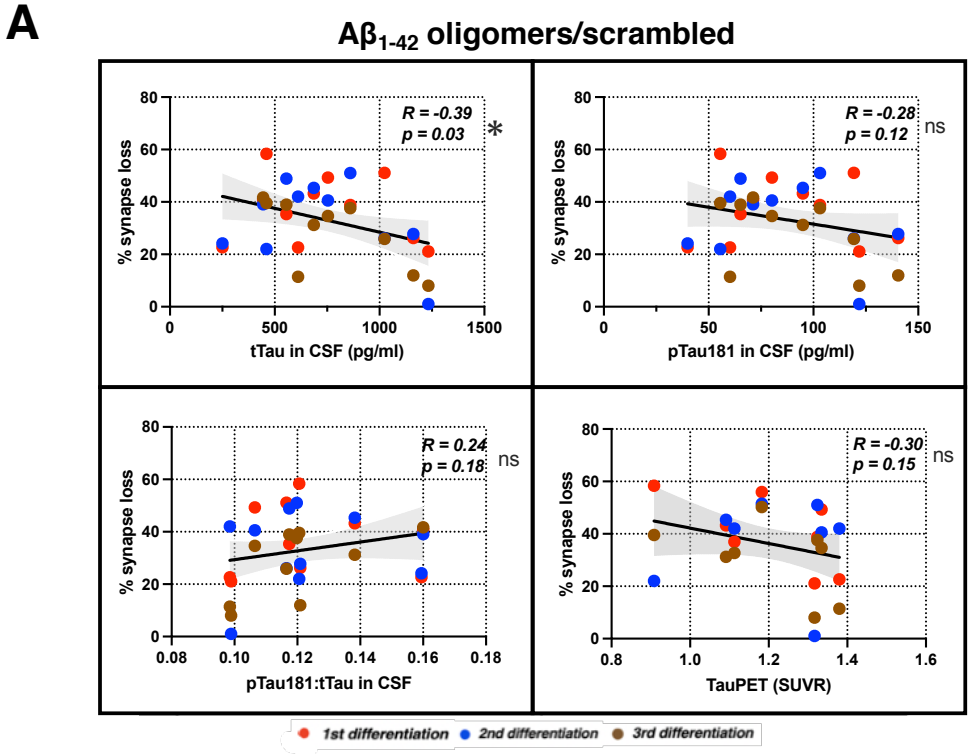


Figure 6.2.3.1: Correlating cellular vulnerability measured by synapse loss with clinical vulnerability to Aβ
Correlations of synapse loss caused by extrinsic Aβ insults on Day 80 DFP pilot cohort patient iPSC-derived cortical neurons with clinical outcomes adjusted for Aβ burden in the brain (clinical vulnerability quotient). Correlations of the degrees of synapse loss caused by (A) 10 μM of $A\beta_{1\text{-}42}$ oligomers relative to the scrambled $A\beta_{1\text{-}42}$ control, (B) 20 μM of $A\beta_{25\text{-}35}$ oligomers relative to the $A\beta_{35\text{-}25}$ control, and (C) 25% (v/v) of AD brain homogenate relative to the aCSF control with clinical outcomes (measured by MMSE score loss rate or MEG) adjusted for Aβ burden in the brain (measured by amyloid PET or $A\beta_{1\text{-}42}$ in the CSF). For (A): N = 32 (MMSE/CSF $A\beta_{1\text{-}42}$), 27 (MMSE/amyloid PET), 18 (MEG/CSF $A\beta_{1\text{-}42}$) or 21 (MEG/amyloid PET); For (B) and (C): N = 33 (MMSE/CSF $A\beta_{1\text{-}42}$), 27 (MMSE/amyloid PET), 18 (MEG/CSF $A\beta_{1\text{-}42}$) or 21 (MEG/amyloid PET) independent neuronal differentiation repeats across all patient lines. Simple linear regression was performed for the statistical analysis and Pearson's coefficient of correlation was reported for all correlation graphs in this figure.

Next, I asked if the cellular vulnerability to Aβ in the patient iPSC-derived cortical neurons is associated with the levels of tau biomarkers in the DFP pilot cohort. The vast majority of the pairwise correlation analyses between the synapse loss caused by various extrinsic Aβ

insults and tau biomarkers did not return any statistical significance in correlation except the correlation between $A\beta_{1-42}$-induced synapse loss in the patient iPSC-derived neurons and the concentration of tTau found in the CSF (Figures 6.2.3.2A, B and C). The $A\beta_{1-42}$ data showed negative correlation where greater synaptic vulnerability to Aβ is associated with lower concentration of tTau in the CSF (Figure 6.2.3.2A). In fact, across all three types of extrinsic Aβ insults used to trigger synapse loss, there is a weak and inverse relationship between the synaptic vulnerability to Aβ in the iPSC-derived cortical neurons and tau biomarkers measured by the concentration of tTau or pTau181 in the CSF or tau PET brain imaging. When the values of pTau181 are normalised to the tTau readout, the negative relationship is either abolished or replaced with a slightly positive relationship. Taken together, tau biomarkers measured in the DFP pilot cohort are not meaningfully associated with the varying levels of synaptic vulnerability in the patient iPSC-derived neurons but the general trend in Figures 6.2.3.2A, B and C provides some indication that more vulnerable patient lines might come from the corresponding patients with less severe tau pathology.



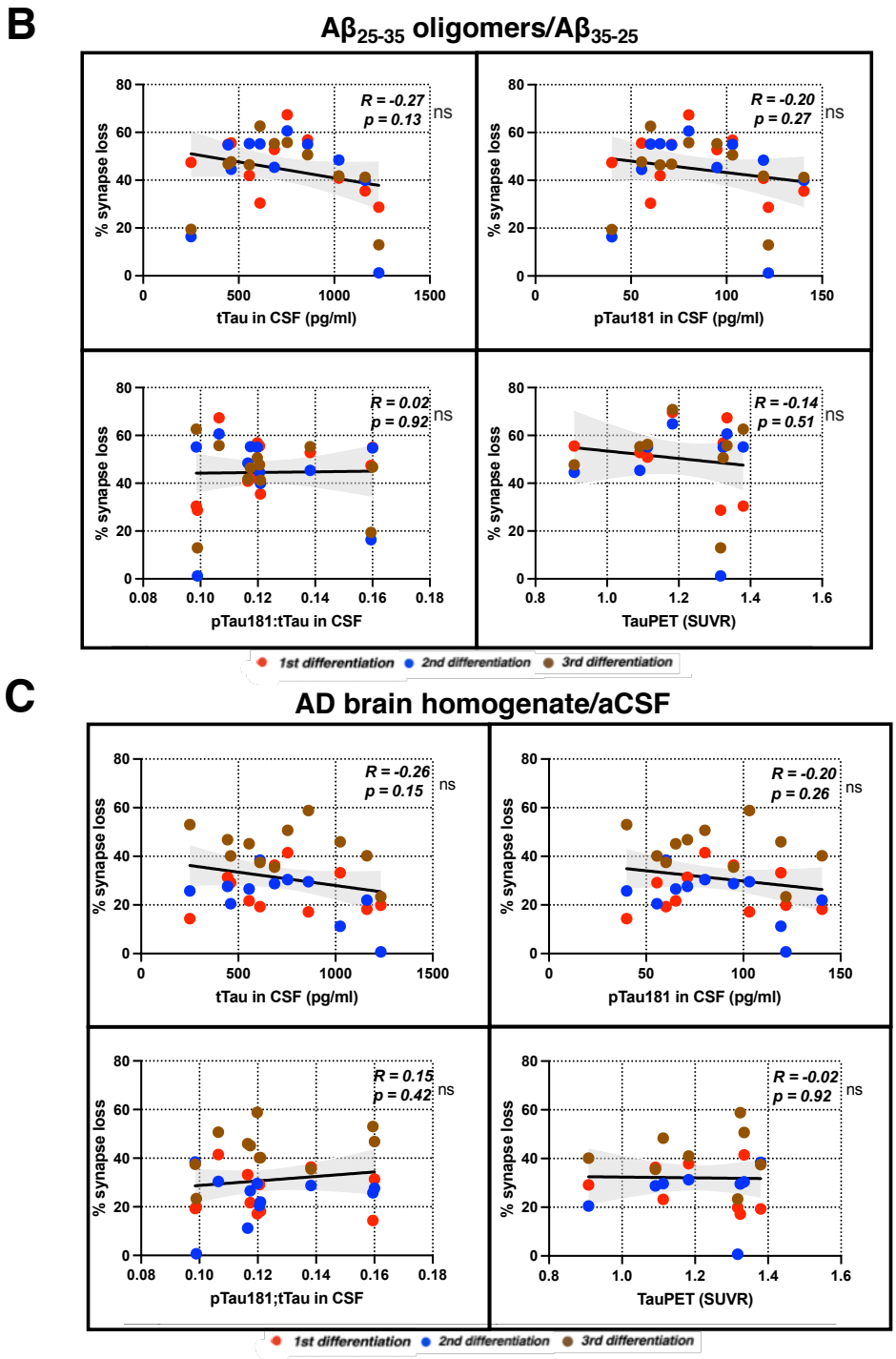


Figure 6.2.3.2: Correlating cellular vulnerability measured by synapse loss with clinical tau biomarkers

Correlations of the degrees of synapse loss caused by (A) 10 μM of $A\beta_{1-42}$ oligomers relative to the scrambled $A\beta_{1-42}$ control, (B) 20 μM of $A\beta_{25-35}$ oligomers relative to the $A\beta_{35-25}$ control, and (C) 25% (v/v) of AD brain homogenate relative to the aCSF control with tau biomarkers measured by the concentration of tTau in the CSF, concentration of pTau181 in the CSF, ratio of pTau181:tTau in the CSF and tau PET. For (A): N = 24 (tau PET) or 32 (all CSF readouts); For (B) and (C): N = 24 (tau PET) or 33 (all CSF readouts) independent neuronal differentiation repeats across all patient lines included. Simple linear regression was performed for the statistical analysis and Pearson's coefficient of correlation was reported for all correlation graphs in this figure.

6.3 Discussion

Strengths and weaknesses of the study design

It has recently been shown that several measures of secreted Aβ peptides in iPSC-derived cortical neurons from AD patients reflect the extent of Aβ neuropathology of their donors [361]. However, I have now demonstrated that the functional consequences of those clinical phenotypes in response to Aβ are also preserved in the patient-derived iPSCs by proving that cellular vulnerability to extrinsic Aβ insults *in vitro* reflects clinical vulnerability to Aβ burden *in vivo*.

In this study, I set out to take advantage of the comprehensive clinical dataset from the DFP pilot cohort. The hypothesis was partially influenced by the fact that both amyloid PET and CSF concentration of Aβ were available together with a wide range of clinical outcomes, hence there was room to explore if any of the clinical aspects could be recapitulated by the patient iPSC-derived neurons. Synapse imaging was chosen to be the cellular readout because the assay can respond consistently to extrinsic Aβ insults hence more likely to be reproducible, be miniaturised for the differentiation of multiple lines in parallel, and the MMSE score was one of the clinical readouts without any missing information together with the MEG data selected to be analogous and relevant to synaptic health *in vitro*.

The one-step cortical neuron differentiation by overexpressing *Ngn2* in iPSCs inducible by the inclusion of doxycycline was straightforward for the laboratories involved to adopt. The simplified protocol meant that the most time-consuming step was the initial phase of differentiation, thus it was possible to stagger the differentiation repeats by several weeks to improve efficiency. However, a couple of technical caveats are associated with the protocol

as compared to the one used for the *MAPT* knockout project where the iPSCs were first differentiated into NPCs first before inducing *Ngn2* overexpression. As the Ngn2-driven differentiation occurred when the cells were highly proliferative, it was challenging to precisely control the final neuronal density present in the culture. This occasionally led to over-proliferation of cells where non-neuronal cells overtook the neuronal culture hence the wells would have to be excluded due to poor image quality. Additionally, the attrition of cells over the initial phase from the viral transduction step meant that it was difficult to predict the amount of cell materials to start with. As a result, a large quantity of iPSCs were needed for each differentiation thus driving up the cost of the experiment.

Having 13 sAD iPSC lines in parallel in a single experiment is considered a relatively large logistical undertaking and would amount to one of the largest iPSC studies for AD. Yet, 13 patients constitute a relatively small clinical cohort hence limiting the clinical relevance one could draw from the study as some of the clinical data were incomplete (Table 2.3.1). This is especially the case for the MEG data where only 7 participants took part. Due to the limited number of datapoints, the correlation could appear skewed as in the case for Figures 6.2.3.1A, B and C on the clinical vulnerability quotient on MEG where a single patient line seems to be driving the positive correlation between the clinical vulnerability quotient and Aβ-driven synapse loss in the iPSC-derived neurons. Nevertheless, the positive correlations persist when the whole picture is taken into account by looking at different clinical outcomes as a function of different types Aβ burden in support of the feasibility that patient-derived iPSC models can recapitulate in-life vulnerability to Aβ measured by their clinical outcomes.

Data interpretations

The results from Figures 6.2.3.1A, B and C indicated that exacerbated cognitive decline measured by MMSE per unit of Aβ burden in the patients correlates with synaptic vulnerability in the patient iPSC-derived cortical neurons, agreeing with the human post-mortem data where synapse loss in the brain correlates significantly with cognitive decline also measured by MMSE [369]. In addition, increasing network activity in the brain measured by MEG global efficiency was also shown to correlate positively with synaptic vulnerability in the iPSC-derived cortical neurons. Although MEG identifies neurophysiological changes that are specific to AD, it remains unclear how different brain MEG signals change at different stages of AD progression [367,370]. This apparently counterintuitive observation where synapse loss correlates with heightened levels of brain activity is in fact in line with a considerable amount of evidence for hyperexcitability in the early phases of AD. The current understanding is that neurons exhibit hyperactivation particularly during the MCI stage before hypoactivation as disease progresses [371,372], and hyperexcitability leading to seizure activity is increased in AD likely as a function of amyloid related pathology [373]. Recently, it was reported that pronounced GAD65/67-positive inhibitory synapse losses were observed in the visual cortex as well as in the proximity of amyloid plaques in the temporal cortex of post-mortem AD brains [374]. This study revealed a potential mechanism to explain how hyperactivity might occur while incurring an overall Aβ-associated loss in synapses.

Aβ burden in the brain was defined by amyloid PET imaging or concentration of $A\beta_{1-42}$ in the CSF in this study. However, the clinical outcomes as a function of Aβ burden quantified by amyloid PET manifested weaker correlations with Aβ-driven synapse loss in the iPSC-

derived cortical neurons as compared to the ones relative to the CSF $A\beta_{1-42}$ perhaps suggesting that CSF $A\beta_{1-42}$ is a more direct reflection of the pathological insult in AD than the aggregations of fibrillated Aβ in plaques measured by amyloid PET [375].

Furthermore, the formation of amyloid plaques detected by PET involves a rate-limiting nucleation event which follows higher order kinetics [376] before the plaques expand in size by following first-order kinetics [377] whereas soluble $A\beta_{1-42}$ in the CSF was shown to exhibit consistent change in concentration along disease progression [42]. As such, a cross-sectional amyloid PET quantification could potentially be skewed depending on the stage of plaque formation thus resulting in more variability as the data were applied for the derivation of clinical vulnerability quotient.

Chapter 7: General discussion and conclusion

Thesis overview

In this thesis, I presented experimental data on the first two human *MAPT-/-* isogenic panels of iPSC-derived cortical neurons generated with CRISPR/Cas9 gene editing strategies. Exon 1 and 4 of the *MAPT* gene were targeted separately in two well-characterised iPSC lines from healthy individuals and verified via DNA sequencing of the targeted regions before the ablation of tau expression was confirmed by immunoblots using three antibodies probing different tau regions. In searching for the *MAPT-/-* clones, several *MAPT+/-* and *MAPT+/+* clones were discovered and adopted into the isogenic panels. Three *MAPT-/-*, two *MAPT+/-* and two *MAPT+/+* iPSC lines, which all underwent the CRISPR/Cas9 gene editing procedures, eventually came through for downstream experiments (Chapter 3). All iPSC lines used in this thesis could differentiate into cortical neurons and expressed comparable levels of synaptic density.

Removal of tau expression in iPSC-derived cortical neurons could lead to neurite outgrowth impairment, bias towards anterograde mitochondrial transport along axons, and reduced AP firing frequency (Chapters 4 and 5). Synapse losses, cytotoxicity, neurite outgrowth impairments, reduction in motile mitochondria along axons, and hyperactivation of neurons were observed upon the exposure to extrinsic Aβ. The answer to whether these aspects of Aβ-driven toxicity are tau-dependent is less straightforward depending on the sources of Aβ employed in the experiments. Overall, there were statistically significant evidence to suggest that synapse losses, cytotoxicity, deficits in mitochondrial transport and hyperactivation caused by extrinsic Aβ could be prevented in *MAPT-/-* iPSC-derived cortical neurons.

Additionally, thirteen sAD patient-derived iPSC lines from the DFP pilot cohort were differentiated into cortical neurons before they were treated with various types of extrinsic Aβ insults to elicit synapse losses (Chapter 6). The cellular vulnerability to Aβ insults measured by synapse loss *in vitro* was compared with clinical vulnerability to Aβ burden in the brain measured by the iPSC donors' individual clinical outcomes such as cognitive decline and levels of brain activity which are broadly analogous to synaptic health *in vivo*. I revealed that there are significant and positive correlations between synapse loss *in vitro* and clinical vulnerability *in vivo* in response to Aβ, showing that it is feasible to model AD cognitive consequences with iPSCs after correcting for Aβ levels.

A range of Aβ-induced phenotypes were chosen on purpose from the most drastic phenotype like cell death to more subtle phenotypes involving subcellular changes to explore if tau-dependent phenotypes observed in mouse models could be recapitulated in human cells. Both synthetic Aβ oligomers, which are more defined and elicit more acute toxic responses, and brain-derived soluble Aβ, which are more physiological and elicit more chronic and relatively less toxic responses, were used in this study. The manifestation of cytotoxicity caused by 10 μM of $A\beta_{1-42}$ oligomers began at least 3 days post-treatment and became significant after 5 days, whereas neurite outgrowth impairment preceding cytotoxicity caused by the same extrinsic Aβ insult became apparent after 48 h of exposure to $A\beta_{1-42}$ oligomers. Early responses like synapse loss and neuronal hyperactivation could be caused by brain-derived Aβ at pM range, while mitochondrial transport along axons could be detected as early as 1 h post-treatment of $A\beta_{1-42}$ oligomers at 2 μM. Taken together, multiple Aβ-driven pathways from the earliest phenotypes to the eventual cell death can be prevented in the absence of tau expression. This observation reflects tau's diverse function neurons as elaborated in Chapter 1.2.2.

However, dissimilar levels of responses in various subcellular phenotypes posed a challenge in experimental designs. As discussed in Chapters 5, certain differential responses in the *MAPT-/-* neurons (e.g., synapse loss and electrophysiological responses) could only be distinguished when the neurons were exposed to less acute and more physiological sources of Aβ, indicating that a strong Aβ challenge with 10 μM of $A\beta_{1-42}$ oligomers may severely shorten the window of detecting protective effects in more sensitive phenotypes like electrophysiological readouts. It is also important to note that the concentration of 10 μM of $A\beta_{1-42}$ oligomers, though necessary to cause cellular phenotypes like cell death and neurite outgrowth impairment, is significantly higher than the levels of Aβ oligomers detected in the CSF of AD patients (<1 pM) [137]. Aβ aggregates to form consistent higher-order structures specific to either sAD or fAD, and these Aβ structures differ from the ones aggregated *in vitro* like the oligomers used in this thesis [378]. Structural differences might partially explain the high concentration of synthetic Aβ oligomers needed *in vitro* since most of the synthetic oligomer structures are not normally found *in vivo*. The unphysiological levels of $A\beta_{1-42}$ oligomers used in this thesis thus raise the question on the relevance of the cellular phenotypes observed in the abovementioned experiments in AD pathophysiology.

Human AD brain-derived Aβ could then serve as a suitable source of extrinsic Aβ insults that is more pathologically relevant, although the extraction efficiency would need to be significantly improved for its routine use in a laboratory setting. By IP followed by glycine-mediated elution, the extraction/elution efficiency sits at merely 3% of the total amount of Aβ available before IP using commercially available antibodies against Aβ (Table 2.9.1). Specifically, the amount of $A\beta_{1-40}$ obtained using the current method yields only 420 pg/g of post-mortem cortical tissue. I propose that high-performance liquid chromatography could be a potential technique to extract both soluble and insoluble Aβ from post-mortem

AD brain tissues with less attrition rate. In retrospect, chronic Aβ exposure with at a low dosage may be a better strategy to more closely mimic AD pathology and differentiate subtle differences due to the loss of tau expression whenever it is logistically feasible.

Tau-driven toxicity

The scope of the thesis focuses on exploring Aβ-driven toxicities which are dependent on the presence of tau, but the effects of downstream tau-driven toxicity involving the phosphorylation and subsequent aggregation of tau were not investigated in the previous Chapters. As Aβ-driven tau hyperphosphorylation can lead to intracellular aggregation of tau (more in Chapter 1.2.2), the toxic effects of tau aggregates are important to understand the mechanisms of Aβ-driven toxicity in human neurons. Indeed, the fact that tauopathies other than AD can also result in dementia and severe brain region-specific degeneration largely in the absence of Aβ suggests that tau aggregates can elicit downstream toxic cascade of events without first being triggered by an Aβ challenge.

It was reported previously that pathological tau aggregates in transgenic mice expressing human *MAPT* with the P301L mutation were mislocalised to dendrites and this led to downstream synaptic dysfunctions [379]. Pathological tau aggregates were also shown to be capable of spreading via neuronal circuits - an event that precedes synapse and neuronal loss [380]. Moreover, it was demonstrated by directly infusing tau oligomers into mouse hippocampal neurons that AP amplitude, presynaptic transmission, and LTP were all impaired by intracellular tau oligomer insults [381]. Apart from electrophysiological disruptions, pathological tau accumulation can also cause mitochondrial distribution deficits

and destabilisation of microtubules in axons in mice [173–175,382]. These data underline the potential mechanisms that may explain how tau mediated Aβ-driven toxicity in the experiments described in this thesis.

Beyond two-dimensional iPSC-derived cortical neurons

Two-dimensional (2D) aged iPSC-derived cortical neuron is the model of choice to study AD-related processes throughout this thesis. However, there are several other options available that could potentially enhance *in vitro* disease modelling or encompass more biological insights into a single experiment owing to the versatility of iPSC models. Neuronal co-culture with other brain resident cell types such as astrocytes, microglia, or oligodendrocytes is a useful technique to probe whether any AD-related processes are cell-autonomous. Indeed, iPSC-derived astrocytes carrying two copies of the *APOE ε4* variant were less effective in promoting neuronal survival and synaptogenesis as compared to the astrocyte carrying two copies of the *APOE ε3* variant [383]. It was also reported that iPSC-derived astrocytes carrying the *PSEN1* ΔE9 mutation displayed hallmarks of AD pathology like increased Aβ production and were again less effective in neuronal support [384]. Although the iPSC-derived cortical neurons were grown in co-culture with rat astrocytes in this thesis, the presence of astrocytes was only intended to supplement the iPSC-derived neurons in maturation, adherence, and neurotrophic support. The abovementioned studies are two examples of how neuronal co-culture with glial cells could provide mechanistic evidence of AD pathogenesis. In fact, it is viable to establish triculture involving iPSC-derived neurons, microglia, and astrocytes *in vitro* and the triculture systems demonstrated

better representations of AD such as neuritic plaque formation, pTau accumulation, and neuroinflammatory responses as opposed to mono- or co-culture systems [385–387].

More recently, three-dimensional (3D) cerebral organoid culture derived from iPSCs has emerged as a cellular model that better recapitulates brain physiology and offers a relatively more native condition as compared to studying interactions of different cell types in 2D cultures [388]. Instead of plating iPSCs down in adherent conditions, organoids form when they are allowed to first differentiate in 3D in a gel droplet containing extracellular matrix proteins and typically kept in long-term culture in a bioreactor. These "mini-brains" were shown to reproducibly represent diverse neuronal and glial subtypes and could even mimic CSF-like fluid secretion from choroid plexus formed within the organoids [389,390]. Furthermore, it was reported that organoids harbouring either the *APOE ε4* variant or fAD mutations robustly demonstrated typical AD pathological phenotypes such as increased Aβ production and accumulation of pTau [295,304,391–393].

It is then relevant to this thesis how these cellular AD models can be adapted to study tau's involvement such as triculture singling out the interaction between neurons and glia or organoid where tau may have differential functions in various neuronal subtypes. Indeed, it was demonstrated in transgenic mice expressing the *MAPT* P301L mutation that excitatory neurons were more vulnerable compared to inhibitory neurons by identifying specific gene expression signatures in excitatory neurons [394]. Additionally, though not the focus of this thesis, tau pathology is also implicated in glial cells such that both oligodendrocytes and astrocytes are capable of tau propagation and depletion of microglia prevented tau propagation whereas depletion of pericytes resulted in tau pathology [395–397]. These evidence further highlight that experimental data using different types of iPSC-derived

cellular models, together with the results from this thesis, can help elucidate a comprehensive picture of tau's pathological role in AD.

Revisiting the amyloid cascade hypothesis

The amyloid cascade hypothesis dictates that accumulation of Aβ is the upstream causative agent that ultimately leads to AD, supported by the evidence that mutations in genes involved in APP processing alone are sufficient to cause early-onset fAD and amyloid plaque deposition begins decades before the age of symptom onset (Chapters 1.1.2 and 1.1.3). Although fAD patients account for a minority of total AD cases, it is also true that by definition (more on Chapter 1.1.2) all AD patients, both fAD and sAD, manifest amyloid plaque accumulation in the brain. The amyloid cascade hypothesis has therefore guided the clinical trial efforts in treating AD for the past 30 years but anti-amyloid drugs have mostly failed to meet primary outcome measures which include halting cognitive decline [398]. It has then prompted researchers to reconsider if the amyloid cascade hypothesis solely explains the pathogenesis of AD.

Having set the scope of the thesis to studying Aβ-driven toxicity that is tau-dependent, a strong emphasis has been put on Aβ, tau, and their unidirectional interaction throughout the text. It is however important to acknowledge that apart from manifesting varying levels of Aβ and tau pathologies, which are unquestionably key to understanding sAD, the pathogenesis of sAD has a strong genetics component (Chapter 1.1.3) which implicates a wide range of subcellular processes without a clear link to APP processing. Indeed, the experiments in Chapter 6 using the sAD patient iPSC-derived neurons demonstrated that

cellular vulnerability to Aβ *in vitro* could reflect clinical outcomes of the donors *after* correcting for Aβ burden *in vivo*. In other words, the cellular-clinical correlation of vulnerability sustains after the accumulation of Aβ has been accounted for. This iPSC modelling experiment showed that intrinsic vulnerability to Aβ underlies the severity of cognitive decline instead of the accumulation of Aβ *per se*. This is perhaps best exemplified by the rare fAD case mentioned in Chapter 1.1.3 where a pathogenic *PSEN1* mutation did not result in EOAD due to the presence of protective *APOE* Christchurch mutations which modulated the effects of toxic Aβ despite the individual manifesting severe amyloid plaque pathology [99]. In a mouse model of AD, crossing transgenic mice carrying human *APP* mutant with *Mapt-/-* mice rescued memory deficits without reducing the amount of amyloid plaque burden in the brain thus suggesting that the accumulation of amyloid plaque alone was insufficient to account for the memory deficits observed [234].

Despite the increasing amount of evidence against the amyloid cascade hypothesis, it is indisputable that Aβ is neurotoxic as shown reproducibly in this thesis and other studies using both synthetic and AD brain-derived Aβ. As such, it is extremely unlikely that Aβ accumulation in an AD brain is completely innocuous. Based on the DFP pilot cohort results, one of the possibilities that may explain the current observations is that different levels of vulnerability to Aβ make an individual more or less likely to respond to the onset of AD pathology. This then determines the severity of dementia symptoms. More recently, a probabilistic model of AD was put forward to revise the amyloid cascade hypothesis [399]. Based on the proposed probabilistic model, AD penetrance is divided into three categories – from the most penetrant fAD, to *APOE ε4*-related sAD, and finally the least penetrant *APOE ε4*-unrelated sAD in the order of decreasing weight of Aβ pathophysiology. Put simply, Aβ pathophysiology affects these categories differently from being the causative

agent in the fAD group to having a decreased weight in penetrance with more contribution from stochastic factors like low-risk gene variants in the *APOE ε4*-unrelated sAD group. This may be a reasonable compromise to clarify that the amyloid cascade hypothesis is still valid to account for a subgroup of AD patients.

Concluding remarks and future work

In this thesis, I provided experimental evidence to support the hypothesis that tau is essential in certain aspects of Aβ-driven toxicity such as cytotoxicity, axonal transport, synapse loss, and neuronal hyperactivation by using the first human *MAPT-/-* iPSC-derived cortical neurons as the cellular model *in vitro*. I also demonstrated that tau depletion itself leads to deficits in neurite outgrowth, axonal transport, and electrophysiological activities in these neurons. Moreover, by studying Aβ-driven synapse loss in sAD patient iPSC-derived cortical neurons, I demonstrated for the first time that cellular vulnerability to extrinsic Aβ insults *in vitro* reflects clinical vulnerability to Aβ burden *in vivo* suggesting that it is feasible to model cognitive decline in response to Aβ in AD patients by measuring synapse loss in their iPSC-derived cortical neurons due to the application of extrinsic Aβ insults. The work described in this thesis corroborated some of the studies using mouse models, but more importantly provided a viable human cellular model to study the role of tau in the context of AD or model sAD clinical vulnerability *in vitro*.

Future extension of the *MAPT* knockout project can involve elucidating the mechanisms on how tau mediates the phenotypes documented in this thesis. For example, one can explore if the reduction in AP firing due to the lack of tau expression implicates the function of AIS

as reported in *Mapt-/-* mice [231], or test if the Aβ-driven cytotoxicity observed in the iPSC-derived cortical neurons is mediated by pTau. In addition, it may be worthwhile to broaden the experimental design by adopting organoid culture, co- or tri-culture with other cell types, or differentiation into various neuronal subtypes. As mentioned earlier in this Chapter, a range of disease-relevant phenotypes were investigated from the more drastic effects of cytotoxicity to more subtle electrophysiological changes. These phenotypes were investigated separately, but it would be important in the future to take a step further to elucidate how these phenotypes are connected to each other. For instance, mitochondria are actively transported to presynaptic terminals to supply energy and buffer Ca^{2+} ions and the influx of which caused by action potentials of a neuron triggers the exocytosis of synaptic vesicles hence neurotransmitter release into the synaptic cleft [400,401]. In Chapters 4 and 5, I showed that there is a bias towards anterograde (towards presynaptic terminals) mitochondrial transport, less frequent and weaker action potential generation and preliminarily greater presynaptic vesicle release in the *MAPT-/-* neurons. Stronger MIRO1-KIF5 linkage, which is needed to facilitate anterograde mitochondrial transport and inhibited by calcium binding, due to less calcium influx resulting from the weaker and less frequent action potential firing could be a possible explanation to the observed phenotypes in the *MAPT-/-* neurons [402]. I have also demonstrated that neurite outgrowth and network activity impairments were observed in the *MAPT-/-* neurons despite normal synaptogenesis as compared to the *MAPT*+/+ neurons. It was previously reported that stable neurite formation led to functional differentiation during synaptogenesis [403], and that synaptotagmin-17 is required for both synaptic health and neurite outgrowth in mice [404]. These observations provide mechanistic insights into how the phenotypes reported in this thesis could be linked to each other. As such, determining the cause-and-effect relationship

among these phenotypes would allow us to isolate the effect of depleting tau which plays a direct role in these subcellular processes.

The results from the *MAPT* knockout project also highlight the potential of tau-lowering strategies in clinical settings of AD. In mice, acute tau knockdown achieved protection against seizures and revered pathological tau deposition [405,406] and there were already seventeen ongoing clinical trials on immunotherapies targeting tau to lower its expression levels as of 2018 [407]. It is however crucial to accurately identify the therapeutic window of tau reduction in the brain as the data presented in this thesis demonstrate functional deficits of human iPSC-derived cortical neurons lacking the expression of tau.

The results from the DFP pilot cohort iPSC study showed that it is feasible to establish a reproducible iPSC modelling system involving multiple patient lines with a defined, optimised, and simplified protocol. Further extension of the DFP project can involve additional patient iPSC lines in a multi-centre setting to improve statistical power from this pilot cohort. Other phenotypes like neurite outgrowth and cytotoxicity are also worth exploring and could potentially be used to correlate with clinical outcomes such as hippocampal volume measured by sMRI. Finally, extrinsic Aβ insults may be substituted by AD brain-derived tau fibrils which can trigger intracellular aggregation in iPSC-derived neurons expressing wild-type tau like the iPSC lines derived from sAD patients [408]. The tau-driven toxicity *in vitro* and clinical vulnerability to pathological tau burden *in vivo* can then be consolidated to investigate if it is also possible to model clinical vulnerability to pathological tau burden using patient-derived iPSCs.

Lastly, the experimental results from the DFP pilot cohort study underscore the potential of precision medicine using patient-derived iPSC lines to model clinical vulnerability *in vivo*. By understanding personal vulnerability towards pathological burdens modelling by patient-derived iPSCs, it is then possible to design the most effective therapeutic regimen that is specific to the individual by using patient-specific iPSC-derived neurons as a proxy for testing *in vitro*. As researchers strive towards harmonising data from larger cohorts of AD patient-derived iPSCs, the accuracy of predicting how a particular AD patient might respond to different levels of disease pathology or a specific treatment *in vivo* based on the experimental measurements from their iPSC-derived neurons *in vitro* will improve. This concerted effort will pave the way for therapeutic interventions tailored to individual patient based on their intrinsic vulnerability to AD.

References

1 **Prince, M. *et al.* (2015) World Alzheimer Report 2015: The Global Impact of Dementia - An analysis of prevalence, incidence, cost and trends. *Alzheimer's Dis. Int.* DOI: 10.1111/j.0963-7214.2004.00293.x**

2 **The top 10 causes of death. . [Online]. Available: https://www.who.int/news-room/fact-sheets/detail/the-top-10-causes-of-death. [Accessed: 30-Dec-2021]**

3 **Gauthier, S. *et al.* (2021) World Alzheimer Report 2021. at <https://www.alzint.org/resource/world-alzheimer-report-2021/>**

4 **Alzheimer, A. (1907) Uber eine eigenartige Erkrankung der Hirnrinde. *Allg ZPsychiat* 64, 146–148**

5 **Graeber, M.B. *et al.* (1998) Histopathology and APOE genotype of the first Alzheimer disease patient, Auguste D. *Neurogenetics* 1, 223–228**

6 **Serrano-Pozo, A. *et al.* (2011) Neuropathological Alterations in Alzheimer Disease. *Cold Spring Harb. Perspect. Med.* 1,**

7 **Wang, X. *et al.* (2019) Sodium oligomannate therapeutically remodels gut microbiota and suppresses gut bacterial amino acids-shaped neuroinflammation to inhibit Alzheimer's disease progression. *Cell Res.* 29, 787–803**

8 **Sevigny, J. *et al.* (2016) The antibody aducanumab reduces Aβ plaques in Alzheimer's disease. *Nature* 537, 50–56**

9 **Alexander, G.C. *et al.* (2021) Revisiting FDA Approval of Aducanumab. *N. Engl. J. Med.* 385, 769–771**

10 **Reitz, C. *et al.* (2020) Late-onset vs nonmendelian early-onset Alzheimer disease. *Neurol. Genet.* 6,**

11 **Panegyres, P.K. and Chen, H.Y. (2013) Differences between early and late onset Alzheimer's disease. *Am. J. Neurodegener. Dis.* 2, 300**

12 Mullan, M. *et al.* (1993) Age of onset in familial early onset Alzheimer's disease correlates with genetic aetiology. *Am. J. Med. Genet.* 48, 129–130

13 Jarmolowicz, A.I. *et al.* (2015) The patterns of inheritance in early-onset dementia: Alzheimer's disease and frontotemporal dementia. *Am. J. Alzheimers. Dis. Other Demen.* 30, 299–306

14 Karantzoulis, S. and Galvin, J.E. (2011) Distinguishing Alzheimer's disease from other major forms of dementia. *Expert Rev. Neurother.* 11, 1579

15 Albert, M.S. *et al.* (2011) The diagnosis of mild cognitive impairment due to Alzheimer's disease: recommendations from the National Institute on Aging-Alzheimer's Association workgroups on diagnostic guidelines for Alzheimer's disease. *Alzheimers. Dement.* 7, 270–279

16 McKhann, G.M. *et al.* (2011) The diagnosis of dementia due to Alzheimer's disease: recommendations from the National Institute on Aging-Alzheimer's Association workgroups on diagnostic guidelines for Alzheimer's disease. *Alzheimers. Dement.* 7, 263–269

17 Sperling, R.A. *et al.* (2011) Toward defining the preclinical stages of Alzheimer's disease: recommendations from the National Institute on Aging-Alzheimer's Association workgroups on diagnostic guidelines for Alzheimer's disease. *Alzheimers. Dement.* 7, 280–292

18 Schneider, L.S. and Dagerman, K.S. (2004) Psychosis of Alzheimer's disease: clinical characteristics and history. *J. Psychiatr. Res.* 38, 105–111

19 Bidzan, L. *et al.* (2012) Aggressive and impulsive behavior in Alzheimer's disease and progression of dementia. *Med. Sci. Monit.* 18, CR182

20 Van Der Mussele, S. *et al.* (2013) Prevalence and associated behavioral symptoms of depression in mild cognitive impairment and dementia due to

Alzheimer's disease. *Int. J. Geriatr. Psychiatry* 28, 947–958

21 Diniz, B.S. *et al.* (2013) Late-life depression and risk of vascular dementia and Alzheimer's disease: systematic review and meta-analysis of community-based cohort studies. *Br. J. Psychiatry* 202, 329–335

22 Peters, M.E. *et al.* (2013) Neuropsychiatric Symptoms as Risk Factors for Progression From CIND to Dementia: The Cache County Study. *Am. J. Geriatr. Psychiatry* 21, 1116–1124

23 Ismail, Z. *et al.* (2016) Neuropsychiatric symptoms as early manifestations of emergent dementia: Provisional diagnostic criteria for mild behavioral impairment. *Alzheimers. Dement.* 12, 195–202

24 Chemerinski, E. *et al.* (2001) The specificity of depressive symptoms in patients with Alzheimer's disease. *Am. J. Psychiatry* 158, 68–72

25 Garre-Olmo, J. *et al.* (2010) Grouping and Trajectories of Neuropsychiatric Symptoms in Patients with Alzheimer's Disease. Part II: Two-Year Patient Trajectories. *J. Alzheimer's Dis.* 22, 1169–1180

26 Zanetti, O. *et al.* (2009) Life Expectancy in Alzheimer's Disease. *Arch. Gerontol. Geriatr.* 49, 237–243

27 Gorelick, P.B. *et al.* (2017) Defining Optimal Brain Health in Adults: A Presidential Advisory From the American Heart Association/American Stroke Association. *Stroke* 48, e284–e303

28 Howard, R. *et al.* (2012) Donepezil and memantine for moderate-to-severe Alzheimer's disease. *N. Engl. J. Med.* 366, 893–903

29 Deture, M.A. and Dickson, D.W. (2019) The neuropathological diagnosis of Alzheimer's disease. *Mol. Neurodegener. 2019 141* 14, 1–18

30 Masters, C.L. *et al.* (1985) Amyloid plaque core protein in Alzheimer disease and

Down syndrome. *Proc. Natl. Acad. Sci. U. S. A.* 82, 4245–9

31 Kosik, K.S. *et al.* (1986) Microtubule-associated protein tau (tau) is a major antigenic component of paired helical filaments in Alzheimer disease. *Proc. Natl. Acad. Sci. U. S. A.* 83, 4044–8

32 Lee, V.M.Y. *et al.* (1991) A68: a major subunit of paired helical filaments and derivatized forms of normal Tau. *Science* 251, 675–678

33 Braak, H. *et al.* (2006) Staging of Alzheimer disease-associated neurofibrillary pathology using paraffin sections and immunocytochemistry. *Acta Neuropathol.* 112, 389–404

34 Jack, C.R. *et al.* (2018) NIA-AA Research Framework: Toward a biological definition of Alzheimer's disease. *Alzheimers. Dement.* 14, 535

35 Bateman, R.J. *et al.* (2012) Clinical and Biomarker Changes in Dominantly Inherited Alzheimer's Disease. *N. Engl. J. Med.* 367, 795–804

36 Klunk, W.E. *et al.* (2004) Imaging brain amyloid in Alzheimer's disease with Pittsburgh Compound-B. *Ann. Neurol.* 55, 306–319

37 Camus, V. *et al.* (2012) Using PET with 18F-AV-45 (florbetapir) to quantify brain amyloid load in a clinical environment. *Eur. J. Nucl. Med. Mol. Imaging* 39, 621

38 Wong, D.F. *et al.* (2010) In vivo imaging of amyloid deposition in Alzheimer disease using the radioligand 18F-AV-45 (florbetapir [corrected] F 18). *J. Nucl. Med.* 51, 913–920

39 Clark, C.M. *et al.* (2012) Cerebral PET with florbetapir compared with neuropathology at autopsy for detection of neuritic amyloid-β plaques: a prospective cohort study. *Lancet. Neurol.* 11, 669–678

40 Spies, P.E. *et al.* (2012) Reviewing reasons for the decreased CSF Abeta42

concentration in Alzheimer disease. *Front. Biosci. (Landmark Ed.* 17, 2024–2034

41 Lewczuk, P. *et al.* (2004) Neurochemical diagnosis of Alzheimer's dementia by CSF Abeta42, Abeta42/Abeta40 ratio and total tau. *Neurobiol. Aging* 25, 273–281

42 Andreasen, N. *et al.* (1999) Cerebrospinal Fluid β-Amyloid(1-42) in Alzheimer Disease: Differences Between Early- and Late-Onset Alzheimer Disease and Stability During the Course of Disease. *Arch. Neurol.* 56, 673–680

43 Shoji, M. *et al.* (1998) Combination assay of CSF tau, A beta 1-40 and A beta 1-42(43) as a biochemical marker of Alzheimer's disease. *J. Neurol. Sci.* 158, 134–140

44 Hansson, O. *et al.* (2019) Advantages and disadvantages of the use of the CSF Amyloid β (Aβ) 42/40 ratio in the diagnosis of Alzheimer's Disease. *Alzheimer's Res. Ther. 2019 111* 11, 1–15

45 Palmqvist, S. *et al.* (2016) Cerebrospinal fluid analysis detects cerebral amyloid-β accumulation earlier than positron emission tomography. *Brain* 139, 1226

46 Schöll, M. *et al.* (2016) PET Imaging of Tau Deposition in the Aging Human Brain. *Neuron* 89, 971–982

47 Cho, H. *et al.* (2016) Tau PET in Alzheimer disease and mild cognitive impairment. *Neurology* 87, 375–383

48 Vanmechelen, E. *et al.* (2000) Quantification of tau phosphorylated at threonine 181 in human cerebrospinal fluid: a sandwich ELISA with a synthetic phosphopeptide for standardization. *Neurosci. Lett.* 285, 49–52

49 Buerger, K. *et al.* (2002) CSF tau protein phosphorylated at threonine 231 correlates with cognitive decline in MCI subjects. *Neurology* 59, 627–629

50 Jack, C.R. *et al.* (2018) Longitudinal tau PET in ageing and Alzheimer's disease.

Brain **141, 1517–1528**

51 Buchhave, P. *et al.* (2012) Cerebrospinal fluid levels of β-amyloid 1-42, but not of tau, are fully changed already 5 to 10 years before the onset of Alzheimer dementia. *Arch. Gen. Psychiatry* 69, 98–106

52 Buerger, K. *et al.* (2006) CSF phosphorylated tau protein correlates with neocortical neurofibrillary pathology in Alzheimer's disease. *Brain* 129, 3035–3041

53 Nakamura, A. *et al.* (2018) High performance plasma amyloid-β biomarkers for Alzheimer's disease. *Nat. 2018 5547691* 554, 249–254

54 Janelidze, S. *et al.* (2020) Plasma P-tau181 in Alzheimer's disease: relationship to other biomarkers, differential diagnosis, neuropathology and longitudinal progression to Alzheimer's dementia. *Nat. Med.* 26, 379–386

55 Paterson, R.W. *et al.* (2018) Cerebrospinal fluid in the differential diagnosis of Alzheimer's disease: Clinical utility of an extended panel of biomarkers in a specialist cognitive clinic. *Alzheimer's Res. Ther.* 10, 1–11

56 Seeburger, J.L. *et al.* (2015) Cerebrospinal Fluid Biomarkers Distinguish Postmortem-Confirmed Alzheimer's Disease from Other Dementias and Healthy Controls in the OPTIMA Cohort. *J. Alzheimer's Dis.* 44, 525–539

57 Ossenkoppele, R. *et al.* (2021) Accuracy of Tau Positron Emission Tomography as a Prognostic Marker in Preclinical and Prodromal Alzheimer Disease: A Head-to-Head Comparison Against Amyloid Positron Emission Tomography and Magnetic Resonance Imaging. *JAMA Neurol.* 78, 961–971

58 Bucci, M. *et al.* (2021) Alzheimer's disease profiled by fluid and imaging markers: tau PET best predicts cognitive decline. *Mol. Psychiatry 2021* DOI: 10.1038/s41380-021-01263-2

59 Bierer, L.M. *et al.* (1995) Neocortical neurofibrillary tangles correlate with dementia severity in Alzheimer's disease. *Arch. Neurol.* 52, 81–88

60 Arriagada, P. V *et al.* (1992) Neurofibrillary tangles but not senile plaques parallel duration and severity of Alzheimer's disease. *Neurology* 42, 631–9

61 Ewers, M. *et al.* (2015) CSF biomarkers for the differential diagnosis of Alzheimer's disease: A large-scale international multicenter study. *Alzheimer's Dement.* 11, 1306–1315

62 Blennow, K. and Hampel, H. (2003) CSF markers for incipient Alzheimer's disease. *Lancet Neurol.* 2, 605–613

63 Blennow, K. *et al.* (1995) Tau protein in cerebrospinal fluid: a biochemical marker for axonal degeneration in Alzheimer disease? *Mol. Chem. Neuropathol.* 26, 231–245

64 Vemuri, P. and Jack, C.R. (2010) Role of structural MRI in Alzheimer's disease. *Alzheimer's Res. Ther.* 2, 1–10

65 Frisoni, G.B. *et al.* (2010) The clinical use of structural MRI in Alzheimer disease. *Nat. Rev. Neurol.* 6, 67

66 Marcus, C. *et al.* (2014) Brain PET in the Diagnosis of Alzheimer's Disease. *Clin. Nucl. Med.* 39, e413

67 Mosconi, L. (2005) Brain glucose metabolism in the early and specific diagnosis of Alzheimer's disease. FDG-PET studies in MCI and AD. *Eur. J. Nucl. Med. Mol. Imaging* 32, 486–510

68 Mosconi, L. *et al.* (2008) Multicenter Standardized 18F-FDG PET Diagnosis of Mild Cognitive Impairment, Alzheimer's Disease, and Other Dementias. *J. Nucl. Med.* 49, 390

69 Ferreira, D. *et al.* (2018) The heterogeneity within Alzheimer's disease. *Aging*

(Albany NY) **10, 3058**

70 Nelson, P.T. *et al.* (2019) Limbic-predominant age-related TDP-43 encephalopathy (LATE): consensus working group report. *Brain* 142, 1503–1527

71 Goate, A. *et al.* (1991) Segregation of a missense mutation in the amyloid precursor protein gene with familial Alzheimer's disease. *Nat. 1991 3496311* 349, 704–706

72 Chartier-Harlin, M.C. *et al.* (1991) Early-onset Alzheimer's disease caused by mutations at codon 717 of the β-amyloid precursor protein gene. *Nat. 1991 3536347* 353, 844–846

73 Murrell, J. *et al.* (1991) A mutation in the Amyloid Precursor Protein Associated with Hereditary Alzheimer's Disease. *Science (80-.).* 254, 97–99

74 Naruse, S. *et al.* (1991) Mis-sense mutation Val→Ile in exon 17 of amyloid precursor protein gene in Japanese familial Alzheimer's disease. *Lancet* 337, 978–979

75 Hardy, J. and Allsop, D. (1991) Amyloid deposition as the central event in the aetiology of Alzheimer's disease. *Trends Pharmacol. Sci.* 12, 383–388

76 Hardy, J.A. and Higgins, G.A. (1992) Alzheimer's disease: The amyloid cascade hypothesis. *Science (80-.).* 256, 184–185

77 Wisniewski, K.E. *et al.* (1985) Occurrence of neuropathological changes and dementia of Alzheimer's disease in Down's syndrome. *Ann. Neurol.* 17, 278–282

78 Head, E. *et al.* (2012) Alzheimer's Disease in Down Syndrome. *Eur. J. Neurodegener. Dis.* 1, 353

79 Prasher, V.P. *et al.* (1998) Molecular mapping of alzheimer-type dementia in Down's syndrome. *Ann. Neurol.* 43, 380–383

80 Rovelet-Lecrux, A. *et al.* (2005) APP locus duplication causes autosomal dominant early-onset Alzheimer disease with cerebral amyloid angiopathy. *Nat. Genet. 2006 381* 38, 24–26

81 Sherrington, R. *et al.* (1995) Cloning of a gene bearing missense mutations in early-onset familial Alzheimer's disease. *Nat. 1995 3756534* 375, 754–760

82 Rogaev, E.I. *et al.* (1995) Familial Alzheimer's disease in kindreds with missense mutations in a gene on chromosome 1 related to the Alzheimer's disease type 3 gene. *Nature* 376, 775–778

83 Levy-Lahad, E. *et al.* (1995) Candidate gene for the chromosome 1 familial Alzheimer's disease locus. *Science* 269, 973–977

84 Wolfe, M.S. *et al.* (1999) Two transmembrane aspartates in presenilin-1 required for presenilin endoproteolysis and γ-secretase activity. *Nat. 1999 3986727* 398, 513–517

85 De Strooper, B. *et al.* (1998) Deficiency of presenilin-1 inhibits the normal cleavage of amyloid precursor protein. *Nat. 1998 3916665* 391, 387–390

86 Scheuner, D. *et al.* (1996) Secreted amyloid β–protein similar to that in the senile plaques of Alzheimer's disease is increased in vivo by the presenilin 1 and 2 and APP mutations linked to familial Alzheimer's disease. *Nat. Med. 1996 28* 2, 864–870

87 Duff, K. *et al.* (1996) Increased amyloid-β42(43) in brains of mice expressing mutant presenilin 1. *Nat. 1996 3836602* 383, 710–713

88 Spillantini, M.G. *et al.* (1998) Tau Pathology in Two Dutch Families with Mutations in the Microtubule-Binding Region of Tau. *Am. J. Pathol.* 153, 1359–1363

89 Kouri, N. *et al.* (2014) Novel mutation in MAPT exon 13 (p.N410H) causes

corticobasal degeneration. ***Acta Neuropathol.*** **127, 271–282**

90 Tacik, P. ***et al.*** **(2015) A Novel Tau Mutation in Exon 12, p.Q336H, Causes Hereditary Pick Disease.** ***J. Neuropathol. Exp. Neurol.*** **74, 1042–1052**

91 Nochlin, D. ***et al.*** **(1993) Comparison of the severity of neuropathologic changes in familial and sporadic Alzheimer's disease.** ***Alzheimer Dis. Assoc. Disord.*** **7, 212–222**

92 Haupt, M. ***et al.*** **(1992) Alzheimer's disease: identical phenotype of familial and non-familial cases.** ***J. Neurol.*** **239, 248–250**

93 Armstrong, R. (2011) Spatial patterns of β-amyloid (Aβ) deposits in familial and sporadic Alzheimer ' s disease. ***Folia Neuropathol.***

94 Rosselli, M. ***et al.*** **(2000) Cognitive Decline in Patients with Familial Alzheimer's Disease Associated with E280a Presenilin-1 Mutation: A Longitudinal Study.** ***J. Clin. Exp. Neuropsychol.*** **22, 483–495**

95 Wattmo, C. and Wallin, Å.K. (2017) Early-versus Late-Onset Alzheimer Disease: Long-Term Functional Outcomes, Nursing Home Placement, and Risk Factors for Rate of Progression. ***Dement. Geriatr. Cogn. Dis. Extra*** **7, 172**

96 Armstrong, R.A. (2014) Factors Determining Disease Duration in Alzheimer's Disease: A Postmortem Study of 103 Cases Using the Kaplan-Meier Estimator and Cox Regression. ***Biomed Res. Int.*** **2014,**

97 Jonsson, T. ***et al.*** **(2012) A mutation in APP protects against Alzheimer's disease and age-related cognitive decline.** ***Nature*** **488, 96**

98 Kero, M. ***et al.*** **(2013) Amyloid precursor protein (APP) A673T mutation in the elderly Finnish population.** ***Neurobiol. Aging*** **34, 1518.e1-1518.e3**

99 Arboleda-Velasquez, J.F. ***et al.*** **(2019) Resistance to autosomal dominant Alzheimer's disease in an APOE3 Christchurch homozygote: a case report.** ***Nat.***

Med. 2019 2511 **25, 1680–1683**

100 Wardell, M.R. ***et al.*** **(1987) Apolipoprotein E2-Christchurch (136 Arg----Ser). New variant of human apolipoprotein E in a patient with type III hyperlipoproteinemia.** ***J. Clin. Invest.*** **80, 483–490**

101 Corder, E.H. ***et al.*** **(1993) Gene dose of apolipoprotein E type 4 allele and the risk of Alzheimer's disease in late onset families.** ***Science*** **261, 921–923**

102 Saunders, A.M. ***et al.*** **(1993) Association of apolipoprotein E allele epsilon 4 with late-onset familial and sporadic Alzheimer's disease.** ***Neurology*** **43, 1467–1472**

103 Corder, E.H. ***et al.*** **(1994) Protective effect of apolipoprotein E type 2 allele for late onset Alzheimer disease.** ***Nat. Genet. 1994 72*** **7, 180–184**

104 Caselli, R.J. ***et al.*** **(2009) Longitudinal modeling of age-related memory decline and the APOE epsilon4 effect.** ***N. Engl. J. Med.*** **361, 255–263**

105 Reiman, E.M. ***et al.*** **(2020) Exceptionally low likelihood of Alzheimer's dementia in APOE2 homozygotes from a 5,000-person neuropathological study.** ***Nat. Commun. 2020 111*** **11, 1–11**

106 Naj, A.C. ***et al.*** **(2011) Common variants at MS4A4/MS4A6E, CD2AP, CD33 and EPHA1 are associated with late-onset Alzheimer's disease.** ***Nat. Genet. 2011 435*** **43, 436–441**

107 Lambert, J.C. ***et al.*** **(2009) Genome-wide association study identifies variants at CLU and CR1 associated with Alzheimer's disease.** ***Nat. Genet. 2009 4110*** **41, 1094–1099**

108 Lambert, J.C. ***et al.*** **(2013) Meta-analysis of 74,046 individuals identifies 11 new susceptibility loci for Alzheimer's disease.** ***Nat. Genet.*** **45, 1452–1458**

109 Hollingworth, P. ***et al.*** **(2011) Common variants at ABCA7, MS4A6A/MS4A4E, EPHA1, CD33 and CD2AP are associated with Alzheimer's disease.** ***Nat. Genet.***

2011 435 **43, 429–435**

110 Harold, D. *et al.* (2009) Genome-wide association study identifies variants at CLU and PICALM associated with Alzheimer's disease. *Nat. Genet. 2009 4110* 41, 1088–1093

111 Jansen, I.E. *et al.* (2019) Genome-wide meta-analysis identifies new loci and functional pathways influencing Alzheimer's disease risk. *Nat. Genet. 2019 513* 51, 404–413

112 Wightman, D.P. *et al.* (2021) A genome-wide association study with 1,126,563 individuals identifies new risk loci for Alzheimer's disease. *Nat. Genet. 2021 539* 53, 1276–1282

113 Kunkle, B.W. *et al.* (2019) Genetic meta-analysis of diagnosed Alzheimer's disease identifies new risk loci and implicates Aβ, tau, immunity and lipid processing. *Nat. Genet. 2019 513* 51, 414–430

114 Coppola, G. *et al.* (2012) Evidence for a role of the rare p.A152T variant in MAPT in increasing the risk for FTD-spectrum and Alzheimer's diseases. *Hum. Mol. Genet.* 21, 3500–3512

115 Lee, S.E. *et al.* (2013) Neurodegenerative disease phenotypes in carriers of MAPT p.A152T, a risk factor for frontotemporal dementia spectrum disorders and Alzheimer disease. *Alzheimer Dis. Assoc. Disord.* 27, 302–309

116 Freudenberg-Hua, Y. *et al.* (2018) The role of genetics in advancing precision medicine for Alzheimer's Disease-A narrative review. *Front. Med.* 5, 108

117 Sims, R. *et al.* (2020) The multiplex model of the genetics of Alzheimer's disease. *Nat. Neurosci. 2020 233* 23, 311–322

118 de Rojas, I. *et al.* (2021) Common variants in Alzheimer's disease and risk stratification by polygenic risk scores. *Nat. Commun.* 12,

119 Livingston, G. *et al.* (2020) Dementia prevention, intervention, and care: 2020 report of the Lancet Commission. *Lancet (London, England)* 396, 413

120 Rosenberg, A. *et al.* (2018) Multidomain lifestyle intervention benefits a large elderly population at risk for cognitive decline and dementia regardless of baseline characteristics: The FINGER trial. *Alzheimers. Dement.* 14, 263–270

121 Kivipelto, M. *et al.* (2020) World-Wide FINGERS Network: A global approach to risk reduction and prevention of dementia. *Alzheimers. Dement.* 16, 1078–1094

122 Stephen, R. *et al.* (2021) Development of the First WHO Guidelines for Risk Reduction of Cognitive Decline and Dementia: Lessons Learned and Future Directions. *Front. Neurol.* 12,

123 Kang, J. *et al.* (1987) The precursor of Alzheimer's disease amyloid A4 protein resembles a cell-surface receptor. *Nature* 325, 733–736

124 Nunan, J. and Small, D.H. (2000) Regulation of APP cleavage by alpha-, beta- and gamma-secretases. *FEBS Lett.* 483, 6–10

125 Chen, G.F. *et al.* (2017) Amyloid beta: structure, biology and structure-based therapeutic development. *Acta Pharmacol. Sin. 2017 389* 38, 1205–1235

126 Cai, Y. *et al.* (2015) Mutations in presenilin 2 and its implications in Alzheimer's disease and other dementia-associated disorders. *Clin. Interv. Aging* 10, 1163

127 Brothers, H.M. *et al.* (2018) The Physiological Roles of Amyloid-β Peptide Hint at New Ways to Treat Alzheimer's Disease. *Front. Aging Neurosci.* 10, 118

128 Dovey, H.F. *et al.* (1993) Cells with a familial Alzheimer's disease mutation produce authentic beta-peptide. *Neuroreport* 4, 1039–1042

129 Iwatsubo, T. *et al.* (1996) Full-length amyloid-beta (1-42(43)) and amino-terminally modified and truncated amyloid-beta 42(43) deposit in diffuse plaques. *Am. J. Pathol.* 149, 1823

130 Gravina, S.A. *et al.* (1995) Amyloid beta protein (A beta) in Alzheimer's disease brain. Biochemical and immunocytochemical analysis with antibodies specific for forms ending at A beta 40 or A beta 42(43). *J. Biol. Chem.* 270, 7013–7016

131 Suzuki, N. *et al.* (1994) An increased percentage of long amyloid beta protein secreted by familial amyloid beta protein precursor (beta APP717) mutants. *Science* 264, 1336–1340

132 Citron, M. *et al.* (1997) Mutant presenilins of Alzheimer's disease increase production of 42-residue amyloid beta-protein in both transfected cells and transgenic mice. *Nat. Med.* 3, 67–72

133 Marina, G.B. *et al.* (2003) Amyloid beta -protein (Abeta) assembly: Abeta 40 and Abeta 42 oligomerize through distinct pathways. *Proc. Natl. Acad. Sci. U. S. A.* 100, 330–335

134 Dickson, D.W. (1997) The Pathogenesis of Senile Plaques. *J. Neuropathol. Exp. Neurol.* 56, 321–339

135 McLean, C.A. *et al.* (1999) Soluble pool of Abeta amyloid as a determinant of severity of neurodegeneration in Alzheimer's disease. *Ann. Neurol.* 46, 860–866

136 Näslund, J. *et al.* (2000) Correlation between elevated levels of amyloid beta-peptide in the brain and cognitive decline. *JAMA* 283, 1571–1577

137 Hölttä, M. *et al.* (2013) Evaluating Amyloid-β Oligomers in Cerebrospinal Fluid as a Biomarker for Alzheimer's Disease. *PLoS One* 8, e66381

138 Savage, M.J. *et al.* (2014) A Sensitive Aβ Oligomer Assay Discriminates Alzheimer's and Aged Control Cerebrospinal Fluid. *J. Neurosci.* 34, 2884–2897

139 Hsia, A.Y. *et al.* (1999) Plaque-independent disruption of neural circuits in Alzheimer's disease mouse models. *Proc. Natl. Acad. Sci. U. S. A.* 96, 3228–3233

140 Mucke, L. *et al.* (2000) High-level neuronal expression of abeta 1-42 in wild-type

human amyloid protein precursor transgenic mice: synaptotoxicity without plaque formation. *J. Neurosci.* 20, 4050–4058

141 Walsh, D.M. *et al.* (2002) Naturally secreted oligomers of amyloid beta protein potently inhibit hippocampal long-term potentiation in vivo. *Nature* 416, 535–539

142 Jin, M. *et al.* (2011) Soluble amyloid β-protein dimers isolated from Alzheimer cortex directly induce Tau hyperphosphorylation and neuritic degeneration. *Proc. Natl. Acad. Sci. U. S. A.* 108, 5819–5824

143 Zempel, H. *et al.* (2010) Aβ Oligomers Cause Localized Ca2+ Elevation, Missorting of Endogenous Tau into Dendrites, Tau Phosphorylation, and Destruction of Microtubules and Spines. *J. Neurosci.* 30, 11938–11950

144 DaRocha-Souto, B. *et al.* (2012) Activation of glycogen synthase kinase-3 beta mediates β-amyloid induced neuritic damage in Alzheimer's disease. *Neurobiol. Dis.* 45, 425

145 De Felice, F.G. *et al.* (2008) Alzheimer's disease-type neuronal tau hyperphosphorylation induced by Aβ oligomers. *Neurobiol. Aging* 29, 1334

146 De Felice, F.G. *et al.* (2007) Aβ oligomers induce neuronal oxidative stress through an N-methyl-D-aspartate receptor-dependent mechanism that is blocked by the Alzheimer drug memantine. *J. Biol. Chem.* 282, 11590–11601

147 Shankar, G.M. *et al.* (2007) Natural oligomers of the Alzheimer amyloid-beta protein induce reversible synapse loss by modulating an NMDA-type glutamate receptor-dependent signaling pathway. *J. Neurosci.* 27, 2866–2875

148 DaRocha-Souto, B. *et al.* (2012) Activation of glycogen synthase kinase-3 beta mediates β-amyloid induced neuritic damage in Alzheimer's disease. *Neurobiol. Dis.* 45, 425–437

149 Alberdi, E. *et al.* (2010) Amyloid beta oligomers induce Ca2+ dysregulation and neuronal death through activation of ionotropic glutamate receptors. *Cell Calcium* 47, 264–272

150 Hector, A. and Brouillette, J. (2021) Hyperactivity Induced by Soluble Amyloid-β Oligomers in the Early Stages of Alzheimer's Disease. *Front. Mol. Neurosci.* 13, 244

151 Neve, R.L. *et al.* (1986) Identification of cDNA clones for the human microtubule-associated protein tau and chromosomal localization of the genes for tau and microtubule-associated protein 2. *Mol. Brain Res.* 1, 271–280

152 Andreadis, A. (2005) Tau gene alternative splicing: expression patterns, regulation and modulation of function in normal brain and neurodegenerative diseases. *Biochim. Biophys. Acta - Mol. Basis Dis.* 1739, 91–103

153 Goedert, M. *et al.* (1989) Multiple isoforms of human microtubule-associated protein tau: sequences and localization in neurofibrillary tangles of Alzheimer's disease. *Neuron* 3, 519–526

154 Kosik, K.S. *et al.* (1989) Developmentally regulated expression of specific tau sequences. *Neuron* 2, 1389–1397

155 Takuma, H. *et al.* (2003) Isoforms changes of tau protein during development in various species. *Dev. Brain Res.* 142, 121–127

156 Wang, S. *et al.* (2020) Correlation between mouse age and human age in anti-tumor research: Significance and method establishment. *Life Sci.* 242, 117242

157 Goedert, M. and Jakes, R. (1990) Expression of separate isoforms of human tau protein: Correlation with the tau pattern in brain and effects on tubulin polymerization. *EMBO J.* 9, 4225–4230

158 Trabzuni, D. *et al.* (2012) MAPT expression and splicing is differentially

regulated by brain region: relation to genotype and implication for tauopathies. *Hum. Mol. Genet.* 21, 4094–4103

159 Hu, W. *et al.* (2017) Expression of tau pathology-related proteins in different brain regions: A molecular basis of tau pathogenesis. *Front. Aging Neurosci.* 9, 311

160 Šimić, G. *et al.* (2016) Tau Protein Hyperphosphorylation and Aggregation in Alzheimer's Disease and Other Tauopathies, and Possible Neuroprotective Strategies. *Biomol. 2016, Vol. 6, Page 6* 6, 6

161 Binder, L.I. *et al.* (1985) The distribution of tau in the mammalian central nervous system. *J. Cell Biol.* 101, 1371–1378

162 Papasozomenos, S.C. and Binder, L.I. (1987) Phosphorylation determines two distinct species of tau in the central nervous system. *Cell Motil. Cytoskeleton* 8, 210–226

163 Sultan, A. *et al.* (2011) Nuclear Tau, a Key Player in Neuronal DNA Protection. *J. Biol. Chem.* 286, 4566–4575

164 Mandelkow, E.M. and Mandelkow, E. (2012) Biochemistry and Cell Biology of Tau Protein in Neurofibrillary Degeneration. *Cold Spring Harb. Perspect. Med.* 2, a006247

165 Feinstein, S.C. and Wilson, L. (2005) Inability of tau to properly regulate neuronal microtubule dynamics: a loss-of-function mechanism by which tau might mediate neuronal cell death. *Biochim. Biophys. Acta - Mol. Basis Dis.* 1739, 268–279

166 Dixit, R. *et al.* (2008) Differential regulation of dynein and kinesin motor proteins by tau. *Science* 319, 1086–1089

167 Stamer, K. *et al.* (2002) Tau blocks traffic of organelles, neurofilaments, and

APP vesicles in neurons and enhances oxidative stress. *J. Cell Biol.* 156, 1051–1063

168 Zhou, L. *et al.* (2017) Tau association with synaptic vesicles causes presynaptic dysfunction. *Nat. Commun. 2017 81* 8, 1–13

169 McInnes, J. *et al.* (2018) Synaptogyrin-3 Mediates Presynaptic Dysfunction Induced by Tau. *Neuron* 97, 823-835.e8

170 Lee, G. *et al.* (1998) Tau interacts with src-family non-receptor tyrosine kinases. *J. Cell Sci.* 111 (Pt 2, 3167–3177

171 Ittner, L.M. *et al.* (2010) Dendritic function of tau mediates amyloid-β toxicity in alzheimer's disease mouse models. *Cell* 142, 387–397

172 Sotiropoulos, I. *et al.* (2017) Atypical, non-standard functions of the microtubule associated Tau protein. *Acta Neuropathol. Commun.* 5, 91

173 Kopke, E. *et al.* (1993) Microtubule-associated protein tau. Abnormal phosphorylation of a non-paired helical filament pool in Alzheimer disease. *J. Biol. Chem.* 268, 24374–24384

174 Grundke-Iqbal, I. *et al.* (1986) Abnormal phosphorylation of the microtubule-associated protein tau (tau) in Alzheimer cytoskeletal pathology. *Proc. Natl. Acad. Sci. U. S. A.* 83, 4913–4917

175 Braak, F. *et al.* (1994) A sequence of cytoskeleton changes related to the formation of neurofibrillary tangles and neuropil threads. *Acta Neuropathol.* 87, 554–567

176 Von Bergen, M. *et al.* (2000) Assembly of tau protein into Alzheimer paired helical filaments depends on a local sequence motif ((306)VQIVYK(311)) forming beta structure. *Proc. Natl. Acad. Sci. U. S. A.* 97, 5129–5134

177 Kadavath, H. *et al.* (2015) Tau stabilizes microtubules by binding at the interface

between tubulin heterodimers. *Proc. Natl. Acad. Sci. U. S. A.* 112, 7501–7506

178 Kenessey, A. and Yen, S.H.C. (1993) The extent of phosphorylation of fetal tau is comparable to that of PHF-tau from Alzheimer paired helical filaments. *Brain Res.* 629, 40–46

179 Wang, J.Z. *et al.* (2007) Kinases and phosphatases and tau sites involved in Alzheimer neurofibrillary degeneration. *Eur. J. Neurosci.* 25, 59

180 Ittner, A. *et al.* (2016) Site-specific phosphorylation of tau inhibits amyloid-β toxicity in Alzheimer's mice. *Science* 354, 904–908

181 Wang, Y. and Mandelkow, E. (2015) Tau in physiology and pathology. *Nat. Rev. Neurosci. 2015 171* 17, 22–35

182 Schneider, A. *et al.* (1999) Phosphorylation that detaches tau protein from microtubules (Ser262, Ser214) also protects it against aggregation into Alzheimer paired helical filaments. *Biochemistry* 38, 3549–3558

183 Goedert, M. *et al.* (2000) Reduced binding of protein phosphatase 2A to tau protein with frontotemporal dementia and parkinsonism linked to chromosome 17 mutations. *J. Neurochem.* 75, 2155–2162

184 Alonso, A.D.C. *et al.* (2004) Promotion of Hyperphosphorylation by Frontotemporal Dementia Tau Mutations *. *J. Biol. Chem.* 279, 34873–34881

185 Hong, M. *et al.* (1998) Mutation-specific functional impairments in distinct tau isoforms of hereditary FTDP-17. *Science* 282, 1914–7

186 Hutton, M. *et al.* (1998) Association of missense and 5′-splice-site mutations in tau with the inherited dementia FTDP-17. *Nat. 1998 3936686* 393, 702–705

187 Sperfeld, A.D. *et al.* (1999) FTDP-17: an early-onset phenotype with parkinsonism and epileptic seizures caused by a novel mutation. *Ann. Neurol.* 46, 708–715

188 Lewis, J. *et al.* (2000) Neurofibrillary tangles, amyotrophy and progressive motor disturbance in mice expressing mutant (P301L) tau protein. *Nat. Genet. 2000 254* 25, 402–405

189 Allen, B. *et al.* (2002) Abundant Tau Filaments and Nonapoptotic Neurodegeneration in Transgenic Mice Expressing Human P301S Tau Protein. *J. Neurosci.* 22, 9340

190 Ashe, K.H. and Zahs, K.R. (2010) Probing the biology of Alzheimer's disease in mice. *Neuron* 66, 631

191 Lewis, J. *et al.* (2001) Enhanced neurofibrillary degeneration in transgenic mice expressing mutant tau and APP. *Science (80-.).* 293, 1487–1491

192 Götz, J. *et al.* (2001) Formation of neurofibrillary tangles in P301l tau transgenic mice induced by Abeta 42 fibrils. *Science* 293, 1491–1495

193 Umeda, T. *et al.* (2014) Neurofibrillary tangle formation by introducing wild-type human tau into APP transgenic mice. *Acta Neuropathol.* 127, 685–698

194 Hsiao, K. *et al.* (1996) Correlative Memory Deficits, Aβ Elevation, and Amyloid Plaques in Transgenic Mice. *Science (80-.).* 274, 99–102

195 Chui, D.H. *et al.* (1999) Transgenic mice with Alzheimer presenilin 1 mutations show accelerated neurodegeneration without amyloid plaque formation. *Nat. Med.* 5, 560–564

196 Hwang, D.Y. *et al.* (2002) Alterations in behavior, amyloid p-42, caspase-3, and Cox-2 in mutant PS2 transgenic mouse model of Alzheimer's disease. *FASEB J.* 16, 805–813

197 Holcomb, L. *et al.* (1998) Accelerated Alzheimer-type phenotype in transgenic mice carrying both mutant amyloid precursor protein and presenilin 1 transgenes. *Nat. Med.* 4, 97–100

198 Pickett, E.K. *et al.* (2019) Amyloid Beta and Tau Cooperate to Cause Reversible Behavioral and Transcriptional Deficits in a Model of Alzheimer's Disease. *Cell Rep.* 29, 3592-3604.e5

199 Jackson, R.J. *et al.* (2016) Human tau increases amyloid β plaque size but not amyloid β-mediated synapse loss in a novel mouse model of Alzheimer's disease. *Eur. J. Neurosci.* 44, 3056–3066

200 Pooler, A.M. *et al.* (2015) Amyloid accelerates tau propagation and toxicity in a model of early Alzheimer's disease. *Acta Neuropathol. Commun.* 3, 14

201 Sasaguri, H. *et al.* (2017) APP mouse models for Alzheimer's disease preclinical studies. *EMBO J.* 36, 2473–2487

202 Gamache, J. *et al.* (2019) Factors other than hTau overexpression that contribute to tauopathy-like phenotype in rTg4510 mice. *Nat. Commun.* 10,

203 Saito, T. *et al.* (2014) Single App knock-in mouse models of Alzheimer's disease. *Nat. Neurosci. 2014 175* 17, 661–663

204 He, Z. *et al.* (2017) Amyloid-β plaques enhance Alzheimer's brain tau-seeded pathologies by facilitating neuritic plaque tau aggregation. *Nat. Med. 2017 241* 24, 29–38

205 Saito, T. *et al.* (2019) Humanization of the entire murine Mapt gene provides a murine model of pathological human tau propagation. *J. Biol. Chem.* 294, 12754

206 Oblak, A.L. *et al.* (2020) Model organism development and evaluation for late-onset Alzheimer's disease: MODEL-AD. *Alzheimer's Dement. Transl. Res. Clin. Interv.* 6, e12110

207 Kotredes, K.P. *et al.* (2021) Uncovering Disease Mechanisms in a Novel Mouse Model Expressing Humanized APOEε4 and Trem2*R47H. *Front. Aging Neurosci.* 13, 634

208 Zheng, H. *et al.* (1995) B-Amyloid Precursor Protein-Deficient Mice Show Reactive Gliosis and Decreased Locomotor Activity. *Cell* 81, 525–531

209 Dawson, G.R. *et al.* (1999) Age-related cognitive deficits, impaired long-term potentiation and reduction in synaptic marker density in mice lacking the beta-amyloid precursor protein. *Neuroscience* 90, 1–13

210 Mallm, J.P. *et al.* (2010) Generation of conditional null alleles for APP and APLP2. *genesis* 48, 200–206

211 Steubler, V. *et al.* (2021) Loss of all three APP family members during development impairs synaptic function and plasticity, disrupts learning, and causes an autism-like phenotype. *EMBO J.* 40,

212 Mehr, A. *et al.* (2020) Lack of APP and APLP2 in GABAergic Forebrain Neurons Impairs Synaptic Plasticity and Cognition. *Cereb. Cortex* 30, 4044–4063

213 Luo, Y. *et al.* (2001) Mice deficient in BACE1, the Alzheimer's β-secretase, have normal phenotype and abolished β-amyloid generation. *Nat. Neurosci. 2001 43* 4, 231–232

214 Roberds, S.L. *et al.* (2001) BACE knockout mice are healthy despite lacking the primary β-secretase activity in brain: implications for Alzheimer's disease therapeutics. *Hum. Mol. Genet.* 10, 1317–1324

215 Barão, S. *et al.* (2016) BACE1 Physiological Functions May Limit Its Use as Therapeutic Target for Alzheimer's Disease. *Trends Neurosci.* 39, 158–169

216 Hu, X. *et al.* (2018) BACE1 deletion in the adult mouse reverses preformed amyloid deposition and improves cognitive functions. *J. Exp. Med.* 215, 927

217 Ou-Yang, M.H. *et al.* (2018) Axonal organization defects in the hippocampus of adult conditional BACE1 knockout mice. *Sci. Transl. Med.* 10,

218 Shen, J. *et al.* (1997) Skeletal and CNS Defects in Presenilin-1-Deficient Mice.

Cell **89, 629–639**

219 Yu, H. *et al.* (2001) APP processing and synaptic plasticity in presenilin-1 conditional knockout mice. *Neuron* 31, 713–726

220 Saura, C.A. *et al.* (2004) Loss of Presenilin Function Causes Impairments of Memory and Synaptic Plasticity Followed by Age-Dependent Neurodegeneration. *Neuron* 42, 23–36

221 Saura, C.A. *et al.* (2005) Conditional inactivation of presenilin 1 prevents amyloid accumulation and temporarily rescues contextual and spatial working memory impairments in amyloid precursor protein transgenic mice. *J. Neurosci.* 25, 6755–6764

222 Beglopoulos, V. *et al.* (2004) Reduced beta-amyloid production and increased inflammatory responses in presenilin conditional knock-out mice. *J. Biol. Chem.* 279, 46907–46914

223 Fujio, K. *et al.* (2007) 14-3-3 proteins and protein phosphatases are not reduced in tau-deficient mice. *Neuroreport* 18, 1049–1052

224 Harada, A. *et al.* (1994) Altered microtubule organization in small-calibre axons of mice lacking tau protein. *Nature* 369, 488–491

225 Tucker, K.L. *et al.* (2001) Neurotrophins are required for nerve growth during development. *Nat. Neurosci.* 4, 29–32

226 Dawson, H.N. *et al.* (2001) Inhibition of neuronal maturation in primary hippocampal neurons from tau deficient mice. *J. Cell Sci.* 114, 1179–1187

227 van Hummel, A. *et al.* (2016) No Overt Deficits in Aged Tau-Deficient C57Bl/6.Mapttm1(EGFP)Kit GFP Knockin Mice. *PLoS One* 11, e0163236

228 Tan, D.C.S. *et al.* (2018) Generation of a New Tau Knockout (tau Δex1) Line Using CRISPR/Cas9 Genome Editing in Mice. *J. Alzheimer's Dis.* 62, 571–578

229 Lei, P. *et al.* (2012) Tau deficiency induces parkinsonism with dementia by impairing APP-mediated iron export. *Nat. Med.* 18, 293–297

230 Lei, P. *et al.* (2014) Motor and cognitive deficits in aged tau knockout mice in two background strains. *Mol. Neurodegener.* 9, 1–12

231 Chang, C.W. *et al.* (2021) Tau reduction affects excitatory and inhibitory neurons differently, reduces excitation/inhibition ratios, and counteracts network hypersynchrony. *Cell Rep.* 37, 109855

232 Tai, C. *et al.* (2020) Tau reduction prevents key features of autism in mouse models. *Neuron* 106, 421

233 Holth, J.K. *et al.* (2013) Tau Loss Attenuates Neuronal Network Hyperexcitability in Mouse and Drosophila Genetic Models of Epilepsy. *J. Neurosci.* 33, 1651–1659

234 Roberson, E.D. *et al.* (2007) Reducing Endogenous Tau Ameliorates Amyloid ß-Induced Deficits in an Alzheimer's Disease Mouse Model. *Science (80-.).* 316,

235 Regan, P. *et al.* (2015) Tau Phosphorylation at Serine 396 Residue Is Required for Hippocampal LTD. *J. Neurosci.* 35, 4804–4812

236 Kimura, T. *et al.* (2014) Microtubule-associated protein tau is essential for long-term depression in the hippocampus. 369,

237 Shipton, O.A. *et al.* (2011) Tau Protein Is Required for Amyloid β-Induced Impairment of Hippocampal Long-Term Potentiation. *J. Neurosci.* 31,

238 Ahmed, T. *et al.* (2014) Cognition and hippocampal synaptic plasticity in mice with a homozygous tau deletion. *Neurobiol. Aging* 35, 2474–2478

239 Burnouf, S. *et al.* (2016) Deletion of endogenous Tau proteins is not detrimental in Drosophila. *Sci. Rep.* 6, 1–11

240 Bolkan, B.J. and Kretzschmar, D. (2014) Loss of Tau results in defects in

photoreceptor development and progressive neuronal degeneration in Drosophila. *Dev. Neurobiol.* 74, 1210–1225

241 Papanikolopoulou, K. *et al.* (2019) Drosophila Tau Negatively Regulates Translation and Olfactory Long-Term Memory, But Facilitates Footshock Habituation and Cytoskeletal Homeostasis. *J. Neurosci.* 39, 8315–8329

242 Rapoport, M. *et al.* (2002) Tau is essential to beta -amyloid-induced neurotoxicity. *Proc. Natl. Acad. Sci. U. S. A.* 99, 6364–9

243 Leroy, K. *et al.* (2012) Lack of tau proteins rescues neuronal cell death and decreases amyloidogenic processing of APP in APP/PS1 mice. *Am. J. Pathol.* 181, 1928–1940

244 Nussbaum, J.M. *et al.* (2012) Prion-like behaviour and tau-dependent cytotoxicity of pyroglutamylated amyloid-β. *Nature* 485, 651–655

245 King, M.E. *et al.* (2006) Tau-dependent microtubule disassembly initiated by prefibrillar beta-amyloid. *J. Cell Biol.* 175, 541–546

246 Zempel, H. *et al.* (2013) Amyloid-β oligomers induce synaptic damage via Tau-dependent microtubule severing by TTLL6 and spastin. *EMBO J.* 32, 2920–2937

247 Vossel, K.A. *et al.* (2015) Tau reduction prevents Aβ-induced axonal transport deficits by blocking activation of GSK3β. *J. Cell Biol.* 209, 419–433

248 Vossel, K.A. *et al.* (2010) Tau Reduction Prevents A b -Induced Defects in Axonal Transport. *Science (80-.).* 041787, 8–10

249 Vargas-Caballero, M. *et al.* (2017) Wild-Type, but Not Mutant N296H, Human Tau Restores Aβ-Mediated Inhibition of LTP in Tau−/− mice. *Front. Neurosci.* 11, 201

250 Cho, J.H. and Johnson, G.V.W. (2003) Glycogen Synthase Kinase 3β Phosphorylates Tau at Both Primed and Unprimed Sites: Differential Impact on

Microtubule Binding. *J. Biol. Chem.* 278, 187–193

251 Puzzo, D. *et al.* (2020) Tau is not necessary for amyloid-β–induced synaptic and memory impairments. *J. Clin. Invest.* 130, 4831–4844

252 Dawson, H.N. *et al.* (2010) Loss of tau elicits axonal degeneration in a mouse model of Alzheimer's disease. *Neuroscience* 169, 516–531

253 Roberson, E.D. *et al.* (2011) Amyloid-β/Fyn–Induced Synaptic, Network, and Cognitive Impairments Depend on Tau Levels in Multiple Mouse Models of Alzheimer's Disease. *J. Neurosci.* 31, 700–711

254 Morris, M. *et al.* (2011) Tau Reduction Does Not Prevent Motor Deficits in Two Mouse Models of Parkinson ' s Disease. *PLoS One* 6, 1–7

255 Jiao, L. *et al.* (2020) Tau knockout exacerbates degeneration of parvalbumin-positive neurons in substantia nigra pars reticulata in Parkinson's disease-related α-synuclein A53T mice. *FASEB J.* 34, 12239–12254

256 Singh, B. *et al.* (2019) Tau is required for progressive synaptic and memory deficits in a transgenic mouse model of α-synucleinopathy. *Acta Neuropathol.* 138, 551–574

257 Espinoza, M. *et al.* (2008) Differential Incorporation of Tau Isoforms in Alzheimer's Disease. *J. Alzheimers. Dis.* 14, 1

258 Llorens-Martin, M. *et al.* (2012) Tau isoform with three microtubule binding domains is a marker of new axons generated from the subgranular zone in the hippocampal dentate gyrus: implications for Alzheimer's disease. *J. Alzheimers. Dis.* 29, 921–930

259 Andorfer, C. *et al.* (2003) Hyperphosphorylation and aggregation of tau in mice expressing normal human tau isoforms. *J. Neurochem.* 86, 582–590

260 Schwab, C. *et al.* (2004) Transgenic mice overexpressing amyloid beta protein

are an incomplete model of Alzheimer disease. *Exp. Neurol.* 188, 52–64

261 Loerch, P.M. *et al.* (2008) Evolution of the Aging Brain Transcriptome and Synaptic Regulation. *PLoS One* 3, 3329

262 Xiang, X. *et al.* (2018) The Trem2 R47H Alzheimer's risk variant impairs splicing and reduces Trem2 mRNA and protein in mice but not in humans. *Mol. Neurodegener.* 13,

263 Wilmut, I. *et al.* (1997) Viable offspring derived from fetal and adult mammalian cells. *Nature* 385, 810–813

264 Takahashi, K. *et al.* (2007) Induction of pluripotent stem cells from adult human fibroblasts by defined factors. *Cell* 131, 861–72

265 Takahashi, K. *et al.* (2006) Induction of pluripotent stem cells from mouse embryonic and adult fibroblast cultures by defined factors. *Cell* 126, 663–76

266 Shi, Y. *et al.* (2016) Induced pluripotent stem cell technology: a decade of progress. *Nat. Rev. Drug Discov. 2016 162* 16, 115–130

267 Zhang, Y. *et al.* (2013) Rapid single-step induction of functional neurons from human pluripotent stem cells. *Neuron* 78, 785–798

268 Shi, Y. *et al.* (2012) Directed differentiation of human pluripotent stem cells to cerebral cortex neurons and neural networks. *Nat. Protoc.* 7, 1836–1846

269 Kriks, S. *et al.* (2011) Dopamine neurons derived from human ES cells efficiently engraft in animal models of Parkinson's disease. *Nat. 2011 4807378* 480, 547–551

270 TCW, J. *et al.* (2017) An Efficient Platform for Astrocyte Differentiation from Human Induced Pluripotent Stem Cells. *Stem Cell Reports* 9, 600

271 Haenseler, W. *et al.* (2017) A Highly Efficient Human Pluripotent Stem Cell Microglia Model Displays a Neuronal-Co-culture-Specific Expression Profile

and Inflammatory Response. *Stem cell reports* 8, 1727–1742

272 Rouhani, F. *et al.* (2014) Genetic Background Drives Transcriptional Variation in Human Induced Pluripotent Stem Cells. *PLOS Genet.* 10, e1004432

273 Kyttälä, A. *et al.* (2016) Genetic Variability Overrides the Impact of Parental Cell Type and Determines iPSC Differentiation Potential. *Stem Cell Reports* 6, 200–212

274 Chandrasegaran, S. and Carroll, D. (2016) Origins of Programmable Nucleases for Genome Engineering. *J. Mol. Biol.* 428, 963–989

275 Cong, L. *et al.* (2013) Multiplex genome engineering using CRISPR/Cas systems. *Science* 339, 819–23

276 Rehbach, K. *et al.* (2020) Integrating CRISPR Engineering and hiPSC-Derived 2D Disease Modeling Systems. *J. Neurosci.* 40, 1176 LP – 1185

277 Deltcheva, E. *et al.* (2011) CRISPR RNA maturation by trans-encoded small RNA and host factor RNase III. *Nature* 471, 602–607

278 Jinek, M. *et al.* (2012) A programmable dual-RNA-guided DNA endonuclease in adaptive bacterial immunity. *Science* 337, 816–821

279 Rodgers, K. and Mcvey, M. (2016) Error-prone repair of DNA double-strand breaks. *J. Cell. Physiol.* 231, 15

280 Mout, R. *et al.* (2017) Direct Cytosolic Delivery of CRISPR/Cas9-Ribonucleoprotein for Efficient Gene Editing. *ACS Nano* 11, 2452–2458

281 Ran, F.A. *et al.* (2013) Double nicking by RNA-guided CRISPR Cas9 for enhanced genome editing specificity. *Cell* 154, 1380

282 Choudhary, E. *et al.* (2015) Gene silencing by CRISPR interference in mycobacteria. *Nat. Commun. 2015 61* 6, 1–11

283 Mladenova, V. *et al.* (2016) Novel biological approaches for testing the

contributions of single DSBs and DSB clusters to the biological effects of high LET radiation. *Front. Oncol.* 6, 163

284 Lee, C. *et al.* (2020) The Use of Patient-Derived Induced Pluripotent Stem Cells for Alzheimer's Disease Modeling. *Prog. Neurobiol.* 192, 101804

285 Yagi, T. *et al.* (2011) Modeling familial Alzheimer's disease with induced pluripotent stem cells. *Hum. Mol. Genet.* 20, 4530–4539

286 Kondo, T. *et al.* (2017) iPSC-Based Compound Screening and In Vitro Trials Identify a Synergistic Anti-amyloid β Combination for Alzheimer's Disease. *Cell Rep.* 21, 2304–2312

287 Arber, C. *et al.* (2019) Amyloid precursor protein processing in human neurons with an allelic series of the PSEN1 intron 4 deletion mutation and total presenilin-1 knockout. *Brain Commun.* 1,

288 Woodruff, G. *et al.* (2013) The Presenilin-1 ΔE9 mutation results in reducedγ-secretase activity, but not total loss of PS1 function, in isogenichuman stem cells. *Cell Rep.* 5, 974–985

289 Ortiz-Virumbrales, M. *et al.* (2017) CRISPR/Cas9-Correctable mutation-related molecular and physiological phenotypes in iPSC-derived Alzheimer's PSEN2N141I neurons. *Acta Neuropathol. Commun.* 5,

290 Ye, T. *et al.* (2021) Efficient manipulation of gene dosage in human iPSCs using CRISPR/Cas9 nickases. *Commun. Biol. 2021 41* 4, 1–10

291 Muratore, C.R. *et al.* (2014) The familial Alzheimer's disease APPV717I mutation alters APP processing and Tau expression in iPSC-derived neurons. *Hum. Mol. Genet.* 23, 3523–3536

292 Muratore, C.R. *et al.* (2017) Cell-type Dependent Alzheimer's Disease Phenotypes: Probing the Biology of Selective Neuronal Vulnerability. *Stem cell*

reports **9, 1868–1884**

293 Moore, S. *et al.* (2015) APP Metabolism Regulates Tau Proteostasis in Human Cerebral Cortex Neurons. *Cell Rep.* 11, 689–696

294 Fong, L.K. *et al.* (2018) Full-length amyloid precursor protein regulates lipoprotein metabolism and amyloid-β clearance in human astrocytes. *J. Biol. Chem.* 293, 11341

295 Arber, C. *et al.* (2019) Familial Alzheimer's disease patient-derived neurons reveal distinct mutation-specific effects on amyloid beta. *Mol. Psychiatry 2019 2511* 25, 2919–2931

296 Hu, N.W. *et al.* (2018) Extracellular Forms of Aβ and Tau from iPSC Models of Alzheimer's Disease Disrupt Synaptic Plasticity. *Cell Rep.* 23, 1932

297 Arber, C. *et al.* (2021) Familial Alzheimer's Disease Mutations in PSEN1 Lead to Premature Human Stem Cell Neurogenesis. *CellReports* 34, 108615

298 Hung, C.O.Y. and Livesey, F.J. (2018) Altered γ-Secretase Processing of APP Disrupts Lysosome and Autophagosome Function in Monogenic Alzheimer's Disease. *Cell Rep.* 25, 3647

299 Maloney, J.A. *et al.* (2014) Molecular mechanisms of Alzheimer disease protection by the A673T allele of amyloid precursor protein. *J. Biol. Chem.* 289, 30990–31000

300 Israel, M.A. *et al.* (2012) Probing sporadic and familial Alzheimer's disease using induced pluripotent stem cells. *Nature* 482, 216–220

301 Kondo, T. *et al.* (2013) Modeling Alzheimer's Disease with iPSCs Reveals Stress Phenotypes Associated with Intracellular Aβ and Differential Drug Responsiveness. *Cell Stem Cell* 12, 487–496

302 Ochalek, A. *et al.* (2017) Neurons derived from sporadic Alzheimer's disease

iPSCs reveal elevated TAU hyperphosphorylation, increased amyloid levels, and GSK3B activation. ***Alzheimers. Res. Ther.*** **9, 90**

303 Armijo, E. ***et al.*** **(2017) Increased susceptibility to Aβ toxicity in neuronal cultures derived from familial Alzheimer's disease (PSEN1-A246E) induced pluripotent stem cells.** ***Neurosci. Lett.*** **639, 74–81**

304 Lin, Y.T. ***et al.*** **(2018) APOE4 causes widespread molecular and cellular alterations associated with Alzheimer's disease phenotypes in human iPSC-derived brain cell types.** ***Neuron*** **98, 1141**

305 Wadhwani, A.R. ***et al.*** **(2019) Neuronal apolipoprotein E4 increases cell death and phosphorylated tau release in alzheimer disease.** ***Ann. Neurol.*** **85, 726–739**

306 Wang, C. ***et al.*** **(2018) Gain of toxic Apolipoprotein E4 effects in Human iPSC-Derived Neurons Is Ameliorated by a Small-Molecule Structure Corrector.** ***Nat. Med.*** **24, 647**

307 McQuade, A. ***et al.*** **(2020) Gene expression and functional deficits underlie TREM2-knockout microglia responses in human models of Alzheimer's disease.** ***Nat. Commun. 2020 111*** **11, 1–17**

308 Hall-Roberts, H. ***et al.*** **(2020) TREM2 Alzheimer's variant R47H causes similar transcriptional dysregulation to knockout, yet only subtle functional phenotypes in human iPSC-derived macrophages.** ***Alzheimers. Res. Ther.*** **12,**

309 Altschul, S.F. ***et al.*** **(1990) Basic local alignment search tool.** ***J. Mol. Biol.*** **215, 403–10**

310 Koychev, I. ***et al.*** **(2019) Deep and Frequent Phenotyping study protocol: An observational study in prodromal Alzheimer's disease.** ***BMJ Open*** **9, e024498**

311 Tallon-Baudry, C. and Bertrand, O. (1999) Oscillatory gamma activity in humans and its role in object representation. ***Trends Cogn. Sci.*** **3, 151–162**

312 Jin, M. *et al.* (2018) An in vitro paradigm to assess potential anti-Aβ antibodies for Alzheimer's disease. *Nat. Commun.* 9,

313 Schindelin, J. *et al.* (2012) Fiji: an open-source platform for biological-image analysis. *Nat. Methods 2012 97* 9, 676–682

314 Tinevez, J.Y. *et al.* (2017) TrackMate: An open and extensible platform for single-particle tracking. *Methods* 115, 80–90

315 Szendrei, G.I. *et al.* (1993) Recognition of the minimal epitope of monoclonal antibody Tau-1 depends upon the presence of a phosphate group but not its location. *J. Neurosci. Res.* 34, 243–249

316 Porzig, R. *et al.* (2007) Epitope mapping of mAbs AT8 and Tau5 directed against hyperphosphorylated regions of the human tau protein. *Biochem. Biophys. Res. Commun.* 358, 644–649

317 Kosik, K.S. *et al.* (1988) Epitopes that span the tau molecule are shared with paired helical filaments. *Neuron* 1, 817–825

318 Arlotta, P. *et al.* (2005) Neuronal Subtype-Specific Genes that Control Corticospinal Motor Neuron Development In Vivo. *Neuron* 45, 207–221

319 Bulfone, A. *et al.* (1995) T-Brain-1: A homolog of Brachyury whose expression defines molecularly distinct domains within the cerebral cortex. *Neuron* 15, 63–78

320 Nieto, M. *et al.* (2004) Expression of Cux-1 and Cux-2 in the subventricular zone and upper layers II-IV of the cerebral cortex. *J. Comp. Neurol.* 479, 168–180

321 Omote, H. *et al.* (2011) Vesicular neurotransmitter transporter: bioenergetics and regulation of glutamate transport. *Biochemistry* 50, 5558–5565

322 Zhang, X.H. *et al.* (2015) Off-target Effects in CRISPR/Cas9-mediated Genome Engineering. *Mol. Ther. - Nucleic Acids* 4, e264

323 Lindeboom, R.G.H. *et al.* (2016) The rules and impact of nonsense-mediated mRNA decay in human cancers. *Nat. Genet.* 48, 1112

324 Mateos-Aparicio, P. *et al.* (2020) Challenges in Physiological Phenotyping of hiPSC-Derived Neurons: From 2D Cultures to 3D Brain Organoids. *Front. Cell Dev. Biol.* 8,

325 Mungenast, A.E. *et al.* (2016) Modeling Alzheimer's disease with human induced pluripotent stem (iPS) cells. *Mol. Cell. Neurosci.* 73, 13–31

326 Gilmore, E.G. and Herrup, K. (1997) Cortical development: Layers of complexity. *Curr. Biol.* 7, R231–R234

327 Beevers, J.E. *et al.* (2017) MAPT Genetic Variation and Neuronal Maturity Alter Isoform Expression Affecting Axonal Transport in iPSC-Derived Dopamine Neurons. *Stem Cell Reports* 9, 587–599

328 Sposito, T. *et al.* (2015) Developmental regulation of tau splicing is disrupted in stem cell-derived neurons from frontotemporal dementia patients with the 10 + 16 splice-site mutation in MAPT. *Hum. Mol. Genet.* 24, 5260–5269

329 Brandt, R. *et al.* (1995) Interaction of tau with the neural plasma membrane mediated by tau's amino-terminal projection domain. *J. Cell Biol.* 131, 1327–1340

330 Liu, C. and Götz, J. (2013) Profiling Murine Tau with 0N, 1N and 2N Isoform-Specific Antibodies in Brain and Peripheral Organs Reveals Distinct Subcellular Localization, with the 1N Isoform Being Enriched in the Nucleus. *PLoS One* 8, e84849

331 Lam, R.S. *et al.* (2017) Functional Maturation of Human Stem Cell-Derived Neurons in Long-Term Cultures. *PLoS One* 12, e0169506

332 Hedegaard, A. *et al.* (2020) Pro-maturational Effects of Human iPSC-Derived

Cortical Astrocytes upon iPSC-Derived Cortical Neurons. *Stem Cell Reports* 15, 38–51

333 Vickers, J.C. *et al.* (1996) Dystrophic neurite formation associated with age-related beta amyloid deposition in the neocortex: clues to the genesis of neurofibrillary pathology. *Exp. Neurol.* 141, 1–11

334 Yuan, A. *et al.* (2008) Axonal Transport Rates In Vivo Are Unaffected by Tau Deletion or Overexpression in Mice. *J. Neurosci.* 28, 1682–1687

335 Sheng, Z.H. and Cai, Q. (2012) Mitochondrial transport in neurons: impact on synaptic homeostasis and neurodegeneration. *Nat. Rev. Neurosci. 2012 132* 13, 77–93

336 Stokin, G.B. *et al.* (2005) Axonopathy and transport deficits early in the pathogenesis of Alzheimer's diseases. *Science (80-.).* 307, 1282–1288

337 Onyango, I.G. *et al.* (2016) Mitochondrial Dysfunction in Alzheimer's Disease and the Rationale for Bioenergetics Based Therapies. *Aging Dis.* 7, 201

338 Pallo, S.P. and Johnson, G.V.W. (2015) Tau facilitates Aβ-induced loss of mitochondrial membrane potential independent of cytosolic calcium fluxes in mouse cortical neurons. *Neurosci. Lett.* 597, 32–37

339 Jara, C. *et al.* (2018) Genetic ablation of tau improves mitochondrial function and cognitive abilities in the hippocampus. *Redox Biol.* 18, 279–294

340 Selznick, L.A. *et al.* (1999) In situ immunodetection of neuronal caspase-3 activation in Alzheimer disease. *J. Neuropathol. Exp. Neurol.* 58, 1020–1026

341 Su, J.H. *et al.* (2001) Activated caspase-3 expression in Alzheimer's and aged control brain: correlation with Alzheimer pathology. *Brain Res.* 898, 350–357

342 Schnapp, B.J. and Reese, T.S. (1989) Dynein is the motor for retrograde axonal transport of organelles. *Proc. Natl. Acad. Sci. U. S. A.* 86, 1548–1552

343 Hirokawa, N. *et al.* (1991) Kinesin associates with anterogradely transported membranous organelles in vivo. *J. Cell Biol.* 114, 295–302

344 Pilling, A.D. *et al.* (2006) Kinesin-1 and Dynein are the primary motors for fast transport of mitochondria in Drosophila motor axons. *Mol. Biol. Cell* 17, 2057–2068

345 Mandelkow, E.M. *et al.* (2003) Clogging of axons by tau, inhibition of axonal traffic and starvation of synapses. *Neurobiol. Aging* 24, 1079–1085

346 Ebneth, A. *et al.* (1998) Overexpression of tau protein inhibits kinesin-dependent trafficking of vesicles, mitochondria, and endoplasmic reticulum: implications for Alzheimer's disease. *J. Cell Biol.* 143, 777–794

347 Kubo, A. *et al.* (2019) Distribution of endogenous normal tau in the mouse brain. *J. Comp. Neurol.* 527, 985

348 Mondragón-Rodríguez, S. *et al.* (2012) Interaction of Endogenous Tau Protein with Synaptic Proteins Is Regulated by N-Methyl-d-aspartate Receptor-dependent Tau Phosphorylation *. *J. Biol. Chem.* 287, 32040–32053

349 Chen, Q. *et al.* (2012) Tau protein is involved in morphological plasticity in hippocampal neurons in response to BDNF. *Neurochem. Int.* 60, 233–242

350 Velazquez, R. *et al.* (2018) Acute tau knockdown in the hippocampus of adult mice causes learning and memory deficits. *Aging Cell* 17,

351 Shankar, G.M. *et al.* (2008) Amyloid-β protein dimers isolated directly from Alzheimer's brains impair synaptic plasticity and memory. *Nat. Med.* 14, 837–842

352 Schneggenburger, R. and Rosenmund, C. (2015) Molecular mechanisms governing Ca(2+) regulation of evoked and spontaneous release. *Nat. Neurosci.* 18, 935–941

353 Liu, S. *et al.* (2017) Accelerated kindling epileptogenesis in Tg4510 tau transgenic mice, but not in tau knockout mice. *Epilepsia* 58, e136–e141

354 Pallo, S.P. *et al.* (2016) Mechanisms of tau and Aβ-induced excitotoxicity. *Brain Res.* 1634, 119–131

355 Bezzina, C. *et al.* (2015) Early Onset of Hypersynchronous Network Activity and Expression of a Marker of Chronic Seizures in the Tg2576 Mouse Model of Alzheimer's Disease. *PLoS One* 10,

356 Morris, M. *et al.* (2011) The Many Faces of Tau. *Neuron* 70, 410

357 Ma, Q. *et al.* (2014) Loss of MAP Function Leads to Hippocampal Synapse Loss and Deficits in the Morris Water Maze with Aging. *J. Neurosci.* 34, 7124–7136

358 Braun, N.J. *et al.* Mechanical injuries of neurons induce tau mislocalization to dendritic spines and tau-dependent synaptic dysfunction. DOI: 10.1073/pnas.2008306117/-/DCSupplemental

359 Pallas-Bazarra, N. *et al.* (2016) Novel function of Tau in regulating the effects of external stimuli on adult hippocampal neurogenesis. *EMBO J.* 35, 1417–1436

360 Busche, M.A. *et al.* (2008) Clusters of hyperactive neurons near amyloid plaques in a mouse model of Alzheimer's disease. *Science (80-.).* 321, 1686–1689

361 Lagomarsino, V.N. *et al.* (2021) Stem cell-derived neurons reflect features of protein networks, neuropathology, and cognitive outcome of their aged human donors. *Neuron* 109, 3402-3420.e9

362 Volpato, V. *et al.* (2018) Reproducibility of Molecular Phenotypes after Long-Term Differentiation to Human iPSC-Derived Neurons: A Multi-Site Omics Study. *Stem Cell Reports* 11, 897–911

363 Davies, C.A. *et al.* (1987) A quantitative morphometric analysis of the neuronal and synaptic content of the frontal and temporal cortex in patients with

Alzheimer's disease. *J. Neurol. Sci.* 78, 151–164

364 RD, T. *et al.* (1991) Physical basis of cognitive alterations in Alzheimer's disease: synapse loss is the major correlate of cognitive impairment. *Ann. Neurol.* 30, 572–580

365 Arevalo-Rodriguez, I. *et al.* (2015) Mini-Mental State Examination (MMSE) for the detection of Alzheimer's disease and other dementias in people with mild cognitive impairment (MCI). *Cochrane Database Syst. Rev.* 2015,

366 Folstein, M.F. *et al.* (1975) "Mini-mental state". A practical method for grading the cognitive state of patients for the clinician. *J. Psychiatr. Res.* 12, 189–198

367 Mandal, P.K. *et al.* A comprehensive review of magnetoencephalography (MEG) studies for brain functionality in healthy aging and Alzheimer's disease (AD). , *Frontiers in Computational Neuroscience*, 12. 23-Aug-(2018) , Frontiers Media SA, 60

368 Proudfoot, M. *et al.* (2014) Magnetoencephalography. *Pract. Neurol.* 14, 336

369 DeKosky, S.T. and Scheff, S.W. (1990) Synapse loss in frontal cortex biopsies in Alzheimer's disease: Correlation with cognitive severity. *Ann. Neurol.* 27, 457–464

370 Ikeda, Y. *et al.* (2020) Spontaneous MEG activity of the cerebral cortex during eyes closed and open discriminates Alzheimer's disease from cognitively normal older adults. *Sci. Rep.* 10, 1–9

371 O'Brien, J.L. *et al.* (2010) Longitudinal fMRI in elderly reveals loss of hippocampal activation with clinical decline. *Neurology* 74, 1969–1976

372 Dickerson, B.C. *et al.* (2005) Increased hippocampal activation in mild cognitive impairment compared to normal aging and AD. *Neurology* 65, 404–411

373 Romoli, M. *et al.* (2021) Amyloid-β: a potential link between epilepsy and

cognitive decline. ***Nat. Rev. Neurol. 2021 178*** **17, 469–485**

374 Kurucu, H. ***et al.*** **(2021) Inhibitory synapse loss and accumulation of amyloid beta in inhibitory presynaptic terminals in Alzheimer's disease.** ***Eur. J. Neurol.*** **00, 1–13**

375 Choi, S.R. ***et al.*** **(2009) Preclinical Properties of 18F-AV-45: A PET Agent for Aβ Plaques in the Brain.** ***J. Nucl. Med.*** **50, 1887**

376 Jarrett, J.T. ***et al.*** **(1993) The Carboxy Terminus of the β Amyloid Protein Is Critical for the Seeding of Amyloid Formation: Implications for the Pathogenesis of Alzheimer's Disease.** ***Biochemistry*** **32, 4693–4697**

377 Esler, W.P. ***et al.*** **(1996) In Vitro Growth of Alzheimer's Disease β-Amyloid Plaques Displays First-Order Kinetics†.** ***Biochemistry*** **35, 749–757**

378 Yang, Y. ***et al.*** **(2022) Cryo-EM structures of amyloid-β 42 filaments from human brains.** ***Science*** **375, 167–172**

379 Hoover, B.R. ***et al.*** **(2010) Tau Mislocalization to Dendritic Spines Mediates Synaptic Dysfunction Independently of Neurodegeneration.** ***Neuron*** **68, 1067–1081**

380 Pickett, E.K. ***et al.*** **(2017) Spread of tau down neural circuits precedes synapse and neuronal loss in the rTgTauEC mouse model of early Alzheimer's disease.** ***Synapse*** **71,**

381 Hill, E. ***et al.*** **(2019) Introduction of Tau Oligomers into Cortical Neurons Alters Action Potential Dynamics and Disrupts Synaptic Transmission and Plasticity.** ***eNeuro*** **6,**

382 Kopeikina, K.J. ***et al.*** **(2011) Tau accumulation causes mitochondrial distribution deficits in neurons in a mouse model of tauopathy and in human Alzheimer's disease brain.** ***Am. J. Pathol.*** **179, 2071–2082**

383 Zhao, J. *et al.* (2017) APOE ε4/ε4 diminishes neurotrophic function of human iPSC-derived astrocytes. *Hum. Mol. Genet.* 26, 2690–2700

384 Oksanen, M. *et al.* (2017) PSEN1 Mutant iPSC-Derived Model Reveals Severe Astrocyte Pathology in Alzheimer's Disease. *Stem cell reports* 9, 1885–1897

385 Park, J. *et al.* (2018) A 3D human triculture system modeling neurodegeneration and neuroinflammation in Alzheimer's disease. *Nat. Neurosci. 2018 217* 21, 941–951

386 Guttikonda, S.R. *et al.* (2021) Fully defined human pluripotent stem cell-derived microglia and tri-culture system model C3 production in Alzheimer's disease. *Nat. Neurosci. 2021 243* 24, 343–354

387 Bassil, R. *et al.* (2021) Improved modeling of human AD with an automated culturing platform for iPSC neurons, astrocytes and microglia. *Nat. Commun. 2021 121* 12, 1–21

388 Lancaster, M.A. *et al.* (2013) Cerebral organoids model human brain development and microcephaly. *Nature* 501, 373–9

389 Velasco, S. *et al.* (2019) Individual brain organoids reproducibly form cell diversity of the human cerebral cortex. *Nat. 2019 5707762* 570, 523–527

390 Pellegrini, L. *et al.* (2020) Human CNS barrier-forming organoids with cerebrospinal fluid production. *Science* 369,

391 Zhao, J. *et al.* (2020) APOE4 exacerbates synapse loss and neurodegeneration in Alzheimer's disease patient iPSC-derived cerebral organoids. *Nat. Commun. 2020 111* 11, 1–14

392 Choi, S.H. *et al.* (2014) A three-dimensional human neural cell culture model of Alzheimer's disease. *Nat. 2014 5157526* 515, 274–278

393 Raja, W.K. *et al.* (2016) Self-Organizing 3D Human Neural Tissue Derived from

Induced Pluripotent Stem Cells Recapitulate Alzheimer's Disease Phenotypes. *PLoS One* 11, e0161969

394 Fu, H. *et al.* (2019) A tau homeostasis signature is linked with the cellular and regional vulnerability of excitatory neurons to tau pathology. *Nat. Neurosci.* 22, 47

395 Asai, H. *et al.* (2015) Depletion of microglia and inhibition of exosome synthesis halt tau propagation. *Nat. Neurosci.* 18, 1584

396 Narasimhan, S. *et al.* (2020) Human tau pathology transmits glial tau aggregates in the absence of neuronal tau. *J. Exp. Med.* 217,

397 Sagare, A.P. *et al.* (2013) Pericyte loss influences Alzheimer-like neurodegeneration in mice. *Nat. Commun.* 4,

398 Hardy, J. and De Strooper, B. (2017) Alzheimer's disease: where next for anti-amyloid therapies? *Brain* 140, 853–855

399 Frisoni, G.B. *et al.* (2021) The probabilistic model of Alzheimer disease: the amyloid hypothesis revised. *Nat. Rev. Neurosci. 2021 231* 23, 53–66

400 Devine, M.J. and Kittler, J.T. (2018) Mitochondria at the neuronal presynapse in health and disease. *Nat. Rev. Neurosci. 2018 192* 19, 63–80

401 Jahn, R. and Fasshauer, D. (2012) Molecular machines governing exocytosis of synaptic vesicles. *Nat. 2012 4907419* 490, 201–207

402 MacAskill, A.F. *et al.* (2009) Miro1 Is a Calcium Sensor for Glutamate Receptor-Dependent Localization of Mitochondria at Synapses. *Neuron* 61, 541–555

403 Reese, D. and Drapeau, P. (1998) Neurite Growth Patterns Leading to Functional Synapses in an Identified Embryonic Neuron. *J. Neurosci.* 18, 5652–5662

404 Ruhl, D.A. *et al.* (2019) Synaptotagmin 17 controls neurite outgrowth and

synaptic physiology via distinct cellular pathways. *Nat. Commun. 2019 101* 10, 1–14

405 DeVos, S.L. *et al.* (2017) Tau reduction prevents neuronal loss and reverses pathological tau deposition and seeding in mice with tauopathy. *Sci. Transl. Med.* 9,

406 DeVos, S.L. *et al.* (2013) Antisense Reduction of Tau in Adult Mice Protects against Seizures. *J. Neurosci.* 33, 12887–12897

407 Congdon, E.E. and Sigurdsson, E.M. (2018) Tau-targeting therapies for Alzheimer disease. *Nat. Rev. Neurol. 2018 147* 14, 399–415

408 Manos, J.D. *et al.* (2021) Uncovering Specificity of Endogenous Tau Aggregation in a Human iPSC-neuron Tau Seeding Model. *iScience* DOI: 10.1016/J.ISCI.2021.103658